High-Latitude Ocean Convection and Gyre Dynamics

Thesis by

Zhan Su

In Partial Fulfillment of the Requirements

for the Degree of

Doctor of Philosophy

California Institute of Technology

Pasadena, California

2016

(Defended May 13, 2016)

© 2016

Zhan Su

ORCID: 0000-0001-7603-7211

All Rights Reserved

To my wife, Wei (Becky) Zhang

Acknowledgements

I sincerely thank my advisor, Andy Ingersoll. During my first year at Caltech, I was struggling a lot in searching for my research interests. It was Andy who introduced me to the amazing world of GFD. I have been often amazed by Andy's ability to understand the physical nature of an unfamiliar problem from first physical principles. This over and over inspires me to sense the true beauty of physics. I also benefit from his emphasis on capturing the physical picture rather than playing with math alone, although Andy has a strong mathematical ability. I have been deeply inspired by Andy's approach of using very simple models to explain complicated phenomenon, which reveals the true charm of physics. I thank Andy for allowing me to "argue" with him freely on difficult questions: I will miss those times when we both became a little loud but still may not have persuaded each other. I am fully grateful that Andy gave me the freedom to pursue the topics I got interested in and to collaborate with other scientists. Further, I deeply thank Andy for his patience with me, especially when I was unproductive. Finally, the simple but wise life philosophy of Andy, in his 70s, has taught me vividly the true meaning of being a scientist: enjoy the fun of science itself rather than focusing on empty/trivial things.

I also thank my co-advisor, Andy Thompson. If Andy (Andy T., as in this para-

graph) did not come to Caltech five years ago, I cannot imagine the terrible consequences for me. Andy is an excellent teacher. I have taken at least three classes of Andy's, attended his weekly group-meeting discussions, and joined the seminars he organized. These quickly built up some crucial fundamentals of GFD for me, broadened my horizon for current research topics, and triggered my great interest to read more related literature/books. I thank him for all the patient answers to my often-naive questions in the past five years. Andy has a strong ability to sense the big physical picture, which significantly inspires me to intentionally connect all pieces of knowledge together. I am deeply inspired by Andy's extreme capability (yes, he is a superman) and wisdom, in doing high-quality science himself, developing well his research group, being gracious to people, and also taking good care of a big family. I benefit from his open-minded attitude and broad exploration in physical oceanography, which always remind me to not narrow myself in research.

I cannot thank Andy Thompson enough since he also brought Andrew Stewart to Caltech. Andrew Stewart is the master of process studies (conceptual physical thinking), which inspire me deeply. I will miss those wonderful two years when I could daily go to Andrew's office to ask him freely all kinds of GFD questions, which very much helped me to explore basic concepts of GFD. I cannot thank Andrew enough for that. Andrew is also very good at using elegant math to vividly illustrate the physics. This helped me significantly to sense the mathematical structure of GFD. The discussions with Andrew have always given me inspiring physical insights, allowed me to sense the fun of GFD, and often made me feel that there is hope ahead.

Finally, I thank Andrew for his career advice for me.

I thank Jess Adkins. I am always inspired by his knowledgeability and his sharp insights on science. I thank Dimitris Menemenlis for his efforts, patience, passion, and physical insights when we wrote proposals together. I thank Run-lie Shia deeply for his friendship, help, grace, and encouragement, especially during my early years at Caltech. He is often like a father to me and his physical insights often inspired me. I thank Patrice Klein for his great class and the productive discussions with him. I am encouraged by his passion for ocean turbulence. I thank Yuk Yung for his career advices and the inspiration from his self-discipline. I thank Simona Bordoni for her class and for her efforts at organizing the very beneficial dynamic reading classes. I thank Ron Kwok for his interests of collaboration on sea ice. I also thank other Caltech professors including Dave Stevenson, Paul Wennberg, Tapio Schneider, etc.

I thank the staff of Caltech/GPS for their many years' help and friendship, including Irma, Margaret, Ulrika, Bronagh, Tony Diaz, Mike Black, Ken, Scott, Liz Muira Boyd, Kathy Young, Nora, Dian, Marcia, Tess, etc. I thank other Caltech/GPSer for their friendship and the interactions, including Xiaolin Mao, Hao Cao, Cheng Li, Qiong Zhang, Yingdi Luo, Dunzhu Li, Yiran Ma, Xiaozhou, Georgy Manucharyan, Zach, Giuliana, Ayah Lazar, Stuart Bishop, Mar Flexas, Xuan Zhang, Peter Gao, Jinqiang, Xi Zhang, Zhihong Tan, Ke Zhang, Da Yang, Shawn, Dyudina, Alex Robel, Junle, Mike Wong, Mike Line, Fai, Pushkar, Nicole, Ting Yang, Ho-Hsuan, Tobias, Ritthink, Salvatore, Sophie, Yuehan, Masha, Zhongwen, Sally, Henry, Jose, Linlin Ye, Adam, etc.

I also give my deep appreciation to my other friends in my life, including Olivia and Sam Li, Daiqi Linghu, John Pang, Murray and Alison Sherk, David Wang, Haolei Weng, Qianfan Chen, Bin Hu, Yongqiang Lv, Dongyoon, Jennifer and Peter Kang, Andre and Raquel, Jomela, Aaron and Linsey, Andrew Del Rio, Charles Cao, Kyle Chen, Audrey Chen, Jose Nunez, Elton and Wenyan Chu, Eva and Bob, Austin and Lu, Bo Hao, Jessica, Ru Chen, Qianli Ma, Annie, Anand, Yang jin, Kein, Kevin and Henry, Zheyu Guo, Ryan, Zhitao, Xiaozhe, etc.

I thank my undergraduate advisors at USTC, Tao Li and Xiaofei Chen, for their advice and recommendations. I deeply thank my parents and my sister, Duanzhen Yin, Fangxing Su and Lu Su, for their many years' love and support. I especially thank my mother for her huge sacrifice as a housewife and taking care of me in every aspect of my life for about two decades. I thank my uncle, Ganhong Yin, for his love and grace to my family for so many years. I owe them too much.

Finally, I give my deepest appreciation to my wife, Wei (Becky) Zhang. Becky is the best blessing that God gives to me. She sacrificed so much for me by giving up her job as a doctor in China and came to US to be with me, a poor PhD student. The past 4 years have often been tough; but Becky was always there with me when I was depressed and felt discouraged. We cry and laugh together. Becky is such a soft, gracious, honest, and understanding wife that she has dramatically influenced my personality in a good way. I thank her so much for helping me to be more easygoing, more honest to my emotion, less judgmental towards others, knowing better about my identity, and freer to enjoy the life. I wish that our love continues to grow.

Abstract

High-latitude ocean deep convection substantially contributes to vertical mixing, vertical heat transport, deep-water formation, and sea-ice budget in the World Ocean. However, the extent of this contribution remains poorly constrained. The concept of ocean convective available potential energy (OCAPE) have been developed to improve the understanding and the prediction for these deep convection events. The kinetic energy (KE) budget of deep convection is explored analytically and numerically based on the observations in the Weddell Sea. OCAPE, which is derived from thermobaricity, is identified as a critical KE source to power ocean deep convection. Other significant contributions to the energetics of convection, including diabatic processes related to cabbeling and stratification, are also carefully quantified. An associated theory is developed to predict the maximum depth of convection. This work may provide a useful basis for improving the convection parameterization in ocean models.

As an application of the theory above, basin-scale OCAPE is found to be significantly built up in the North Atlantic at the end of Heinrich Stadial 1 ($\sim$17,000 years ago). This OCAPE is ultimately released to power strong ocean deep convection in North Atlantic as simulated by numerical models. This causes a $\sim$2 ^{o}C

sea surface warming for the whole basin (∼700 km) within a month and exposes a huge heat reservoir to the atmosphere. This may invigorate the Atlantic meridional overturning circulation and provide an important mechanism to explain the abrupt Bolling-Allerod warming.

Mesoscale turbulence is another crucial process for high-latitude ocean dynamics. From the physical nature of baroclinic instability, the framework of eddy-size-constrained Available Potential Energy (APE) density is developed, which is capable of well-detecting individual eddies and local eddy kinetic energy (EKE) in the World Ocean. This new framework is likely useful in parameterizing mesoscale eddies in ocean GCMs. Mesoscale turbulence are found to be coupled to the wind-driven Ekman pumping in determining the temperature and salinity budgets in subpolar gyres such as the Weddell Gyre. A conceptual model of the evolution of isopycnals has been developed in which the isopycnal responds to a seasonal oscillation in the surface wind stress. The model accurately predicts the observed phases of the temperature and salinity variability in relationship to the surface wind stress. The model, despite its heavy idealization, also accounts for more than 50% of the observed oscillation amplitude, which depends on the strength of the seasonal wind variability and the parameterized eddy diffusivity. These results highlight the importance of mesoscale eddies in modulating the export of AABW in narrow boundary layers around the Antarctic margins.

PUBLISHED CONTENT AND CONTRIBUTIONS

Su, Z., A.L. Stewart and A.F. Thompson (2014). "An idealized model of Weddell Gyre export variability". In: *Journal of Physical Oceanography*, 44, pp. 1671-1688. doi: 10.1175/JPO-D-13-0263.1.

Z.S. participated in developing the conceptual model, preparing the observational data, and writing the manuscript.

Su, Z., et al. (2016). "Information-rich spectral channels for simulated retrievals of partial column-averaged methane". In: *Earth and Space Science*, 3, pp. 2-14. doi: 10.1002/2015EA000120.

Z.S. participated in proposing the problem, analyzing the modeling, and writing the manuscript.

Su, Z., A.P. Ingersoll, A.L. Stewart and A.F. Thompson, (2016). "Ocean Convective Available Potential Energy. Part I: Concept and Calculation". In: *Journal of Physical Oceanography*, 46, pp. 1081-1096. doi: 10.1175/JPO-D-14-0155.1

Z.S. participated in developing the physical concept and writing the manuscript.

Su, Z., A.P. Ingersoll, A.L. Stewart and A.F. Thompson, (2016). "Ocean Convective Available Potential Energy. Part II: Energetics of Thermobaric Convection and Thermobaric Cabbeling". In: *Journal of Physical Oceanography*, 46, pp. 1097-1115. doi: 10.1175/JPO-D-14-0156.1

Z.S. participated in analyzing the simulation, and writing the manuscript.

Su, Z., A.P. Ingersoll, and F. He (2016). "On the abruptness of Bølling-Allerød warming". In: *Journal of Climate*, in press. doi:10.1175/JCLI-D-15-0675.1.

Z.S. participated in proposing the physical idea, and writing the manuscript.

Contents

[†]Appeared as: Su, Z., A.P. Ingersoll, A.L. Stewart and A.F. Thompson, 2016a. Ocean Convective Available Potential Energy. Part I: Concept and Calculation. Journal of Physical Oceanography, 46, 1081-1096

[†]Appeared as: Su, Z., A.P. Ingersoll, A.L. Stewart and A.F. Thompson, 2016b. Ocean Convective Available Potential Energy. Part II: Energetics of Thermobaric Convection and Thermobaric Cabbeling. Journal of Physical Oceanography, 46, 1097-1115

[†]Appeared as: Su, Z., A.P. Ingersoll and H. Feng, 2016. On the abruptness of Bolling-Allerod warming. Journal of Climate, doi:10.1175/JCLI-D-15-0675.1

[†]Appeared as: Su, Z. and A.P. Ingersoll, 2016. On the Minimum Potential Energy State and the eddy-size-constrained APE Density. Journal of Physical Oceanography, accepted

[†]Appeared as: Su, Z., A.L. Stewart and A.F. Thompson, 2014. An idealized model of Weddell Gyre export variability. Journal of Physical Oceanography, 44, 1671-1688

List of Tables

List of Figures

Introduction

High-latitude oceans are special due to the weak stratification, small deformation radius (∼5-20km), strong surface buoyancy forcing during wintertime (cooling, brine reject), rich bathymetry features (e.g. around continental shelf), and unusual boundary conditions such as sea ice on the top. Therefore, the dynamics in high-latitude oceans can be significantly different from lower-latitude regions. The associated dynamics have received increasing attentions in recent decades, either for the urgency of understanding the significant climatic effects of polar oceans, or simply for the joy of playing with geophysical fluid dynamics (GFD). This thesis mainly explores two important types of dynamics occurring in high-latitude oceans: deep convection and gyre dynamics.

0.1 Ocean deep convection

Ocean deep convection commonly occurs during wintertime, such as in the Labrador, Greenland, Mediterranean, and Weddell Seas. It is a powerful mechanism that exchanges tracers vertically, such as heat, salt and nutrients, between ocean surface and ocean depths (0.5-3 km) in typical very short timescales (days to weeks) (Marshall and Schott, 1999). Ocean deep convection produces ocean deep water, especially in the North Atlantic, and is a crucial diabatic closure for the global meridional overturning

circulation (MOC) (Wolfe and Cessi, 2011). Ocean deep convection can also significantly contribute to vertical mixing and the sea-ice budget (through the modification of sea surface temperature).

Ocean deep convection, despite its importance, has not been well understood due to the following reasons. (i) The observation of ocean deep convection is rare. This is because of the harsh wintertime observational conditions, and the short duration timescale and sporadic occurrence of deep convection. Therefore, the characteristics of ocean deep convection have not been well identified by observations. (ii) Numerically speaking, ocean deep convection occurs at such small horizontal scales (0.1-10 km) that it is usually unresolved in current ocean general circulation models (GCMs). There is potentially a large error bar, even when using the currently best-performing convective mixing parameterizations in GCMs, as demonstrated in Chapter 3. (iii) The traditional study for ocean deep convection typically focuses on the surface buoyancy forcing and the rotation effect (Marshall and Schott, 1999). However, the nonlinear effects of the equation of state of seawater (e.g., thermobaricity, cabbeling) may dramatically change the properties of ocean deep convection (Denbo and Skyllingstad, 1996). This, however, has been poorly studied and has not been integrated well (or at all) into ocean models (Denbo and Skyllingstad, 1996; Akitomo, 2011).

In Chapter 2 and Chapter 3 of this thesis, we study the energetics of ocean deep convection, from fundamental thermodynamics and fluid theories. Analyzing energetics is extremely useful in systematically understanding the dynamics and characterizing the convection properties (e.g., velocity magnitude, convection depth, vertical

mixing efficiency). We develop the framework of ocean convective available potential energy (OCAPE) to fully account for the contribution of thermobaricity to deep convection. This new framework can be easily applied in pragmatic diagnosis for the energy source of ocean convection, for either observations or numerical simulations. We also develop analytical methods to characterize the cabbeling's effect in convection energetics. These two kinds of nonlinearities are shown to strongly modulate the convection strength, convective timescale, and convection range (the upper and lower bounds of convective mixing) in typical wintertime polar oceans. Our theory of energetics is shown to be highly useful to predict the magnitude of convection and the convection depth, which are key for improving the parameterization of deep convection in ocean GCMs.

In Chapter 4 of this thesis, we apply our developed energy theory to analyze the paleoclimate. We show the significant errors that the current ocean GCM can cause, in contrast to a convection-resolved model, in simulating the effects of ocean deep convection. We show how thermobaricity can build up a huge magnitude of basin-scale ($\sim$700 km) OCAPE pattern through thousands of years' background buoyancy evolution. This OCAPE can be eventually and suddenly released to power a dramatic convection that overturns the basin-scale ocean within a month. This phenomenon, however, is totally missed in the ocean GCM.

0.2 The APE framework

Our Chapter 4 is also related to ocean energetics. The Available potential energy (APE), either in the Lorenz's form or the QG form, is recognized as the key energy

source for geostrophic ocean turbulence (Pedlosky, 1987). Unlike eddy kinetic energy (EKE) that is defined straightforwardly, APE is a complicated quantity related to the surrounding stratification for the considered parcel. This is associated with the physical picture of baroclinic instability, which extracts large-scale APE (mean APE) from the background stratification (or say, the vertical shear of mean flow) and converts it to eddy-scale (eddy APE). The eddy APE is then converted to EKE at around the deformation radius. Therefore, the APE around the eddy scale is essentially the direct energy source for EKE. In contrast, the classic definition of APE is based on whole-domain-scale parcel rearrangement to obtain the minimum potential energy (PE) state. Therefore, inspired by this contrast, we develop a new framework of APE in chapter 4 to better represent the APE source for baroclinic instability, which we show is useful to detect local eddies and EKE. Our study can also be treated as a new strategy to characterize the mesoscale eddies' signature in the ocean stratification.

0.3 High-latitude Gyre dynamics

Gyre dynamics are crucial for the heat and mass transport in subtropical and subpolar oceans (not for the Southern Ocean, though). The impacts of gyre can reach as deep as around 1-km depths (Vallis, 2006). Classic models for subtropical or subpolar gyre, i.e., the Munk's or Stommel's model, typically treat the gyre laminar and emphasize the Sverdrup effect and the resulting strong western boundary current due to the differential planetary rotation. However, recent high-resolution ocean simulations, such as ECCO2 products, reveal highly turbulent gyre features, such as around the Greenland and Weddell Seas. In chapter 5 of this thesis, we explore the crucial role

of mesoscale eddies in modulating the gyre evolution in both the stratification and the velocity field, at the gyre interior and boundaries.

Chapter 1

Ocean Convective Available Potential Energy. Part I: Concept and Calculation[†]

1.1 Abstract

Thermobaric convection (type II convection) and thermobaric cabbeling (type III convection) might substantially contribute to vertical mixing, vertical heat transport, and deep-water formation in the World Ocean. However, the extent of this contribution remains poorly constrained. The concept of ocean convective available potential energy (OCAPE), the thermobaric energy source for type II and type III convection, is introduced to improve the diagnosis and prediction of these convection events. OCAPE is analogous to atmospheric CAPE, which is a key energy source for atmospheric moist convection and has long been used to forecast moist convection. OCAPE is the potential energy (PE) stored in an ocean column arising from thermobaricity, defined as the difference between the PE of the ocean column and its minimum possible PE under adiabatic vertical parcel rearrangements. An ocean

[†]Appeared as: Su, Z., A.P. Ingersoll, A.L. Stewart and A.F. Thompson, 2016a. Ocean Convective Available Potential Energy. Part I: Concept and Calculation. Journal of Physical Oceanography, 46, 1081-1096

column may be stably stratified and still have nonzero OCAPE. I present an efficient theory for computing OCAPE accurately for any given column of seawater. They further derive analytical expressions for OCAPE for approximately two-layer ocean columns that are widely observed in polar oceans. This elucidates the dependence of OCAPE on key physical parameters. Hydrographic profiles from the winter Weddell Sea are shown to contain OCAPE (0.001-0.01 J/kg), and scaling analysis suggests that OCAPE may be substantially enhanced by wintertime surface buoyancy loss. The release of this OCAPE may substantially contribute to the kinetic energy of deep convection in polar oceans.

1.2 Introduction

Deep-water formation in the Labrador, Greenland and Mediterranean Seas is the result of open-ocean deep convection (Schott and Leaman, 1991; Clarke and Gascard, 1983; Marshall and Schott, 1999; Harcourt et al., 2002). Formation of Antarctic bottom water (AABW) is induced either by deep convection or by processes occurring around the continental margins (Gordon, 1978). Deep convection significantly contributes to the global ocean overturning circulation and has a prominent influence on the global transport of heat, salt and nutrients (Macdonald and Wunsch, 1996).

Akitomo (1999a,b) classified ocean deep convection into two types. The first type (Type I) is the convection of a "gradually deepening mixed layer" in a nearly homogeneous ocean, driven mainly by a continuous negative surface buoyancy flux and other preconditioning processes. The second type (Type II) is thermobaric convection. The term thermobaricity refers to the thermal expansion coefficient of seawater increasing

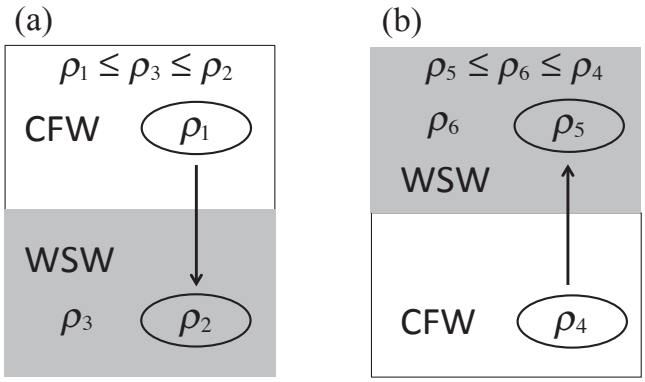

Figure 1.1: Illustration of thermobaric instability by an adiabatic parcel displacement from cold fresh water (CFW) to warm salty water (WSW) in either case (a) when CFW lies above WSW, or case (b) when CFW lies below WSW.

with pressure, which is larger near the freezing point than at higher temperatures (McDougall, 1987). Harcourt (2005) was the first to simulate Type III convection, also called thermobaric cabbeling, which involves strong modulation from cabbeling as well as thermobaricity. Type II convection involves plumes of cold fresh water (CFW) sinking into warm salty water (WSW). Type III convection involves convective plumes of a CFW/WSW mixture sinking into WSW due to cabbeling instability (Harcourt, 2005). Cabbeling instability is a convective phenomenon that occurs when water masses with different temperatures are mixed diabatically to produce a water mass with greater density than the parent waters (Carmack, 1979). For both types, thermobaricity and cabbeling are critical for the acceleration of convective plumes by generating negative buoyancy anomalies. Note that "cabbeling" in this manuscript always means the quadratic dependency of water density on potential temperature (McDougall, 1987).

Harcourt (2005) suggested that Type III convection may be responsible for thick, deep internal layers and localized "chimney" structures observed in the Weddell Sea.

Akitomo (2006) suggested that the overturning of Type II convection may penetrate to a depth of about 1.5 km on the flanks of the Maud Rise in the Weddell Sea. Type II and Type III convection may contribute to the observed water properties and velocities ($\sim$ 10 cm s^{-1}) of convective plumes in the Greenland Sea (Akitomo, 2011; Denbo and Skyllingstad, 1996). Type II and Type III convection may also be formation mechanisms for certain open-ocean Weddell polynyas, due to their ability to transport heat rapidly upwards resulting in sea ice melt (McPhee, 2000, 2003; Harcourt, 2005; Akitomo, 2007).

In this chapter we focus on the effect of thermobaricity only. As illustrated in Figure 1(a) (Figure 1(b)), for a column that is stably stratified, the movement of a parcel of CFW, or a CFW/WSW mixture, downward (upward) through the WSW adiabatically, may lead to the density of that parcel becoming greater (smaller) than that of the surrounding WSW. This is a result of the thermobaric effect: the effect of temperature on density increases with depth, so the CFW may become denser (less dense) than the WSW at depth (height). In this case potential energy (denoted as PE) will be released as the parcel sinks (rises) further. Note that moving a WSW parcel up (down) through the CFW never leads to a lower PE state. This is because the WSW parcel loses (gains) buoyancy relative to the CFW as it rises (sinks). Therefore, both Type II and Type III convection have an important source of kinetic energy (KE) that comes from the stored PE of the ocean column due to thermobaricity.

In this chapter (Su et al., 2016b) and next chapter (hereinafter Part II; Su et al., 2016c), we define and investigate a new concept, the Ocean Convective Available

Potential Energy (OCAPE) as an energy source for Type II and Type III convection due to thermobaricity. In this chapter we focus on the conceptual importance of OCAPE and provide examples of its amplitude based on observations in the Weddell Sea. Dynamical analyses relevant to OCAPE release and its transformation efficiency into KE are presented in Part II. In Part II, we also evaluate the KE contribution to Type II and Type III convection due to diabatic processes (*e.g.*, effects due to cabbeling and stratification).

OCAPE is conceptually important: it parallels atmospheric Convective Available Potential Energy (CAPE), a key energy source in atmospheric moist convection that has long been used to forecast moist convection (see, *e.g.*, chapter 7.4.1 of Salby, 1996; Arakawa and Schubert, 1974; Emanuel et al., 1994; Trenberth, 2005; Zhang, 2009). Both CAPE and OCAPE measure the maximum stored PE that can be released under adiabatic vertical parcel rearrangements[1]. CAPE arises from moisture in the lower atmosphere, whereas OCAPE arises from the ocean stratification with CFW lying above or below WSW. CAPE is released when moist air parcels gain buoyancy via the release of latent heat, when they are perturbed upward and saturate at a critical pressure. OCAPE is released when parcels of CFW, or a CFW/WSW mixture, lose (gain) buoyancy via thermobaricity, when they are moved down (up) through the WSW layer past a critical depth. CAPE can be calculated by comparing the adiabatic lapse rate of moist parcels with the background temperature profile (Salby, 1996). OCAPE can be calculated by the strategy developed in this chapter. CAPE is

[1]An adiabatic process in this chapter always refers to a reversible process with no viscous dissipation and no exchanges of heat and salt.

widely used in subgrid-scale convective parameterization closures in atmopheric general circulation models (GCMs) (Zhang and McFarlane, 1995; Gregory et al., 2000). OCAPE might be similarly useful to improve the subgrid-scale parameterizations of Type II and Type III convection in present ocean GCMs, as demonstrated in this chapter and Part II.

In section 1.3, we quantitatively define OCAPE, which is the maximal PE, including internal energy and gravitational energy, of an ocean column available to be transformed into KE by vertical adiabatic parcel rearrangements. OCAPE is similar to available potential energy (APE) in the sense that they are both based on adiabatic parcel rearrangements and are both based on the global minimum-PE state. However, OCAPE arises from thermobaricity whereas APE arises mainly from baroclinicity (For APE, see Winters et al., 1995; Huang, 2005; Vallis, 2006). In section 1.4, we develop an accurate strategy to compute OCAPE, which is applicable to any vertical profile of seawater. In section 1.5 we derive analytical expressions for OCAPE in approximately two-layer profiles to elucidate the dependence of OCAPE on key parameters in the real ocean. In section 1.6, we investigate OCAPE in the Weddell Sea using hydrographic profiles. Section 1.7 comprises our discussion and conclusions.

1.3 Definition of Ocean Convective Available Potential Energy (OCAPE)

A system tends to deform to minimize its PE according to the principle of minimum total potential energy (*e.g.*, Reddy, 2002). For most complex systems, there is one state of global minimum PE and many states of local minimum PE in which the system can reside. This is true for ocean columns because of the nonlinear equation

of state (EOS) of seawater (see section 1.4 for details). Specifically, stably stratified profiles of temperature and salinity may not be equivalent to a global minimum PE state. For these profiles, Type II or Type III convection may release PE and evolve the system from a state of local minimum PE into a state of lower local minimum PE or even global minimum PE. Note that the states of local or global minimum PE may be modified significantly by diabatic processes that typically occur during the convection.

In this chapter, we follow the definition of APE, a key concept for ocean mesoscale geostrophic turbulence, to define OCAPE. APE is defined as the maximal PE that can be released by adiabatic parcel rearrangements, arising mainly from the baroclinicity of the system[2]. OCAPE is defined for an ocean column (*i.e.*, without horizontal inhomogeneity and thus without baroclinicity) as the maximal PE that can be released by adiabatic vertical parcel rearrangements, arising from thermobaricity. We use the term "Reference state" with regard to the state of global minimum PE that can be reached by adiabatic parcel rearrangements from the "Current state". Therefore our definition of OCAPE is

$$\text{OCAPE} = \text{PE}(\text{Current state}) - \text{PE}(\text{Reference state}), \tag{1.1}$$

where PE includes gravitational energy and internal energy. As mentioned above, the Reference state (and thus OCAPE) may evolve over time if water properties are modified diabatically during convection. In other words, all the terms in (1.1) may

[2]See section 3.10 of Vallis (2006), section 2b of Huang (2005), and section 3 of Winters et al. (1995).

be a function of time. We investigate this effect of diabatic processes for OCAPE (and Type II and Type III convection) in Part II.

Calculating OCAPE directly using (1.1) is awkward because PE is not a thermodynamic variable. For a single column with the bottom at constant level z_{bot}, PE can be generally defined as

$$\frac{\mathrm{PE}}{area} = \int_{z_{bot}}^{z_{top}} (U + gz)\rho \mathrm{d}z + z_{top}P_{top}, \tag{1.2}$$

where U is the internal energy, gz is the gravitational energy with g constant, $z_{top}P_{top}$ is the work done by atmospheric pressure on the column, and z_{top} is the level of the ocean surface. By inserting hydrostatic balance $\int_{z_{bot}}^{z_{top}} gz\rho \mathrm{d}z = -zP|_{bot}^{top} + \int_{z_{bot}}^{z_{top}} P \mathrm{d}z$ into (1.2), we obtain

$$\frac{\mathrm{PE}}{area} = \int_{z_{bot}}^{z_{top}} (U + P/\rho)\rho \mathrm{d}z + z_{bot}P_{bot} = H + z_{bot}P_{bot}, \tag{1.3}$$

where $(U + P/\rho)$ is the specific enthalpy and $H = \int_{z_{bot}}^{z_{top}} (U + P/\rho)\rho \mathrm{d}z$ is the total enthalpy of the column per unit area. For an isolated column with a fixed bottom, $z_{bot}P_{bot}$ is constant during convection due to mass conservation. Thus from (1.3) we can use column enthalpy to represent column PE, consistent with Reid et al. (1981). Therefore OCAPE can also be defined as

$$\mathrm{OCAPE} = H(\mathrm{Current\,state}) - H(\mathrm{Reference\,state}). \tag{1.4}$$

Here OCAPE has dimensions of energy/area; later for convenience we also use dimensions of energy/mass for OCAPE (column-averaged). Enthalpy is a thermodynamic variable, and is therefore easier to diagnose than PE for both theoretical and numerical studies. Given the vertical profiles of temperature and salinity of an ocean column, we can calculate the column enthalpy directly, *e.g.*, using the Gibbs function (Feistel, 2003).

For a stably or neutrally stratified ocean column ($N^2 \geqslant 0$) the existence of OCAPE is entirely due to thermobaricity. To demonstrate this, we perform the following thought experiment. First note that the salinity contraction coefficient is nearly independent of pressure (as shown in section 1.5). That is the density satisfies $\partial^2\rho/\partial S\partial P|_\theta \approx 0$, where S and θ are salinity and potential temperature respectively. If there is no thermobaricity, *i.e.* $\partial^2\rho/\partial\theta\partial P|_S = 0$, then the adiabatic compressibility $\partial\rho/\partial P$ is independent of θ and S. Therefore, ρ must have the form $\rho = \rho_1(\theta, S) + \rho_2(P)$ and ρ_1 increases monotonically with depth since $N^2 \geqslant 0$ here[3]. Therefore any exchange of parcels with different ρ_1 leads to an unstable stratification, as the rearrangement necessarily leads to a non-monotonic profile of ρ_1 with depth. Now we demonstrate that in this scenario the PE (or enthalpy) of the system can not be reduced by adiabatically swapping the positions of any parcels of equal mass. First, note that in general any parcel rearrangement can be decomposed into a series of equal-mass two-parcel exchanges. For adiabatic exchanges there is no change in entropy nor salinity, so the variation of specific enthalpy $\mathrm{d}\eta$ of any exchanged parcel

[3]In this scenario, N^2 is independent from $\rho_2(P)$ by its definition. See section 2.9.2 of Vallis (2006).

is $\mathrm{d}P/\rho$. We denote the swapped parcels as i and j with equal masses m, and their initial pressures as P_i and P_j, where $P_i < P_j$. It may be shown that the change in system's enthalpy associated with the exchange is

$$m \int_{P_j}^{P_i} \left(\frac{1}{\rho_1(\theta_j, S_j) + \rho_2(P)} - \frac{1}{\rho_1(\theta_i, S_i) + \rho_2(P)} \right) \mathrm{d}P. \tag{1.5}$$

This quantity is always positive or zero because $\rho_1(\theta_j, S_j) \geqslant \rho_1(\theta_i, S_i)$ and $\mathrm{d}P < 0$. Thus any parcel exchanges can not decrease the system's enthalpy, and so thermobaricity is necessary for a column to contain non-zero OCAPE.

1.4 Calculation strategy for OCAPE

Equation (1.4) shows that we can calculate OCAPE only if we are able to find the Reference state. Again, the Reference state has global minimum PE (or global minimum enthalpy) and can be reached through an adiabatic rearrangement of parcels from the Current state. However, this Reference state is difficult to determine due to the nonlinear EOS of seawater (Huang, 2005).

Consider a statically-stable ocean column, divided into M vertical layers with the same mass. Thus we have M parcels, and M vertical pressure positions defined by hydrostatic balance. We need to adiabatically rearrange the M parcels into the M vertical pressure positions to find the Reference state. For realistic continuous profiles, each parcel has its own unique salinity and potential temperature and the column has a total of $M!$ (the factorial of M) Rearrangement states, among which the Reference state is the one with minimum enthalpy. Note that M typically needs

to be larger than 50 to ensure sufficient accuracy of the OCAPE calculation. The number of Rearrangement states is so large ($M! > 3 \times 10^{64}$ even for $M = 50$) that it would be impossible for any modern computer to iterate through all of them (*e.g.*, see Burkard et al., 2009). We therefore need to develop a more effective strategy to solve this problem.

We label the M parcels as $1, 2, ..., M$ and label the M vertical pressure positions as $P_1, P_2, ..., P_M$. For parcel i with salinity S_i and potential temperature θ_i, its enthalpy at P_j is $h_{i,j} = h(\theta_i, S_i, P_j)$. Note again that salinity and potential temperature of a parcel are conserved under an adiabatic rearrangement. For a Rearrangement state in which parcel m ($m = 1, 2, ..., M$) is at pressure position P_k, we can define a matrix $\mathbf{x} = [x_{i,j}]\,(i, j = 1, ..., M)$ that maps the Current state to the Rearrangement state, with $x_{m,k} = 1$ and $x_{m,l} = 0\,(l \neq k, 1 \leqslant l \leqslant M)$ for $m = 1, 2, ..., M$. Thus the column enthalpy in this Rearrangement state is $\sum_{i=1}^{M}\sum_{j=1}^{M} h_{i,j}x_{i,j}$. Similarly we can define a matrix $\boldsymbol{h} = [h_{i,j}]\,(i, j = 1, ..., M)$. Therefore, the problem of searching for the Reference state with global minimum enthalpy is to solve the following problem:

$$\begin{aligned} &\text{Given an } M \times M \text{ matrix } \boldsymbol{h}, \text{ find an } M \times M \text{ matrix } \mathbf{x} \\ &\text{to minimize } \sum_{i=1}^{M}\sum_{j=1}^{M} h_{i,j}x_{i,j}\,, \text{ where } x_{i,j} = 0 \text{ or } 1, \\ &\text{subject to } \sum_{i=1}^{M} x_{i,j} = 1 \text{ for any } j, \text{ and} \sum_{j=1}^{M} x_{i,j} = 1 \text{ for any } i. \end{aligned} \tag{1.6}$$

Equation (1.6) is easy to solve if $h_{i,j}$ is a linear function of $j\,(j = 1, ..., M)$. However, in our case it is difficult to solve (1.6) because enthalpy $h_{i,j}$ is a nonlinear

function of pressure P_j due to thermobaricity. Fortunately, our problem (1.6) is actually the famous "assignment problem" in computational mathematics (Derigs, 1985; Martello and Toth, 1987; Bertsekas, 1988; Martello et al., 2000; Burkard et al., 2009; Krokhmal and Pardalos, 2009). This problem was effectively solved by the Hungarian algorithm (HA) with 100% accuracy (Kuhn, 1955; Lawler, 1976; Burkard et al., 2009). The HA is an iterative procedure that employs combinatorial optimization to find the minimum cost assignment $\sum_{i=1}^{M}\sum_{j=1}^{M} h_{i,j}x_{i,j}$. It can achieve a time complexity of $O(M^3)$, which is many orders of magnitude smaller than the $O(M!)$ time complexity of iterating through all the Rearrangement states.

In summary, given profiles of potential temperature and salinity of an ocean column, we interpolate them vertically into M continuous layers with the same mass in each layer. Then we compute the $M \times M$ matrix $\boldsymbol{h}$ numerically using the formula for enthalpy from Feistel (2003), and solve for the Reference state following the HA. Finally, we compute OCAPE using (1.4). In this manuscript, we use the shorthand "HA-FullEOS" to refer to the strategy of computing OCAPE using the HA with the full nonlinear EOS. Our algorithm takes less than 0.2 seconds on a personal computer with $M = 200$. The calculation converges quickly with M: for almost all the profiles, the difference between the calculated OCAPE at $M = 200$ and $M = 4000$ is less than 1%.

1.5 The parameter dependence of OCAPE

In this section we elucidate the mechanism for the existence of OCAPE quantitatively and exhibit the dependence of OCAPE on key ocean parameters. In subsections

1.5.1-1.5.2 we derive analytical expressions for the OCAPE of idealized two-layer profiles (*i.e.* piecewise-constant θ and S, one of which is CFW and the other is WSW). In section 1.5.4 we derive approximate analytical expressions for the OCAPE of more realistic profiles with a finite-thickness interface and a stably-stratified WSW layer. Such analytical expressions allow OCAPE to be estimated for many real ocean profiles, since approximately two-layer profiles are frequently observed in wintertime polar oceans (see examples in section 1.6; Garwood Jr et al., 1994; Akitomo, 1999a; Harcourt, 2005). This approach offers clearer insights as compared to the complex steps of the HA-FullEOS discussed in section 1.4; however, the HA-FullEOS has the advantage of being applicable to any profile of seawater. The accuracy of the analytical expressions is verified by comparison to OCAPE computed via the HA-FullEOS in sections 1.5 and 1.6.

1.5.1 Two-layer configuration

To simplify our analysis we make the Boussinesq approximation. Since OCAPE is based on adiabatic parcel rearrangement, cabbeling has a minimal impact on OCAPE[4]. Thus we use the following EOS that excludes cabbeling but includes thermobaricity,

$$\rho = \rho_0(1 - \alpha_\theta \delta\theta + \beta\delta S + \gamma\delta P), \tag{1.7}$$

[4]This is because the leading cabbeling density term, $-\rho_0\gamma_{\theta\theta}\Delta\theta^2$ (*e.g.*, see Equation (17) of Harcourt, 2005), remains approximately constant for a parcel undergoing adiabatic rearrangements. Here $\gamma_{\theta\theta} = -1/(2\rho)(\partial^2\rho/\partial\theta^2)|_{P,S}$, which is the coefficient of cabbeling, is essentially independent of pressure: it varies by less than 10% for a pressure change from the sea level to 1500 m depth (IOC et al., 2010). The independence of OCAPE from cabbeling is verified in Figure 1.3 or Table 1.1, which compares the OCAPE computed via the HA-FullEOS and the OCAPE computed analytically via the simplified EOS (1.7) that excludes cabbeling.

where ρ_0 is the constant basic state density equal to 1030 $\mathrm{kg\,m^{-3}}$. The anomalies of potential temperature, salinity and pressure are given by $\delta\theta$, δS and δP, respectively; the basic states are θ_0, S_0, and P_0. The coefficients of thermal expansion, salinity contraction and adiabatic compressibility are denoted as α_θ, β and γ, respectively. Note that θ_0 and S_0 are constant, but α_θ, β, γ and P_0 may depend on the vertical coordinate z. Under these approximations, Ingersoll (2005) derived the following expression for the column PE (internal energy plus gravitational energy) per unit area,

$$\frac{\mathrm{PE}}{area} = \int_{-D}^{0} (\psi_0 \delta\theta + \mu_0 \delta S)\rho_0 \mathrm{d}z + \text{constant}, \tag{1.8a}$$

$$\psi_0(z) = \int_z^0 \alpha_\theta g \mathrm{d}z', \qquad \mu_0(z) = -\int_z^0 \beta g \mathrm{d}z'. \tag{1.8b}$$

Equation (1.8a) is essentially the Boussinesq dynamic enthalpy of the ocean column (see equation (13) of Young, 2010) that represents the system's enthalpy (thus PE) under adiabatic conditions. Here D is the column depth; $z = 0$ corresponds to the ocean surface and $z = -D$ corresponds to the base of the column. The "constant" on the right-hand side of (1.8a) is a fixed reference PE that makes no contribution to OCAPE; only PE variations are dynamically meaningful. The symbols μ_0 and ψ_0 are the thermodynamic potentials for salinity and potential temperature, respectively.

Consider an ocean column with a homogeneous upper CFW layer $(\theta_{\mathrm{CFW}}, S_{\mathrm{CFW}})$ stably overlying a homogeneous lower WSW layer $(\theta_{\mathrm{WSW}}, S_{\mathrm{WSW}})$, as illustrated in Figure 1.2(a). We refer to this as the Current state. The interface between the layers lies at $z = -(1-\lambda)D$, where $0 < \lambda < 1$ represents the fraction of WSW in the whole

column. We denote $\Delta\rho \geqslant 0$ as the downward density jump across the CFW/WSW interface. In this case, the basic state variables and their anomalies in each layer are defined as

$$\theta_0 = \frac{\theta_{\mathrm{WSW}} + \theta_{\mathrm{CFW}}}{2}, \quad S_0 = \frac{S_{\mathrm{WSW}} + S_{\mathrm{CFW}}}{2}, \tag{1.9a}$$

$$\delta\theta_{\mathrm{WSW}} = -\delta\theta_{\mathrm{CFW}} = \Delta\theta = \frac{\theta_{\mathrm{WSW}} - \theta_{\mathrm{CFW}}}{2}, \tag{1.9b}$$

$$\delta S_{\mathrm{WSW}} = -\delta S_{\mathrm{CFW}} = \Delta S = \frac{S_{\mathrm{WSW}} - S_{\mathrm{CFW}}}{2}. \tag{1.9c}$$

Figure 1.2(b) shows that β is almost independent of depth while α_θ varies almost linearly with depth. For simplicity we approximate β as a constant and α_θ as a linear function of z,

$$\alpha_\theta(z) = \alpha_0 + \alpha_z z, \tag{1.10a}$$

$$\alpha_0 = -\frac{1}{\rho_0}\left.\frac{\partial\rho}{\partial\theta}\right|_{\theta_0,S_0,z=0}, \tag{1.10b}$$

$$\alpha_z = -\frac{1}{\rho_0 D}\int_{-D}^{0}\left.\frac{\partial^2\rho}{\partial\theta\partial z}\right|_{\theta_0,S_0,z}\mathrm{d}z, \tag{1.10c}$$

$$\beta = \frac{1}{\rho_0 D}\int_{-D}^{0}\left.\frac{\partial\rho}{\partial S}\right|_{\theta_0,S_0,z}\mathrm{d}z, \tag{1.10d}$$

where α_0 is the surface thermal expansion coefficient. Both α_0 and β are positive constants while α_z is a negative constant, all of which can be computed according to the full EOS of seawater (*e.g.*, Jackett et al., 2006). It follows from (1.7) and (1.9b)–(1.10d) that

$$\beta\Delta S = (\alpha_0 - (1-\lambda)D\alpha_z)\Delta\theta + \frac{\Delta\rho}{2\rho_0}. \tag{1.11}$$

This equation illustrates that the variation in S and θ across the CFW/WSW interface at $z = -(1-\lambda)D$, denoted as ΔS and $\Delta\theta$ respectively, produce a downward density jump $\Delta\rho$.

When $\Delta\rho > 0$, the CFW/WSW interface is stable: The WSW beneath the interface is denser than the CFW above. Consider moving a parcel of CFW down across the CFW/WSW interface and through the WSW layer adiabatically. Its density increases due to thermobaricity (see Figure 1.1(a)) and finally equals the density of background WSW at a depth that we refer to as the critical depth $z = z_S$. Therefore this level z_S lies below the CFW/WSW interface $z_{int} = -(1-\lambda)D$. Using (1.7), (1.9b)–(1.11) we obtain

$$z_S = z_{int} + \frac{\Delta\rho}{2\rho_0\alpha_z\Delta\theta} = -(1-\lambda)D + \frac{\Delta\rho}{2\rho_0\alpha_z\Delta\theta}. \tag{1.12}$$

Parcels of CFW and WSW conserve their θ and S properties during an adiabatic parcel rearrangement. Thus z_S is a uniquely-defined depth at which the rearranged parcels of CFW and WSW have the same density, according to our simplified EOS (1.7).

While the CFW parcel is above the level z_S and below the CFW/WSW interface z_{int}, it is positively buoyant and this region represents an energy barrier; thus extra energy is required to make the parcel sink. Below the critical depth z_S, the parcel experiences a negative buoyancy force, and potential energy is released as it sinks. Horizontal convergence caused by wind forcing may be responsible for deepening a well-mixed layer of CFW to this critical depth z_S, and therefore triggering convection,

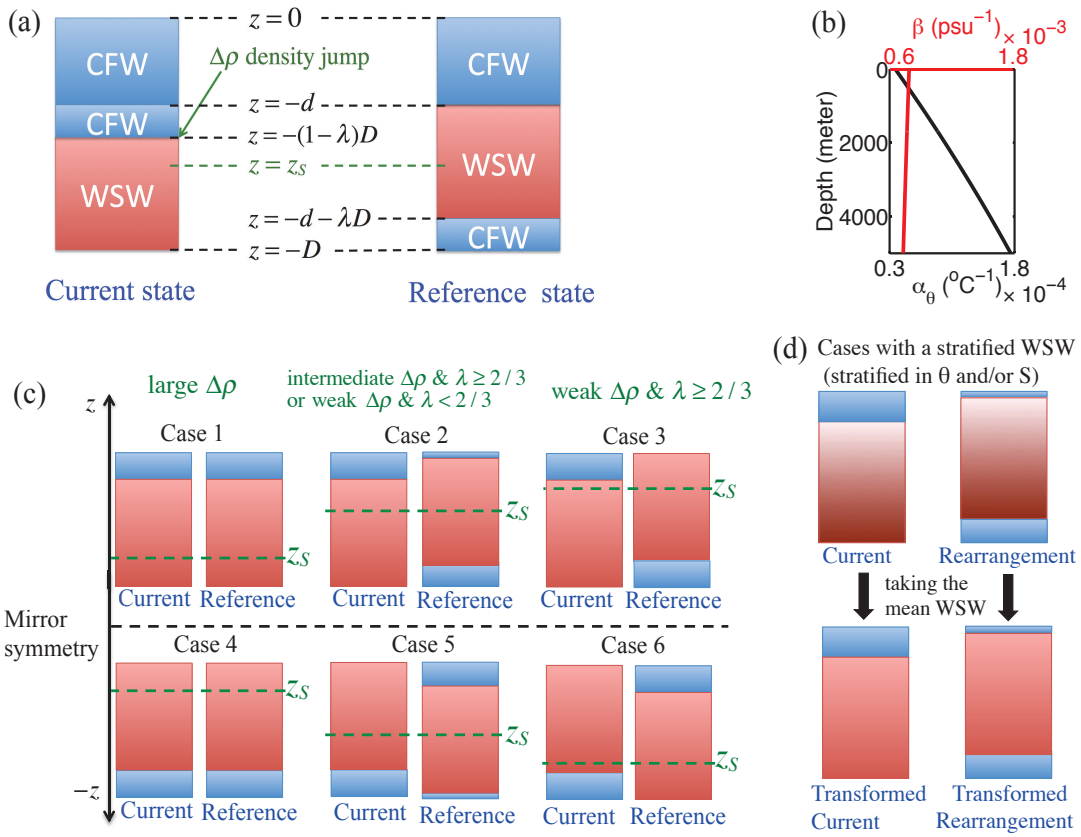

Figure 1.2: (a) Schematic of the Current and Reference states for two-layer profiles. The column depth is D, of which λD is WSW and $(1-\lambda)D$ is CFW. There is a downward density jump $\Delta\rho \geqslant 0$ at the CFW/WSW interface in the Current state. The densities of adiabatically-repositioned CFW and WSW parcels would be equal at the critical depth $z = z_S$. We define d as the thickness of the upper CFW layer in the Reference state. (b) The vertical profile of thermal expansion coefficient α_θ (black line) and saline contraction coefficient β (red line), computed from constant vertical profiles, $\theta = -1\,^\circ\mathrm{C}$ and $S = 34.0$ psu, via the full EOS of seawater (Jackett et al., 2006). The linearity of α_θ and the independence of β on depth validate our assumptions in (1.10a)–(1.10d). (c) The Current and Reference states of 6 distinct cases, discussed in section 1.5. The cases are distinguished by the position of the critical depth z_S (and thus $\Delta\rho$) and λ, as described in the text. Cases 1–3 have vertical mirror symmetry to Cases 4–6, respectively. (d) Schematic of the "Transformed Current state" and the "Transformed Rearrangement state" discussed in section 1.5.4. Consider a Current state that has a homogeneous CFW overlying a stratified WSW (the stratification is represented by the variation of the red color). We take the mean WSW (θ and S) to define the "Transformed Current state". Further, we consider a Rearrangement state that is statically-stable (since the Reference state is always statically-stable). Analogously, we take the mean WSW and define a corresponding "Transformed Rearrangement state".

as is the case in deep lakes (Weiss et al., 1991; Akitomo et al., 1995b; Schmid et al., 2008).

1.5.2 Analytical expressions for OCAPE in idealized two-layer profiles

Conceptually we have the following three cases for OCAPE:

(i) If z_S lies at the mid-plane of the WSW layer, the energy input (required to move a CFW parcel from the upper boundary of the WSW layer to z_S) is approximately equal to the energy release (from moving the same CFW parcel from z_S to the bottom of the WSW layer). This equality is due to the nearly linear dependence of α_θ on depth (see details in section 1.5.3). If z_S lies below the mid-plane of the WSW layer, the energy input to the fluid in crossing the barrier is greater than the energy released once the barrier is crossed. In both scenarios moving CFW downward cannot produce a lower energy state. Thus the Current state is the Reference state and OCAPE=0. We refer to this as Case 1, and illustrate it in Figure 1.2(c).

(ii) When z_S lies above the mid-plane of the WSW layer in the Current state, the energy required to move a CFW parcel from the upper boundary of the WSW layer to $z = z_S$ is smaller than the energy released when the parcel descends from $z = z_S$ to the bottom of the WSW layer. Thus moving CFW to the bottom of the WSW layer leads to a lower column PE (*i.e.* OCAPE>0). This process also raises the mid-plane of the WSW. Eventually the mid-plane will coincide with the level z_S and then moving more CFW to the bottom of the WSW layer can no longer lead to a lower column PE, as in (i) above. This is the Reference

state for Case 2, in which a portion of the CFW lies above the WSW layer and a portion below the WSW layer.

(iii) Case 3 occurs when moving all of the CFW below the WSW layer still does not raise the mid-plane of the WSW layer as high as the level z_S. This state is the Reference state. For similar reasons to (ii) above, OCAPE is positive for case 3.

We now analytically derive the Reference state and OCAPE for these three cases.

The Reference (minimum-PE) state, by definition, has zero OCAPE and is statically stable to infinitesimal perturbations. Consider moving CFW and WSW parcels adiabatically to the same level z. According to the definition of z_S, CFW is less dense than WSW if $z > z_S$, is as dense as WSW if $z = z_S$, and is denser than WSW if $z < z_S$. Therefore, for the Reference state to be statically stable it must have CFW above WSW for $z \geqslant z_S$ and CFW beneath WSW for $z < z_S$ (Figure 1.2(a)). Therefore, the WSW/CFW interface $z = -d - \lambda D$ in the Reference state has to lie beneath $z = z_S$, where d is the thickness of the upper layer of CFW in the Reference state (Figure 1.2(a)). Thus the lower bound of d is $(-z_S - \lambda D)$. The upper bound of d is the total thickness of CFW (*i.e.* $(1 - \lambda)D$). Therefore, given a Current state with parameters D, z_S and λ $(0 < \lambda < 1)$, the possible Reference states are:

$$\begin{aligned} &\text{CFW at :} \quad -d < z < 0, \quad -D < z < -d - \lambda D, \\ &\text{WSW at :} \quad -d - \lambda D < z < -d, \\ &\text{with} \ \ \max(0,\ -z_S - \lambda D) \leqslant d \leqslant (1 - \lambda)D. \end{aligned} \tag{1.13}$$

Here d is a variable; the Reference state by definition corresponds to a d that globally minimizes the PE of the state (1.13), where

$$\frac{\text{PE}}{area} = -\rho_0 g \alpha_z \Delta\theta \lambda D \left[d^2 + 2(z_S + \tfrac{1}{2}\lambda D)d\right] + \text{constant}. \tag{1.14}$$

This can be derived by evaluating the integral on the right-hand side of (1.8a). The "constant" on the right of (1.14) again makes no contribution to the OCAPE.

Every possible Reference state belongs to one of three cases, distinguished by whether no CFW (Case 1), a fraction of the CFW (Case 2), or all of the CFW (Case 3) moves beneath the WSW. These cases are determined by solving d that minimizes PE given by (1.14). These cases are detailed individually below.

1.5.2.1 Case 1

For stratification ($\Delta\rho$) sufficiently large that z_S lies beneath the center of the WSW,

$$z_S \leqslant -(1 - \lambda/2)D, \;\; i.e. \;\; \Delta\rho \geqslant -\rho_0 \alpha_z \Delta\theta \lambda D, \tag{1.15a}$$

the Reference state is simply the Current state (Figure 1.2(c)), *i.e.*, (1.13) with

$$d = (1 - \lambda)D, \tag{1.15b}$$

and therefore the column contains no OCAPE,

$$\text{OCAPE} = 0. \tag{1.15c}$$

1.5.2.2 Case 2

For sufficiently weak stratification ($\Delta\rho$) such that z_S lies above the center of the WSW and deeper than half the WSW layer thickness,

$$
\begin{aligned}
&-(1-\lambda/2)D < z_S < -(\lambda/2)D, \\
&i.e. \quad -\rho_0\alpha_z\Delta\theta\lambda D > \Delta\rho \geqslant -\rho_0\alpha_z\Delta\theta\,(3\lambda-2)D,
\end{aligned}
\tag{1.16a}
$$

the Reference state is (1.13) with

$$
d = (1-\tfrac{3}{2}\lambda)D - \frac{\Delta\rho}{2\rho_0\alpha_z\Delta\theta} = -z_S - \tfrac{1}{2}\lambda D. \tag{1.16b}
$$

In this case a portion of the CFW moves below the WSW, leaving the WSW exactly centered around $z = z_S$ to reach the Reference state (Figure 1.2(c)), and

$$
\mathrm{OCAPE} = -g\alpha_z\Delta\theta D^2\left[\frac{1}{4}\lambda\left(\lambda + \frac{\Delta\rho}{D\rho_0\alpha_z\Delta\theta}\right)^2\right]. \tag{1.16c}
$$

Here OCAPE is column-averaged, with dimensions of energy/mass.

1.5.2.3 Case 3

For only $\lambda \geqslant 2/3$ and sufficiently weak stratification ($\Delta\rho$), such that both the level $z = z_S$ and the CFW/WSW interface lie no deeper than half the WSW thickness,

$$z_S \geqslant -(\lambda/2)D, \;\; -(1-\lambda)D \geqslant -(\lambda/2)D,$$
$$i.e. \;\; -\rho_0\alpha_z\Delta\theta(3\lambda-2)D > \Delta\rho \geqslant 0, \tag{1.17a}$$

then the Reference state is (1.13) with

$$d = 0. \tag{1.17b}$$

Thus in this case all of the CFW moves below the WSW to reach the Reference state (Figure 1.2(c)), and OCAPE (column-averaged, with dimensions of energy/mass) is

$$\text{OCAPE} = -g\alpha_z\Delta\theta D^2\left[\lambda(\lambda-1)\left((1-2\lambda) - \frac{\Delta\rho}{D\rho_0\alpha_z\Delta\theta}\right)\right]. \tag{1.17c}$$

Type II convection can also occur in a two-layer profile with WSW overlying CFW. This type of convection has not yet been observed, but in principle it could occur in the real ocean (see discussion in section 1.7). In this scenario, following similar derivations as above, we find that there are still 3 cases, denoted as Cases 4, 5, and 6. They have mirror symmetry in the vertical (including the critical depth z_S) with Cases 1, 2, and 3, respectively, as shown in Figure 1.2(c). The analytical expressions for their OCAPE are therefore also identical (for Cases 4–6, d should

denote the bottom CFW thickness in the Reference state; $\Delta\rho$ is still the positive downward density jump across the interface in the Current state). Note again that the PE release is always associated with moving CFW through the WSW vertically, and never the reverse (see Figure 1.1).

1.5.3 Alternative explanation for the threshold of Cases 1–3

Here we explain the thresholds of $\Delta\rho$ (or z_S) of Cases 1–3 from the viewpoint of a single parcel rearrangement, similar as (i)–(iii) in section 1.5.4 but using a quantitative approach. We begin from a hypothetical state in which a thickness Δz of CFW has already been displaced adiabatically from the CFW/WSW interface $z = z_{int}$ to the bottom $z = z_{bot}$. Now consider moving a single CFW parcel adiabatically from the new upper CFW/WSW interface $z_{int} + \Delta z$ to the lower WSW/CFW interface $z_{bot} + \Delta z$. The associated change in the column's PE, ΔPE, is equal to the change of column's enthalpy, ΔH, as in section 1.3. The entropy and salinity of this parcel remain unchanged. Via a derivation similar to that of Equation (A.5) of Adkins et al. (2005), we obtain an expression for ΔH as follows:

$$\Delta\mathrm{PE} = \Delta H = \frac{mg}{\rho_0} \int_{z_{int}+\Delta z}^{z_{bot}+\Delta z} \rho'(z)\mathrm{d}z, \tag{1.18a}$$

$$z_{int} = -(1-\lambda)D, \quad z_{bot} = -D, \tag{1.18b}$$

$$\rho'(z_{int}) = -\Delta\rho, \quad \rho'(z_S) = 0, \quad \frac{\partial\rho'}{\partial z} = \text{constant}. \tag{1.18c}$$

Here m is the mass of this moving parcel and $\rho'(z)$ is the density anomaly of this parcel with respect to the ambient WSW, which depends linearly on z since α_θ varies

linearly with z.

This parcel rearrangement can be considered as a two-step process. The first step is the displacement from $z_{int} + \Delta z$ to z_S, which requires external work input to overcome buoyancy resistance ($\rho' < 0$). The second step is the displacement from z_S to $z_{bot} + \Delta z$, which releases PE (*i.e.* decreases ΔPE) because ρ' is positive throughout these depths (due to thermobaricity). If the PE released in the second step is larger than the external work input in the first step, then ΔPE is negative and this column contains OCAPE. Since $\rho'(z)$ is linear with depth, this situation occurs only if $z_S > z_c$ according to (1.18a) and (1.18c). Here z_c is the depth of the center of the two new interfaces:

$$\begin{aligned} z_c &= 0.5[(z_{int} + \Delta z) + (z_{bot} + \Delta z)] \\ &= -(1 - 0.5\lambda)D + \Delta z, \\ \text{where} \quad & -(1 - 0.5\lambda)D \leqslant z_c \leqslant -0.5\lambda D, \\ \text{since} \quad & 0 \leqslant \Delta z \leqslant (1 - \lambda)D. \end{aligned} \tag{1.19}$$

Therefore, there are three categories for the initial OCAPE, which are determined by z_S. (i) When $z_S \leqslant -(1 - 0.5\lambda)D$, this ensures $z_S \leqslant z_c$ for any Δz according to (1.19). Thus the initial column contains no OCAPE; this corresponds to Case 1. (ii) When $-(1 - 0.5\lambda)D < z_S \leqslant -0.5\lambda D$, there exists a range of Δz such that $z_S > z_c$. Therefore the initial column contains OCAPE, and the Reference state corresponds to the value of Δz that makes $z_S = z_c$. This is Case 2. (iii) When $-0.5\lambda D < z_S$,

the condition $z_S < z_c$ is satisfied for any Δz. Therefore the initial column contains OCAPE, and the Reference state corresponds to $\Delta z = (1-\lambda)D$ (*i.e.* all of the CFW moves beneath the WSW). This is Case 3.

1.5.4 Analytical expressions for OCAPE of more realistic profiles: with stably stratified WSW

Example #	1	2	3	4	5	6	7	8
λ	0.7	0.7	0.9	0.9	0.7	0.7	0.9	0.9
interface thickness (m)	0	0	40	40	40	40	40	40
$\Delta\rho$ (kg/m^3)	5×10^{-3}	3×10^{-3}	4×10^{-3}	5×10^{-3}	5×10^{-3}	4×10^{-3}	1×10^{-3}	6×10^{-3}
$N^2_{\rm wsw}$(s^{-2})	6×10^{-7}	1×10^{-7}	4×10^{-7}	5×10^{-7}	2×10^{-7}	1×10^{-7}	4×10^{-7}	3×10^{-7}
$\delta\rho$ (kg/m^3)	2.7×10^{-2}	6.7×10^{-3}	2.2×10^{-2}	2.8×10^{-2}	1.2×10^{-2}	7.4×10^{-3}	1.9×10^{-2}	2.0×10^{-2}
Classification	Case 1	Case 2	Case 3	Case 2	Case 2	Case 2	Case 3	Case 3
OCAPE, analytical (J/kg)	0	1.8×10^{-2}	7.2×10^{-3}	2.6×10^{-3}	8.1×10^{-3}	1.5×10^{-2}	1.0×10^{-2}	0.9×10^{-2}
OCAPE, HA-FullEOS (J/kg)	0	1.7×10^{-2}	7.5×10^{-3}	2.5×10^{-3}	7.7×10^{-3}	1.4×10^{-2}	1.1×10^{-2}	1.0×10^{-2}

Table 1.1: OCAPE by analytical expressions derived in section 1.5.4 vs. the OCAPE computed via the HA-FullEOS described in section 1.4. The latter uses the exact water column stratification described below, whereas the former neglects the finite-thickness interface between the CFW and WSW (assumed to be CFW instead). These two methods differ by less than $\sim 10\%$ in all eight examples. All examples have a column depth of 1000 m and a homogeneous CFW ($\theta = -1.6$°C and $S = 34.47$ psu) overlying a stratified WSW layer that has a constant positive buoyancy frequency $N^2_{\rm wsw}$. λ is the fraction of the WSW in the whole column; $\Delta\rho$ is the downward density jump across the CFW/WSW interface; $\delta\rho$ is the density change from the bottom of the CFW to the mid-depth of the WSW (defined in (1.20)). Examples 1–4 have a WSW of constant $\theta = 0.9$°C, with a S stratification (which can be determined from $\Delta\rho$, $N^2_{\rm wsw}$, the S of the CFW, and the column's θ profile). Examples 5–8 have a WSW of constant $S = 34.65$ psu, with a θ stratification (similarly determinable as above). Within the finite-thickness CFW/WSW interface, the θ and S properties vary linearly with depth. The classification into Cases 1–3 follows section 1.5.4.

We now derive analytical expressions for the OCAPE in somewhat more realistic water column profiles. The profiles still have two layers, as above, but we consider a CFW/WSW interface of finite thickness and introduce a constant positive strati-

fication in the WSW layer. Harcourt (2005) pointed out that realistic CFW/WSW transitions have finite vertical extent due to mixed layer entrainment or shear, which can significantly impact the dynamics by inducing cabbeling instability. However, the thickness of this interface is still much thinner than the ocean column under consideration (about 20–100 m vs 1000 m; see realistic profiles in section 1.6 and also Harcourt, 2005). It therefore minimally impacts the OCAPE value ($< 10\%$ in our tests), since the OCAPE is defined by adiabatic rearrangements of water parcels throughout the entire column parcels. We verify this later in Table 1.1.

To estimate the OCAPE for this configuration we modify the two-layer Current state discussed in the previous sections: the Current state now not only has a stable density jump $\Delta\rho$ across the CFW/WSW interface, but also has a linearly-stratified WSW layer with positive buoyancy frequency N^2_{wsw} (see examples in Table 1.1). To a good approximation, our analytical expressions for the OCAPE (1.15a)-(1.17c) still apply, except that $\Delta\rho$ must be replaced by $\delta\rho$ throughout, where $\delta\rho$ is the density change from the bottom of the CFW to the mid-depth of the WSW:

$$\delta\rho = \Delta\rho + \frac{\rho_0}{2g}\int_{-D}^{-(1-\lambda)D} N^2_{\text{wsw}} dz, \tag{1.20}$$

where $-D$ and $-(1-\lambda)D$ are again respectively the depths of the lower and upper boundary of the WSW layer in the Current state. We define a "Transformed Current state", which is identical to the Current state except that the WSW layer is replaced by a homogeneous layer having the depth-averaged WSW properties of the Current state (Figure 1.2(d)). By definition, N^2_{wsw} is zero in the "Transformed Current state",

and the downward density jump across the interface is approximately $\delta\rho$, defined in (1.20). Recall that any Rearrangement state is attainable via adiabatic vertical parcel rearrangements from the Current state. We only consider those Rearrangement states that are potentially the Reference state: they always have the denser WSW lying beneath the less dense WSW, since the Reference (minimum-PE) state should be statically stable. Similarly we can define a "Transformed Rearrangement state", which is the same as the Rearrangement state except that its WSW layer(s) should be again replaced by the mean WSW (Figure 1.2(d)). Thus this "Transformed Rearrangement state" is a Rearrangement state from the "Transformed Current state". The key point is that the PE difference between the Current state and the Rearrangement state is well approximated by the PE difference between the "Transformed Current state" and the "Transformed Rearrangement state"[5]. This PE difference is exactly the OCAPE when the Rearrangement state is the Reference state. Therefore, the Current state has approximately the same OCAPE as the corresponding "Transformed Current state", whose OCAPE can be computed analytically from (1.15a)-(1.17c) (using $\delta\rho$ to replace $\Delta\rho$). Note that N^2_{WSW} has an upper bound, above which the water column contains zero OCAPE (from (1.20) the upper bound of N^2_{WSW} is determined by the upper bound of $\delta\rho$ stated in (1.16a) and (1.17a), where we again should use $\delta\rho$ to replace $\Delta\rho$). This upper bound of N^2_{WSW} ensures that the Reference state, as estimated by the OCAPE-calculation strategy above, is always statically-stable at its

[5]In other words, the PE difference between the Current state and the "Transformed Current state" is well approximated by the PE difference between the Rearrangement state and the "Transformed Rearrangement state". This PE difference is approximately equal to the change of the system's gravitational energy when the stratified WSW is replaced by the mean WSW (Figure 1.2d).

CFW/WSW and WSW/CFW interfaces (by following the arguments (ii) and (iii) in the beginning of section 1.5.4).

This is verified by the eight examples in Table 1.1, which shows agreement between the OCAPE estimated analytically and the OCAPE computed via the HA-FullEOS (see also section 1.6 for further verification using realistic profiles). Note that the OCAPE computed via the HA-FullEOS uses the exact water column stratification described in Table 1.1, whereas our analytical estimate neglects the finite-thickness interface between the CFW and WSW, as described above.

1.5.5 Implications

Equations (1.15a)–(1.17c) provide thorough information about the parameter dependence of OCAPE in a two-layer profile, which is uniquely determined by the following five parameters: α_z, $\Delta\theta$, D, λ and $\Delta\rho$ (or more generally, $\delta\rho$). The sensitivity of OCAPE to these five parameters is plotted in panels (a–e) of Figure 1.3 respectively. The dashed black lines in Figure 1.3(a)–1.3(d) have been computed using the HA-FullEOS in section 1.4. The solid black lines in Figure 1.3(a)–1.3(d) and the colored lines in Figure 1.3(e) have been computed using the analytical expressions in section 1.5.2. The strong agreement of these methods (differing by less than 2%) confirms the accuracy of our analytical approach.

As shown in Figure 1.3(a), OCAPE is linearly proportional to α_z, which is defined by (1.10c) and represents the strength of thermobaricity. We found that α_z is essentially independent of S_0 and D (not shown), but it is sensitive to θ_0 (the mean θ of the CFW and WSW). This is illustrated in the inset in Figure 1.3(a), in which

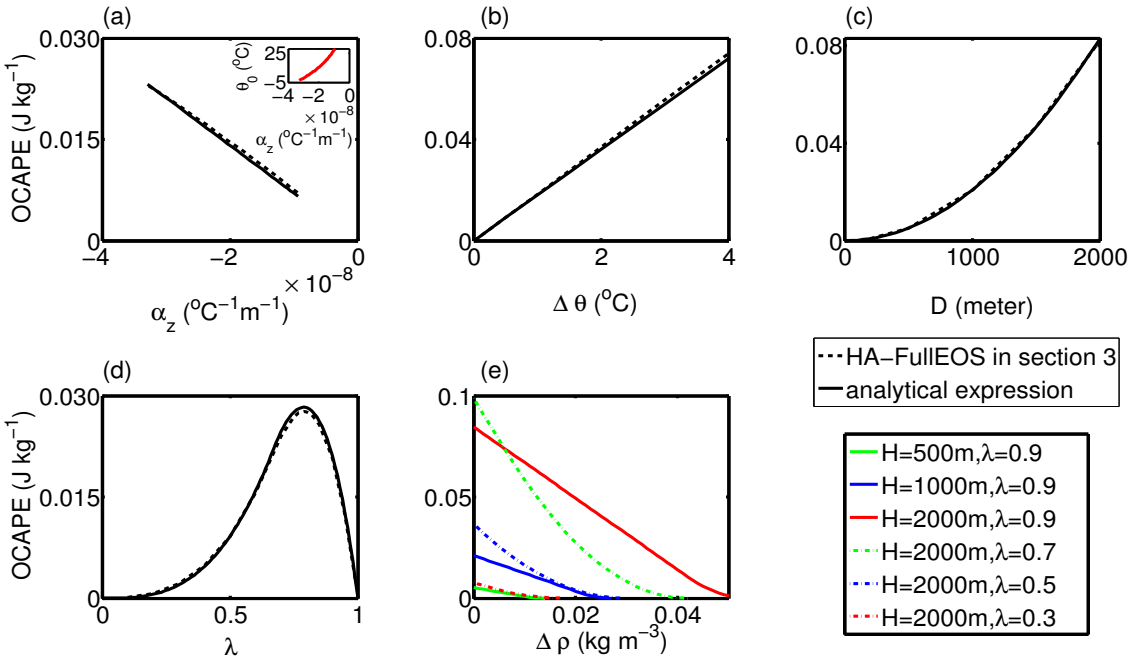

Figure 1.3: Parameter dependence of OCAPE, as discussed in section 1.5.5. The dashed black lines in (a)–(d) have been computed using the HA-FullEOS in section 1.4. The solid black lines in (a)–(d) and the colored lines in (e) have been computed using analytical expressions in section 1.5. These are for two-layer profiles with CFW overlying WSW. Here α_z is the derivative of thermal expansion coefficient with respect to vertical coordinate; $\Delta\theta$ is half of the difference of potential temperature between the CFW and the WSW; D is the ocean column depth; λ is the fraction of the WSW in the whole column; $\Delta\rho$ is the downward density jump across the CFW/WSW interface. (a) Sensitivity to α_z, with fixed $\Delta\theta = 1\,^{\circ}\mathrm{C}$, $D = 1000$ m, $\lambda = 9/10$ and $\Delta\rho = 0$. The inset shows the sensitivity of α_z to potential temperature (θ_0), computed via (1.10c) using the full EOS of seawater (Jackett et al., 2006) with fixed S_0=34.0 psu and D=1000 m. (b) Sensitivity to $\Delta\theta$, with fixed $\alpha_z = -2.4 \times 10^{-8}$ °C^{-1}m^{-1} ($\theta_0 = 4\,^{\circ}\mathrm{C}$) and the same D, λ and $\Delta\rho$ as (a). (c) Sensitivity to D, with fixed $\alpha_z = -3 \times 10^{-8}$ °C^{-1}m^{-1} ($\theta_0 = 0\,^{\circ}\mathrm{C}$) and the same $\Delta\theta$, λ and $\Delta\rho$ as (a). (d) Sensitivity to λ, with the same α_z as (c) and the same $\Delta\theta$, D and $\Delta\rho$ as (a). (e) Sensitivity to $\Delta\rho$ for different D and λ, with the same α_z and $\Delta\theta$ as (c).

we have computed α_z using fixed $S_0 = 34.0$ psu and $D = 1000$ m and the full EOS for seawater (Jackett et al., 2006). Therefore, the polar oceans may contain more OCAPE due to the larger magnitude of α_z at lower temperatures. This may partially explain less frequent observations of thermobaric instability at lower latitudes (*e.g.* see the summary of observations in the modeling studies of Akitomo, 1999a,b). In

wintertime polar oceans θ_0 is approximately in the range of -2°C to 4 °C (Garwood Jr et al., 1994; McPhee, 2000; Wadhams et al., 2002), so α_z is approximately a constant $\sim -3 \times 10^{-8}$ °C^{-1} m^{-1}.

Figure 1.3(b) shows that OCAPE is linearly proportional to the potential temperature contrast between CFW and WSW (*i.e.* $2\Delta\theta$), which is required for thermobaric instability. In the winter Weddell Sea $\Delta\theta$ is approximately 0.5–2 °C (Gordon, 1991; Gordon and Huber, 1995; McPhee, 2003).

OCAPE depends quadratically on the column depth D, as shown in Figure 1.3(c). This quadratic dependence occurs because the vertical distance that CFW must move to reach the Reference state, and the thermobarically-induced density change of the adiabatially transported CFW, both increase linearly with D. The most dynamically-relevant D is the maximum depth of convection, which we propose a strategy to predict in Part II.

OCAPE depends strongly on λ, the WSW fraction in the whole column (Figure 1.3(d)). Different WSW fractions may result in qualitatively different Reference states and thus different OCAPE (*e.g.*, Case 3 requires $\lambda \geqslant 2/3$ as in section 1.5.2). When λ equals 0 or 1, OCAPE is zero as there is no temperature variation. OCAPE has a maximum at $\lambda \sim 0.8$ for profiles with zero stratification (Figure 1.3(d)).

The downward density jump across the interface, $\Delta\rho$, may have values between 0 and 0.1 kg m^{-3} in the winter Weddell Sea (McPhee, 2000, 2003). Figure 1.3(e) shows that $\Delta\rho$ can significantly impact OCAPE within this range. This dependence is quadratic for Case 2 and linear for Case 3. The dashed blue line and the dashed

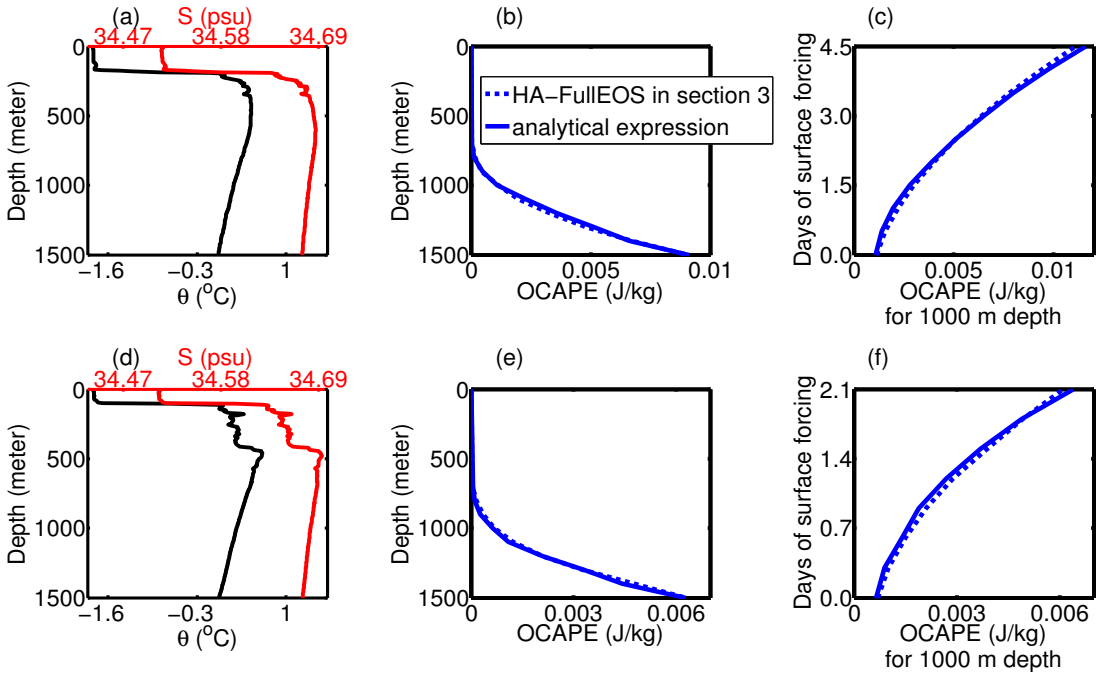

Figure 1.4: (a) Profiles of potential temperature (θ) and salinity (S) from the wintertime Weddell Sea, obtained from Maud Rise (65.4605°S, 2.4007°E) on August 2, 1994, ANZFLUX CTD profile station 48 (courtesy of Bruce Huber; McPhee et al., 1996). (b) OCAPE vs the depth of the profiles shown in panel (a); at each depth we computed the OCAPE, assuming that depth to be the bottom of the ocean (i.e. not permitting any adiabatic rearrangement of the fluid below that depth). The dashed and solid blue lines are from the HA-FullEOS in section 1.4 and the analytical solution derived from section 1.5.4, respectively (see section 1.6 for details). (c) Estimated temporal evolution of OCAPE for 1000 m depth of profiles in panel (a) during a winter surface brine rejection forcing. This forcing equals an ice formation rate of 1.5 cm/day, which is common for the winter Weddell Sea (Harcourt, 2005; Lange et al., 1989). Calculation methods are described in the text of section 1.6. (d,e,f) As (a,b,c) but for profiles observed over Maud Rise (65.5177 °S, 1.1315 °E) on August 1, 1994, ANZFLUX CTD profile station 46. 1500 m is approximately the maximum depth of measurement for profiles in both panels (a) and (d). Panels (b), (c), (e) and (f) share the same legend.

red line both suggest the transition from Case 1 to Case 2 with a decreasing $\Delta\rho$ but never reach Case 3, since λ is $< 2/3$. All other curves have $\lambda > 2/3$ and therefore suggest the transition from Case 1 to Case 2, and then from Case 2 to Case 3 with a decreasing $\Delta\rho$. OCAPE is always positive for $\Delta\rho = 0$.

Given the parameter space, Figure 1.3 produces a rough estimate for the magni-

tude of OCAPE in wintertime polar oceans, which is about 0–0.05 J/kg. The release of this OCAPE can induce convection with vertical velocities ∼0–10 cm/s, using a 10% release fraction[6] (see Part II for detailed discussions). This value might partly contribute to the observed strong deep convection ∼7–10 cm/s in polar oceans (Schott et al., 1993; Marshall and Schott, 1999).

1.6 OCAPE in the winter Weddell Sea

We estimate OCAPE in profiles from wintertime observations in the Weddell Sea. A characteristic feature of the Weddell Sea water masses is the warm (∼ 0–1 °C) and salty deep water (Circumpolar Deep Water) found immediately beneath the pycnocline at 100 to 200 m depth, especially around Maud Rise, known as the "warm pool" (Gordon and Huber, 1995; De Steur et al., 2007). During winter, nearly the entire extent of the Weddell Sea is covered by sea ice due to strong surface cooling, and the mixed layer is close to the freezing point ∼ −1.9 °C (Parkinson and Cavalieri, 2012; Renfrew et al., 2002). This gives rise to an approximately two-layer stratification (CFW overlying WSW) that is frequently observed (Gordon and Huber, 1990; McPhee, 2003; Harcourt, 2005).

Figure 1.4(a) shows one such two-layer observation (McPhee et al., 1996), in which the water column properties were measured down to ∼1500 m depth. The CFW/WSW interface is located between depths of ∼180 m and ∼200 m. The finite thickness of this interface, as opposed to a discontinuous jump, is due to mixed layer entrainment or shear and is key to inducing cabbeling instability (Harcourt, 2005).

[6] *i.e.* $(2 \times 0.05\text{J/kg} \times 10\%)^{0.5} = 0.1$ m/s according to KE=0.5×mass × velocity^2

The OCAPE of this profile is displayed in Figure 1.4(b) as a function of depth (*i.e.*, the OCAPE for the part of the ocean between the surface and the specified depth), and has been calculated using both the HA-FullEOS from section 1.4 and the analytical method described in section 1.5.4. For the analytical method, λ is estimated based on an interface depth of 190 m; $\Delta\theta$ is estimated using (1.9b) based on the mean properties of the CFW (above 180 m depth) and the mean of the WSW (beneath 200 m depth); $\delta\rho$ is estimated using (1.20). Similar to Figure 1.3(c), OCAPE has a quadratic dependence on the depth (see (1.16c) and (1.17c)). OCAPE is approximately zero between depths of 0–700 m, and increases to 0.009 J/kg at 1500 m depth. For an actual convection event, the OCAPE based on the maximum depth of convection ($\sim$1000 m for this case) is most dynamically relevant. In Part II we propose to evaluate the maximum depth of convection from an energetic perspective.

The OCAPE of a profile can be significantly modified due to wintertime surface buoyancy forcing. The profiles of Figure 1.4(a) come from sea ice-covered regions and we assume a sea ice production rate of 1.5 cm/day (1–1.5 cm/day is common for winter Weddell sea, see Harcourt, 2005; Lange et al., 1989). Therefore, CFW remains at the freezing point but becomes saltier by brine rejection; thus the interface between the mixed layer and the WSW beneath becomes less stably stratified (*i.e.* $\Delta\rho$ decreases) which leads to increased OCAPE. Here we estimate the increase of OCAPE based on the profiles of Figure 1.4(a), except with a homogeneously saltier mixed layer following sea ice production. This is rather a scaling analysis and the assumption is idealized (see similar assumptions applied in Garwood Jr et al., 1994; Årthun et al., 2013): In

reality cabbeling instability at the interface could induce Type III convection before $\Delta\rho$ is completely eroded (Harcourt, 2005) resulting in the shoaling of the mixed layer and also the partial release of OCAPE (see simulation in Part II). Our result is shown in Figure 1.4(c) for the column depth of 1000 m (the maximum depth of convection): 4.5 days' ice formation reduces $\Delta\rho$ to approximately zero and increases the OCAPE from $\sim$0.001 J/kg to $\sim$0.01 J/kg. Figure 1.4(c) resembles Figure 1.3(e) and is determined by the dependence of OCAPE on $\Delta\rho$, which is quadratic for $\Delta\rho$ of moderate strength (case 2, see (1.16c)) and becomes linear for smaller $\Delta\rho$ (case 3, see (1.17c)).

In Figure 1.4(d) we show another approximately two-layer profile from observations (McPhee et al., 1996). In this case the dependence of the OCAPE on the column depth (Figure 1.4(e)) and on the surface buoyancy forcing (Figure 1.4(f)) are similar to the previous example (Figure 1.4(b,c)). There is a difference ($\leq$35%) between their OCAPE values for the same parameters (the column depth and the days of surface forcing). This is mainly due to the differing thickness of CFW and also the stratification (N^2) of the WSW layer. In all of these examples the OCAPE calculated via the HA-FullEOS and our analytical expressions agree well with each other (differing by less than 15%).

1.7 Discussion and Conclusion

1.7.1 Key results

We summarize our key results as follows:

(i) We develop the concept of OCAPE to evaluate the contribution of thermobaric-

ity to the KE of ocean deep convection. OCAPE parallels Convective Available Potential Energy (CAPE), a key energy source for atmospheric moist convection that has long been used to forecast moist convection. Both OCAPE and CAPE measure the upper limit of stored PE in a fluid column that can be released under adiabatic vertical parcel rearrangements.

(ii) OCAPE can also be conceptually compared to available potential energy (APE), a major energy source for ocean mesoscale geostrophic turbulence. OCAPE arises from thermobaricity, while APE arises mainly from baroclinicity. OCAPE is due to vertical rearrangement of parcels, while APE requires both vertical and lateral rearrangement of parcels. Both OCAPE and APE are based on adiabatic parcel rearrangements[7].

(iii) We propose an innovative strategy, the HA-FullEOS, to accurately solve the global minimum-PE state of an ocean column and thus determine OCAPE for any ocean column profile (section 1.4).

(iv) For approximately two-layer profiles, which are widely observed in wintertime polar oceans, we derive an analytical solution for OCAPE. This illustrates the dependence of OCAPE on key parameters in the real ocean such as the column depth and the density stratification (Figure 1.3). We quantitatively classify OCAPE into three different cases (section 1.5.2).

(v) We find an OCAPE $\sim$0.001–0.01 J/kg from hydrographic profiles from the winter-time Weddell Sea. Wintertime surface buoyancy loss may significantly

[7]For APE, see section 2b of Huang (2005), section 3 of Winters et al. (1995) and Vallis (2006).

enhance OCAPE (*e.g.* by ∼0.01 J/kg, Figure 1.4). This OCAPE of 0.01 J/kg, if totally released into KE, would induce a significant vertical velocity of ∼14 cm/s and hence cause strong vertical tracer transports and mixings.

1.7.2 Limitations

OCAPE is a quantitative concept that evaluates the contribution of KE due to thermobaricity in Type II and Type III convection. OCAPE, like APE and CAPE, is defined based on adiabatic parcel rearrangements. As a result, it excludes the effects of diabatic processes. It also excludes cabbeling, since cabbeling essentially contributes nothing to the density change of a parcel under adiabatic rearrangements (see footnote 4 for details). However, cabbeling and diabatic processes, like thermobaricity, are also key factors that modulate Type II and Type III convection (Harcourt, 2005; Akitomo, 2011). In Part II, we investigate their associated contributions to the KE budget of Type II and Type III convection. We also investigate the dynamics of the conversion of OCAPE to KE that is not included in this chapter.

1.7.3 Discussion

Hoppema et al. (2006) have observed frequent and precipitous warming events (sometimes up to 1 ^{o}C warming) at 91 m depth in Maud Rise occurring in late winter and early spring (the same region and timing of our Weddell Sea profiles in Figure 1.4). The release of OCAPE may contribute to these warming events. Indeed, Maud Rise has a semipermanent two-layer stratification (*e.g.*, see Figure 8 of De Steur et al., 2007) that could easily accumulate OCAPE during the winter. OCAPE may exist in the Greenland Sea and may contribute to the formation of North Atlantic Deep

Water (NADW) by deep convection. The potential role of OCAPE in other deep convection sites, such as the Ross, Labrador and Mediterranean Seas, requires further evaluation. Especially in the Ross Sea, an important region for the production of AABW, two-layer stratification with CFW overlying WSW has been frequently observed over the western continental slope (see Figure 2 of Gordon et al., 2009). For the Arctic deep water at the Canada Basin (below 2.7 km depth), a recent study by Carmack et al. (2012) proposes that thermobaric instability might effectively transfer geothermal heat upward. They have observed CFW overlying WSW (see their Figure 2 and 3), which indicates the potential existence of OCAPE in the Arctic Ocean.

Our theory demonstrates that OCAPE can also exist when WSW lies above CFW (Figure 1.2(c), Cases 5–6). A potential instance is the two-layer stratification in the winter Japan Sea (see Figure 6 of Talley et al., 2004). Talley et al. (2003) observe Japan Sea deep convection in late winter 2000 and 2001. They find that the strong surface cooling densifies the warm salty surface water (about 0.6 to 1.6 °C) outside the ice-covered area, until it finally becomes as dense as or denser than the cold fresh water beneath (about 0 °C) (see Figure 3 of Talley et al., 2003). This nearly neutrally-stratified two-layer profile may contain positive OCAPE according to our theory in section 1.5. Thus OCAPE might contribute to the observed convection events down to 1.5 km depth.

Chapter 2

Ocean Convective Available Potential Energy. Part II: Energetics of Thermobaric Convection and Thermobaric Cabbeling[†]

2.1 Abstract

The energetics of thermobaricity- and cabbeling-powered deep convection occurring in oceans with cold freshwater overlying warm salty water are investigated here. These quasi-two-layer profiles are widely observed in wintertime polar oceans. The key diagnostic is the ocean convective available potential energy (OCAPE), a concept introduced in Chapter 1. For an isolated ocean column, OCAPE arises from thermobaricity and is the maximum potential energy (PE) that can be converted into kinetic energy (KE) under adiabatic vertical parcel rearrangements. This study explores the KE budget of convection using two- dimensional numerical simulations and analytical estimates. I find that OCAPE is a principal source for KE. However, the complete

[†]Appeared as: Su, Z., A.P. Ingersoll, A.L. Stewart and A.F. Thompson, 2016b. Ocean Convective Available Potential Energy. Part II: Energetics of Thermobaric Convection and Thermobaric Cabbeling. Journal of Physical Oceanography, 46, 1097-1115

conversion of OCAPE to KE is inhibited by diabatic processes. Further, this study finds that diabatic processes produce three other distinct contributions to the KE budget: (i) a sink of KE due to the reduction of stratification by vertical mixing, which raises water columns center of mass and thus acts to convert KE to PE; (ii) a source of KE due to cabbeling-induced shrinking of the water columns volume when water masses with different temperatures are mixed, which lowers the water columns center of mass and thus acts to convert PE into KE; and (iii) a reduced production of KE due to diabatic energy conversion of the KE convertible part of the PE to the KE inconvertible part of the PE. Under some simplifying assumptions, I also propose a theory to estimate the maximum depth of convection from an energetic perspective. This study provides a potential basis for improving the convection parameterization in ocean models.

2.2 Introduction

Akitomo (1999a) classified ocean deep convection into two types: Type I is the deepening of the mixed layer in a relatively homogeneous ocean driven mainly by the loss of surface buoyancy. Type II is thermobaric convection, in which plumes of cold fresh water (CFW) sink into warm salty water (WSW) with significant modulation from thermobaricity and cabbeling (Garwood Jr et al., 1994; Akitomo, 1999a,b; McPhee, 2000; Ingersoll, 2005; Adkins et al., 2005; Akitomo, 2007). Harcourt (2005) was the first to simulate Type III convection, also called thermobaric cabbeling, in which convective plumes of CFW/WSW mixture sink into WSW due to cabbeling instability, and later accelerate further due to thermobaricity and cabbeling. Cabbeling

instability is a convective phenomenon that occurs when water masses with different temperatures are mixed diabatically to produce a denser water mass than the parent waters (Carmack, 1979).

In this chapter, we focus on the energetics of Type II and Type III convection. But we do not distinguish between them: Their dynamics are both strongly influenced by thermobaricity and cabbeling (discussed more in section 2.7.2) and they both occur in oceans with CFW overlying WSW. These quasi-two-layer stratifications are widely observed in winter-time polar oceans (Gordon and Huber, 1990; Garwood Jr et al., 1994; McPhee, 2000). These convection events rapidly transport heat vertically and may make substantial contributions to local vertical mixing, deep-water production, and open-ocean polynyas in polar regions (Akitomo, 1999b; McPhee, 2003; Harcourt, 2005). However, these contributions are poorly understood due to the paucity of observations and the inability of large-scale ocean models to resolve convection (Denbo and Skyllingstad, 1996). In this chapter (Su et al., 2016c) and its companion (hereinafter Part I; Su et al., 2016b), we introduce a new diagnostic for thermobaricity, the Ocean Convective Available Potential Energy (OCAPE), to facilitate the analysis of these convection events.

OCAPE is conceptually important (Part I): it parallels atmospheric Convective Available Potential Energy (CAPE), a key energy source in atmospheric moist convection that has long been used to forecast moist convection (Arakawa and Schubert, 1974; Emanuel et al., 1994; Trenberth, 2005). Both OCAPE and CAPE measure the potential energy (PE) of a fluid column minus the PE of its reference (global

minimum-PE) state that is achievable under adiabatic vertical parcel rearrangements. Here PE is the sum of the gravitational and internal energies. OCAPE arises from thermobaricity and it is computable following Part I. In principle, OCAPE can be entirely released into kinetic energy (KE) if the ocean column evolves adiabatically from the current state to the reference state (Part I). In this chapter we simulate the release of OCAPE and find that diabatic processes inhibit this complete conversion of OCAPE to KE. We generalize the part of OCAPE that can be released to KE (S_{tb} below).

A central diagnostic quantity in our analysis is the cumulative KE production in a convection event, denoted as KE_{cum}, which measures the accumulated intensity of convective motions. At any instant, KE_{cum} is equal to the current KE plus the time-integrated viscous dissipation of KE up to that time (denoted as $Heat_{vis}$). In this study we pose a conceptual decomposition of KE_{cum} into four different contributions

$$KE_{cum} = KE + Heat_{vis} = S_{tb} - S_{strat} + S_{cab} - C_{H^D toH^P}. \tag{2.1}$$

Equation (2.1) gives a conceptual overview of the physics before getting into the details in the following sections. The physical nature of each term in (2.1) is explained by bullet points below, while its mathematical derivation is provided in Appendix. This decomposition is derived for simplified equation of state (EOS) and initial stratification (CFW overlying WSW, as widely observed in winter-time polar oceans; see, *e.g.*, Gordon and Huber, 1990), but for more general initial stratifications it does not hold exactly. The effectiveness of this decomposition is verified by its prediction

of $\mathrm{KE_{cum}}$ and the maximum depth of convection that are in close agreement with numerical simulations presented in sections 2.4–2.6.

The energy terms/relations in (2.1), as introduced below, are summarized schematically in Figure 2.1. For an isolated system, KE+PE is constant by energy conservation. Thus the KE production is converted from PE. The PE of a system can be divided into two parts: dynamic enthalpy, H^D, and potential enthalpy, H^P (Young, 2010; McDougall, 2003); only PE stored in H^D is convertible to KE. We consider below conceptually how the four terms in Equation (2.1) are related to three energy reservoirs: KE, H^D and H^P.

- $\mathrm{C_{H^DtoH^P}}$, as detailed in section 2.5.3 and (2.15b), represents the time-integrated conversion of H^D to H^P due to diabatic processes. Thus the time-integrated conversion of H^D to KE, which is $\mathrm{KE_{cum}}$, is equal to the state change of H^D (compared to the initial state) minus $\mathrm{C_{H^DtoH^P}}$. We derive in Appendix that three sources/sinks contribute to the state change of H^D ($= \mathrm{KE_{cum}} + \mathrm{C_{H^DtoH^P}}$) as follows.

- $\mathrm{S_{tb}}$, as detailed in section 2.4.1–2.4.2 and (2.21c), represents the conversion of H^D into KE and H^P due to thermobaricity (OCAPE).

- $-\mathrm{S_{strat}}$ is detailed in section 2.4.3 and (2.20a). For an initially stably stratified ocean column ($N^2 > 0$), vertical mixing during convection reduces the stratification, which raises the water column's center of mass and thus converts KE and H^P to H^D. Note that H^D and H^P may essentially represent the gravitational and internal energies, respectively (illustrated in section 2.4.3 and 2.5.2),

although not exactly the same.

- S_{cab} is detailed in section 2.5.2 and (2.25). When water masses with different temperatures (*i.e.* CFW and WSW) are mixed during convection, cabbeling reduces the water column's volume, which lowers the water column's center of mass and thus converts H^D ($\sim$ gravitational energy) into KE and H^P ($\sim$ internal energy).

These four terms are not coupled but are independent of each other (see (2.A1) and (2.A10)-(2.A11) in Appendix). $C_{H^D toH^P}$ is the process-based conversion between the energy reservoirs of H^D and H^P (Figure 2.1), totally determined by the full diabatic processes governed by the equation of motion (see (2.15b)). In other words, knowing only the initial (pre-convection) and the final (post-convection) states, but without knowing the processes for the transition, one cannot quantify $C_{H^D toH^P}$. In contrast, H^D is a thermodynamic function of the system: The change of H^D (and its three components: S_{tb}, $-S_{strat}$ and S_{cab}; see (2.A11) and Figure 2.1) due to convection are totally determined from the initial and the final states, despite the (unpredictable turbulent) diabatic processes that transform the initial state to the final state[1]. We also show that the final state can be determined *a priori* given the initial quasi-two-layer state (section 2.5.5). S_{strat} and S_{cab} are also independent from each other: the latter is determined by the reduction of system's temperature variance during convection and is independent of N^2; the former is determined from the reduction

[1]Similarly, the change of gravitational potential energy of an object only depends on its initial and final heights, despite the numerous pathways (processes) that connect the initial and the final position.

of N^2. Note that S_{strat}, S_{cab} and $C_{H^D toH^P}$ will only be non-zero if diabatic processes occur. Adiabatic processes, which define OCAPE, affects S_{tb} (see (2.21b)). However, S_{tb} is also influenced by the diabatic processes since it is state-based.

In section 2.3 we derive the fundamentals of energy conservation and describe the numerical model. It would be very helpful for the reader to go through the fundamentals of thermodynamics in section 2.3 to better capture the main points of this study. In section 2.4, we isolate and explain S_{tb} and S_{strat} using simplified simulations (excluding cabbeling in the EOS). In section 2.5 we increase the complexity of our simulation (using the full EOS) to evaluate and explain S_{cab} and $C_{H^D toH^P}$. We further propose a theory to predict the maximum depth of convection. In section 2.6, we apply this theory and (2.1) to a convection event initially based on a realistic profile from Weddell Sea. Section 2.7 comprises our discussion and conclusions. Numerical experiments (Tables 2.1-2.5; Figures 2.2, 2.4, 2.5, 2.6, 2.7) in this chapter is organized following step-by-step diagnosis for our energy decomposition, as stated by their titles.

2.3 Fundamentals for the energetics of Type II and Type III convection

2.3.1 Energy conservation, potential/dynamic enthalpy and model description

We introduce a Boussinesq model that conserves energy for an isolated system, which is key for our energy analysis. For computational efficiency the model is restricted to two dimensions: horizontal y and vertical z, with vertical velocity $w = -\partial\psi/\partial y$ and horizontal velocity $v = \partial\psi/\partial z$ defined via a streamfunction ψ. We neglect Coriolis

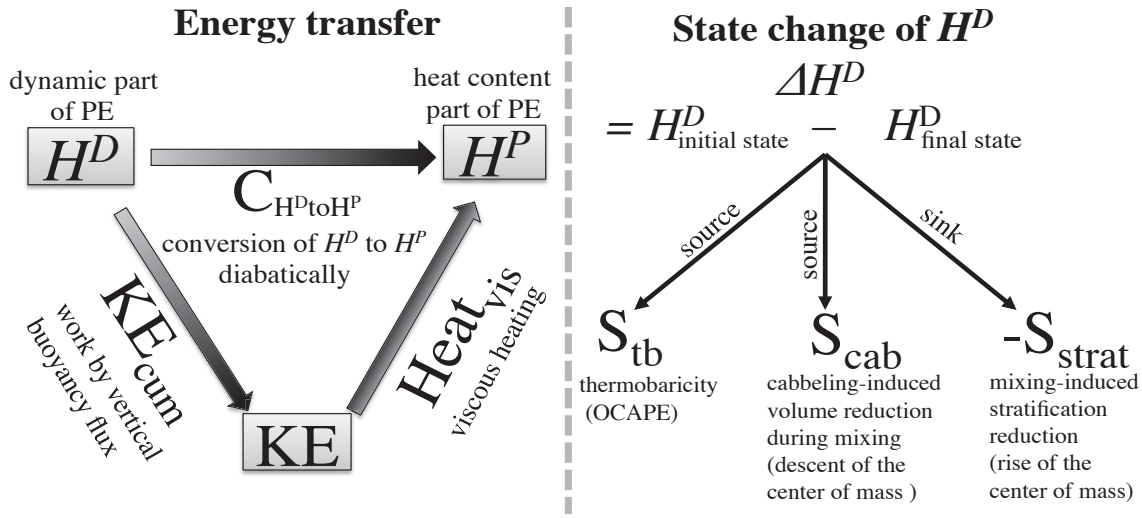

Figure 2.1: Schematic of the proposed energetics for thermobaricity- and cabbeling-powered convection. Definitions and denotations here follow section 2.3.1. (left panel) Potential energy (PE) can be represented by the system's enthalpy H, which includes the dynamic part H^D and the heat content part H^P (defined in (2.11a)–(2.11d)). $C_{H^D toH^P}$ is the time-integrated energy transfer from the H^D reservoir to the H^P reservoir diabatically (defined in (2.15b)). $Heat_{vis}$ is the time-integrated viscous heating (defined in (2.15a)), which transfers energy from the KE reservoir to the H^P reservoir. KE_{cum} is the time-integrated work done by vertical buoyancy flux (defined in (2.14b)), which transfers energy from the H^D reservoir to the KE reservoir. Thus KE_{cum} equals the current KE plus $Heat_{vis}$, as well as equaling the state change of H^D minus $C_{H^D toH^P}$ (see (2.13b)). (right panel) The state change of H^D is due to three distinct sources/sinks: S_{tb}, S_{cab}, and $-S_{strat}$ (defined in (2.21b),(2.25),(2.20a), respectively). Therefore, KE_{cum} has four contributions: $-C_{H^D toH^P}$, S_{tb}, S_{cab}, and $-S_{strat}$ (*i.e.* (2.1)). The mathematical derivation of Equation (2.1) is provided in Appendix.

accelerations (see section 2.7.2 for associated discussion). By taking the curl of the momentum equation, we obtain the vorticity equation

$$\frac{D\nabla^2\psi}{Dt} = -\frac{\partial b}{\partial y} + \nu\nabla^2\nabla^2\psi, \tag{2.2}$$

where ν is the kinematic viscosity. More sophisticated schemes for turbulent viscosity could better parameterize subgrid turbulence. Here we adopt a Laplacian viscosity

because it is convenient for enforcing energy conservation. In equation (2.2) we use the modified buoyancy of Young (2010):

$$b = b(\theta, S, P) \equiv b(\theta, S, z) = -g(\rho - \rho_0)/\rho, \tag{2.3}$$

where θ, S, P and ρ_0 are potential temperature, salinity, pressure and constant reference density, respectively. Here we replace P with z following the hydrostatic relation under Boussinesq approximation (Young, 2010). Following Equations (57.3) and (57.6) of Landau and Lifshitz (1959), we have the salinity and thermodynamic equations

$$\frac{DS}{Dt} = -\frac{1}{\rho_0}\nabla \cdot \mathbf{i}, \tag{2.4a}$$

$$T\frac{D\eta}{Dt} = \frac{1}{\rho_0}\left[-\nabla \cdot (\mathbf{q} - \mu\mathbf{i}) - \mathbf{i} \cdot \nabla\mu + \rho_0\nu(\nabla^2\psi)^2\right], \tag{2.4b}$$

where η is specific entropy, T is temperature, $\mathbf{i}$ is diffusive salt flux, $\mathbf{q}$ is diffusive energy flux, μ is the relative chemical potential of salt in seawater, and $\rho_0\nu(\nabla^2\psi)^2$ is viscous heating. Following $\eta = \eta(\theta, S)$ we rewrite (2.4b) as

$$T\frac{D\eta}{Dt} = C_p\frac{D\theta}{Dt} - T\mu_\theta\frac{DS}{Dt}, \tag{2.5a}$$

$$C_p = T\left.\frac{\partial\eta}{\partial\theta}\right|_S, \qquad -\mu_\theta = -\left.\frac{\partial\mu}{\partial T}\right|_{S,P_r} = \left.\frac{\partial\eta}{\partial S}\right|_\theta, \tag{2.5b}$$

following Maxwell's relations. Here P_r is the reference pressure at sea level. Substituting (2.4a) into (2.5a) and using (2.4b), we obtain the evolution equation for

θ

$$\frac{D\theta}{Dt} = -\frac{\nabla\cdot[\mathbf{q}-(\mu-T\mu_\theta)\mathbf{i}]}{C_p\rho_0} - \frac{\mathbf{i}\cdot\nabla(\mu-T\mu_\theta)}{C_p\rho_0} + \frac{\nu(\nabla^2\psi)^2}{C_p}. \tag{2.6}$$

Note that C_p is proportional to T and is not a constant, as shown in (2.5b). Therefore viscous heating and diffusion lead to the non-conservation of θ, according to (2.6).

We demonstrate that equations (2.2), (2.3), (2.4a) and (2.6) (following Ingersoll, 2005; Young, 2010; Landau and Lifshitz, 1959) compose a non-hydrostatic energy-conserving (NHEC) model. From Part I, PE can be represented by the system's enthalpy (the energy in this chapter, if not otherwise stated, is always column-averaged and in units of J/kg):

$$\mathrm{PE} = H = \frac{1}{\iint \rho_0 \mathrm{d}y\mathrm{d}z}\iint h\,\rho_0 \mathrm{d}y\mathrm{d}z\,, \tag{2.7}$$

where h is specific enthalpy and has the following thermodynamic potential

$$\left.\frac{\partial h}{\partial\theta}\right|_{S,P} = C_p, \qquad \left.\frac{\partial h}{\partial S}\right|_{\theta,P} = \left.\frac{\partial h}{\partial S}\right|_{\eta,P} + \left.\frac{\partial h}{\partial\eta}\right|_{S,P}\left.\frac{\partial\eta}{\partial S}\right|_{\theta} = \mu - T\mu_\theta. \tag{2.8}$$

where we have applied $\partial h/\partial S|_{\eta,P} = \mu$, $\partial h/\partial\eta|_{S,P} = T$ and (2.5b). One derives the energy conservation by multiplying (2.2) by $-\rho_0\psi$, multiplying (2.6) by $\rho_0\partial h/\partial\theta$ as expressed in (2.8), multiplying (2.4a) by $\rho_0\partial h/\partial S$ as expressed in (2.8), and then

adding the result and integrating:

$$\frac{\partial}{\partial t}(\mathrm{KE}+H)=\frac{1}{\iint \rho_0 \mathrm{d}y\mathrm{d}z}\iint\Big\{\rho_0\psi J(\psi,\nabla^2\psi)-\rho_0 J(\psi,h)-\nabla\cdot\mathbf{q} \\ +\ \rho_0\nabla\cdot\Big[\nu\nabla^2\psi\nabla\psi-\nu\psi\nabla\nabla^2\psi\Big]\Big\}\mathrm{d}y\mathrm{d}z\quad=0, \tag{2.9}$$

where J is the Jacobian. All terms on the right-hand side of (2.9) vanish provided there is no viscous stress, no normal velocity, and no diffusion of energy at/across the boundaries. In deriving the second term on the right-hand side of (2.9) we have applied $\partial h/\partial z|_{S,\theta}=-b$, $J(\psi,z)=w=-\partial\psi/\partial y$ and integration by parts. Therefore the energy conservation of (2.9) is independent of the form of $\mathbf{q}$, $\mathbf{i}$, and the EOS of (2.3).

To close the NHEC model we follow equations (58.11) and (58.12) of Landau and Lifshitz (1959) and adopt the parameterization

$$\mathbf{i}=-\rho_0\kappa_s\nabla S,\qquad \mathbf{q}-(\mu-T\mu_\theta)\mathbf{i}=-\rho_0 C_{p0}\kappa_\theta\nabla\theta, \tag{2.10}$$

where C_{p0} is a constant equal to $4000\,\mathrm{J\,kg^{-1}\,{}^{o}C^{-1}}$ and κ_s and κ_θ are the kinematic diffusivities of salt and heat, respectively. Equation (2.10) acts to parameterize the unresolved grid-scale turbulent diffusion that tends to bring the fluid closer to an isohaline and isentropic state.

Only part of H (PE), called dynamic enthalpy H^D, contributes to the dynamics; the remaining part of H, called potential enthalpy H^P, represents the heat content of the system (Young, 2010; McDougall, 2003). In analogy to θ, H^P is simply the sys-

tem's enthalpy when all parcels are displaced adiabatically to the reference pressure. H^P and H^D are defined as

$$H = H^P + H^D, \quad H^P = \frac{\iint h^P \rho_0 \, \mathrm{d}y\mathrm{d}z}{\iint \rho_0 \mathrm{d}y\mathrm{d}z}, \quad H^D = \frac{\iint h^D \rho_0 \, \mathrm{d}y\mathrm{d}z}{\iint \rho_0 \mathrm{d}y\mathrm{d}z}, \tag{2.11a}$$

$$h^P(\theta, S) = h(\theta, S, P_r), \tag{2.11b}$$

$$h^D(\theta, S, P) = h(\theta, S, P) - h^P(\theta, S) = \int_{P_r}^{P} \left.\frac{\partial h}{\partial P'}\right|_{\theta,S} dP' = \int_{P_r}^{P} \frac{dP'}{\rho(\theta, S, P')} \tag{2.11c}$$

$$= (P - P_r)/\rho_0 + \int_z^0 b(\theta, S, z')\mathrm{d}z'. \tag{2.11d}$$

Again P is the hydrostatic pressure by using Boussinesq approximation (Young, 2010). The domain integral of $(P - P_r)/\rho_0$ in (2.11d) is approximately constant and does not contribute to the evolution of H^D (Young, 2010). The thermodynamic potentials of h^P and h^D are

$$C_p^P = \left.\frac{\partial h^P}{\partial \theta}\right|_S, \qquad C_p^D = \left.\frac{\partial h^D}{\partial \theta}\right|_{S,z} = \int_z^0 \left.\frac{\partial b}{\partial \theta}\right|_{S,z'} \mathrm{d}z', \tag{2.12a}$$

$$\mu^P = \left.\frac{\partial h^P}{\partial S}\right|_\theta, \qquad \mu^D = \left.\frac{\partial h^D}{\partial S}\right|_{\theta,z} = \int_z^0 \left.\frac{\partial b}{\partial S}\right|_{\theta,z'} \mathrm{d}z', \tag{2.12b}$$

$$C_p^P + C_p^D = C_p = \frac{T}{\theta} C_p^P, \qquad \mu^P + \mu^D = \mu - T\mu_\theta. \tag{2.12c}$$

Equation (2.12c) follows from (2.5b) and (2.8), and uses $T\partial\eta/\partial\theta|_S = (T/\theta)C_p^P$ (McDougall, 2003).

By definition H^P can only be modified diabatically. By contrast, H^D relies on the vertical distribution of fluid and represents the gravitational PE (GPE), which is required to generate KE (see (2.14b) below). Similar to the derivation of (2.9), we

evaluate $\partial h^D/\partial t$ and $\partial h^P/\partial t$ in terms of $\partial\theta/\partial t$ and $\partial S/\partial t$ (through thermodynamic potentials) and derive

$$\frac{\partial H^D}{\partial t} + \frac{\partial H^P}{\partial t} = -\frac{\partial \mathrm{KE}}{\partial t}, \tag{2.13a}$$

$$\frac{\partial H^D}{\partial t} = \frac{1}{\iint \rho_0 \mathrm{d}y\mathrm{d}z} \iint \frac{\partial h^D}{\partial t} \rho_0 \mathrm{d}y\mathrm{d}z = -\frac{\partial \mathrm{KE_{cum}}}{\partial t} - \frac{\partial \mathrm{C_{H^D toH^P}}}{\partial t}, \tag{2.13b}$$

$$\frac{\partial H^P}{\partial t} = \frac{1}{\iint \rho_0 \mathrm{d}y\mathrm{d}z} \iint \frac{\partial h^P}{\partial t} \rho_0 \mathrm{d}y\mathrm{d}z = \frac{\partial \mathrm{Heat_{vis}}}{\partial t} + \frac{\partial \mathrm{C_{H^D toH^P}}}{\partial t}, \tag{2.14a}$$

$$\mathrm{KE_{cum}} = \mathrm{KE} + \mathrm{Heat_{vis}} = \frac{1}{\iint \rho_0 \mathrm{d}y\mathrm{d}z} \int_0^t \iint (wb)\, \rho_0 \mathrm{d}y\mathrm{d}z\, \mathrm{d}t, \tag{2.14b}$$

$$\mathrm{Heat_{vis}} = \frac{1}{\iint \rho_0 \mathrm{d}y\mathrm{d}z} \int_0^t \iint \nu(\nabla^2\psi)^2 \rho_0 \mathrm{d}y\mathrm{d}z\, \mathrm{d}t, \tag{2.15a}$$

$$\begin{aligned} \mathrm{C_{H^D toH^P}} = -\frac{1}{\iint \rho_0 \mathrm{d}y\mathrm{d}z} \int_0^t \iint \Bigg[& \frac{C_p^D \nabla \cdot (C_{p0} \kappa_\theta \nabla\theta)}{C_p} + \frac{C_p^D \nu (\nabla^2\psi)^2}{C_p} \\ & + \mu^D \nabla \cdot (\kappa_s \nabla S) + \frac{C_p^D \kappa_s \nabla S \cdot \nabla(\mu^P + \mu^D)}{C_p} \Bigg] \rho_0 \mathrm{d}y\mathrm{d}z\, \mathrm{d}t. \end{aligned} \tag{2.15b}$$

$\mathrm{Heat_{vis}}$ is the cumulative viscous dissipation of KE (Figure 2.1). $\mathrm{KE_{cum}}$ is the cumulative KE production by vertical buoyancy flux (derived from $\psi\times$ (2.2)). $\mathrm{C_{H^D toH^P}}$ is the time-integral of the rate of energy conversion of H^D to H^P (expressed using (2.10)), which depends on the unpredictable turbulent diabatic processes and can not be determined *a priori* (section 2.5.3).

In contrast to H^P, H^D contributes little to the system's heat content, because

$$\frac{\partial h^D/\partial\theta}{\partial h^P/\partial\theta} = \frac{C_p^D}{C_p^P} = \frac{T-\theta}{\theta} < 0.3\%, \tag{2.16}$$

following (2.12a) and (2.12c). Thus the H^D variation is insensitive to the nonconservation of θ.

2.3.2 Numerical scheme

Equations (2.2), (2.3), (2.4a), (2.6), (2.10) define a closed system for numerical integration. Throughout this chapter, except section 2.4, we use the full nonlinear EOS (Jackett et al., 2006). We compute h^P, h^D and their derivatives (μ^P, C_p^P, μ^D and C_p^D) using the state functions of Jackett et al. (2006). We use periodic boundaries in y and stress-free, zero-flux boundaries at the top/bottom. We discretize Laplacians using second-order-centered finite differences. We compute Jacobians following Arakawa (1997). We use the Adams-Bashforth scheme (Press, 2007) for time integration. To resolve cabbeling instability, our default grid resolution is 0.83 m $\times$ 0.83 m. To ensure numerical stability while minimally affecting the turbulence, our default vertical and horizontal viscosity and tracer diffusivity are $3 \times 10^{-4}\,\mathrm{m^2/s}$. This model conserves salinity to within the round-off error of the computer, and conserves energy to within 5% of the KE (PE+KE deviates by <5% of KE) in almost all simulations.

2.4 KE contributions from OCAPE and the reduction of stratification

In this section we temporarily exclude cabbeling to isolate and explain the contributions of $\mathrm{S_{tb}}$ (section 2.4.1–2.4.2) and $-\mathrm{S_{strat}}$ (section 2.4.3). This also helps to

illustrate the effects of cabbeling when it is included later (section 2.5.1). We use the following EOS for (2.3) that includes thermobaricity but excludes cabbeling (see Equation (29) of Ingersoll, 2005),

$$b(\theta, S, z) = -g(\rho - \rho_0)/\rho = [\alpha_\theta(z)\delta\theta - \beta(z)\delta S]\, g. \tag{2.17}$$

Here $\delta\theta$, δS are departures of θ and S, respectively, from the basic state (θ_0, S_0). This basic state is the mean of the CFW and the WSW in the initial profile. The thermal expansion coefficient (α_θ) and the saline contraction coefficient (β) are functions of pressure with respect to θ_0 and S_0, and are computed from the full EOS (Jackett et al., 2006).

2.4.1 Unstratified simulation without cabbeling

We start with the a simple case: excluding cabbeling by using (2.17), and excluding stratification by employing an idealized initial two-layer unstratified profile: a CFW layer (0–0.5 km, -1.6 ^{o}C, 34.47 psu) overlying a WSW layer (0.5–1 km, 0.9 ^{o}C, 34.67 psu) (Figure 2.2(a)). From Part I we analytically determine its reference (minimum PE) state (Figure 2.2(f)). The column-averaged OCAPE is 1.1×10^{-2} J/kg. In this configuration the release of OCAPE can be triggered by infinitesimal vertical perturbations of the CFW into the WSW. Our domain size is $L \times L$ where L equals 1 km. To trigger the release of OCAPE we impose a uniform surface cooling of $100\,\mathrm{W\,m^{-2}}$ for 0.1 days between $y = L/12$ and $L/6$. The KE produced by this cooling is negligible. Ekman pumping caused by wind forcing could also trigger the

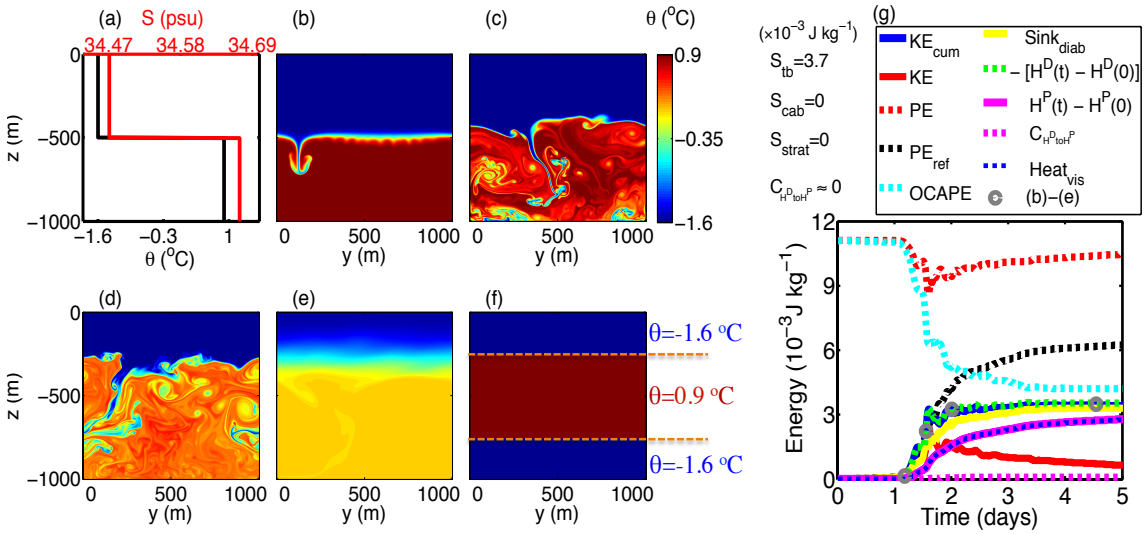

Figure 2.2: Unstratified simulation without cabbeling in the EOS, as discussed in section 2.4.1. Here z and y are the vertical and horizontal coordinates, respectively. (a) The initial θ/S profile. Snapshots of the θ (°C) field are shown (b) at t=1.18 days, (c) at t=1.56 days, (d) at t=2.01 days, and (e) at t=4.54 days (the quasi-steady state after convection). (f) The reference (minimum PE) state for the initial profile. (g) Time series of the energy budget (curves). We also show values of the four KE contributions (S_{tb}, S_{cab}, $-S_{strat}$ and $-C_{H^D toH^P}$) based on the whole convection (Equation (2.1)). See Figure 2.1 for the detailed energy relations. S_{cab}, S_{strat} and $C_{H^D toH^P}$ are all about zero here since the simulation excludes cabbeling and has a zero initial stratification ($C_{H^D toH^P}$ also relies on cabbeling, see section 2.5.3). OCAPE is equal to PE minus PE_{ref} (the PE of the reference state). Both PE and PE_{ref} are computed relative to the initial PE_{ref}. The sinks of OCAPE include S_{tb} and $Sink_{diab}$: S_{tb} is the cumulative contribution of OCAPE to KE (Figure 2.1), while $Sink_{diab}$ is the cumulative dissipation of OCAPE by diabatic processes (defined in (2.18b)).

convection (*e.g.*, Weiss et al., 1991; Schmid et al., 2008).

Figure 2.2(b)–(e) shows a series of simulated convection snapshots. The imposed surface cooling induces small velocities at the CFW/WSW interface and perturbs the initial plume of CFW into the WSW (Figure 2.2(b)). The plume gains negative buoyancy by thermobaricity as it descends. The velocity shear at the margins of the plume induces secondary Kelvin-Helmholtz instabilities. This generates local turbulent stirrings at smaller and smaller length scales. Our 2D system does not conserve

vorticity and thus does not develop an inverse cascade of energy. The turbulence perturbs the CFW/WSW interface and induces a succession of descending CFW plumes that convert OCAPE into KE. Thus convection becomes a self-sustaining process and the interface rises accordingly until the new interface is no longer unstable to turbulent perturbations. The convective motions are largely dissipated by $t = 2.3$ days (Figure 2.2(e)).

Figure 2.2(g) shows the time evolution of energy diagnostics. According to (2.13b)–(2.14a), H^D (dashed green curve) is converted to KE (solid red curve) via $\mathrm{KE_{cum}}$ (solid blue curve), and to H^P (solid magenta curve) via $\mathrm{C_{H^D toH^P}}$ (dashed magenta curve). H^P also gains energy from viscous dissipation ($\mathrm{Heat_{vis}}$, dashed blue curve) (Figure 2.1). Here $\mathrm{C_{H^D toH^P}}$ is negligible due to the absence of cabbeling (section 2.5.3). $\mathrm{S_{cab}}$ and $\mathrm{S_{strat}}$ are zero due to the absence of cabbeling and initial stratification. Therefore, according to (2.1), the only contribution to $\mathrm{KE_{cum}}$ is $\mathrm{S_{tb}}$ due to thermobaricity (OCAPE). OCAPE is defined as the PE minus the reference-state PE ($\mathrm{PE_{ref}}$). As our isolated system conserves (KE+PE) and has no KE initially, it follows that $\mathrm{PE}(0) = \mathrm{PE}(t) + \mathrm{KE}(t)$. Thus the cumulative loss of OCAPE is

$$\mathrm{OCAPE}(0) - \mathrm{OCAPE}(t) = \mathrm{KE}(t) + \mathrm{PE_{ref}}(t) - \mathrm{PE_{ref}}(0) = \mathrm{KE_{cum}}(t) + \mathrm{Sink_{diab}}(t)\,, \tag{2.18a}$$

$$\mathrm{Sink_{diab}}(t) = [\mathrm{PE_{ref}}(t) - \mathrm{PE_{ref}}(0)] - \mathrm{Heat_{vis}(t)}\,. \tag{2.18b}$$

Therefore, OCAPE has two sinks: $\mathrm{KE_{cum}}$ (equal to $\mathrm{S_{tb}}$ for this scenario) and $\mathrm{Sink_{diab}}$. Here $\mathrm{Sink_{diab}}$ is due to diabatic modification of the reference state (since $\mathrm{PE_{ref}}$ is

constant for adiabatic processes; see Part I), and the viscous heating (Heat_{vis}).

As shown in Figure 2.2(g), for the initial OCAPE, ∼31.9% is released to KE_{cum} and ∼31.1% is removed diabatically via $\text{Sink}_{\text{diab}}$ (solid yellow curve), leaving ∼34.7% unreleased. This ∼1/3 conversion ratio of OCAPE to KE_{cum} is essentially independent of the initial trigger (as long as its direct contribution to KE is small). This ratio is also insensitive to the viscosity/grid resolution (Table 2.1): As viscosity tends to zero, the dissipation scale becomes smaller such that the energy dissipation equals the cascade rate of turbulent energy (*e.g.*, Vallis, 2006).

KE_{cum} \ dz / ν	No cabbeling, in §2.3.1				Full EOS, in §2.4.1				Full EOS, case 4.4 in §2.4.4			
	1.67m	1.11m	0.83m	0.67m	1.67m	1.11m	0.83m	0.67m	1.67m	1.11m	0.83m	0.67m
$3\times10^{-4}\text{m}^2/\text{s}$	x	x	30.1%	31.5%	x	x	64.6%	64.7%	x	x	89.7%	90.2%
$1\times10^{-3}\text{m}^2/\text{s}$	33.6%	32.4%	31.8%	31.6%	65.6%	68.2%	67.2%	65.0%	94.5%	91.0%	89.5%	90.5%
$3\times10^{-3}\text{m}^2/\text{s}$	32.1%	32.6%	31.4%	34.5%	67.4%	66.4%	66.8%	69.0%	92.8%	94.1%	94.4%	89.7%

Table 2.1: Sensitivity of KE_{cum}, as a fraction of the initial OCAPE, to viscosity ν (same value as diffusivity) and grid resolution (dz=dy). The first reference simulation (in §3a) has thermobaricity but no cabbeling and stratification, with initial OCAPE=1.1×10^{-2} J/kg; The second (in §4a) has thermobaricity and cabbeling but no stratification, with initial OCAPE=1.1×10^{-2} J/kg; The third (case 4.4 in §4d) has all three effects, with initial OCAPE=3.9×10^{-3} J/kg. Their model domain dimensions are 1000 m × 1000 m, 1000 m × 1000 m and 700 m × 700 m, respectively. In all simulations except the ones denoted as "x", the flow is resolved without unphysical KE accumulation at the grid scale. The results indicate that KE_{cum} are insensitive (variation < 5%) to ν and dz (as long as they are small enough to enable cabbeling instability if cabbeling is allowed).

2.4.2 Contribution of thermobaricity (OCAPE) to KE: S_{tb}

We demonstrate that S_{tb} is ∼1/3 of OCAPE for any two-layer unstratified profile. For stratified profiles, a similar 1/3 ratio still holds (section 2.4.3; (2.21b)-(2.21c)). This ratio holds in the presence of cabbeling since thermobaricity and cabbeling contribute independently to KE_{cum} (section 2.2). Table 2.2 details four simulations without

	Case 2.1	Case 2.2	Case 2.3	Case 2.4
Interface depth of initial state (CFW above WSW)	100 m	300 m	500 m	700 m
Initial reference state (by depths)	WSW, 0-900 m CFW, 900-1000 m	WSW, 0-700 m CFW, 700-1000 m	CFW, 0-250 m WSW, 250-750 m CFW, 750-1000 m	CFW, 0-550 m WSW, 550-850 m CFW, 850-1000 m
Depth of the upper boundary of CFW/WSW mixture at the final quasi-steady state	$\sim$ 0 m	$\sim$ 0 m	$\sim$ 250 m	$\sim$ 550 m
Initial OCAPE	2.7×10^{-2} J/kg	3.1×10^{-2}J/kg	1.1×10^{-2} J/kg	2.0×10^{-3} J/kg
$\mathrm{KE_{cum}}$ (% of initial OCAPE)	32.9%	34.5%	31.9%	31.1%
$\mathrm{Sink_{diab}}$ (% of initial OCAPE)	66.9%	64.1%	31.1%	24.9%
Remaining OCAPE (% of initial OCAPE)	0.5%	0.8%	34.7%	43.0%
$\mathrm{C_{H^DtoH^P}}$ (% of initial OCAPE)	0.15%	0.06%	0.04%	0.11%

Table 2.2: Characterization of unstratified simulations without cabbeling in the EOS, as discussed in section 2.4.2. We show the initial OCAPE, its two sinks: $\mathrm{KE_{cum}}$ and $\mathrm{Sink_{diab}}$ (see (2.18a)), and the remaining OCAPE after convection. All simulations have a 1000 m $\times$ 1000 m modeling domain. They all have the CFW (θ=-1.6 °C, S=34.47 psu) overlying the WSW (θ=0.9 °C) initially but with different CFW/WSW interface depths. The S of the initial WSW is 34.63 psu, 34.65 psu, 34.67 psu, 34.69 psu, respectively, for Cases 2.1–2.4 to ensure a zero stratification ($N^2 = 0$). Their experimental configurations are otherwise identical to the reference simulation in Figure 2.2 (Case 2.3). About 1/3 of OCAPE is consistently released to $\mathrm{KE_{cum}}$ for all these simulations. $\mathrm{C_{H^DtoH^P}}$ is the energy conversion of dynamic enthalpy to potential enthalpy (see (2.15b)), which is consistently negligible for no-cabbeling simulation (see explanation in section 2.5.3).

cabbeling (cases 2.1-2.4): their profiles are all initially unstratified and two-layer, with the CFW/WSW interface lying at different depths. In all simulations, $\sim$1/3 of the initial OCAPE is consistently converted to $\mathrm{KE_{cum}}$ (*i.e.* $\mathrm{S_{tb}}$ here). Further, $\mathrm{C_{H^DtoH^P}}$ is negligible (see section 2.5.3).

We now derive the 1/3 OCAPE-to-$\mathrm{KE_{cum}}$ conversion ratio analytically. Only the H^D part of PE contributes to OCAPE (since H^P is constant for adiabatic processes). Further, $\mathrm{C_{H^DtoH^P}}$ is negligible in the absence of cabbeling. From (2.13b) we derive

$$\frac{\mathrm{KE_{cum}}}{\mathrm{OCAPE}} = \frac{H_i^D - H_f^D - \mathrm{C_{H^DtoH^P}}}{\mathrm{PE}_i - \mathrm{PE}_{ref}} \approx \frac{H_i^D - H_f^D}{H_i^D - H_{ref}^D}. \tag{2.19}$$

Here the subscripts i, f and ref denote the initial, the final, and the initial reference states. The initial reference state is determined following Part I. $(H_i^D - H_{ref}^D)$ is expressed following (2.11a), (2.11d) and (2.17). $(H_i^D - H_f^D)$ is expressed by (2.A10), with an unknown D_f (the depth of the upper boundary of CFW/WSW mixture in the final state; Figure 2.3(c)). Here we determine the value of D_f that maximizes[2] $(H_i^D - H_f^D)$, which predicts a D_f that is in agreement with the simulations mentioned above. This strategy of solving the final state (D_f) is consistent with the principle that a system tends to deform to a final state that minimizes PE (*i.e.* H_f^D here) (Reddy, 2002). Using a linearly depth-dependent α_θ profile and a constant β, the predicted $\mathrm{KE_{cum}}$/OCAPE by (2.19) is exactly 1/3 (with deviation $\leq$ 6% if using realistic α_θ and β profiles). This 1/3 ratio reveals the fundamental relation between the PE released by adiabatic movement of CFW (OCAPE) vs. the PE released by mixing of CFW into WSW ($\mathrm{KE_{cum}}$).

2.4.3 Contribution of reduced stratification to KE: $-\mathrm{S_{strat}}$

Conceptually, mixing out the stratification of an ocean column during convection raises the water column's center of mass. This would increase GPE by an amount S_{strat}, which is partly converted from KE. In the framework of section 2.3 (Figure 2.1), this process converts KE and H^P into H^D (note that H^D may essentially represent GPE; that is why S_{strat} derived below has the same expression as S_{strat} in (2.A10) and (2.A11) derived using the concept of H^D). We again exclude cabbeling. We only

[2]In (2.A10), $\gamma_{\theta\theta}$, N^2_{WSW} and $\delta\rho$ are zero since we exclude cabbeling and stratification here. D is a constant. Thus we determine D_f that maximizes $(H_i^D - H_f^D)$ by solving $\mathrm{d}(2.\mathrm{A10})/\mathrm{d}D_f$=0 and $\mathrm{d}^2(2.\mathrm{A10})/\mathrm{d}D_f^2$ <0. In this scenario, the analytical expression for D_f is zero when $\lambda > 2/3$ and is $(1 - 3/2 \times \lambda)D$ when $\lambda \leq 2/3$.

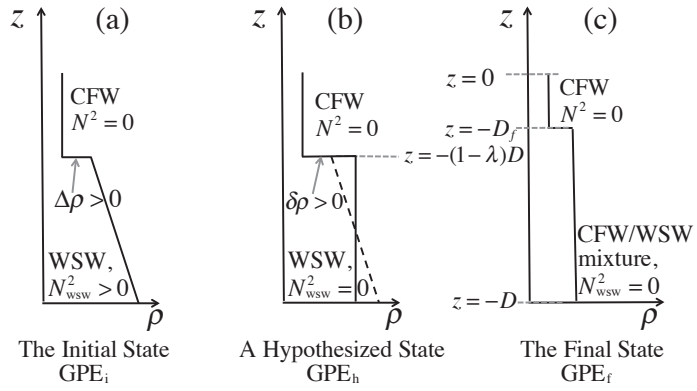

Figure 2.3: Schematic of three states for illustrating the reduction of stratification (N^2) during convection, which leads to a KE sink: $-\mathrm{S}_{\mathrm{strat}}$, as discussed in section 2.4.3. (a) The initial state. It has a stable density jump $\Delta\rho$ at the CFW/WSW interface and a stratified WSW ($N^2 = N^2_{\mathrm{WSW}}$). ρ is the density variation associated with N^2: $\rho = \int_{-D}^{z}(-\rho_0/g)N^2(z)dz$. (b) A hypothesized state, same as the initial state except taking the mean property of WSW from the initial state (*i.e.* from the dash to the solid line). $\delta\rho$ is the change of ρ from the bottom of CFW to the middle depth of WSW, defined in (2.20b) (states in (a) and (b) have the same $\delta\rho$). (c) The final quasi-steady state after convection, with a interface at depth $z = -D_f$. The gravitational potential energy (GPE) of these three states are $\mathrm{GPE_i}$, $\mathrm{GPE_h}$ and $\mathrm{GPE_f}$, respectively. Then $-\mathrm{S}_{\mathrm{strat}}$ is equal to $(\mathrm{GPE_i} - \mathrm{GPE_h}) + (\mathrm{GPE_h} - \mathrm{GPE_f})$. Cabbeling and thermobaricity are excluded here (for section 2.4.3, not for the appendix) in order to compute S_{strat}: therefore the column depth ($z = -D$) is assumed unchanged in this figure.

.

modify our previous two-layer initial profiles by adding the stratification: a stable density gap $\Delta\rho$ across the CFW/WSW interface and a uniform positive stratification in the WSW layer ($N^2 = N^2_{\mathrm{WSW}}$=constant). We consider scenarios in which the initial WSW is stratified in salinity only.

Figure 2.3 shows schematics of the initial and the final states of convection: D is the water column's depth and λ is the initial fraction of WSW of the whole column. We also consider a hypothesized state (Figure 2.3(b)), the same as the initial state except that the stratified WSW is replaced by the mean WSW. The GPEs of these three states (Figure 2.3(a)–(c)) are denoted as $\mathrm{GPE_i}$, $\mathrm{GPE_h}$, and $\mathrm{GPE_f}$, respectively.

	Case 3.1	Case 3.2	Case 3.3	Case 3.4	Case 3.5	Case 3.6	Case 3.7	Case 3.8
λ	0.9	0.9	0.9	0.9	0.7	0.7	0.7	0.7
$\Delta\rho$ (kg/m^3)	0	8×10^{-3}	2×10^{-3}	4×10^{-3}	12×10^{-3}	0	1×10^{-3}	6×10^{-3}
$N^2_{\rm wsw}$ (s^{-2})	0.6×10^{-7}	0	0.2×10^{-7}	0.4×10^{-7}	0	1.0×10^{-7}	0.8×10^{-7}	0.4×10^{-7}
$\delta\rho$(kg/m^3)	2.8×10^{-3}	8.0×10^{-3}	3.0×10^{-3}	5.9×10^{-3}	12×10^{-3}	3.7×10^{-3}	3.9×10^{-3}	7.5×10^{-3}
OCAPE (J/kg)	2.39×10^{-2}	1.92×10^{-2}	2.37×10^{-2}	2.10×10^{-2}	0.89×10^{-2}	2.32×10^{-2}	2.30×10^{-2}	1.61×10^{-2}
$\rm S_{tb}$ (J/kg) by (2.21b)	8.8×10^{-3}	8.8×10^{-3}	8.8×10^{-3}	8.8×10^{-3}	5.8×10^{-3}	10.0×10^{-3}	9.9×10^{-3}	8.6×10^{-3}
$-\rm S_{strat}$(J/kg) by (2.20a)	-4.9 $\times 10^{-3}$	-3.4 $\times 10^{-3}$	-2.5 $\times 10^{-3}$	-5.0 $\times 10^{-3}$	-4.7 $\times 10^{-3}$	-6.3 $\times 10^{-3}$	-5.9 $\times 10^{-3}$	-6.3 $\times 10^{-3}$
$\rm KE_{cum}$ (J/kg) by (2.21a)	3.9×10^{-3}	5.4×10^{-3}	6.3×10^{-3}	3.8×10^{-3}	1.1×10^{-3}	3.7×10^{-3}	4.0×10^{-3}	2.3×10^{-3}
$\rm KE_{cum}$ (J/kg) by simulation	4.1×10^{-3}	5.3×10^{-3}	6.5×10^{-3}	3.7×10^{-3}	1.2×10^{-3}	3.6×10^{-3}	4.3×10^{-3}	2.6×10^{-3}
D_f (m) by theory	0	0	0	0	185	22	27	96
D_f (m) by simulation	0	0	0	0	~ 190	~ 30	~ 30	~ 110

Table 2.3: Characterization of stratified simulations without cabbeling in the EOS, as discussed in section 2.4.3. All simulations have a 1000 m $\times$ 1000 m modeling domain. They all have the same configurations (*e.g.* the θ and S of the initial CFW, the θ of the initial WSW, and the initial cooling) as the reference simulation in Figure 2.2 except the following parameters: λ, $\Delta\rho$, $N^2_{\rm wsw}$ and $\delta\rho$ (see the text for their definitions). The S of the initial WSW in each case can be determined by $\Delta\rho$ and $N^2_{\rm wsw}$. OCAPE also differs from one case to another. $\rm S_{tb}$ and $(-\rm S_{strat})$ are the KE contributions from thermobaricity and the reduction of stratification, respectively. D_f is the depth of the upper boundary of CFW/WSW mixture at the final state. "D_f by theory" maximizes $H_i^D - H_f^D$ as given by (2.21a) along with (2.21c) and (2.20a). In all simulations $\rm KE_{cum}$ and D_f are both well predicted by (2.21a) and the strategy above, respectively.

Excluding thermobaricity and cabbeling, we derive $(\rm GPE_i - GPE_h)$ and $(\rm GPE_h - GPE_f)$ by multiplying gravity g by the change of depth of the water column's center of mass in either case. They are expressed by the first and the second brace term in (2.20a) below, respectively. Their sum is $(\rm GPE_i - GPE_f)$ due to the reduction of stratification, *i.e.*, equal to

$$-\rm S_{strat} = \left\{-\frac{1}{12} N^2_{\rm WSW} \lambda^3 D^2\right\} + \left\{-\frac{1}{2}\lambda\left[(1-\lambda)D - D_f\right]\frac{\delta\rho}{\rho_0} g\right\}, \tag{2.20a}$$

$$\delta\rho = \Delta\rho + \frac{\rho_0 N^2_{\rm WSW}\lambda D}{2g}. \tag{2.20b}$$

Equation (2.20a) is consistent with a more rigorous derivation from Appendix ((2.A10)-(2.A11)).

Therefore, in the absence of cabbeling, we derive $\mathrm{KE_{cum}}$ following (2.A1) and (2.A10):

$$\mathrm{KE_{cum}} = H_i^D - H_f^D = \mathrm{S_{tb}} - \mathrm{S_{strat}}, \tag{2.21a}$$

$$\mathrm{S_{tb}} = \frac{1}{3}\mathrm{OCAPE_c}(\delta\rho = 0) \tag{2.21b}$$

$$= \frac{1}{3}\left\{-g\alpha_z\Delta\theta D^2\left[\lambda(\lambda-1)(1-2\lambda) + (2\lambda-3\lambda^2)\frac{D_f}{D} - \lambda\frac{D_f^2}{D^2}\right]\right\}. \tag{2.21c}$$

Denotations follow Appendix. Here $\mathrm{OCAPE_c}$ is the initial-state OCAPE for the part of water column where convection occurs[3]. For unstratified profiles, this solution simply reduces to $\mathrm{S_{tb}} = (1/3)\mathrm{OCAPE}$, as in section 2.4.2. Following section 2.4.2, we predict the final state *a priori* by determining a D_f that maximizes $(H_i^D - H_f^D)$. At any instant during convection, the associated state cannot be determined *a priori* from initial conditions, and thus $\mathrm{S_{tb}}$ and $\mathrm{S_{strat}}$ (and also $\mathrm{S_{cab}}$) at that instant cannot be determined analytically. In table 2.3, we detail eight numerical test simulations with different stratifications. In all cases $\mathrm{KE_{cum}}$ and D_f are well predicted by (2.21a) and the strategy above, respectively.

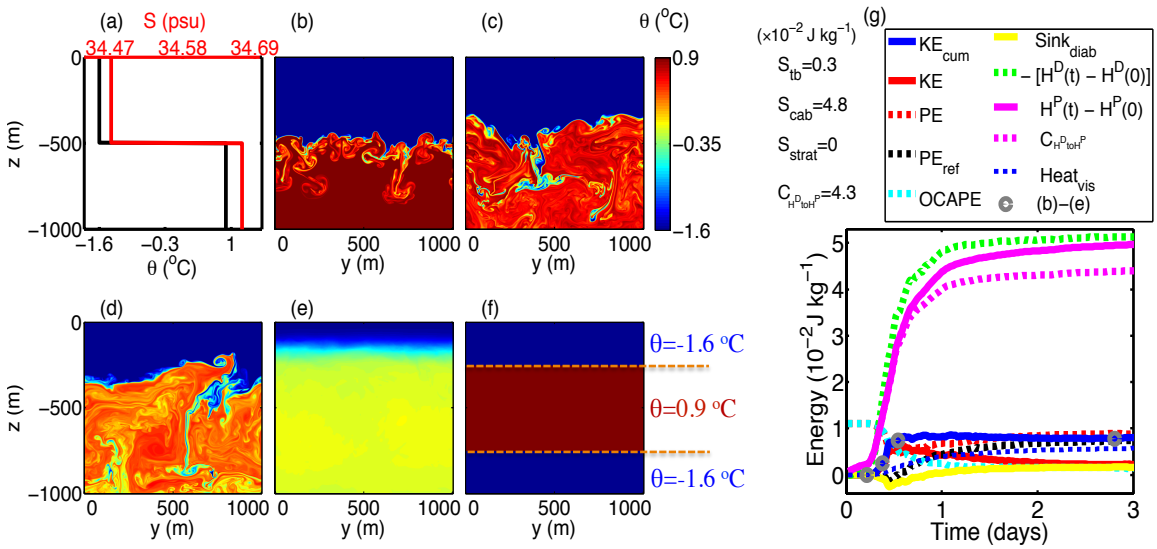

Figure 2.4: As Figure 2.2 but for an unstratified simulation with cabbeling included in the EOS, discussed in section 2.5.1. It is the same simulation as that in Figure 2.2 but uses the full nonlinear EOS of seawater (Jackett et al., 2006). Snapshots of the model's θ (°C) are shown (b) at t=0.22 day, (c) at t=0.38 day, (d) at t=0.53 day, and (e) at t=2.71 days. For (g), see Figure 2.1 for the detailed energy relations.

2.5 KE contributions from cabbeling-induced volume reduction and the conversion of H^D to H^P

In this section, we illustrate that cabbeling alone induces two KE components: S_{cab} and $-C_{H^D toH^P}$. Harcourt (2005) notes that the CFW/WSW transition is of finite vertical extent due to mixed layer entrainment or shear, which is key to inducing the cabbeling instability. To resolve cabbeling instability, our simulation adopts the full nonlinear EOS (Jackett et al., 2006) and prescribes a initial CFW/WSW interface of finite thickness (∼20 m; section 2.5.4), with numerical grid sizes of 0.83 m and a viscosity of $3 \times 10^{-4} m^2/s$.

[3]Since convection only occurs from $z = -D_f$ to $-D$, when expressing $OCAPE_c$ using the OCAPE equation ((17c) of Part I), we should replace D, λ and $\Delta\rho$ by $(D - D_f)$, $\lambda D/(D - D_f)$ and $\delta\rho$, respectively, and finally multiply by a factor $(D - D_f)/D$. This gives (2.21c), as consistent with (2.A10) and (2.A11).

2.5.1 Unstratified simulation with cabbeling

We reproduce the same simulation in section 2.4.1 (Figure 2.2) but now using the full EOS (Figure 2.4). This comparison identifies significant differences introduced by cabbeling:

(i) The initialization of convection is more rapid (∼0.22 day vs 1.18 day) since cabbeling-involved entrainment/mixing at the initial interface generates negative buoyancy and entrains CFW plumes into WSW more rapidly. Additional acceleration of plumes by cabbeling also shortens the whole convective period (∼2.5 day vs 3.5 day; see Figures 2.4(f) and 2.2(f)).

(ii) The interface depth of the final state (D_f) is shallower in the presence of cabbeling (∼ 130 m vs 250 m). This is because a transient state with interface at 250 m depth is still susceptible to cabbeling instability that drags more CFW downward. This modification to the final state also leads to a smaller $\mathrm{S_{tb}}$ (0.0029 vs 0.0037 J/kg) following (2.21c).

(iii) Cabbeling contributes ∼0.005 J/kg to the final $\mathrm{KE_{cum}}$ by producing two additional terms: $\mathrm{S_{cab}}$ =0.0481 J/kg and $-\mathrm{C_{H^D toH^P}} = -0.0432$ J/kg. The resulting $\mathrm{KE_{cum}}$ is more than doubled. $\mathrm{KE_{cum}}$ is insensitive to grid resolution and viscosity (Table 2.1). Therefore, in the presence of cabbeling, the energy budget should be updated from (2.21a) to

$$H_i^D - H_f^D = \mathrm{S_{tb}} - \mathrm{S_{strat}} + \mathrm{S_{cab}}, \tag{2.22}$$

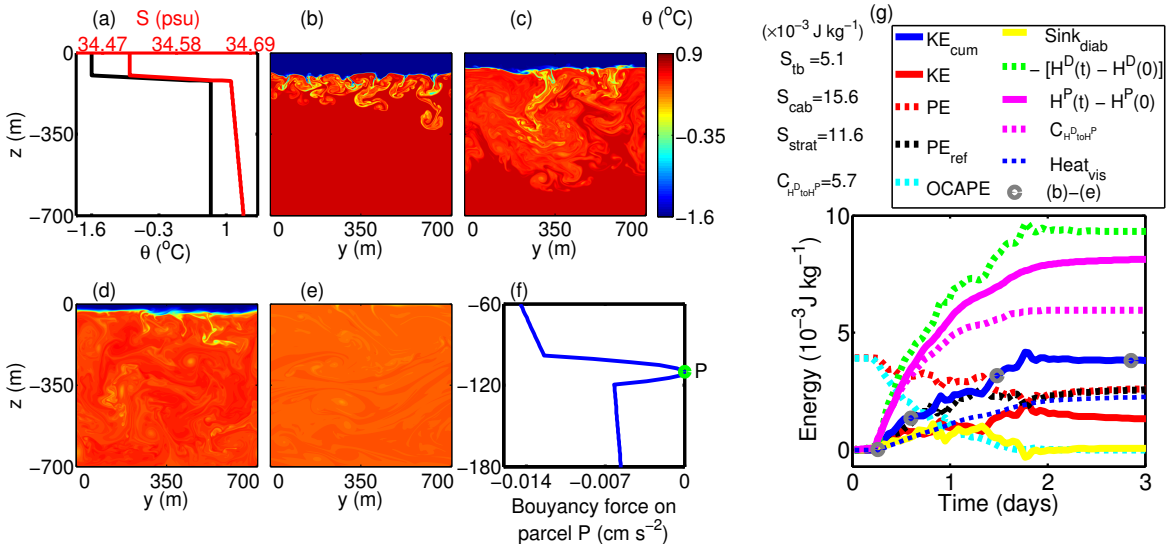

Figure 2.5: As Figure 2.2, except panel (f), for a stratified simulation with cabbeling included in the EOS. This is case 4.4 of Table 2.4 discussed in section 2.5.4. It adopts the full nonlinear EOS of seawater (Jackett et al., 2006) and a detailed model configuration is described in Table 2.4. Snapshots of the model's θ (°C) are shown (b) at t=0.26 day, (c) at t=0.59 day, (d) at t=1.49 days, and (e) at t=2.8 days. Panel (f) follows Figure 9(b) of Harcourt (2005): it shows the buoyancy force on parcel P using the full nonlinear EOS when it is displaced vertically and adiabatically across the initial profile. Parcel P is originally located at the depth of 115 m within the initial interface (100-120 m depths). Panel (f) suggests a cabbeling instability when moving parcel P downward, since it becomes negatively buoyant. For (g), see Figure 2.1 for the detailed energy relations.

and Equation (2.1). These two equations are derived mathematically in Appendix and are verified numerically in section 2.5.4 (Figure 2.7(a)–2.7(b)).

2.5.2 KE contribution from cabbeling-induced volume reduction: S_{cab}

Cabbeling shrinks the water column's volume when the initial CFW and WSW are mixed by convection. This acts to lower the water column's center of mass and thus releases GPE by an amount S_{cab}, which is partly converted into KE. In the framework of section 2.3 (Figure 2.1), this process converts H^D into KE and H^P

(again H^D may essentially represent GPE; that is why S_{cab} derived below has the same expression as S_{cab} in (2.A10) and (2.A11) derived using the concept of H^D). Again we consider initial states (Figure 2.3(a)) with WSW stratified in salinity only. Using the second-order Taylor series of potential density, the initial CFW and WSW both have a cabbeling term of density (see Equation (10) of Harcourt, 2005):

$$\rho_i^c = -\rho_0 \gamma_{\theta\theta} (\Delta\theta)^2, \quad \gamma_{\theta\theta}(\theta, P, S) = -\frac{1}{2\rho_0} \left.\frac{\partial^2 \rho}{\partial \theta^2}\right|_{P,S}, \tag{2.23}$$

where $\Delta\theta$ is the departure of the initial WSW from basic state θ_0, the mean θ of the initial CFW and WSW. Here $\gamma_{\theta\theta}$ is the coefficient of cabbeling. For wintertime polar seawater at sea level (*e.g.*, 30 psu< S <40 psu and $-2\,^{\circ}\mathrm{C} < \theta < 4\,^{\circ}\mathrm{C}$), $\gamma_{\theta\theta}$ is roughly constant: $(6.5 \pm 0.6) \times 10^{-6}\,^{\circ}\mathrm{C}^{-2}$ (Figure 3(a) of Huang, 2014). $\gamma_{\theta\theta}$ varies by $< 10\%$ from sea level pressure to 1500 m depth (IOC et al., 2010). Thus we approximate $\gamma_{\theta\theta} \equiv 6.5 \times 10^{-6}\,^{\circ}\mathrm{C}^{-2}$ throughout for simplicity.

The CFW/WSW mixture of the final state, which has a thickness of $(D - D_f)$, assumes complete mixing (Figure 2.3(c); see simulations in Figures 2.2(e), 2.4(e), 2.5(e) and 2.7(e)). In contrast to (2.23), this final CFW/WSW mixture has a cabbeling density term:

$$\rho_f^c = -\rho_0 \gamma_{\theta\theta} (\Delta\theta_f)^2, \quad \Delta\theta_f = \left[2\lambda \frac{D}{D - D_f} - 1\right] \Delta\theta, \tag{2.24}$$

where $\Delta\theta_f$ is the CFW/WSW mixture's departure[4] from the basic state θ_0. Therefore,

[4]For the expression of $\Delta\theta_f$ in (2.24), we neglect the nonconservation of θ during mixing because H^D (and thus $\mathrm{S_{cab}}$) is insensitive to this nonconservation according to (2.16).

in a compressible fluid, cabbeling shrinks the CFW/WSW mixture's thickness by $(D - D_f)(\rho_f^c - \rho_i^c)/\rho_0$. Thus the center of mass of the whole column is lowered by $[(D - D_f)(\rho_f^c - \rho_i^c)/\rho_0](D + D_f)/(2D)$. Multiplying this by gravity g gives the release of GPE by

$$\begin{aligned} \mathrm{S_{cab}} &= \left[(D - D_f)\frac{\rho_f^c - \rho_i^c}{\rho_0}\frac{D + D_f}{2D}\right] \times g \\ &= 2g[\gamma_{\theta\theta}(\Delta\theta)^2](D + D_f)\left(\lambda - \lambda^2\frac{D}{D - D_f}\right). \end{aligned} \tag{2.25}$$

This expression agrees with a more rigorous derivation from Appendix ((2.A10)-(2.A11)).

2.5.3 KE contribution from energy conversion of H^D to H^P: $-\mathrm{C_{H^D toH^P}}$

$\mathrm{C_{H^D toH^P}}$, as expressed in (2.15b), is the irreversible diabatic energy conversion of H^D to H^P, which reduces the KE production from H^D ((2.13b); Figure 2.1). As shown in (2.1), the terms $\mathrm{C_{H^D toH^P}}$ and $\mathrm{KE_{cum}}$ are the two parts of (S_{tb}- S_{strat}+S_{cab}), resulting from the three processes identified above (S_{tb}, S_{strat}, and S_{cab}). We address the following question: why is $-\mathrm{C_{H^D toH^P}}$ only significant in the presence of cabbeling (section 2.5.1)?

We diagnose (2.15b) numerically and find that the first term dominates $\mathrm{C_{H^D toH^P}}$:

$$\mathrm{C_{H^D toH^P}} \approx \frac{1}{\iint \rho_0 \mathrm{d}y\mathrm{d}z}\int_0^t \iint -\frac{C_p^D \nabla\cdot(C_{p0}\kappa_\theta\nabla\theta)}{C_p}\rho_0 \mathrm{d}y\mathrm{d}z\,\mathrm{d}t, \tag{2.26}$$

Including cabbeling, the leading-order buoyancy expression is updated from (2.17) to

be

$$b(\theta, S, z) = \left[\alpha_\theta(z)\delta\theta - \beta(z)\delta S + \gamma_{\theta\theta}(\delta\theta)^2\right] g. \tag{2.27}$$

Thus C_p^D, according to (2.12a), can be decomposed as follows:

$$C_p^D = \int_z^0 \left.\frac{\partial b}{\partial \theta}\right|_{S,z'} \mathrm{d}z' = C_p^\alpha + C_p^{cab}, \tag{2.28a}$$

$$C_p^\alpha = \int_z^0 \alpha_\theta g \mathrm{d}z'; \quad C_p^{cab} = \int_z^0 2\gamma_{\theta\theta}\delta\theta g \mathrm{d}z' = (-z)2\gamma_{\theta\theta}\delta\theta g, \tag{2.28b}$$

We diagnose numerically that the effect of C_p^{cab} dominates the factor C_p^D in (2.26), where C_p is approximately $C_{p0} = 4000\,\mathrm{J\,kg^{-1}\,{}^oC^{-1}}$. Thus we update (2.26) to

$$\mathrm{C_{H^D toH^P}} \approx \frac{1}{\iint \rho_0 \mathrm{d}y\mathrm{d}z} \int_0^t \iint -C_p^{cab} \nabla\cdot(\kappa_\theta \nabla\theta)\mathrm{d}y\mathrm{d}z\,\mathrm{d}t \tag{2.29a}$$

$$= \frac{-2\gamma_{\theta\theta} g}{\iint \rho_0 \mathrm{d}y\mathrm{d}z} \int_0^t \iint \nabla(\delta\theta z)\cdot(\kappa_\theta \nabla\theta)\mathrm{d}y\mathrm{d}z\,\mathrm{d}t \tag{2.29b}$$

$$\approx \frac{2\gamma_{\theta\theta} g}{\iint \rho_0 \mathrm{d}y\mathrm{d}z} \int_0^t \iint (-z)\kappa_\theta(\nabla\theta)^2 \mathrm{d}y\mathrm{d}z\,\mathrm{d}t \quad > 0, \tag{2.29c}$$

using (2.28b), the no-flux boundary condition and $\nabla(\delta\theta) = \nabla\theta$, and neglecting a small term proportional to $\partial(\delta\theta)^2/\partial z$. In (2.29c), $(-z)$ is always positive. Equation (2.29c) is verified numerically.

In summary, cabbeling contributes to heat capacity by a factor of $(\gamma_{\theta\theta}\delta\theta)$ as in (2.28b). This factor couples with the heat diffusion $\nabla\cdot(\kappa_\theta\nabla\theta)$ as in (2.29a) and generates a positive-definite contribution ($\propto (\nabla\theta)^2$) to $\mathrm{C_{H^D toH^P}}$ as in (2.29c), which accumulates over time. Thus $\mathrm{C_{H^D toH^P}}$ is only significant in the presence of cabbel-

ing. From (2.29c), $C_{H^D toH^P}$ is proportional to κ_θ as well as $(\nabla\theta)^2$, while the mean $(\nabla\theta)^2$ decreases with κ_θ. Thus these two factors act to compensate each other and induces the insensitivity of $C_{H^D toH^P}$ to diffusivity κ_θ, as diagnosed numerically. Due to the process-dependent nature, $C_{H^D toH^P}$, a component of KE_{cum} in (2.1), cannot be predicted *a priori*, but rather must be diagnosed numerically.

	Case 4.1	Case 4.2	Case 4.3	Case 4.4	Case 4.5	Case 4.6	Case 4.7	Case 4.8
D (m)	700	700	700	700	700	700	2000	2000
$\Delta\rho$ (kg/m^3)	1×10^{-3}	1×10^{-3}	5×10^{-3}	5×10^{-3}	9×10^{-3}	9×10^{-3}	5×10^{-3}	5×10^{-3}
N^2_{wsw} (s^{-2})	0.5×10^{-7}	2.5×10^{-7}	0.5×10^{-7}	2.5×10^{-7}	0.5×10^{-7}	2.5×10^{-7}	0.2×10^{-7}	0.8×10^{-7}
$\delta\rho$ (kg/m^3)	2.6×10^{-3}	8.8×10^{-3}	6.6×10^{-3}	12.8×10^{-3}	10.6×10^{-3}	16.8×10^{-3}	7.0×10^{-3}	12.9×10^{-3}
OCAPE (J/kg)	1.33×10^{-2}	0.78×10^{-2}	0.98×10^{-2}	0.43×10^{-2}	0.62×10^{-2}	0.10×10^{-2}	5.77×10^{-2}	4.98×10^{-2}
S_{tb} (J/kg) by (2.21b)	5.1×10^{-3}	5.1×10^{-3}	5.1×10^{-3}	5.1×10^{-3}	5.1×10^{-3}	5.1×10^{-3}	20.9×10^{-3}	20.9×10^{-3}
$-S_{strat}$(J/kg) by (2.20a)	-2.3×10^{-3}	-1.0×10^{-2}	-4.1×10^{-3}	-1.16×10^{-2}	-5.6×10^{-3}	-1.33×10^{-2}	-8.9×10^{-3}	-2.87×10^{-2}
S_{cab}(J/kg) by (2.25)	15.6×10^{-3}	15.6×10^{-3}	15.6×10^{-3}	15.6×10^{-3}	15.6×10^{-3}	15.6×10^{-3}	17.5×10^{-3}	17.5×10^{-3}
$-C_{H^D toH^P}$ (J/kg) by simulation	-7.0×10^{-3}	-6.2×10^{-3}	-7.4×10^{-3}	-5.6×10^{-3}	-6.6×10^{-3}	-4.6×10^{-3}	-4.5×10^{-3}	-4.1×10^{-3}

Table 2.4: Characterization of stratified simulations with cabbeling (using the full EOS), as discussed in section 2.5.4. Denotations follow Table 2.3. In all simulations the horizontal size of the modeling domain is the same as its vertical size (*i.e.* D). All simulations initially have the same CFW (θ =-1.6°C, S=34.51 psu) at 0–100 m depths, a linear variation of θ and S across 100–120 m depths, and a WSW layer beneath (θ =0.7°C). The S of the initial WSW in each case can be determined by $\Delta\rho$ and N^2_{wsw}. The initial cooling applied to the simulation in Figure 2.2 is also applied to all simulations here. These perturbations, along with the cabbeling instability, trigger convection in the simulations. All simulations have a final state of total column mixing. See $(H_i - H_f)$ and KE_{cum} diagnosed from simulations here vs. the predictions by (2.22) and (2.1) in Figure 2.6(a)–2.6(b).

2.5.4 Stratified simulations with cabbeling

We conduct eight numerical experiments (Table 2.4). Since our energy decomposition (2.A10) relies on the ocean column depth D, we perform cases with various sizes of D to test the sensitivity. They initially all have a linear variation of θ and S across the CFW/WSW interface (100–120 m depths). But they have differing initial

	Case 5.1	Case 5.2	Case 5.3	Case 5.4	Case 5.5	Case 5.6	Case 5.7	Case 5.8	Case 5.9
$\Delta\rho$ (kg/m^3)	1×10^{-3}	1×10^{-3}	1×10^{-3}	5×10^{-3}	5×10^{-3}	5×10^{-3}	9×10^{-3}	9×10^{-3}	9×10^{-3}
$N^2_{\rm wsw}$ (s^{-2})	1×10^{-7}	2×10^{-7}	4×10^{-7}	1×10^{-7}	2×10^{-7}	4×10^{-7}	1×10^{-7}	2×10^{-7}	4×10^{-7}

Table 2.5: Characterization of stratified simulations with cabbeling (using the full EOS), focusing on the convection depth, as discussed in section 2.5.5. Unlike Table 2.4, all simulations here do not have a convection depth that reaches the bottom of the 2000 m $\times$ 2000 m modeling domain. They all initially have a CFW (θ =-1.6°C, S=34.51 psu) at 0–100 m depths, a linear variation of θ and S across 100–120 m depths, and a WSW layer (θ =0.7°C) beneath. The S of the initial WSW in each case can be determined by $\Delta\rho$ and $N^2_{\rm wsw}$. The initial cooling applied to the simulation in Figure 2.2 is also applied to all simulations here. All simulations have a final state where all CFW sinks into WSW (*i.e.* D_f=0). See the convection depths diagnosed from simulations here vs. our predictions in Figure 2.6(c).

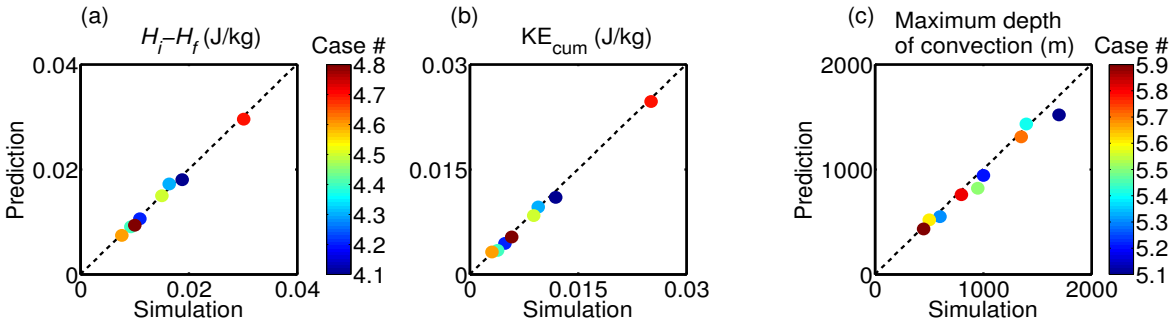

Figure 2.6: (a) Prediction of $H_i - H_f$ by (2.22), (b) prediction of KE$_{\rm cum}$ by (2.1) vs. numerical simulations for cases 4.1–4.8 described in Table 2.4. Here the prediction of KE$_{\rm cum}$ adopts the value of C$_{\rm H^D toH^P}$ diagnosed from simulation since C$_{\rm H^D toH^P}$ has no analytical solution. Panels (a) and (b) share the same colorbar. (c) Prediction of the maximum depth of convection by our strategy in section 2.5.5 vs. numerical simulations for cases 5.1–5.9 described in Table 2.5. As shown in panels (a)-(c), these predictions agree closely with numerical simulations. All simulations here have a final state where all CFW sinks into WSW.

stratifications. The initial cooling applied to the simulation in Figure 2.2 is also applied to all simulations here, which triggers convection along with the cabbeling instability. For all simulations, $H_i - H_f$ and KE$_{\rm cum}$ are well predicted by (2.22) and (2.1) (Figure 2.6(a)–2.6(b)). As in Table 2.4, S$_{\rm tb}$ is larger than S$_{\rm cab}$ for cases 4.7–4.8 (column depth= 2 km), while smaller than S$_{\rm cab}$ for cases 4.1–4.6 (column depth= 0.7 km). This is because S$_{\rm tb}$ and S$_{\rm cab}$ have a quadratic (see (2.21c)) and a near-linear

(see (2.25)) dependence on column depth, respectively. We analyze case 4.4 in detail (Figure 2.5). Figure 2.5(f) suggests a cabbeling instability for the initial interface. Cabbeling contributes to the final $\mathrm{KE_{cum}}$ by $\mathrm{S_{cab}} - \mathrm{C_{H^D toH^P}} = 0.01$ J/kg, which is comparable to $\mathrm{S_{tb}} = 0.0051$ J/kg and $-\mathrm{S_{strat}} = -0.0116$ J/kg. $\mathrm{KE_{cum}}$ here is again insensitive to grid size and viscosity (Table 2.1).

2.5.5 A theory to estimate the maximum depth of convection

Previous studies predict the maximum depth that convective plumes can reach using a Lagrangian approach: this approach follows an individual plume and estimates its acceleration based on entrainment assumptions (*e.g.*, Turner, 1979; Akitomo, 2007). Here we propose to estimate the maximum depth of convection from an energetic perspective by the followings steps.

(i) Begin with the initial θ and S profiles that have CFW overlying WSW with a column depth of D_{max}. We assume the final state of convection comprises a CFW layer on top for $-D_f \leq z \leq 0$, a CFW/WSW mixture at the middle for $-D \leq z \leq -D_f$, and a WSW layer below for $-D_{max} \leq z \leq -D$. Here D always denotes the maximum depth of convection, which also equals the ocean-column depth in previous sections.

(ii) The θ/S profile of the final state is a known function of the variables D_f and D: we assume that fluid in the regions $-D_f \leq z \leq 0$ and $-D_{max} \leq z \leq -D$ remain unmodified from the initial state. For $-D \leq z \leq -D_f$, θ and S are assumed to be homogeneous due to a complete mixing of the initial state within the corresponding depths (see, *e.g.*, Figures 2.2(e), 2.4(e) and 2.5(e))). Given

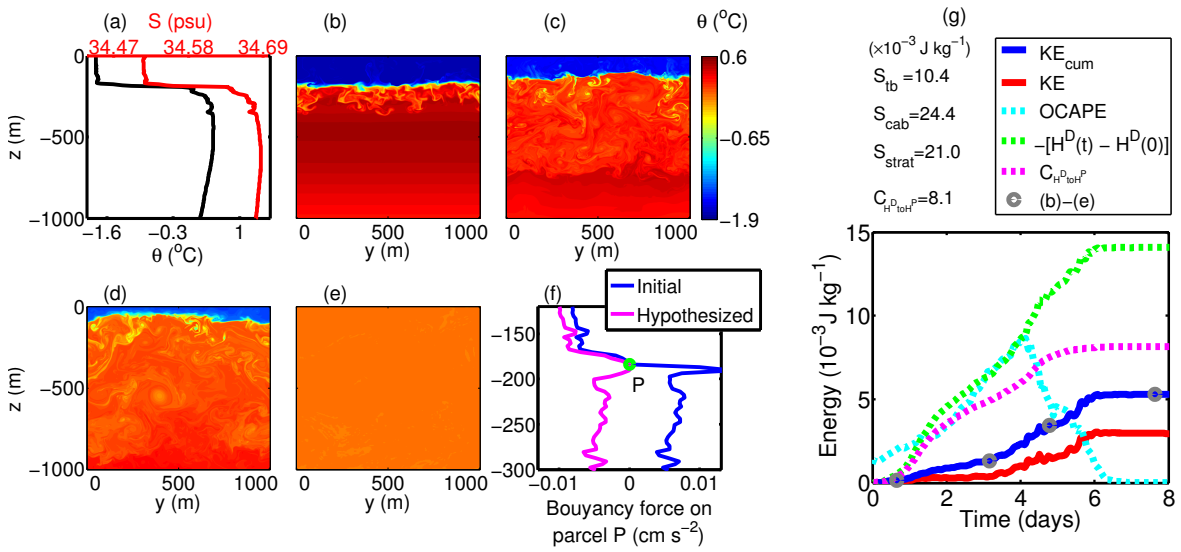

Figure 2.7: As Figure 2.5 but for a stratified simulation with cabbeling based on realistic initial profiles, discussed in section 2.6. The model configuration is the same as that in Figure 2.5, except with a uniform surface salinity flux enforced from t=0 to t=4.2 days, equivalent to an ice formation rate of 1.5 cm/day. (a) The initial profile, from Maud Rise (65.4605°S, 2.4007°E) on August 2, 1994, station 48 of ANZFLUX CTD profile (courtesy of Bruce Huber; McPhee et al., 1996). 1000 m is about the maximum depth of convection in our simulation. Snapshots of the model's θ field are shown (b) at t=0.65 day, (c) at t=3.1 days, (d) at t=4.7 days, and (e) at t=7.5 days. Panel (f) is similar to Figure 2.5(f) but with a additional magenta curve computed from a hypothesized profile. It is the same as initial profile except with a saltier mixed layer (at 0–180 m depths) due to 6.3 cm of ice formation (*i.e.* 1.5 cm/day×4.2 days). It has a linear variation of θ and S across the CFW/WSW interface at 180–200 m depths. This magenta curve suggests that brine rejection may generate a cabbeling instability for parcel P at the interface (*i.e.* become negatively buoyant when it is moved downward). For (g), see Figure 2.1 for the detailed energy relations.

the θ/S profiles above, the H^D difference between the initial and the final states, $(H_i^D - H_f^D)$, is given by (2.A10) in terms of D_f and D (or given by (2.11a) and (2.11d) using the full EOS).

(iii) We assume that the final state is the one that has the minimum PE, which is consistent with simulations (see below) and the principle of minimum total

potential energy (Reddy, 2002). While PE is defined as $H^D + H^P$ according to (2.7) and (2.11a), we use PE $\approx H^D$ because H^P does not contribute to KE (see Figure 2.1). Here we only discuss the cases with $D_f = 0$ in the final state, which have realistic applications such as for Weddell Polynya (McPhee, 2003) (see also Figures 2.5(e) and 2.7(e)). Discussing nonzero D_f would also have important applications but is out of this chapter's scope. Thus we determine the final state by solving for the value of D that maximizes[5] $(H_i^D - H_f^D)$. This solution for D is treated as the maximum depth of convection.

The assumption PE $\approx H^D$ above should be treated with caution: H^D is not converted completely to KE due to $\mathrm{C_{H^D toH^P}}$, *i.e.* $\Delta H^D = \mathrm{KE_{cum}} + \mathrm{C_{H^D toH^P}}$ (Figure 2.1 and (2.13b)). Further, $\mathrm{C_{H^D toH^P}}$ is process-dependent and cannot be determined *a priori* given the initial and the final states (section 2.5.3). The uncertainty by neglecting $\mathrm{C_{H^D toH^P}}$ above in predicting the final state remains the focus of future studies. We test nine simulations with different initial stratifications (Table 2.5). Our predictions of the convection depth by the strategy above agree closely with those diagnosed from the numerical simulations (Figure 2.6(c)), which are diagnosed based on the maximum depth that convective plumes and the subsequent mixing can reach. This strategy may be useful in improving the parameterizations of deep convection in ocean models.

[5]We should maximize $(H_i^D - H_f^D)$ in units of J, as expressed by ((2.A10)$\times D \times \rho_0 \times 1\mathrm{m}^2$) ((2.A10) has a unit of J/kg). In (2.A10), we use $D_f = 0$ and $\lambda = (1 - D_i/D)$ by definition (*i.e.*, λ varies with D), where D_i is the fixed initial depth of CFW. Thus we determine D by solving $\mathrm{d}[(2.A10)\times D]/\mathrm{d}D{=}0$ and $\mathrm{d}^2[(2.A10)\times D]/\mathrm{d}D^2 < 0$.

2.6 Application to observed profiles

We apply our analysis of energy and maximum depth of convection to an example with the initial profile (Figure 2.7(a)) obtained from the Weddell Sea. It has CFW overlying WSW, with a interface at about 180–200 m depths. It has an OCAPE of 1.1×10^{-3} J/kg. Figure 2.7(f) (blue curve) suggests that the initial profile is not susceptible to cabbeling instability. To trigger convection in simulation, we impose a uniform surface salinity flux equivalent to an ice formation rate of 1.5 cm/day since the initial mixed layer is at the freezing point. This idealized configuration ignores the ice-ocean dynamic interaction. The salinity flux is enforced for the first 4.2 days, which induces cabbeling instability at the interface (magenta curve in Figure 2.7(f)). Our simulation shows convective plumes continuously sinking from the interface (Figures 2.7(b)–2.7(d)), due to cabbeling instability. The surface flux introduces additional complications to the energetics (*e.g.*, for H^P) and we focus on some key energy quantities (Figure 2.7(g)). ΔH^D is still partitioned into $\mathrm{KE_{cum}}$ and $\mathrm{C_{H^DtoH^P}}$ ((2.13b) and Figure 2.1). OCAPE is generated and partially released simultaneously for the first 4.2 days due to the surface forcing. Evaluation of $\mathrm{S_{tb}}$ by (2.21b), $\mathrm{S_{cab}}$ by (2.25) and $\mathrm{S_{strat}}$ by (2.20a) give 0.0104, 0.0244 and 0.0210 J/kg, respectively, using the initial profile except with a saltier mixed layer by the 4.2 days' surface salt input[6]. $\mathrm{C_{H^DtoH^P}}$ is 0.0081 J/kg as diagnosed from simulation. These lead to $H_i^D - H_f^D =$ 0.0138 J/kg by (2.22) and $\mathrm{KE_{cum}} =$ 0.0057 J/kg by (2.1); both agree with the simulation (Figure 2.7(g)). The strategy in section 2.5.5 predicts the maximum depth

[6]Parameters are: $\Delta\theta \sim 1.115^{\circ}$C, $H = 1000$ m, $\lambda \sim 0.81$, $\delta\rho \sim 0.0101$kg/m^3 , $N^2_{\mathrm{wsw}} \sim 3.06 \times 10^{-7}\mathrm{S}^{-2}$.

of convection ∼910 m, consistent with simulation (∼1000 m in our test simulation, whose domain depth is 1500 m). This simulation implies that thermobaricity- and cabbeling-powered deep convection can cause strong vertical mixing in the Weddell Sea, which hence impacts the gyre dynamics and the production of Antarctic bottom water there (*e.g.* Su et al., 2014).

2.7 Discussion and Conclusion

2.7.1 Key results

We summarize our key results as follows:

(i) Dynamic enthalpy H^D is insensitive to the nonconservation of potential temperature (see (2.16)), allowing us to predict the change of H^D due to convection (Figure 2.6(a)).

(ii) The KE budget of Type II and Type III convection can be decomposed into four components (Equation (2.1) and Figure 2.1): (1) A source of KE due to thermobaricity/OCAPE; (2) A sink of KE due to the reduction of stratification by vertical mixing, which raises the water column's center of mass and converts KE and H^P to H^D; (3) A source of KE due to cabbeling-induced shrinking of the water column's volume when water masses with different temperatures are mixed, which lowers the water column's center of mass and releases H^D to KE and H^P; (4) A reduced production of KE due to cabbeling-related diabatic energy conversion of dynamic enthalpy to potential enthalpy[7]. Our analysis is

[7]See Figure 2.1 (left) and section 2.3. There are only three energy reservoirs here: H^D, H^P and KE.

based on the initial profiles with CFW overlying WSW as widely observed in winter-time polar oceans. We derived analytical expressions to predict the first three components (Appendix). The fourth component is diagnosed numerically (Table 2.4 and Figure 2.6(b)).

(iii) Thermobaricity (the first KE component above) dominates over cabbeling (the third KE component above) for deeper convection depths, while the latter dominates over the former for shallower convection depths (Table 2.4, cases 4.1–4.6 vs cases 4.7–4.8).

(iv) We develop a theory to predict the maximum depth of convection from the initial profile, which is reproduced by the numerical simulations (Figure 2.6(c)).

2.7.2 Model limitations

Our simulations were designed to build up a conceptual understanding for the energy partitioning during convection. As a result, numerous physical processes that could affect convection have not been included. For example, abrupt vertical mixing during convection might couple with baroclinic instability (Akitomo, 2005, 2006). Earth's rotation might impact the OCAPE/cabbeling dynamics directly via the Coriolis force and indirectly via the background geostrophic circulation/eddies. Double diffusive convection also occurs in two-layer stratifications (Radko et al., 2014) and may couple with thermobaric/cabbeling dynamics (*e.g.*, Carmack et al., 2012). Other factors such as surface wind stress, topography and horizontal buoyancy gradient may also impact convection.

Our choice to use 2D simulations reduces the computational burden and permits a greater exploration of the parameter space. These 2D simulations fail to resolve 3D instabilities that may occur following deep convection and laterally mix the sinking water (Jones and Marshall, 1997). However, the 2D and 3D associated simulations in Akitomo (2006) result in small differences. Our simulations use a constant viscosity, which may induce unrealistic effects.

Type II and Type III convection may or may not be distinguished clearly (see also section 2.2). Their main difference seems to be the initial trigger for the convection: type III is defined as being triggered uniquely by cabbeling instability (Harcourt, 2005), while type II has no limitation for the initial trigger (e.g., internal waves, buoyancy forcing). At least the energetic perspective discussed in this study can not distinguish them. It is possible that a more dynamical difference between these convection types may be identified from a buoyancy perspective (see Harcourt, 2005).

2.7.3 Implications

Our simulation includes viscous heating in the thermodynamic equation, which converts KE to PE. This is key for energy conservation (Landau and Lifshitz, 1959) as well as for characterizing the dynamics (Figure 2.1). However, inclusion of viscous heating is not necessary for an accurate prediction of the convective dynamics. All viscous heating is converted to H^P (Figure 2.1), but only H^D contributes to the KE (Young, 2010). Further, viscous heating causes negligible changes to the temperature field as well as to the buoyancy force, due to the large specific heat capacity of water. In this study we also account for the changes in thermodynamic potentials

(*e.g.* chemical potential; see (2.12a)-(2.12c)). While these terms are not necessary for an accurate prediction of the convective evolution (recall that only (2.2), (2.3), (2.4a), (2.6), (2.10) define the closed model for numerical integration), they remain important for characterizing the dynamics.

The mixing parameterizations in current ocean general circulation models (GCMs) typically apply strong local diapycnal mixing in the vertical wherever the water column is statically unstable (*e.g.*, the KPP parameterization, Large et al., 1994). A parameterization for Type II and Type III convection, however, should include the vertical movement of ocean parcels to large depths without substantial mixing at intermediate depths. This chapter may help improve this parameterization (*e.g.*, parameterize tracer diffusivities from the estimated KE and the convection depth). This may resemble the parameterizations of moist convection in atmospheric GCMs using CAPE (Gregory et al., 2000; Zhang, 2009).

2.8 Appendix: Mathematical derivation of Equation (2.1)

Equation (2.1) summarizes our energy decomposition of the KE budget for Type II and Type III convection. In this appendix we derive (2.1) based on the whole convection. Following definitions and denotations in section 2.3.1, from (2.13b) we derive

$$\mathrm{KE_{cum}} = -\mathrm{C_{H^D toH^P}} + (H_i^D - H_f^D), \tag{2.A1}$$

where the subscripts 'i' and 'f' denote the initial and final states, respectively. Now we derive the expression of $(H_i^D - H_f^D)$ based on idealized initial/final states shown schematically in Figure 2.3. The initial state approximates widely observed quasi-two-layer stratification in winter-time polar oceans (Gordon and Huber, 1990): it has a homogeneous CFW (constant $\theta_{\rm CFW}$ and $S_{\rm CFW}$) at depths $-(1-\lambda)D < z < 0$, overlying a constant-stratified WSW ($\theta_{\rm WSW}$ and $S_{\rm WSW}$, constant $N^2 = N^2_{\rm WSW}$) at depths $-D < z < -(1-\lambda)D$ (Figure 2.3a). We only consider WSW stratified in salinity, *i.e.*, with $\theta_{\rm WSW}$=constant and $S_{\rm WSW}$ linear with depth:

$$\frac{{\rm d}S_{\rm WSW}(z)}{{\rm d}z} = -\frac{N^2_{\rm WSW}}{\beta g}, \tag{2.A2}$$

following the definition of N^2 (Gill, 1982). We use simplified Taylor series of buoyancy

$$b = g[(\alpha_0 + \alpha_z z)\delta\theta - \beta\delta S + \gamma_{\theta\theta}\delta\theta^2], \tag{2.A3}$$

where α_0, α_z and β are treated constant following the denotations of Part I ($\alpha_z = -3\times10^{-8}\,{}^{\rm o}{\rm C}^{-1}{\rm m}^{-1}$). $\gamma_{\theta\theta}$ is the constant cabbeling coefficient defined in section 2.5.2. $\delta\theta$ and δS are the anomalies from the mean of the initial CFW and WSW properties

$$\delta\theta(z) = \theta(z) - 0.5(\theta_{\rm CFW} + \theta_{\rm WSW}), \qquad \delta S(z) = S(z) - 0.5(S_{\rm CFW} + \overline{S_{\rm WSW}}), \tag{2.A4}$$

where $\overline{S_{\mathrm{WSW}}}$ is the vertical mean of S_{WSW} in the WSW layer following (2.A2). We define

$$\Delta\theta = 0.5(\theta_{\mathrm{WSW}} - \theta_{\mathrm{CFW}}), \qquad \Delta S = 0.5(S_{\mathrm{WSW}} - \overline{S_{\mathrm{WSW}}}). \tag{2.A5}$$

Then $\delta\rho$, the density difference between the CFW and the mean WSW at the level of the CFW/WSW interface initially, has an expression

$$\delta\rho = \rho_0 \left[-(\alpha_0 - \alpha_z(1-\lambda)D) \times 2\Delta\theta - \beta \times 2\Delta S\right]. \tag{2.A6}$$

Further, from (2.A4)-(2.A5) we get the vertical profiles of $\delta\theta$ and δS for the initial state

$$\begin{cases} \delta\theta_i = -\Delta\theta, \quad \delta S_i = -\Delta S, & \text{for} -(1-\lambda)D < z < 0, \\ \delta\theta_i = \Delta\theta, \quad \delta S_i = \Delta S - \dfrac{N^2_{\mathrm{WSW}}}{\beta g}(z + (1-0.5\lambda)D), & \text{for} -D < z < -(1-\lambda)D, \end{cases} \tag{2.A7}$$

where the upper and the lower describe the initial CFW and WSW, respectively. Similarly, we derive the final state: we assume that the CFW is unmodified for $-D_f < z < 0$ and the fluid column becomes completely mixed for $-D < z < -D_f$ (Figure 2.3c; based on numerical simulations such as Figures 2.2(e), 2.4(e) and 2.5(e)),

i.e.,

$$\begin{cases} \delta\theta_f = -\Delta\theta, \quad \delta S_f = -\Delta S, & \text{for} - D_f < z < 0, \\ \delta\theta_f = \dfrac{(2\lambda-1)D + D_f}{D - D_f}\Delta\theta, \quad \delta S_f = \dfrac{(2\lambda-1)D + D_f}{D - D_f}\Delta S, & \text{for} - D < z < -D_f, \end{cases} \tag{2.A8}$$

where for the expression of $\delta\theta_f$, we neglect the nonconservation of θ during mixing because H^D is insensitive to this nonconservation according to (2.16).

Following the definition of H^D ((2.11a) and (2.11d)), and using (2.A3), (2.A6)–(2.A8), we derive

$$\begin{aligned} H_i^D - H_f^D &= \frac{1}{D}\int_{-D}^{0}(\delta\theta_i - \delta\theta_f)(-g\alpha_0 z - 0.5g\alpha_z z^2)\mathrm{d}z + \frac{1}{D}\int_{-D}^{0}(\delta S_i - \delta S_f)(g\beta z)\mathrm{d}z \\ &\quad + \frac{1}{D}\int_{-D}^{0}(\delta\theta_i^2 - \delta\theta_f^2)(-g\gamma_{\theta\theta} z)\mathrm{d}z, \qquad (2.A9) \\ &= \left\{-\frac{1}{3}g\alpha_z\Delta\theta D^2\left[\lambda(\lambda-1)(1-2\lambda) + (2\lambda-3\lambda^2)\frac{D_f}{D} - \lambda\frac{D_f^2}{D^2}\right]\right\} \\ &\quad + \left\{-\frac{1}{12}N_{\mathrm{WSW}}^2\lambda^3 D^2 - \frac{1}{2}\lambda[(1-\lambda)D - D_f]\frac{\delta\rho}{\rho_0}g\right\} \\ &\quad + \left\{2g\gamma_{\theta\theta}\Delta\theta^2(D + D_f)(\lambda - \frac{\lambda^2 D}{D - D_f})\right\} \qquad (2.A10) \\ &= \mathrm{S_{tb}} - \mathrm{S_{strat}} + \mathrm{S_{cab}}. \qquad (2.A11) \end{aligned}$$

In (2.A10), the three brace terms are proportional to thermobaricity (α_z), stratification factors (N_{WSW}^2, $\delta\rho$), and cabbeling coefficient ($\gamma_{\theta\theta}$), respectively. We denote them in (2.A11) as $\mathrm{S_{tb}}$, $-\mathrm{S_{strat}}$ and $\mathrm{S_{cab}}$, respectively, representing the sinks/sources of the state change of H^D related to thermobaricity, stratification and cabbeling. These

expressions are consistent with (2.20a), (2.21b) and (2.25) that are based on more physically intuitive derivation. By combining (2.A11) and (2.A1), we finally derive (2.1). Note that $(H_i^D - H_f^D)$ expressed by (2.A10) is in units of J/kg.

Chapter 3

On the abruptness of Bolling-Allerod warming[†]

3.1 Abstract

Previous observations (*e.g.* Thiagarajan et al. 2014) and simulations (*e.g.* He et al. 2013) suggest that a ∼3-5°C warming occurred at intermediate depths in the North Atlantic over several millennia during Heinrich Stadial 1 (HS1), which induces warm salty water (WSW) lying beneath surface cold fresh water. This arrangement eventually generates Ocean Convective Available Potential Energy (OCAPE), the maximum potential energy releasable by adiabatic vertical parcel rearrangements in an ocean column (Su et al., 2016a, 2016b). We find that basin-scale OCAPE starts to appear in the North Atlantic (∼67.5°-73.5° N) and builds up over decades at the end of HS1 with a magnitude of ∼0.05 J kg^{-1}. OCAPE provides a key kinetic energy source for thermobaric-cabbeling convection (TCC). Using a high-resolution TCC-resolved regional model, we find that this decadal-scale accumulation of OCAPE ultimately overshoots its intrinsic threshold and is released abruptly (∼a month) into kinetic

[†]Appeared as: Su, Z., A.P. Ingersoll and H. Feng, 2016. On the abruptness of Bolling-Allerod warming. Journal of Climate, doi:10.1175/JCLI-D-15-0675.1

energy of TCC, with further intensification from cabbeling. TCC has convective plumes with ∼0.5-1 km horizontal scales and large vertical displacements (∼1 km), which make TCC difficult to be resolved/parameterized by current general circulation models. Our simulation indicates that these local TCC events are spread quickly throughout the OCAPE-contained basin by internal wave perturbations. Their convective plumes have large vertical velocities (∼8-15 cm s^{-1}) and bring the WSW to the surface, causing a ∼2 ^{o}C sea surface warming for the whole basin (∼700 km) within a month. This exposes a huge heat reservoir to the atmosphere, which helps to explain the abrupt Bolling-Allerod warming.

3.2 Introduction

In the last deglaciation, the North Atlantic region experienced notable surface cooling during Heinrich Stadial 1 (HS1, ∼17 ka) (ka: 1000 years ago) (Clark et al. 2002; Hemming 2004). Potential surface meltwater discharge to the North Atlantic, as assumed in numerous studies (Broecker 1994; Ganopolski and Rahmstorf 2001; Buizert et al. 2014; Carlson and Clark 2012), contributes to this cooling. The cooling is followed by an abrupt (years to decades) surface warming at the end of HS1, i.e., at the onset of the Bolling-Allerod (BA, ∼14.5 ka) (McManus et al. 2004; Alley 2007). This abrupt warming is one of the Dansgaard-Oeschger (D/O) warm events (i.e., the warming phase of D/O events). As reviewed by Rahmstorf (2002), there are many mechanisms proposed to explain the D/O events. (e.g., Liu et al. 2009; Weaver et al. 2003; Knorr and Lohmann 2007; Ganopolski and Rahmsdorf 2001). With exceptions (e.g., Clement et al. 1999), most mechanisms are closely related to the Atlantic

meridional overturning circulation (AMOC) such as the idea of thermohaline circulation bistability (Broecker et al. 1985) and salt oscillator (Broecker et al. 1990). Ganopolski and Rahmsdorf (2001), (2002) propose a mechanism associated with the stability of AMOC and stochastic resonance, which explains many key observed features of D/O events, including the three-phase time evolution, spatial pattern and hemispheric see-saw (see also Rahmstorf and Alley 2002). In this chapter, we focus on the mechanism for explaining the abruptness of the D/O surface warm events (e.g., the abrupt BA warming during the transition of HS1 to BA). This has not received as much attention as the cooling in the North Atlantic induced by, e.g., the shutdown of the AMOC.

Many previous studies for the D/O warm events involve an established convective-threshold mechanism (e.g., Ganopolski and Rahmsdorf 2001; Winton 1995; Rasmussen and Thomsen 2004; Winton and Sarachik 1993): the cold fresh water (CFW) typically overlies the warm salty water (WSW) in the North Atlantic after Heinrich events, where the WSW gradually warms up (as detailed below). This warming of intermediate-depth WSW and the potential reduction of surface freshwater supply, reduce the static stability of the ocean until the threshold of static instability is exceeded in the North Atlantic. Then the convection renews and brings the WSW upward. This rapidly releases a large amount of stored potential energy of heat to the surface and invigorates the AMOC. Therefore this convective-threshold mechanism may explain the abrupt D/O warm events. Rahmsdorf (2001) have investigated in detail the threshold onset of convection (for CFW overlying WSW) and its bistable

nature, which could strongly modulate AMOC and the climate of the North Atlantic (see also Rahmsdorf 1994, 1995a, 1995b).

In this study (Su et al., 2016a) we propose a modified convective-threshold mechanism, as an amendment to the above established convective-threshold mechanism. The main difference is as follows. In the modified mechanism, convection occurs due to thermobaric instability, which occurs before static instability (the established mechanism) is reached. In contrast to the static instability, thermobaric instability is a different type of fluid instability (Ingersoll 2005). Further, it not only releases the stored heat of WSW, but also releases the Ocean Convective Available Potential Energy (OCAPE) into kinetic energy of the convection. Finally, it typically induces a much more abrupt ocean overturning (vertical mixing) and typically reaches deeper depths than static instability in convection events (Denbo and Skyllingstad 1996; Akitomo 1999). However, whether it substantially changes the evolution of the BA-warming is less clear. It is possible that both the modified and the established convective-threshold mechanisms would eventually lead to a similar final overturning state of the North Atlantic after years/decades.

Both the modified and the established convective-threshold mechanisms are associated with the observed millennial-scale ($\sim$3-5 ^{o}C) warming at intermediate depths ($\sim$1-2 km depths) of the North Atlantic during HS1 (Thiagarajan et al. 2014; Marcott et al. 2011; Alvarez-Solas et al. 2010). The induced intermediate-depth ocean is $\sim$4 ^{o}C warmer than the shallower water above (Thiagarajan et al. 2014. See similar observations in Rasmussen et al. 2003, 2004; Dokken and Jansen 1999). Many

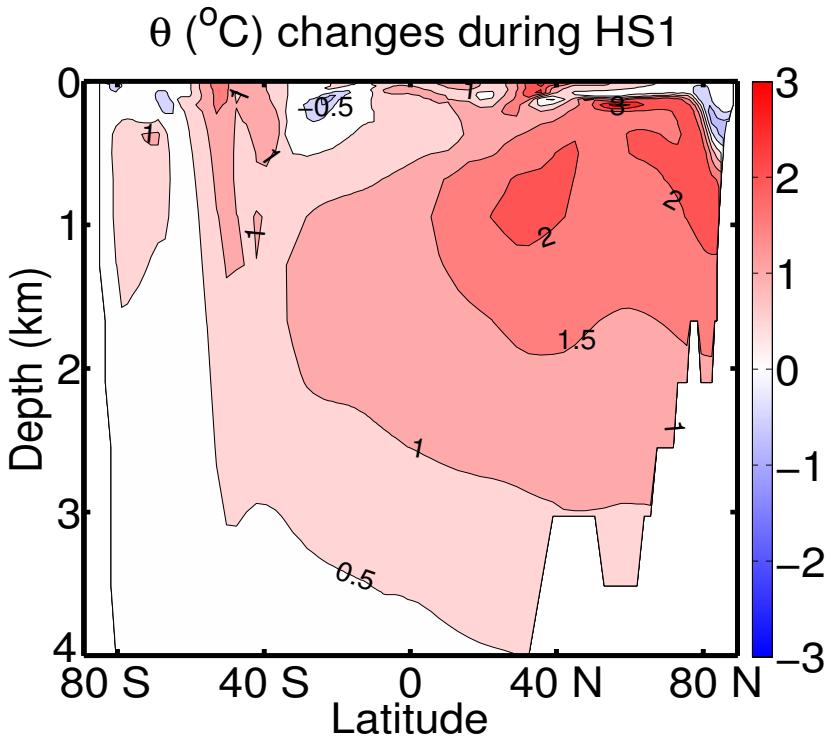

Figure 3.1: The changes of Atlantic zonal mean potential temperature θ(°C) during HS1 (∼2300 years duration), from the CCSM3 simulation of the last deglaciation (Liu et al. 2009; He et al. 2013). The figure shows that the North Atlantic became warmer (∼ 1.5-3 °C) at intermediate depths (beneath ∼200 m depth), but remained unchanged or became colder at the ocean surface at 40°-80° N. This millennial-scale process generates warm salty water (WSW) lying beneath cold fresh water (CFW), which could accumulate OCAPE (Figure 3.3).

numerical simulations also indicate similar millennial-scale warming (∼2-9 °C) at intermediate depths of North Atlantic, as a response to the largely reduced AMOC during stadials (Shaffer et al. 2004; Stouffer et al. 2006; Clark et al. 2007; Arzel et al. 2010; Brady and Otto-Bliesner 2011). For example, Figure 3.1 illustrates the ∼3 °C warming at ∼0.3-2 km depths in the North Atlantic during HS1 (∼2300 years duration) from the Community Climate System Model 3.0 (CCSM3) simulation of the last deglaciation (Liu et al. 2009; He et al. 2013). This phenomenon may have at least two explanations: (i) Less convective heat is lost into the atmosphere from

the intermediate-depth North Atlantic due to the suppressed deep convection during stadials (Knutti et al. 2004). (ii) Heat is transported from the Southern Ocean and Tropical Atlantic to the North Atlantic at intermediate depths by the subpolar gyre and the weakened AMOC during stadials (Winton 1995; Mignot et al. 2007; Shaffer et al. 2004). In section 3.3, we demonstrate that millennial-scale warming at intermediate depths of the North Atlantic during HS1 could eventually generate OCAPE to a large magnitude ($\sim$0.05 J kg^{-1}). OCAPE is a vital kinetic energy source for thermobaric-cabbeling convection (TCC; see TCC studies in Akitomo et al. 1995, Akitomo 1999, 2006 and Harcourt 2005). In section 3.4, we present high-resolution numerical simulations for our modified convective-threshold mechanism: We illustrate that this continual accumulation of OCAPE eventually overshoots its intrinsic threshold and causes a sudden release of OCAPE that powers dramatic TCC events. This brings warm salty water to the surface and warms the sea surface of the whole basin ($\sim$700 km scale) by $\sim$2 ^{o}C within one month. In sections 3.5 we discuss implications.

3.3 Basin-scale OCAPE in the North Atlantic at the end of HS1

OCAPE is a newly developed and well-defined concept (Su et al. 2016a, 2016b). It quantifies the maximal potential energy of an ocean column that is available to be released into kinetic energy by the transition from the current state to the minimum-PE state through adiabatic vertical parcel rearrangements:

$$\text{OCAPE} = \text{PE(current state)} - \text{PE(minimum PE state)}. \tag{3.1}$$

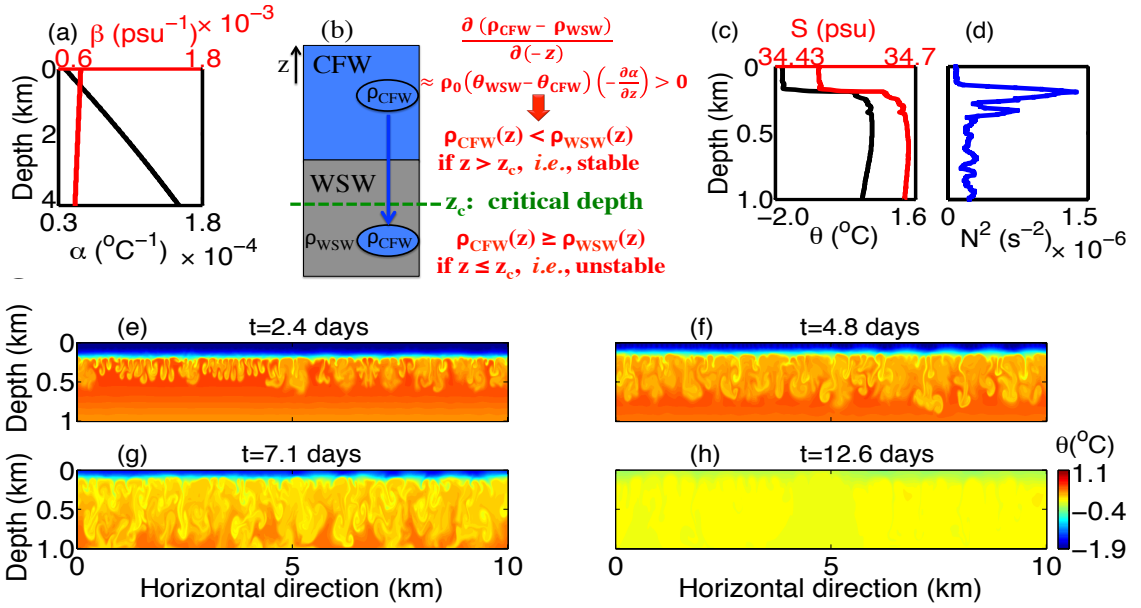

Figure 3.2: (a) The vertical profile of thermal expansion coefficient α(black line) and saline contraction coefficient β (red line). These are computed from constant profile of θ= 1 °C and S= 34.0 psu. OCAPE arises from thermobaricity: the strong dependency of α on depth. (b) Schematic illustration for the triggering of TCC and the release of OCAPE based on an idealized adiabatic argument. The θ and S of the adiabatically displaced CFW parcel does not change with depth. Also, $\partial\beta/\partial z$ is around 0 from panel (a). Therefore, using the first-order Taylor series for density, one derives that $(\rho_{\rm CFW} - \rho_{\rm WSW})$ increases with depth due to thermobaricity $(-\partial\alpha/\partial z > 0)$, i.e., $\partial(\rho_{\rm CFW} - \rho_{\rm WSW})/\partial(-z) > 0$. Thus there is a critical (threshold) depth z_c, above which the displaced CFW parcel remains lighter than the background WSW. If the CFW parcel is perturbed across z_c, it would be denser than the WSW and thus trigger the instability for TCC. The accumulation of OCAPE means the rise of the critical depth z_c, which weakens the threshold and makes it easier to be overcame (see also footnote 2). (c) Observed profiles of θ and S, obtained from the Weddell Sea on August 2, 1994, ANZFLUX CTD station 48 (McPhee et al. 1996). (d) shows their statically stable stratification (i.e., positive buoyancy frequency). This water column contains OCAPE of 1.1×10^{-3} J/kg, which is approximately ready to be released: (e)-(h) show the snapshots of θ in our two-dimensional simulation of TCC initialized by the observed profiles of (c) in a 10 km horizontal domain. The model is nonhydrostatic and eddy-resolving in a rotating frame (essentially the same model of Akitomo et al. 1995 and Akitomo 2006).

The same energy concept, although not as formally formulated as OCAPE, was discussed in section 7 of Ingersoll (2005) and sections 2-3 of Adkins et al. (2005). Although OCAPE can be computed numerically for any idealized equation of state,

all OCAPEs in this chapter are computed based on the full nonlinear equation of state of seawater (Jackett et al. 2006). OCAPE typically appears in an ocean column when cold fresh water lies above warm salty water. This type of ocean column may be susceptible to TCC even if the column has a statically stable stratification. Thus TCC is not the regular surface buoyancy-driven convection. OCAPE offers a main kinetic energy source for TCC and it arises from thermobaricitythe significant increase of the thermal expansion coefficient of seawater with the depth (Figure 3.2a). TCC is difficult to be directly observed due to its short timescales and severe polar observational conditions during wintertime. However, indirect observational evidences and theoretical/numerical analysis suggest that the modern Weddell Sea is susceptible to TCC (i.e., the release of OCAPE to kinetic energy) (detailed in Akitomo et al. 1995; Akitomo 1999, 2006; McPhee 2000, 2003; Harcourt 2005). OCAPE exists in the modern ocean: Figures 3.2c-d display a statically stable stratified profile with CFW overlying WSW that was observed in the Weddell Sea (McPhee et al. 1996). This profile contains a column-averaged OCAPE of 1.1×10^{-3} J kg^{-1} (equivalent to a velocity of 4.7 cm s^{-1} if converted into kinetic energy, following the scaling of velocity $\sim$ (2 $\times$ kinetic energy/mass)$^{0.5}$). Figures 3.2e-h show our simulated TCC initialized by this observed profile and triggered by realistic surface perturbations (homogeneous brine rejection equivalent to 1 cm day^{-1} sea ice formation, applied to the whole domain for the initial 4.2 days). The model is two-dimensional (vertical and horizontal) and nonhydrostatic in a rotating frame (essentially the same model of Akitomo et al. 1995 and Akitomo 2006, using the full nonlinear equation of state from Jackett

et al. 2006). We apply a numerical resolution of 50 meters in the horizontal and 10 meters in the vertical, which allows the resolving of TCC (Akitomo 2006; Harcourt 2005). TCC begins after ∼2 days and drives a thorough mixing within 10 days for the whole 10-km domain. The convective plumes have a horizontal scale of ∼0.5-1 km and vertical velocities of 4-7 cm s^{-1}, which are powered by OCAPE and cabbeling effect. This result is consistent with Akitomo (2006), who simulates that TCC causes a ∼1 km depth of convective overturning for a ∼10-km horizontal-scale water column around Maud Rise of the Weddell Sea.

Next we demonstrate that OCAPE could exist in the North Atlantic at the end of HS1. We use the monthly output from the CCSM3 simulation of the last deglaciation (Liu et al. 2009; He et al. 2013. See Figure 3.1 for its simulated intermediate-depth warming during HS1, which induces CFW overlying WSW and thus may generate OCAPE). As shown in Figures 3.3a-d, we find that a basin-scale OCAPE pattern first appears in the North Atlantic (∼67.5°-73.5° N) at about the end of HS1 (14.542 ka) and grows larger in both the horizontal scale (∼700 km) and the magnitude (∼0.05 J kg^{-1}) for a few decades until the BA warming. In detail, we show in Figure 3.3c a dashed white line (∼6° W and 67.5°-73.5° N; 14.536 ka) that approximately crosses the center of the OCAPE pattern. It has CFW (∼0-0.5 km depths) overlying WSW and has a statically stable stratification (Figure 3.3e). Its averaged OCAPE is about 0.05 J kg^{-1}, meaning a convection velocity of ∼30 cm s^{-1} if all this OCAPE is converted into kinetic energy. We now discuss the credibility of the build-up of OCAPE found in CCSM3 (Figures 3.3a-d). (i) The OCAPE of an ocean column is totally determined

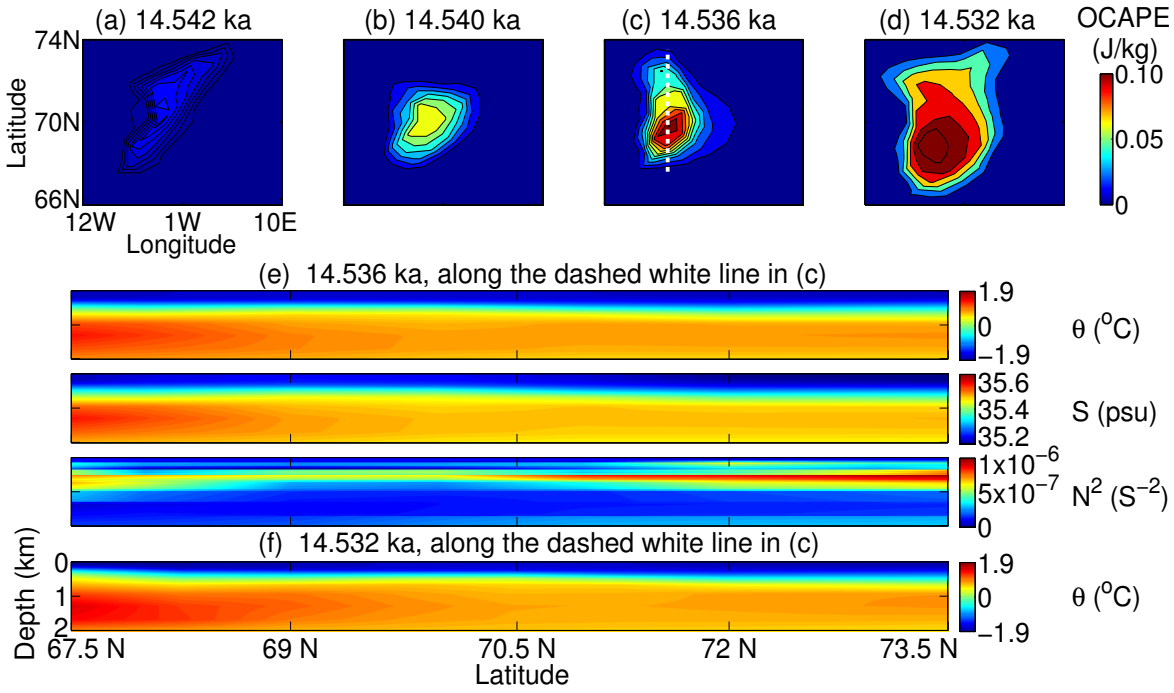

Figure 3.3: (a)-(d) Decadal-scale accumulation of a basin-size (∼700 km) OCAPE pattern in the North Atlantic at about the end of HS1, diagnosed using the monthly output (March data shown here) of the CCSM3 simulation of the last deglaciation (Liu et al. 2009; He et al. 2013). The OCAPE pattern starts to appear ∼14.542 ka (ka: 1000 years ago), as in (a), and grows in size and magnitude in the following decade, as in (b)-(d). As an example, (e) shows the vertical section of θ, S and N^2 for the dashed white line displayed in (c) (∼6° W and 67.5°-73.5° N; 14.536 ka). This section has CFW overlying WSW, as required for OCAPE generation (see Figure 3.2b). It has a statically stable stratification (N^2 >0) despite of its large OCAPE. Due to this statically stable stratification, this section is not followed by obvious convection or vertical mixing in the CCSM3 simulation: e.g., (f) shows that even after 4 years (14.532 ka), the θ field still remains roughly unchanged in the CCSM3 simulation. This lack of activity is in strong contrast to our eddy-resolving simulation of TCC shown in Figure 3.4. Panels (a)-(d) share the same horizontal and vertical axis, and so do Panels (e)-(f).

by its T/S profile (Su et al. 2016a). Accurate T/S data for the deglacial climate are scarce. CCSM3 offers currently one of the most advanced coupled GCM simulations for the T/S estimate: Through realistic changes in boundary conditions and forcing, it captures many major features of the deglacial climate evolution, including some T/S signals as inferred from observations (Liu et al. 2009; Shakun et al 2012; Buizert et al.

2014). Diagnosing OCAPE in other GCMs would be our future work. (ii) Vertical mixing could partly dissipate OCAPE (Su et al. 2016b). CCSM3 parameterizes vertical mixing due to breaking internal waves and other processes (Collins et al., 2006). CCSM3 includes the mechanism for the diabatic dissipation of OCAPE and yet OCAPE is present. (iii) As introduced in section 3.2, observations indicate ∼3-5 ^{o}C warming at intermediate depths of the North Atlantic during HS1 (Thiagarajan et al. 2014; Marcott et al. 2011; Alvarez-Solas et al. 2010). This induces CFW overlying WSW. Further, the North Atlantic should have a very weak stratification before the transition from HS1 to BA, either due to intermediate-depth warming or the surface buoyancy loss (e.g., a decrease of freshwater supply at surface) (Ganopolski and Rahmsdorf 2001; Rasmussen and Thomsen 2004; Winton 1995). From Su et al. (2016a) (Equations 16c and 17c there), for weakly stratified quasi-2-layer oceans, the OCAPE is always positive and would increase following the warming of WSW (see also footnote 2). Therefore, in principle, OCAPE would be built up due to the intermediate-depth (i.e., WSW) warming before the transition of HS1 to BA. OCAPE keeps accumulating to a large magnitude while the water column remains in a statically stable stratification. This OCAPE accumulation continuously weakens the intrinsic threshold (see footnote 2) until the threshold is finally overshot, after which OCAPE is then released. Based on an idealized adiabatic argument, this intrinsic threshold is estimated by the energy barrier in a stable stratification that CFW parcels have to overcome to reach the critical depth within the WSW, where CFW parcels become equally dense as the surrounding WSW and thermobaricity allows them to

accelerate downward and release OCAPE (Figure 3.2b). This estimate of threshold, however, should be treated only conceptually rather than quantitatively because real-ocean diabatic processes like cabbeling instability at the CFW/WSW interface would complicate this estimation (Harcourt 2005). Although climate models like CCSM3 are capable of resolving the accumulation of OCAPE as shown above (Figures 3.3a-d), it is difficult for them to account for the rapid release of OCAPE and thus TCC, for two reasons: (i) Current ocean GCMs have resolutions that are too coarse to resolve TCC, which has convective plumes with a typical horizontal scale of ∼0.5-1 km (e.g. Figures 3.2e-h. See also Akitomo et al. 1995 and Akitomo 2006). (ii) The GCM convective parameterizations typically apply strong local diapycnal mixing in the vertical wherever the column is statically unstable (e.g., the KPP parameterization, Large et al. 1994). This cannot account for the effect of TCC: the acceleration from thermobaricity produces vertical movement of CFW parcels to large depths (∼1 km, e.g., Figures 3.2f-h) without substantial mixing at intermediate depths. Therefore, in the CCSM3 simulation the hydrographic section shown in Figure 3.3e is not followed by obvious convection (or strong vertical mixing) due to its statically stable stratification (e.g., Figure 3.3e vs. Figure 3.3f, showing minimal changes of potential temperature even after 4 years). In contrast, we demonstrate in section 3.4 that the hydrographic section shown in Figure 3.3e is actually susceptible to TCC using a high-resolution simulation (Figure 3.4).

3.4 Simulated abrupt TCC events at the end of HS1

The decadal-scale OCAPE accumulation shown in Figures 3.3a-d may induce TCC at the end of HS1, once the intrinsic threshold is overshot. Here we use a two-dimensional high-resolution simulation to investigate this possibility. The model and its numerical resolution are the same as the one mentioned in section 3.3 (for Figures 3.2e-h). We have done simulations at finer resolutions, and they yield consistent results. A 2D model reduces the computational burden and generates a simulation of TCC consistent with a 3D model (Akitomo 2006; see section 3.5 for more discussion). Our simulation domain is a depth-latitude section located at ∼6° W and 67.5°-73.5° N (white dashed line section shown in Figure 3.3c, ∼700 km horizontally). The bathymetry of this section is about 2-2.2 km deep and for convenience we set the domain bottom at a fixed 2-km depth. Numerous simulations are tested using various initializations from decadal-scale monthly outputs of CCSM3 that contain OCAPE (e.g., the ones shown in Figures 3.3a-d). There are many examples in these hydrographic snapshots where TCC could occur, among which the earliest one is most relevant to real-ocean processes. Here we test various perturbation strengths: 50-200 W m-2 homogeneous surface cooling applied for the whole domain for the initial 1 day[1], which also generates internal waves. These perturbations represent the regular strength of wintertime surface buoyancy forcing in the North Atlantic (Marshall and Schott 1999). We find that all OCAPE patterns earlier than March 14.536 ka

[1]This magnitude of cooling changes the ocean stratification by only a small amount. As a scaling, consider 100 W m^{-2} cooling applies to the top 100 m of water (turbulent mixed layer) for 1 day. Then this water is cooled by (100 W m^{-2} × 1 day × 1 m^2)/(4200 J kg^{-1} °C^{-1} × 10^3 kg m^{-3} × 100 m × 1 m^2) ∼ 0.02 °C, which is much smaller than typical sea surface cooling from a big hurricane system ∼ 1 °C (Cornillon et al. 1987).

(e.g., Figures 3.3a,b) cannot be released at all into kinetic energy in our test simulations. This is because for these snapshots, the prescribed perturbations are not strong enough to cross the threshold of thermobaric instability (section 4c of Su et al. 2016a). However, with the build-up of OCAPE due to intermediate-depth warming, the threshold becomes weaker until it is eventually crossed by the regular strength of perturbations[2]. This is the threshold mechanism of why OCAPE can be accumulated to a large amount and suddenly triggered to be released into kinetic energy of TCC (Ingersoll 2005; Adkins et al. 2005). The earliest snapshot from CCSM3 that is susceptible to thermobaric instability under our prescribed perturbations is from March 14.536 ka, which initially has a statically stable stratification (Figure 3.3e). Therefore, the triggered TCC is not based on the established convective-threshold mechanism, which requires a static instability (i.e., $N^2 < 0$; see also footnote 1). Here TCC could be triggered in our simulation by a surface cooling perturbation that is stronger than ~ 70 W m^{-2} (applied for the whole domain for the initial 1 day), which characterizes the magnitude of threshold for thermobaric instability for this snapshot of ocean. Further, the triggered TCC and the impact are essentially independent of the initial trigger as long as the direct contribution of the perturbation to kinetic energy is small (Su et al. 2016b). In contrast, the snapshot 1 month earlier (i.e., February 14.536 ka from CCSM3) requires a domain-wide 1-day surface cooling larger than ~ 800 W m^{-2} for the triggering of TCC. This contrast of the required perturbations (800 W m^{-2} vs. 70 W m^{-2}) is mainly because that from February to March the North Atlantic expe-

[2]i.e., following section 4c of Su et al. (2016a) and the notations there, the warming of WSW or the surface buoyancy loss induces a smaller $\Delta\rho$, which leads to a larger OCAPE and also a weaker threshold as represented by a higher z_S (see Eq(12) there, noting α_z <0).

riences strong surface buoyancy loss (Marshall and Schott 1999), which weakens the stratification and reduces the threshold for thermobaric instability (see also footnote 2). Once triggered, both snapshots of ocean have been similarly overturned by TCC for the whole domain within a month. Here we focus on the simulation initialized by the snapshot of March 14.536 ka, as detailed below.

The associated simulation of TCC is visualized in Figure 3.4 (for the whole domain, ∼700 km wide) and Figure 3.5 (for a local zooming, ∼40 km wide). After only ∼0.6 days of surface cooling of 100 W m^{-2}, the perturbed CFW plumes sink into the WSW at two separate locations (∼69.8^o N and 70.8^o N) nearly simultaneously (Figure 3.4b and 3.5b; see schematic in Figure 3.2b). These two locations have about the maximal initial OCAPE in the whole domain (Figure 3.3c) and are most susceptible to TCC. These initial convective plumes generate strong internal waves that spread the initial huge local convective perturbations (∼ 2 km vertically) northward and southward, which are much stronger perturbations than normal background internal waves. These trigger other TCC events quickly along the way for the whole domain (Figures 3.4c-e and 3.5c-d). These TCC events have convective plumes with horizontal scales of ∼0.5-1 km and large vertical velocities of ∼8-15 cm s^{-1}. They only occur within the region that initially contains OCAPE, because TCC is powered by the release of OCAPE into kinetic energy with further intensification from the cabbeling effect. TCC causes strong local (∼1 km depth) turbulent stirring, which vertically mixes the local water column within ∼8 days (Figure 3.5f). For the entire basin (∼700 km scale), these TCC events cause a thorough vertical mixing (Figure 3.4f)

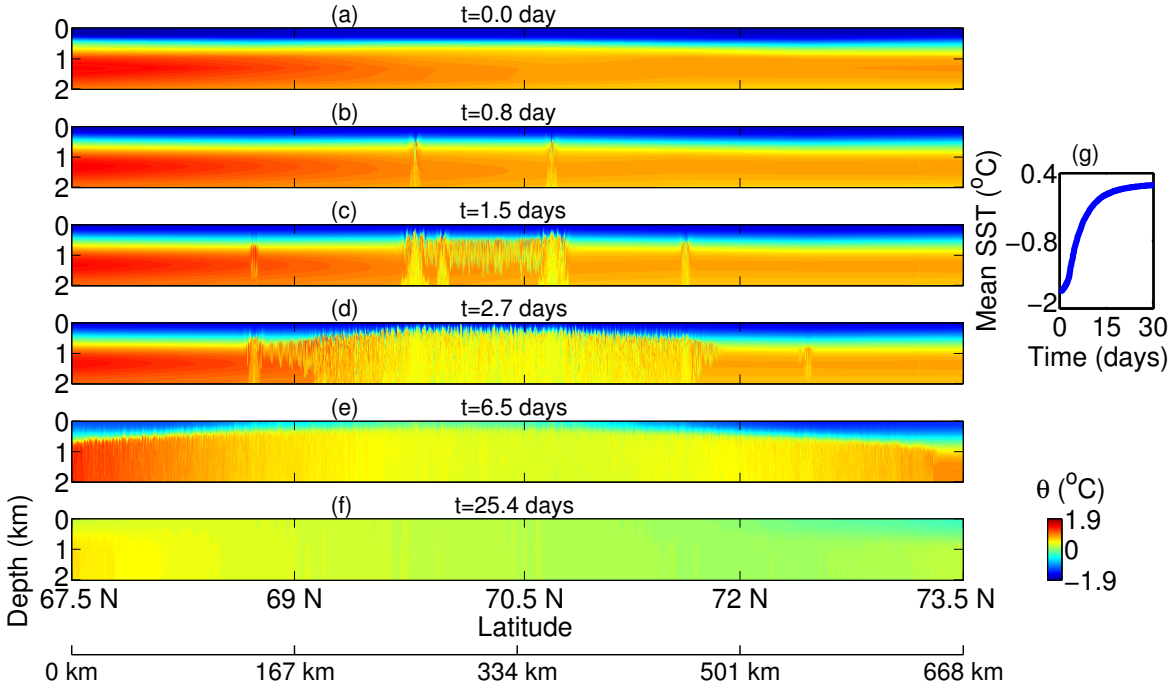

Figure 3.4: (a)-(f) The snapshots of θ field in our eddy-resolving two-dimensional simulation of TCC events in North Atlantic at about the end of HS1 (∼6° W and 67.5°-73.5° N; 14.536 ka). The model is nonhydrostatic and eddy-resolving in a rotating frame (essentially the same model of Akitomo et al. 1995 and Akitomo 2006), using the full equation of state of seawater (Jackett et al. 2006). We apply a vertical resolution of 10 m and a horizontal resolution of 50 m, which allow the resolving of TCC (Akitomo 2006; Harcourt 2005). The simulation is initialized by the θ and S snapshot output from CCSM3 simulation shown in Figure 3.3e. This is the earliest monthly snapshot output that contains OCAPE (e.g. among Figures 3.3a-d and many others) and is also susceptible to TCC in our simulations. Before that, this region is not susceptible to TCC. The domain size is ∼700 km horizontally and 2 km vertically, with a sponge layer on the sides (not shown). TCC is triggered by 1 days perturbation from inhomogeneous surface cooling of ∼100 W m^{-2}. Due to the release of OCAPE, TCC starts at about t=0.6-0.8 day simultaneously at two locations as shown in (b). The convective plumes have a horizontal size of ∼0.5-1 km and spread quickly northward and southward by internal wave perturbations as shown in (c)-(f). Within a month, this basin-scale North Atlantic region (∼700 km) has been thoroughly mixed by TCC events as shown in (f), which increases the sea surface temperature (SST) abruptly by ∼2°C as shown in (g). See Figure 3.5 for the detail of convective plumes and its lateral spreading (by zooming into a ∼40 km horizontal local domain).

and thus increases the domain-averaged sea surface temperature by ∼2 °C within a month (Figure 3.4g). This dramatic surface warming in North Atlantic exposes a

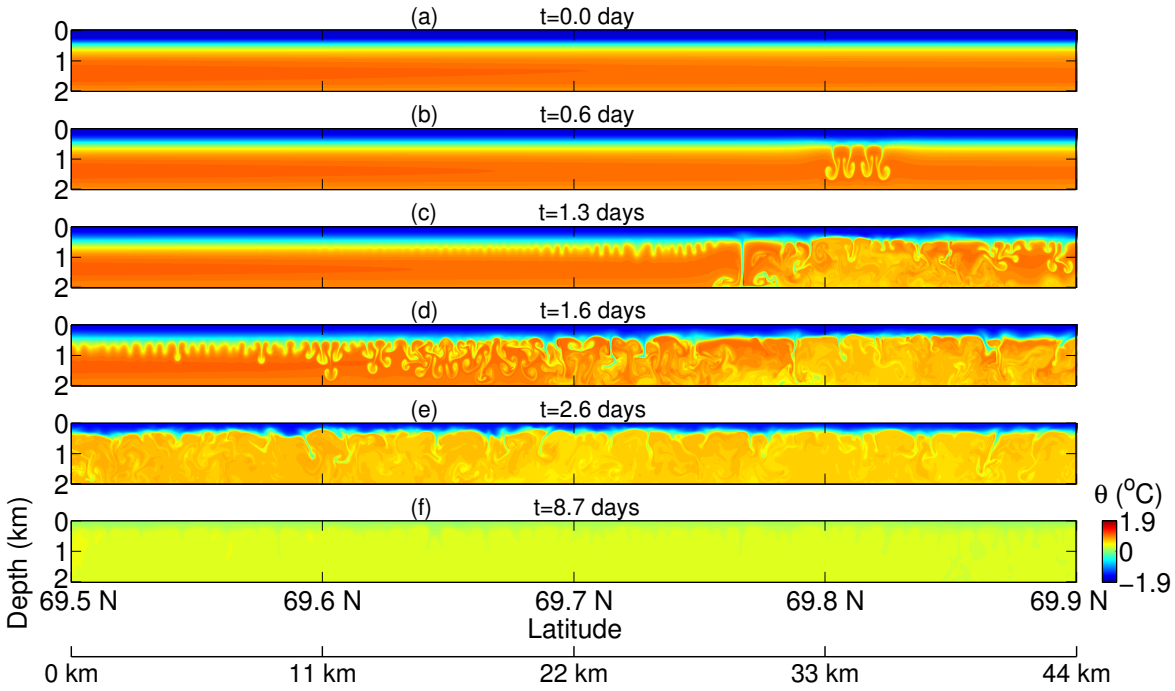

Figure 3.5: (a)-(f) Same as Figures 3.4a-f but zooming into a ∼40 km horizontal local domain where TCC first appears. The convective plumes have a horizontal size of ∼0.5-1 km. They first appear at t=0.6 day as shown in (b) and the consequent perturbations spread laterally and quickly by internal waves. These trigger further TCC events southward and northward as in (c)-(e). Within 10 days, this ∼40 km domain has been thoroughly mixed by TCC events.

huge basin-scale heat reservoir to the atmosphere and thus may directly contribute to the abrupt BA warming. These TCC events may further contribute to the BA warming by strengthening the AMOC, which causes more northward heat transport by decadal timescales (e.g., Banderas et al. 2012; Hogg et al. 2013; Buizert et al. 2014). We also test simulation with the same configuration as above but excluding thermobaricity in the equation of state [the equation of state here follows (17) of Su et al. (2016b): the vertical profile of thermal expansion coefficient α(z) should be replaced by a constant α(z=500m), i.e., the value of α at the CFW/WSW interface at ∼500m depth in this scenario]. In this scenario the convection does not occur. This is because

our mechanism relies on OCAPE to power the convection, while OCAPE is zero if excluding thermobaricity (see Equations (16c) and (17c) of Su et al. 2016a). This is consistent with Denbo and Skyllingstad (1996), who compare thermobaric-included and thermobaric-excluded simulations. In contrast to non-thermobaric convection, thermobaric instability supports deep penetrative convection that alters water properties to greater depths ($\sim$ 2 km), occurs by a more abrupt timescale ($\sim$ days), and spreads horizontally in the OCAPE region.

3.5 Implications and further work

Our proposed convective threshold is provided by a quasi-two-layer structure (CFW overlying WSW; Figure 3.4a) and thermobaricity, which permits decadal-scale accumulation of OCAPE to a large amplitude. This accumulation process weakens and finally overshoots the threshold, which releases OCAPE abruptly into kinetic energy to minimize the systems potential energy (Reddy 2002). An advantage of our modified convective-threshold mechanism for the BA warming is that the timescale of basin-size sea surface warming by TCC events is only about one month, which is much shorter than the years to hundreds of years timescales of regular buoyancy-driven convection events from the established convective-threshold mechanism (Ganopolski and Rahmstorf 2001; see also Buizert et al. 2014 and Clark et al. 2002). This is consistent with previous studies that TCC typically occurs in a much shorter timescale than regular convection (Akitomo 1999; Denbo and Skyllingstad 1996). Thus the timescale of our result is helpful to explain the one to three years abrupt transition observed from the Greenland during the BA warming (Steffensen et al. 2008). However, the differ-

ence between the modified and the established convective-threshold mechanisms may not be easily reflected from the paleo observations due to their relatively low temporal/spatial resolutions (e.g. Thiagarajan et al. 2014). Further, our TCC mechanism is likely to mix the ocean to deeper depths in a single convection event (Denbo and Skyllingstad 1996), but it is possible that after years/decades the final overturning state at the end of the BA warming is the same. Finally, in the real world whether the modified mechanism or the established mechanism dominates the BA warming mainly relies on the strength of the intermediate-depth warming, which determines the CFW/WSW temperature difference and thus the magnitude of OCAPE. This deserves further investigations as a future study. As far as we know, our study provides a first simulation to explore the potential importance of thermobaric instability for the abrupt paleoclimate changes. Our current simulation is highly idealized and should be treated with caveats: (i) Our model does not (and is difficult to) include the sea ice cover. Martinson (1990) and McPhee (2003) demonstrate the principal role of sea-ice in maintaining the ocean columns stability. During convection the warm water brought to the surface would melt the sea-ice and thus restratify the ocean column. This may offer a strong negative feedback on TCC. McPhee (2000), (2003) illustrate that thermobaric instability may still overcome this sea-ice-induced barrier in the modern Weddell Sea. Harcourt (2005) simulates that TCC may fully melt the sea-ice cover (see his Figure 19c). These studies provide important insights to explain the Weddell Polynya of the 1970s, which should be compared to the sea-ice melting during the BllingAllerd warming. (ii) Sea-ice and surface heat fluxes cool the warm water

brought to the surface during convection, which provides a destabilizing mechanism. As a test simulation, we restore the SST to the initial SST with a short relaxation timescale of 10 days to 1 month. This effect strengthens the TCC by only a small amount, since TCC has a short dynamic timescale ($\sim$ days, Figures 3.4b-d). In general, the mixed-boundary-condition (e.g., restoring SST and the differential surface salinity flux) is important to modulate the stability of the thermohaline circulations especially over a timescale of decades or longer (Yin 1995; Cai 1995; Mikolajewicz and Maier-Reimer 1994).

More questions need to be investigated in subsequent studies. (i) Millennial-scale geothermal heating during HS1, which is not included in this study and in most climate models, may likely cause significant warming at ocean depths (Adkins et al. 2005). Thus it may contribute to a larger OCAPE pattern compared to this study. (ii) Appropriate GCM convection parameterizations for TCC need to be developed such that TCC effects can be included in climate models. (iii) TCC is unlikely to be the only mechanism responsible for the whole BA warming. It is necessary to investigate the potential coupling effects between TCC and other important AMOC-related feedback mechanisms including ice-sheets (e.g., Zhu et al. 2014), sea ice (e.g., the sea-ice switch mechanism. see Gildor et al. 2014; Gildor and Tziperman 2003; Ashkenazy et al. 2013), atmospheric circulation (e.g., Banderas et al. 2012), greenhouse effect (e.g., Zhang et al. 2014), and salt feedback (e.g., Knorr and Lohmann 2007). (iv) Our two-dimensional simulation does not resolve baroclinic instability, which may trigger TCC (Killworth 1979). It may also occur shortly after TCC at

density fronts formed between the TCC-induced overturned regions and unoverturned regions (Akitomo 2006; from a 3D simulation). By comparing a 3D simulation to a 2D simulation, Akitomo (2006) finds that baroclinic instability produces additional upward heat transport (other than that from TCC) and does not qualitatively change the impacts of TCC. Thus, including baroclinic instability and using a 3D simulation should not qualitatively influence our conclusions.

Chapter 4

On the Minimum Potential Energy State and the eddy-size-constrained APE Density[†]

4.1 Abstract

Hieronymus and Nycander (2015) recently develop an algorithm to exactly solve the Lorenz reference (absolute minimum potential energy) state, which is a difficult problem due to the nonlinear nature of the equation of state of seawater. However, as they point out, their algorithm comes at a high computational cost. As the first part of this study, we develop an algorithm that is $\sim 10^3 - 10^5$ times faster, making it useful for energy diagnosis in ocean models. As the second part of this study, we show that the global patterns of Lorenz available potential energy (APE) density are distinct from those of eddy kinetic energy (EKE). This is because Lorenz APE density is based on entire-domain-wide parcel rearrangement, while mesoscale eddies, if related to baroclinic instability, are typically generated through local par-

[†]Appeared as: Su, Z. and A.P. Ingersoll, 2016. On the Minimum Potential Energy State and the eddy-size-constrained APE Density. Journal of Physical Oceanography, accepted

cel rearrangement approximately around eddy size. Inspired by this contrast, we develop a locally-defined APE framework: the eddy-size-constrained APE density, defined based on the strong constraint that the parcel rearrangement/displacement to achieve the minimum-potential-energy state should not exceed the local eddy size horizontally. This concept typically identifies baroclinically unstable regions. It is shown to be helpful to detect individual eddies/vortices and local EKE patterns, e.g., around the Southern Ocean fronts and subtropical western boundary currents. This is consistent with the physical picture that mesoscale eddies are associated with a strong signature in both the velocity field (i.e., EKE) and the stratification (i.e., local APE). Our new APE concept may be useful in parameterizing mesoscale eddies in ocean models.

4.2 Introduction

Available Potential Energy (APE) mainly arises from baroclinicity and is the primary energy source for generating mesoscale eddies (e.g., Vallis 2006). The Lorenz APE is the most widely used framework of APE (Lorenz 1955; see Tailleux 2013b that distinguishes the general concept of APE and the Lorenz APE). For a given ocean system, the Lorenz APE is commonly defined as the potential energy (PE) of the system minus its PE of the Lorenz reference state (the absolute/global minimum PE state), achievable through unconstrained adiabatic parcel rearrangement. Exactly solving the Lorenz reference state is theoretically difficult due to the nonlinear nature (e.g., thermobaricity) of the equation of state (EOS) of seawater (Huang 2005; see Tailleux 2013a for a review). Huang (2005) and Saenz et al. (2015) provide fast

but essentially approximate methods to solve the Lorenz reference state, the latter of which is based on an extension of the approach proposed by Tseng and Ferziger (2001). Hieronymus and Nycander (2015, hereafter HN15) are the first to exactly solve the Lorenz reference state by using the linear assignment algorithm (LAA, i.e. the Hungarian algorithm). This result is very encouraging due to its absolute accuracy. However, as they point out, LAA comes at a high computational cost that makes it difficult to be applied in ocean GCMs. As the first part of this study (section 4.3, see Su and Ingersoll, 2016), we develop an algorithm that is $\sim 10^3 - 10^5$ times faster than LAA in achieving the same exact Lorenz reference state for the examined World Ocean datasets, making it useful for energy diagnosis in ocean GCMs.

Our algorithm has applications to calculate APE density. Lorenz APE density is commonly defined based on the Lorenz reference state and is a positive-definite function of position that integrates to the systems Lorenz APE (Roullet and Klein 2009; Winters and Barkan 2013; see Tailleux 2013a for a review). Tailleux 2013b extends the concept of APE density to one based on an arbitrary reference state (i.e., not necessarily the Lorenz reference state): it is still positive-definite and defined for the fluid parcels in the considered system. Global Lorenz APE density is largest around Antarctica and the Arctic, where significant amounts of dense water masses have to move thousands of kilometers to tropical ocean bottoms to achieve the Lorenz reference state with flat isopycnals (Figure 3d of Tailleux 2013b). Although very useful for many purposes, this globally-defined concept does not directly represent the local ($\sim$10-300 km) parcel rearrangement that releases local APE into eddy kinetic energy

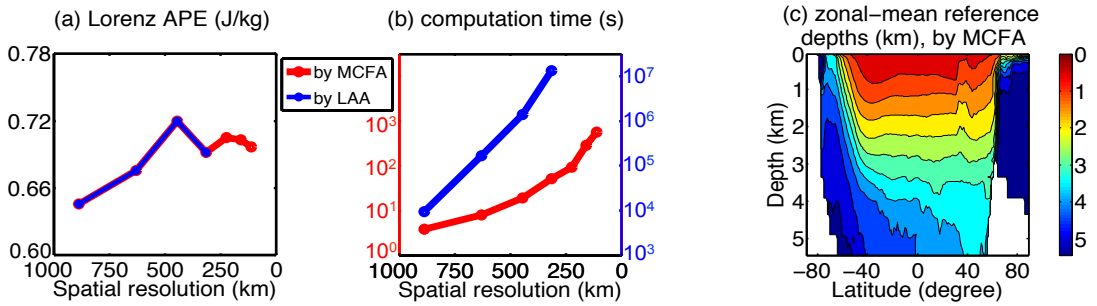

Figure 4.1: (a) Lorenz APE of the World Ocean and (b) the associated computation time vs the horizontal spatial resolution of the applied dataset. All applied datasets in Figure 4.1 have 50 vertical levels and are interpolated from the 1°-grid World Ocean Atlas (WOA) 2009 climatology. The code of LAA and MCFA are both non-parallelized and are performed on a normal unix workstation (a Dell PowerEdge SC1435 rackmount server, two quad core AMD Opteron 2372HE 2.1Ghz CPU, totally 8 cores, 16GB of memory), which is used for all the computation in this chapter (Figures 4.2b-f, 4.5b-f, and 4.6c-d). From (a) the solution converges with increasing resolution. From (b) for the 314-km gridded global dataset, LAA takes $\sim$1.3 $\times 10^7$ s $\approx$155 days while MCFA only takes $\sim$52 seconds. (c) The zonal-mean depth (km) where the current-state parcels reside in the Lorenz reference state. The contour interval is 0.5 km. It is solved by MCFA using the 111-km gridded global dataset. Clearly Antarctic Bottom Water (AABW), North Atlantic Deep Water (NADW), and Arctic Bottom Water (ABW) are rearranged to the ocean bottom at the Lorenz reference state, since they are the densest water masses in the world ocean. See section 4.3 for details.

(EKE) through baroclinic instability (e.g., Vallis 2006). This causes a significant mismatch between the global patterns of Lorenz APE density and those of EKE (as shown in section 4.4). In the second part of this study (section 4.4) we aim to develop a locally-defined APE framework, in strong contrast to the Lorenz APE framework, in order to well detect the EKE patterns. Our defined APE framework could compare the APE products derived from different rearrangement lengthscales (from the whole-domain scale to the eddy scale) and decide their quality for the eddy detection.

4.3 Solving the Lorenz Reference State

Inspired by HN15 and under their framework, with caveats mentioned in their section 1, here we efficiently and exactly solve the Lorenz reference (absolute minimum-PE) state for an arbitrary ocean system with a nonlinear EOS. For convenience we grid the 3D system continuously into columns with the same horizontal area; each column is further divided continuously into vertical parcels with the same mass m_0. This can be done accurately in the presence of bottom topography, with caveats as noted below, and does not impact the solution provided that the grid spacing has a sufficiently high resolution (e.g., the solution converges with increasing resolution; Figure 4.1a). Note that the widely used WOA 2009 dataset (Antonv et al. 2010) itself, as applied in this section, only has 50 levels and can not accurately represent the real-ocean bottom topography. Thus there may always be some unaccounted masses on the ocean bottom, no matter how small m_0 is. Further, m_0, if smaller, can only approach the resolution limit of the applied original dataset, while unable to completely reach that limit in our scenario here. This is a common problem for the finite-difference scheme. For parcel i with salinity S_i and potential temperature θ_i, we label its current-state pressure as $P_i(i{=}1, 2, ..., n)$, where n is the total parcel number of our gridded system. Therefore, the 3D system have n parcels located uniquely in the n pressure positions (note that lots of pressure positions have the same value of pressure, e.g., those pressure positions at the top layer). Assuming hydrostatic balance, any adiabatic parcel rearrangement, which can be decomposed into a series of two-parcel exchanges, does not change the pressure positions of the

system. It is to redistribute the n parcels among the n pressure positions P_i(i=1, 2, ..., n), as a transition from the current state to a rearrangement state. Our goal is to find the rearrangement state that has the absolute minimum-PE (i.e., the Lorenz reference state). Here the assumption of hydrostatic balance is typically accurate for the global-ocean system or for a mesoscale-dynamics system that we focus on: the pressure error percentage (i.e., the error here equals real pressure minus hydrostatic pressure) should be $\leq Ro \times \alpha^2 \ll 1\%$, where Ro is the Rossby number and α is the aspect ratio (typically $Ro \ll 1$ and $\alpha \leq 0.01$ for a system $\geq$ mesoscale) (section 2.8.5 of Vallis 2006). We define $\boldsymbol{h} = [h_{i,j}]$ $(i, j = 1, 2, ..., n)$ where $h_{i,j} = h(\theta_i, S_i, P_j)$ is the specific enthalpy (in units of J kg^{-1}) of parcel i at pressure P_j. Note that the θ_i and S_i of parcel i are always conserved under adiabatic parcel rearrangements. For a rearrangement state where parcel k $(k = 1, 2, ..., n)$ is at P_l, we define a matrix $\boldsymbol{x} = [x_{i,j}]$ $(i, j = 1, 2, ..., n)$ that maps the current state to the rearrangement state, with $x_{k,l} = 1$ and $x_{k,e} = 0$ $(e \neq l, 1 \leq e \leq n)$ (i.e, $x_{i,j}$ is either 0 or 1). Therefore, each rearrangement state has a unique $\boldsymbol{x}$ (the total number of rearrangement states is the factorial of n). The systems enthalpy (in units of J) at this rearrangement state is $m_0 \sum_{i=1}^{n} \sum_{j=1}^{n} h_{i,j} x_{i,j}$, which represents the system's PE (Reid et al. 1981). Thus solving for the Lorenz reference state, which has the absolute minimum enthalpy/PE,

requires solving the following problem:

$$\begin{aligned} &\text{Given a } n \times n \text{ matrix } \boldsymbol{h}, \text{ find a } n \times n \text{ matrix } \boldsymbol{x} \\ &\text{to minimize } \sum_{i=1}^{n}\sum_{j=1}^{n} h_{i,j}x_{i,j}\,, \text{ where } x_{i,j} = 0 \text{ or } 1, \\ &\text{subject to } \sum_{i=1}^{n} x_{i,j} = 1 \text{ for any } j, \text{ and} \sum_{j=1}^{n} x_{i,j} = 1 \text{ for any } i. \end{aligned} \tag{4.1}$$

HN15 have derived (4.1) and demonstrated that the above problem is the classic linear assignment problem (LA) in applied mathematics (Kuhn 1955), which can be exactly solved by LAA. However, as they point out, LAA is too slow to be useful for energy diagnosis in a GCM. We confirm this by using one of the fastest codes of LAA (Jonker and Volgenant 1987): LAA takes ∼2 days and ∼155 days, respectively, to solve the Lorenz reference state for a 628-km- and 314-km-gridded global ocean (blue curves in Figure 4.1a, b). This is performed on a normal unix workstation (detailed in the caption of Figure 4.1b). All global datasets in section 4.3 here have 50 vertical levels and are interpolated from WOA 2009 climatology of 1° grid (Antonv et al. 2010).

Here we extremely reduce the complexity of the problem (4.1) by simplifying the spatial dependence of $[h_{i,j}]$. This simplification is according to the fact that the $n \times n$ matrix $[h_{i,j}](i, j = 1, 2, ..., n)$ includes huge amounts of repetition numbers, as illustrated below. For the deepest column among the gridded system, we denote its total parcel/layer number as s. Here s, the maximum vertical-layer number of the system, is much smaller than n, the total parcel number of the 3D system (i.e.,

$s \ll n$). So totally the system has s vertical pressure layers (i.e., each layer has a unique pressure value), by utilizing the assumption of hydrostatic balance and noting that all gridded parcels have the same mass and the same horizontal area. For vertical pressure layer k ($k = 1, 2, ..., s$) we denote its number of horizontal positions as n_k, subject to $\sum_{k=1}^{s} n_k = n$. These n_k positions in layer k correspond to n_k numbers of P_j (j here are among $1, 2, ..., n$ and are the indexes for these n_k positions), which all have a unique pressure value, denoted as Pr_k. Therefore, the $n \times 1$ array $[P_j](j = 1, 2, ..., n)$ has substantial repetition numbers and includes only s unique values: $Pr_k(k = 1, 2, ..., s)$. Thus $[h_{i,j}] = h(\theta_i, S_i, P_j)(i, j = 1, 2, ..., n)$ also has substantial repetition numbers (due to the repetition of P_j values) and can be reduced to $[\widetilde{h}_{i,k}] = h(\theta_i, S_i, Pr_k)(i = 1, 2, ..., n; k = 1, 2, ..., s)$, i.e., the $n \times n$ matrix $[h_{i,j}]$ can be largely reduced into a $n \times s$ matrix $[\widetilde{h}_{i,k}]$, by noting $s \ll n$. Essentially the Lorenz reference state is not unique: the redistribution of parcels along the corresponding pressure surfaces does not alter the enthalpy/PE of the system. We define $\widetilde{\boldsymbol{h}} = [\widetilde{h}_{i,k}]$ and $\widetilde{\boldsymbol{x}} = [\widetilde{x}_{i,k}]$ ($i = 1, 2, ..., n$; $k = 1, 2, ..., s$), where $\widetilde{x}_{i,k} = 1$ represents parcel i located at pressure Pr_k in the rearrangement state. Thus the problem (4.1) can be modified as follows by taking advantage of the fact that $s \ll n$:

$$
\begin{aligned}
&\text{Given a } n \times s \text{ matrix } \widetilde{\boldsymbol{h}}, \text{ find a } n \times s \text{ matrix } \widetilde{\boldsymbol{x}} \\
&\text{to minimize } \sum_{i=1}^{n} \sum_{k=1}^{s} \widetilde{h}_{i,k} \widetilde{x}_{i,k}\,, \text{ where } \widetilde{x}_{i,k} = 0 \text{ or } 1, \\
&\text{subject to } \sum_{i=1}^{n} \widetilde{x}_{i,k} = n_k \text{ for any } k, \text{ and } \sum_{k=1}^{n} x_{i,k} = 1 \text{ for any } i.
\end{aligned}
\tag{4.2}
$$

We find that this belongs to the classical Minimum-cost flow problem (MCF)[1] in applied mathematics (Goldenberg and Tarjan 1989; Bland and Jensen 1992; Ahuja et al. 1992). From (4.1) and (4.2), clearly LA is just a special case of MCF by prescribing $s = n$ and n_j =1. Solving the Lorenz reference state is extremely simplified by using (4.2) rather than (4.1), since n/s is $\gg 1$ due to a typical large aspect ratio in ocean systems with mesoscale circulation (e.g., $n/s \sim 10^4$ for a 100-km-gridded global ocean; s=50 for our cases). We use one of the fastest codes of the MCF algorithm (MCFA) (Goldberg 1997). We find that MCFA achieves the exact same[2] Lorenz reference state as LAA (Figure 4.1a) but is $10^3 - 10^5$ times faster, depending on the data resolution (Figure 4.1b; see footnote 1 for the related time complexity). MCFA only takes ∼10 minutes to solve for a 111-km gridded global dataset. This is efficient enough for useful energy diagnosis in ocean GCMs. The exact Lorenz reference state solved by MCFA (Figure 4.1c) is largely consistent with that solved by approximate methods (e.g., Figure 3d of Tailleux 2013b), while nonlinear effects of EOS (e.g., thermobaricity) can cause a difference between them (see Appendix B of HN15).

[1]In the framework of MCF, the flow network of (4.2) includes one source, one sink, n edges representing all parcels, and s edges representing Pr_k ($k = 1, 2, ..., s$). The n arcs from the source to parcel edges all have a capacity of [1, 1] with a zero cost. The s arcs from Pr_k edges to the sink all have a zero cost with a capacity of $[n_k, n_k]$. The left arcs (totally $n \times s$) are from the parcel edges (e.g. parcel i) to the Pr_k edges with a flow of $\widetilde{x}_{i,k}$ =0 or 1 (i.e., a capacity of [0, 1]) and a cost of $\widetilde{h}_{i,k}$. Here $[\widetilde{x}_{i,k}]$ is to be solved. Denote A as the total arc number ($A = n + s + n \times s$) and E as the total edge number ($E = 2 + n + s$), the fastest known polynomial MCFA runs in O(A (log E) (A + E log E)) ∼ O(A^2) ∼ O($n^2 s^2$) since $A \gg E$, log $E < 10$, and $A \sim ns$. In contrast, the time complexity of LAA is ∼ O(n^3).

[2]For a given dataset, the discrete optimization problems (4.1) and (4.2) can be solved by LAA and MCFA, respectively, both with 100% accuracy (Kuhn 1955; Lawler 1976; Goldberg 1997). Therefore, their solutions for the Lorenz reference state are exactly the same.

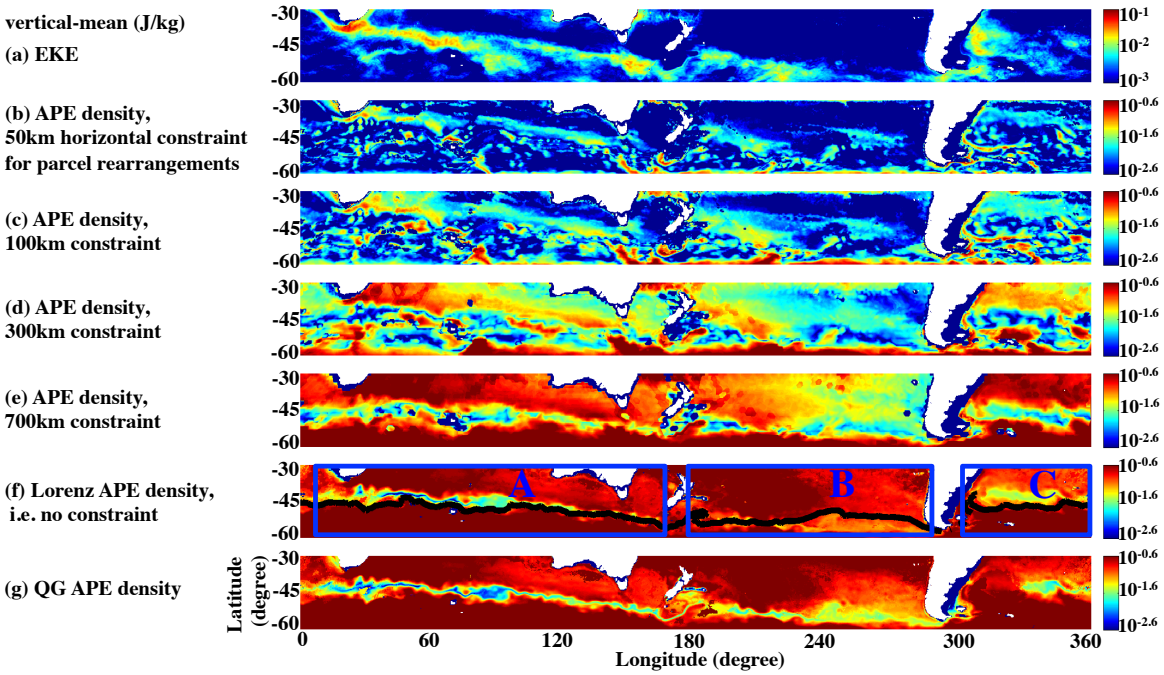

Figure 4.2: (a) Vertical-mean EKE (J/kg) in the Southern Ocean. It is calculated from a 3-year dataset (August 2003 - July 2006) of global ECCO2 state estimate (Menemenlis et al. 2008). This dataset is observation- and model-constrained, with 18-km horizontal grid spacing and 50 vertical levels. The time-mean of this dataset is used for Figures 4.2b-f. (b) Vertical-mean APE density (J/kg), defined based on the constraint that the adiabatic parcel rearrangement from the current state to the reference (minimum-PE) state should not exceed 50 km horizontally. The reference state is solved by MCFA. The 50 km here is approximately the size of mesoscale eddies in the Southern Ocean (Figure 4.6b). The pattern of APE density here is close to the EKE pattern shown in (a). (c)-(f) As (b) but with the horizontal constraint of parcel rearrangement loosened to 100 km, 300 km, 700 km, and no constraint (i.e., the Lorenz APE case), respectively. As shown in (f) the Southern Ocean is approximately divided into region A, B, and C (blue boxes). In (f), the black curve denotes the positions whose current-state surface density is equal to the surface density at the Lorenz reference state (which is a constant, e.g., see the rightmost panel of Figure 4.4a). This black curve agrees well with the area that has the minimum Lorenz APE density in panel (f) (blue or green areas), since the Lorenz APE density reflects the deviation of local current-state stratification from the Lorenz reference state in the considered system (Southern Ocean here; see Figure 4.4a, leftmost vs rightmost panel). In contrast, eddy-size-constrained APE density in (b) reflects local baroclinicity (e.g., Figure 4.3b). (g) QG APE density of the Southern Ocean. See section 4.4 for details.

4.4 Eddy-size-constrained APE density

In this section we aim to develop a new APE framework that may detect local EKE patterns and even individual eddies/vortices. We first investigate the energetic mesoscale eddy field in the Southern Ocean (SO) system (Figure 4.2a; from 18-km-grid ECCO2 state estimate as described in the caption). The EKE patterns are distinct from those of the Lorenz APE density (Figure 4.2a vs 4.2f; vertically averaged). This is because the Lorenz APE density is based on entire-domain-wide parcel rearrangement, which reflects the deviation of the local current-state stratification from the Lorenz reference state in the considered system. For example, Lorenz APE density has a minimum at $\sim$45^{o} S (Figure 4.2f), since at this latitude the current-state stratification is approximately closest to the Lorenz reference state (Figure 4.4a, leftmost vs rightmost panel). In contrast, mesoscale eddies are generated by local parcel rearrangement, which acts to flatten local isopycnals and releases local APE into EKE through baroclinic instability (Pedlosky 1987). The horizontal scale of this local parcel rearrangement may not be uniquely quantified due to the nonlinear development of eddies; but it is close to the local eddy size, the deformation radius, and the width of baroclinic zone with essentially the similar magnitude (Visbeck et al. 1997). We have done a related sensitivity test as discussed later in Figure 4.2 and find that the local eddy size is generally a good proxy for the local parcel rearrangement[3]. To better represent the generation of EKE, it is intuitive to consider a

[3]As shown in our sensitivity study in Figure 4.2, using a smaller size as the constraint would consistently decrease the APE density. The first baroclinic radius of deformation is typically smaller than the eddy size (Figure 12 of Chelton et al. 2011), thus using it rather than the eddy size as the constraint would decrease the APE density.

locally-defined APE framework: eddy-size-constrained APE density that reflects the local baroclinicity. It is still based on adiabatic parcel rearrangement from the current state to the reference (minimum-PE) state, but with the strong constraint that the rearrangement should not exceed the local eddy size horizontally. Solving this new reference state is identical to problem (4.1), except with extra enforced condition of $x_{i,j} = 0$ $(i, j = 1, 2, ..., n)$ provided that parcels i and j in the current state have a horizontal distance larger than the local eddy size around parcel i. This problem can be exactly and efficiently solved by MCFA[4]. Based on the solved reference state we obtain the eddy-size-constrained APE density (APE density can be defined for an arbitrary reference state following Tailleux 2013b).

From observations the SO has an eddy size around 40-80 km (Sallee et al. 2008). As a test, we prescribe an eddy-size constraint of 50 km arbitrarily for the entire SO domain. The resulting eddy-size-constrained APE density is in general consistent with the EKE patterns (Figure 4.2b vs 4.2a; vertically averaged), e.g., enhancement of EKE around strong ACC fronts and subtropical western boundary currents (Figure 4.3a). This is consistent with the physical picture that local APE is a critical energy source[5] for EKE. We note that there is high APE density along the southern/northern boundaries (Figure 4.2b), while there is little EKE there. This is because that we

[4]This problem is essentially LA and a special case of MCF. Here MCFA would exclude all arcs that connect parcel i to pressure P_j if knowing $x_{i,j}= 0$ a priori, which largely reduces computational complexity. In contrast, LAA is extremely slow: $h_{i,j}$ is set as an artificially large value to represent $x_{i,j}= 0$ (i.e. too high cost to be a solution). MCFA takes a few hours to obtain the results of Figures 4.2b-e, 4.5b-e, and 4.6c, due to a 18-km grid spacing of ECCO2 dataset, contrasting to the $\geq$111-km WOA09 grid spacing in section 4.3.

[5]via baroclinic instability, mean APE is the direct source for eddy APE, while eddy APE is the direct source for EKE (Chen et al. 2014). Thus mean APE is the indirect source for EKE. Therefore, our defined eddy-size-constrained APE, no matter for the time-mean part or for the eddy part, is the direct or indirect source of EKE via baroclinic instability.

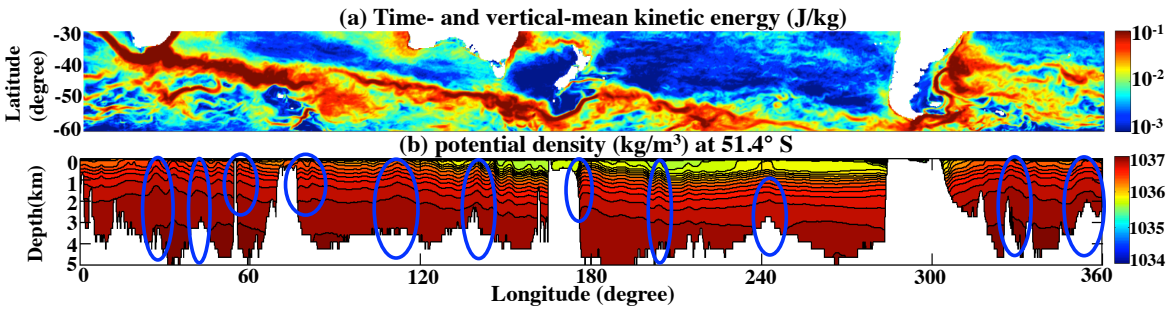

Figure 4.3: (a) Time- and vertical-mean kinetic energy (MKE) (J/kg), from the same dataset as Figure 4.2a. It shows strong southeastward ACC fronts that can advect eddies southward. This partly explains why the EKE patterns in Figure 4.2a are generally located downstream of the corresponding APE density patterns in Figure 4.2b. (b) Potential density (kg m^{-3}, referenced to the 2-km depth) at 51.4° S. The contour interval is 0.1 kg m^{-3}. Topographic highs may generate local APE density through inducing local isopycnal bumps (marked by blue ellipses). These bumps also cause the interfacial form drag of transient/standing eddies (Rintoul et al. 2001). For (b), we choose to use potential density rather than neutral density because the former achieves qualitatively the same result as the latter but with a much better computational efficiency, similarly for Figures 4.4a-b. See section 4.4 for details.

consider the closed SO system with solid southern/northern boundaries; this artificial inconsistency disappears in the World Ocean case as discussed later. Note that the conversion rate of local APE density to EKE can be highly inhomogeneous spatially due to intricate influences from standing meanders, topography, zonal fronts, non-local energy propagation, turbulent energy cascade, etc (Thompson and Salle 2012; Chen et al. 2014; Champan et al. 2015). Interestingly, high EKE between 30°-240° longitude are generally located downstream of the corresponding APE density patterns (Figures 4.2a vs 4.2b), while the maximum EKE is also found downstream of baroclinically unstable regions (indicated by Eady growth rate; Williams et al. 2007). This similarity suggests the usefulness of our defined APE density to diagnose baroclinically unstable regions. This downstream relationship is likely contributed from the southward advection of eddies by the southeastward ACC fronts (Figure

4.3a), while also associating with the fact that high EKE is often found downstream of significant topographic features and standing meanders (Thompson and Naveira Garabato 2014). Local baroclinicity, and hence eddy-size-constrained APE density, may be strongly modulated by topography (Figure 4.3b), baroclinic instability, Ekman pumping (Marshall and Speer 2012), ocean jet formation (Thompson 2010), differential surface heating (Bryan and Cox 1968), etc. A detailed discussion of these is beyond the scope of this study.

As a sensitivity study, we loosen the eddy-size constraint from 50 km to 100, 300, and 700 km, respectively. As expected, this generally leads to flatter isopycnals in the reference state (Figure 4.4a) and a resulting larger APE density (Figures 4.2b-e), which matches better with Lorenz APE density (Figure 4.2f) but matches worse with EKE (Figure 4.2a). Figures 4.4c and 4.4b schematically explain the following two features, respectively: (i) Contrasting Figure 4.2e with 4.2f, the 700-km constrained APE (note 700km domain scale $\sim$3000km) already accounts for most ($\sim$75%) of the Lorenz APE in the SO system; (ii) there is a strong zonal asymmetry between region A, B, and C (Figure 4.2e vs 4.2f). There is a striking feature that the minimum Lorenz APE density (blue or green areas in Figure 4.2f) is located in areas with roughly the maximum eddy-size-constrained APE density (red or yellow areas in Figure 4.2b), which are also the ACC front areas characterized by the maximum EKE in Figure 4.2a. This feature is explained as follows. In Figure 4.2f, the black curve denotes the positions whose current-state surface density is equal to the surface density at the Lorenz reference state (which is a constant, e.g., see the rightmost panel of Figure

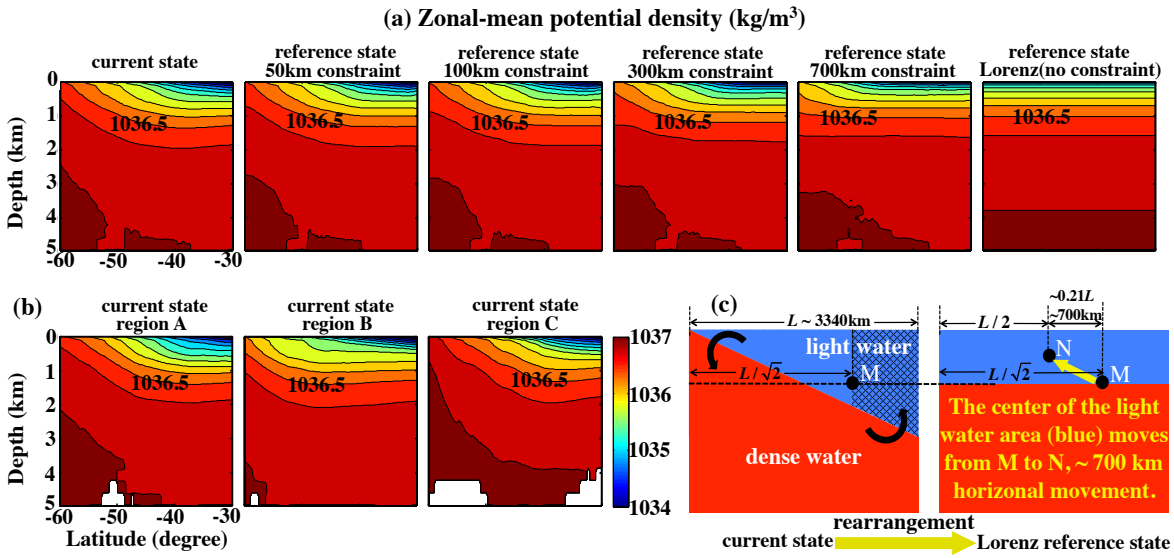

Figure 4.4: (a) Zonal-mean potential density (kg m^{-3}, referenced to the 2-km depth) of the current state and five reference states that define the APE density in Figures 4.2b-f, respectively. The contour interval is 0.25 kg m^{-3}. The loosening of constraint (i.e., from 50 km to Lorenz) decreases the baroclinicity of the reference state and leads to a larger APE density as shown in Figures 4.2b-f. (b) As (a) but showing the zonal-mean current state for region A, B, and C labeled in Figure 4.2f. Region A, B, and C have similar-depth, deeper, and shallower isopycnals, respectively, contrasting to the mean of the whole Southern Ocean (the leftmost panel in (a)) (e.g., comparing the isopycnals $\geq$1036.5 kg m^{-3}; see Orsi et al. 1999). Therefore, current-state dense parcels in region C are still constrained in region C in the reference state of Figure 4.2e, but are rearranged to region B in the Lorenz reference state (Figure 4.2f). Thus, the 700-km constrained APE density has similar, smaller, and larger values than the Lorenz APE density counterpart in regions A, B, and C, respectively (Figure 4.2e vs 4.2f). (c) Schematic that illustrates the ~700-km scale for the horizontal parcel rearrangement from the current state to the Lorenz reference state. The interface may represent the isopycnal of 1036.5 kg m^{-3} shown in (a). Here M and N denote the center of the light water (blue) in the current and the Lorenz reference state, respectively; the light-water area on the right of M (grid shading) is about half of the whole light-water area. In a zonal-mean sense, this schematic explains why the second-rightmost panel in (a) has almost flat isopycnals and why the APE in Figure 4.2e can account for most (~75%) of the Lorenz APE in Figure 4.2f. See section 4.4 for details.

4.4a). This black curve agrees well with the areas that have the minimum Lorenz APE density in Figure 4.2f (blue or green areas). This is because the Lorenz APE density reflects the deviation of local current-state stratification from the Lorenz reference

state (i.e., the black curve areas have roughly a zero deviation and hence no need of parcel rearrangement to reach the Lorenz reference state, and therefore has the minimum Lorenz APE density). Further, the surface density at the Lorenz reference state (i.e., also the density along the black curve) is approximately the surface-mean density of the current state in the QG limit (e.g., Vallis 2006). Thus the black curve, which has about the mean density, is located meridionally right between the maximum density in the south and the minimum density in the north (see the leftmost panel in Figure 4.4a). Therefore the black curve roughly represents the locations with the maximum meridional density gradient, where the ACC fronts are located with about the maximum EKE and the maximum eddy-size-constrained APE density. Figure 4.2g shows the QG-APE of the SO, which acts to approximate the Lorenz APE under the QG approximation (Roullet and Klein 2009; Huang 2005; Pedlosky 1987). Contrasting Figure 4.2g with 4.2f, clearly QG-APE is basically consistent with the Lorenz APE (e.g., in region A), although having evident departures in region B and C. This is because region A, B, and C have similar-depth, ($\leq$ 500m) deeper, and ($\leq$ 500m) shallower isopycnals, respectively, contrasting to the mean of the whole SO (Figure 4.4b vs the leftmost panel of Figure 4.4a; especially around 50^{o}-60^{o} S). Therefore, region B and C require strong isopycnal displacements to reach the Lorenz reference state and hence cause the departure of QG-APE from the Lorenz APE in these regions (see Roullet and Klein 2009 for a valuable study of this). This suggests that QG approximation for APE, although useful, should be treated with caution for the SO.

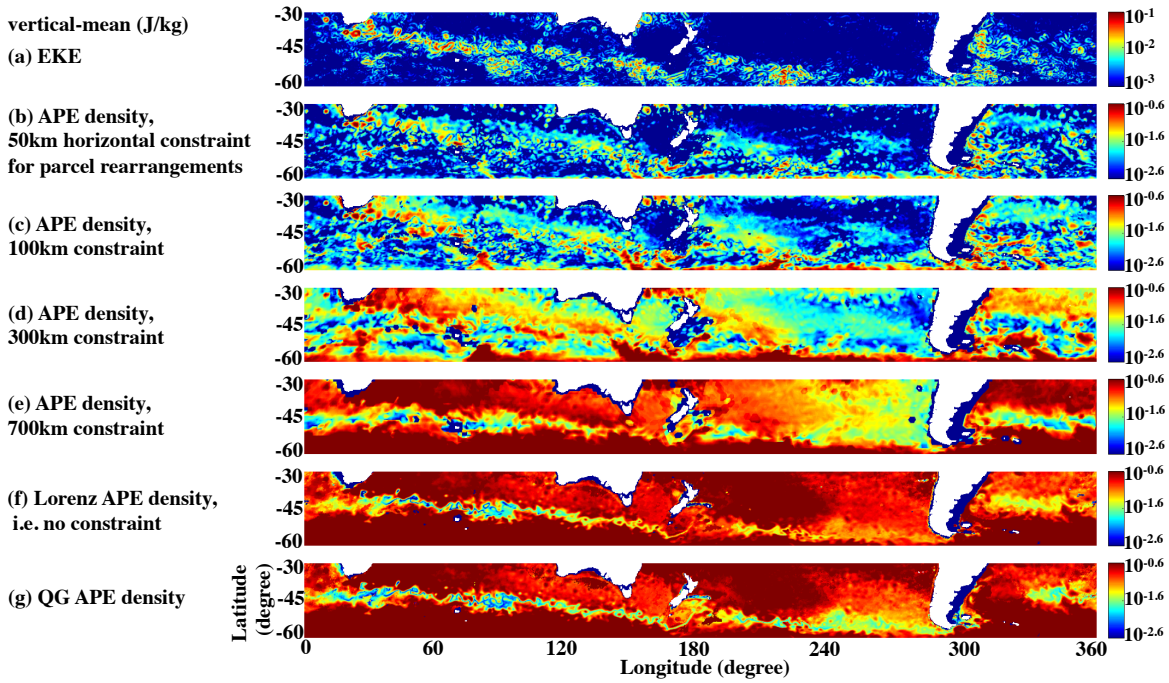

Figure 4.5: As Figure 4.2 but panels (b)-(f) here are based on a snapshot of ECCO2 state estimate (February 16, 2005) rather than the 3-year mean in Figure 4.2. The EKE snapshot in panel (a) defined as $0.5 \times [(u - \bar{u})^2 + (v - \bar{v})^2]$ where u and v are, respectively, the zonal and meridional velocity for this snapshot, and $\bar{u}$ and $\bar{v}$ are the time-mean (August 2003-July 2006) counterparts. These transient patterns of vertical-mean APE density are generally consistent with the time-mean counterparts in Figure 4.2, but have much more mesoscale turbulent features, as expected. There is a high correspondence between the eddies in panel (a) and the APE patches in panel (b), which demonstrate the potential usefulness of our defined eddy-size-constrained APE density to diagnose/parameterize mesoscale eddies. See section 4.4 for details.

Figures 4.5 show the same energy quantities as Figures 4.2 but based on a snapshot of dataset. These transient APE densities are generally consistent with the 3-year-mean counterpart in Figure 4.2, but with much more mesoscale turbulent features, as expected. There is a high correspondence between the eddies (vortices) in Figure 4.5a and the APE patches in Figure 4.5b (e.g., at the south of Africa; around Australia). This further demonstrates the potential usefulness of our defined eddy-size-constrained APE density to diagnose/parameterize mesoscale eddies. This

correspondence should be contributed by two factors: (i) local APE is a critical energy source for mesoscale eddies and is partly converted to EKE via baroclinic instability; (ii) baroclinic eddies (vortices) are associated with local stratification (and hence APE) signals, i.e., corresponding to local baroclinicity (a doming or a bowling of the isopycnals) through thermal wind balance (Roullet and Patrice 2010). Indeed, EKE and APE for an eddy would scale directly with one another in the QG limit [see equation (4.4) below]. These two factors above are related and may not be separated explicitly.

We now consider the World Ocean. Using the altimeter-observed eddy size (Figure 4.6b; Chelton et al. 2011) as the constraint for parcel rearrangement, we obtain the global eddy-size-constrained APE density (Figure 4.6c). Its mean magnitude is ∼2.5 times larger than the EKE (Figure 4.6c vs 4.6a), which can be explained by QG scaling (e.g., (5.160) of Vallis 2006):

$$\frac{\text{EKE}}{\text{QG-APE}} \sim \frac{\text{KE}}{\text{QG-APE}} \sim \frac{L_d^2}{L^2}. \tag{4.3}$$

where we have applied EKE∼KE since geostrophic eddies account for most of the KE of the oceans (section 6 of Ferrari and Wunsch 2009). In (4.3), L_d is the deformation radius and L is the considered scale. Now we consider a closed system of only eddy scale, i.e., L is equal to the eddy scale L_e. Then the Lorenz APE of this eddy-size system, which is approximated by the QG-APE of this system, is essentially equivalent to the eddy-size-constrained APE we focus here (note again that the system considered here is of only eddy scale; in contrast, the Lorenz APE and QG-APE in

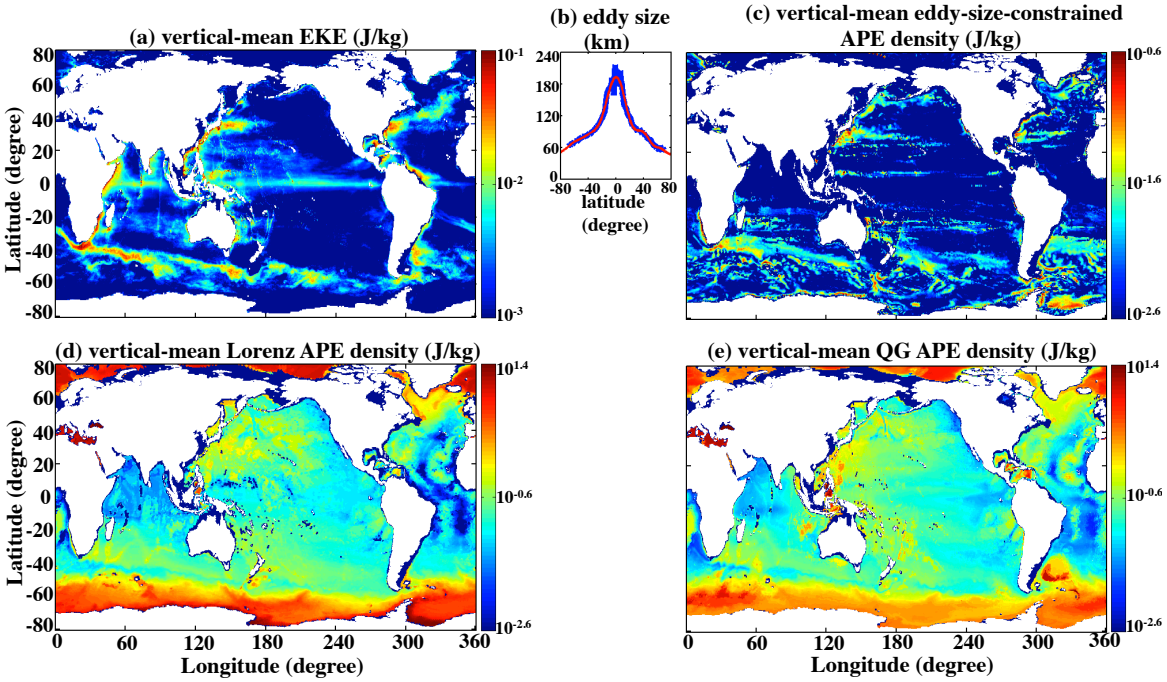

Figure 4.6: (a) Global vertical-mean EKE (J/kg). It uses the same dataset as Figure 4.2a. (b) Meridional profile of zonal-mean surface eddy size by altimeter observations (blue; Chelton et al. 2011). The observed eddy size is highly homogenous zonally (Figure 12 of Chelton et al. 2011) and hence we only consider its meridional variation. The polynomial fitting (red; using matlabs polynomial fitting of degree 17) extends the blue curve from the observation edge at ∼70° latitude to 80°, by which we approximate the eddy size for 70°-80° regions. (c) Global vertical-mean eddy-size-constrained APE density (J/kg). It applies the observed eddy size (red curve in (b)) as the horizontal constraint for adiabatic parcel rearrangement from the current state to the reference (minimum-PE) state. The match between (c) and (a) is consistent with the physical picture that baroclinic instability is crucial for the generation of EKE in most ocean regions. (d) Global vertical-mean Lorenz APE density (J/kg). It has large values (red, $\sim 10^1$ J/kg) mainly around Antarctica and the Arctic, where dense water is produced and circulated (i.e. AABW, NADW, and ABW). In contrast, it has medium values (yellow, $\sim 10^0$ J/kg) in broad ocean areas including regions with strong ocean currents/EKE, e.g., around ACC fronts, Kuroshio Current, and Gulf Stream. The Lorenz APE density, as in (d), reflects the deviation of local current-state stratification from the Lorenz reference state in the considered system. See section 4.4 for details. (e) QG APE density of the World Ocean.

Figures 4.2 and 4.5 are for the whole SO system). Thus equation (4.3) implies:

$$\frac{\text{EKE}}{\text{eddy-size-constrained APE}} \sim \frac{L_d^2}{L_e^2}. \tag{4.4}$$

The eddy scale L_e is typically larger than L_d (Figure 12 of Chelton et al. 2011), due to nonlinear processes such as the inverse cascade of turbulent energy (Vallis 2006). Therefore from (4.4), eddy-size-constrained APE should be typically larger than EKE, as shown by Figure 4.6a vs 4.6c. Note that equation (4.4), due to its scaling-analysis nature, should be only treated as a qualitative argument rather than an accurate description.

The distribution of eddy-size-constrained APE in general well captures the high EKE in most ocean regions (Figure 4.6c vs 4.6a), especially around the SO fronts and subtropical western boundary currents (e.g., Gulf Stream; Kuroshio, Agulhas, Brazil/Malvinas, and East Australian Currents). This is consistent with the classic hypothesis that baroclinic instability provides the dominant source for local eddy growth in most ocean regions (e.g., Arbic 2000), i.e., by converting local APE to EKE (e.g., Vallis 2006). The mismatching part between Figures 4.6a and 4.6c may be caused by interactions as discussed before. For example, barotropic instability is an important EKE source, e.g. in Gulf Stream (Gula et al. 2015) and significantly in tropical oceans (Jochum et al. 2003). Subpolar oceans have much larger eddy-size-constrained APE density than EKE (Figure 4.6c vs 4.6a; e.g., around the Weddell and Greenland Seas, Antarctic continental shelf). This is likely because L_d/L_e decreases with latitude and becomes very small at high latitude regions (Figure 12 of Chelton et al. 2011). According to (4.4) we should have APE much larger than EKE in these regions. Further, this may also be contributed by the underestimate of EKE in our applied 18-km-grid ECCO2 dataset, the suppression of baroclinic instability above

continental slope and along the ocean front (Stewart and Thompson 2013), and the potential smallness of real-ocean parcel-rearrangement scale relative to our applied eddy size. Global patterns of Lorenz APE density are again distinct from EKE (see Figure 4.6d and its caption): it mainly reflects the ocean regions with dense water production/circulation. QG-APE of the World Ocean (Figure 4.6e vs 4.6d) has generally consistent patterns with the Lorenz APE. However, they have a significant discrepancy in magnitude especially around high-latitude regions, where the densest water are located and hence strong isopycnal displacements are required to reach the global Lorenz reference state. This makes QG approximation less effective (Roullet and Klein 2009), in contrast to the lower latitude regions.

4.5 Discussion

Our proposed MCFA efficiently and exactly solves the Lorenz reference state for an ocean system with a nonlinear EOS. This may be helpful for associated energy diagnosis in ocean models, especially for regions where the nonlinear effect of EOS is significant to determine the Lorenz APE (thermobaricity may compete with baroclinicity, e.g., in the Weddell Sea; Su et al. 2016a, b). In contrast, approximate methods such as QG-APE typically cannot capture this nonlinear effect (see Appendix B of HN15). There is a general match, although with non-neglectable difference, between the patterns of high EKE and high eddy-size-constrained APE density (i.e., high local baroclinicity) (Figure 4.6a vs 4.6c). Our APE framework is also shown to be helpful to detect individual eddies/vortices (Figure 4.5a vs 4.5b). These suggest the likely usefulness of our APE framework in diagnosing/parameterizing mesoscale ed-

dies and identifying the mechanisms that cause non-local EKE development. These results open new routes to understand the dynamics that influences the conversion of local APE to EKE (e.g., related eddy-mean energy fluxes, the vertical structure of energy transfer, the influences from topography, standing meanders, nonlocal energy propagation, waves, etc).

Roullet et al. (2014) provide a valuable study by showing the global map of the eddy APE as diagnosed from Argo data, which is highly consistent with the surface EKE patterns estimated from satellite altimetry. Note that the eddy APE is the direct source for EKE (Figure 1 of Chen et al. 2014). In contrast, our eddy-size-constrained APE density is defined only from a given dataset (rather than from a time series of datasets as required for the definition of eddy APE). However, it can still well capture the EKE patterns in most ocean regions: the strong connection between them is again explained qualitatively by equation (4.4). From a time series of datasets, we can investigate the time-mean part and the eddy part of our APE concept, which will be explored in a future study. The temporal evolution of APE is related to the buoyancy budgets (e.g., Hieronymus and Nycander 2013a, 2013b; Hieronymus 2014) and baroclinic dynamics (e.g., Chen et al. 2014), which will be investigated in a subsequent study.

This study focuses on the energy reservoirs (i.e., APE, EKE) rather than the conversion rate between them. Via the baroclinic instability, the mean APE is converted to the eddy EKE, while the eddy APE is then converted to EKE (Chen et al. 2014). Roullet et al. (2012) (see their Figures 8, 11), Zhai and Marshall (2013) (see

their Figure 5-7), and Chen et al. (2014) (see their Table 1) have provided valuable discussions on these conversions. Figures 5a and 5b of Chen et al. (2014) show the global map of the conversion term from eddy APE to EKE, and the conversion term from the mean APE to eddy APE, respectively, as diagnosed from the ECCO2 state estimate[6]. Their patterns generally agree with the patterns of EKE and our defined eddy-size-constrained APE density (our Figures 4.6a, 4.6c): this is consistent with the classic hypothesis that the dominant source for local eddy growth is the energy released locally from the mean flow (i.e., APE) through baroclinic instability (Tulloch et al. 2011; Chen et al. 2014). Exploring the conversion terms using our defined new APE framework will be investigated in a following study.

The QG-APE shown in Figure 4.2g and 4.6e are for the SO system and the World Ocean system, respectively. The QG-APE of a parcel is traditionally defined based on the deviation of density/buoyancy of this parcel from the horizontal mean of the considered system [e.g., equation (4) of Huang 2005; (3.183) of Vallis 2006]. It is possible to define a new QG-APE concept, defined not based on the horizontal mean of the considered system, but based on the horizontal mean of an eddy-size domain surrounding the considered parcel (i.e., the domain here is a small part of the system, of only eddy size). This is essentially a similar concept as the eddy-size-constrained APE density we defined in this study: the former is based on the QG approximation while the later is based on adiabatic parcel rearrangements. This potential new concept of QG-APE may similarly capture the EKE patterns as the

[6]This ECCO2 dataset of Chen et al. (2014) is essentially the same as our ECCO2 dataset for our Figure 4.6, although the former has a lower resolution (3^o vs 18-km).

eddy-size-constrained APE density. A detailed discussion of this is beyond the scope of this study and will be investigated in a future study.

Chapter 5

An idealized model of Weddell Gyre export variability[†]

5.1 Abstract

Recent observations suggest that the export of Antarctic Bottom Water (AABW) from the Weddell Sea has a seasonal cycle in its temperature and salinity that is correlated with annual wind stress variations. This variability has been attributed to annual vertical excursions of the isopycnals in the Weddell Gyre, modifying the water properties at the depth of the Orkney Passage. Recent studies attribute these variations to locally wind-driven barotropic dynamics in the northern Weddell Sea boundary current. This chapter explores an alternative mechanism in which the isopycnals respond directly to surface Ekman pumping, which is coupled to rapidly responding mesoscale eddy buoyancy fluxes near the gyre boundary. A conceptual model of the interface that separates Weddell Sea Deep Water from Circumpolar Deep Water is described in which the bounding isopycnal responds to a seasonal oscillation in the surface wind stress. Different parameterizations of the mesoscale

[†]Appeared as: Su, Z., A.L. Stewart and A.F. Thompson, 2014. An idealized model of Weddell Gyre export variability. Journal of Physical Oceanography, 44, 1671-1688

eddy diffusivity are tested. The model accurately predicts the observed phases of the temperature and salinity variability in relationship to the surface wind stress. The model, despite its heavy idealization, also accounts for more than 50% of the observed oscillation amplitude, which depends on the strength of the seasonal wind variability and the parameterized eddy diffusivity. These results highlight the importance of mesoscale eddies in modulating the export of AABW in narrow boundary layers around the Antarctic margins.

5.2 Introduction

Observations show that the properties of Antarctic Bottom Water (AABW) in the Weddell Sea's northern boundary current undergo a seasonal cycle in temperature and salinity (Gordon et al., 2010; McKee et al., 2011) at a fixed depth. This variability is found upstream of a key export site, the Orkney Passage. Evidence of a link between this property variations and surface wind forcing is given by Jullion et al. (2010), who find that Weddell Sea Deep Water (WSDW) properties in the Scotia Sea correlate with local wind stress variation along the South Scotia Ridge with a phase lag of five months. Meredith et al. (2011) similarly find that temperature anomalies of WSDW in the Scotia Sea, and at the entrance of the Orkney Passage, lag the local surface wind stress by 2 to 4 months. This study presents a mechanism to describe these observed time lags.

Here we focus on the transit of WSDW through the the Weddell Gyre (Figure 5.1), an important component of the global circulation. A significant fraction of Antarctic Bottom Water (AABW), which ventilates the deep ocean, originates as WSDW,

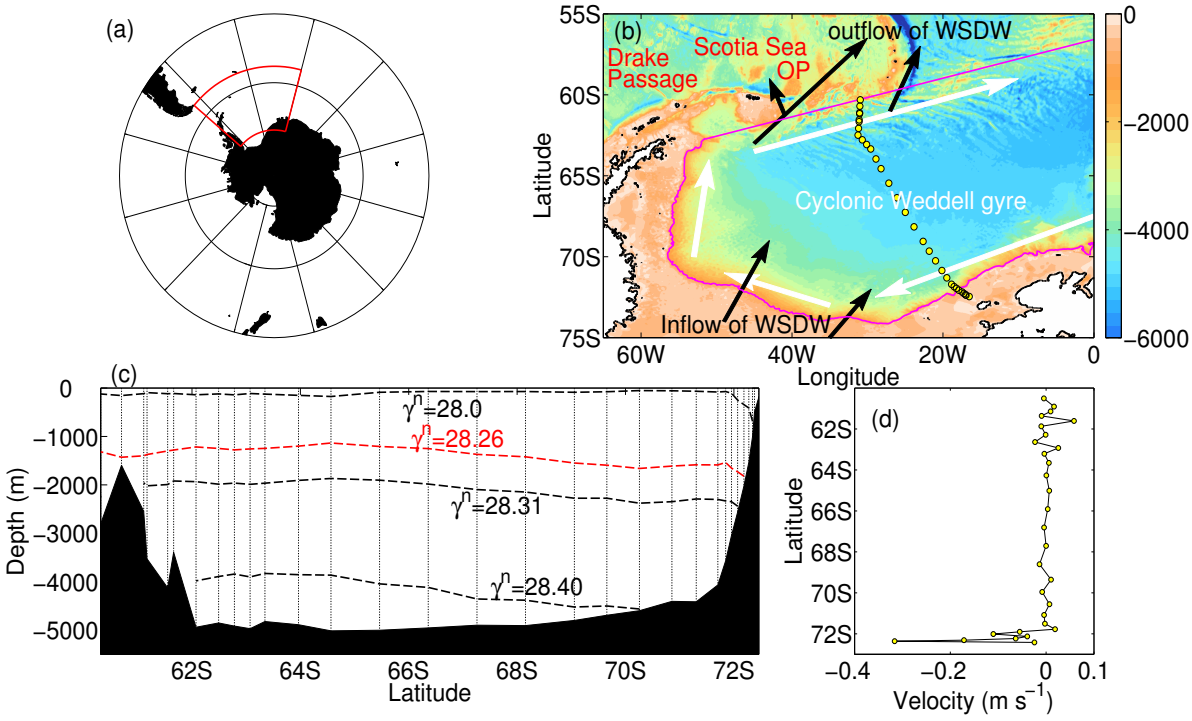

Figure 5.1: (a) Map of the Southern Ocean. The highlighted region is enlarged in panel (b). (b) Bathymetry (ETOPO1) of the Weddell Sea and neighboring basins (depth in meters); land is marked by black contours. The white arrows depict the cyclonic gyre circulation. The black arrows depict the inflow of Weddell Sea Deep Water (WSDW) and primary outflow paths of WSDW through Orkney Passage (OP) in the South Scotia Ridge. The magenta contour indicates the 1000 m isobath in the southern and western part of the gyre. The northern boundary is approximated by a straight line. The yellow circles mark the position of the WOCE A23 hydrographic section, indicated by dotted lines in panel (c). (c) Contours of neutral density from A23. The red curve with $\gamma^n = 28.26\,\mathrm{kg\,m^{-3}}$ serves as the focus of this study, as it separates WSDW from the Circumpolar Deep Water above. (d) Depth-averaged geostrophic velocity across A23, referenced to zero velocity at the surface.

which is typically defined as having a neutral density greater than $\gamma^n \sim 28.26\,\mathrm{kg\,m^{-3}}$ (Naveira Garabato et al., 2002). WSDW circulates cyclonically around the Weddell Gyre (Figure 5.1b) (Deacon, 1979) with the strongest velocities found within narrow boundary currents (Figure 5.1d). As this boundary current intersects the South Scotia Ridge, WSDW may flow through deep passages and enter the Scotia Sea (Locarnini et al., 1993). Naveira Garabato et al. (2002) measure the LADCP-referenced

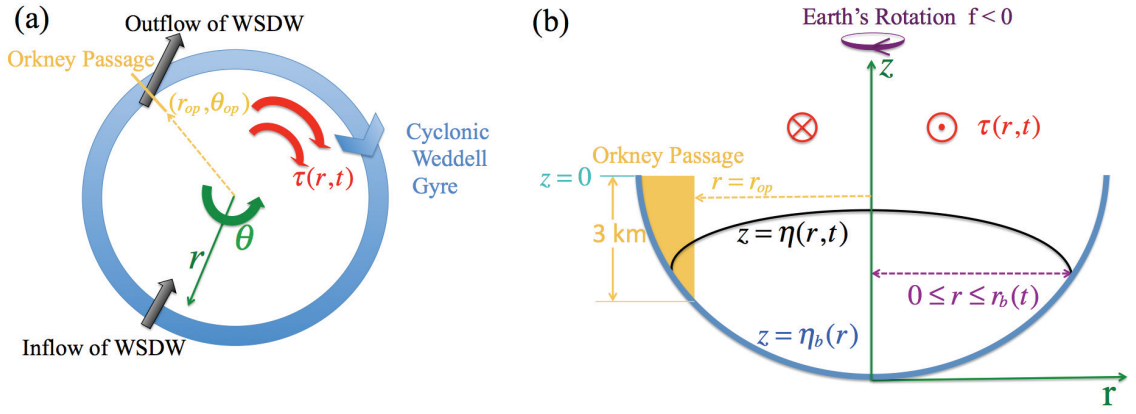

Figure 5.2: Schematic of the idealized Weddell Gyre used in our residual-mean model. (a) The gyre is approximated as a circular basin with cyclonic surface wind stress $\tau(r,t)$ and forced by inflow and outflow of Weddell Sea Deep Water (WSDW). (b) Profile view of the of the idealized gyre in cylindrical coordinates. The gyre bathymetry (blue) is described by $z = \eta_b(r)$ and the bounding isopycnal (black) is described by $z = \eta(r,t)$ marking the interface between Circumpolar Deep Water and WSDW, at a depth of roughly 1500 m. The isopycnal intersects the bathymetry at $r = r_b(t)$. The yellow box indicates the cross-sectional area through which water exits the Orkney Passage, which extends to around 3 km depth (see *e.g.* Figure 7 of Naveira Garabato et al., 2002).

geostrophic transport of WSDW to be 6.7±1.7 Sv through the South Scotia Ridge (this value is modified to 4.7±0.7 Sv by their box inverse model of the western Weddell Gyre). The majority of this outflow, around 4 to 6 Sv of WSDW colder than 0°C, traverses the Orkney Passage and merges with the Antarctic Circumpolar Current (ACC) (Meredith et al., 2008; Naveira Garabato et al., 2002).

The correlation between surface winds and WSDW export suggests an adjustment of the structure of the Weddell Gyre stratification to a modified surface wind stress curl. At large scales, the circulation of the Weddell Gyre is consistent with Sverdrup balance: the negative surface wind stress curl leads to a southward transport in the gyre interior that is balanced by a northward return flow in a western boundary current (Gordon et al., 1981; Muench and Gordon, 1995). Radiation of Rossby waves

is a key mechanism by which a gyre-like flow responds to changes in wind forcing. For a Weddell Sea-sized basin, the barotropic component of the gyre circulation can adjust over a time scale of a few days, but the baroclinic component requires several years because the barotropic and baroclinic Rossby wave speeds differ by 3–4 orders of magnitude (Anderson and Gill, 1975). Therefore, it seems that baroclinic adjustment of the gyre via linear waves occurs too slowly to explain the annual variations of WSDW outflow properties. Appreciating this problem, recent work has ascribed the WSDW export variability to barotropic processes occurring within the boundary current of the northwestern Weddell Sea, in particular changes in bottom Ekman layer transport near Orkney Passage (Jullion et al., 2010; Meredith et al., 2011).

Despite the relatively weak flows throughout the gyres, the circulation remains turbulent and especially in the western boundary layer mesoscale eddies make a leading contribution to exchanges of mass, heat and salt across the Antarctic shelf break (Nøst et al., 2011; Dinniman et al., 2011; Stewart and Thompson, 2013). In this study we propose that mesoscale eddies, arising through baroclinic instability that extracts potential energy from vertical isopycnal displacements related to the divergence and convergence in the surface Ekman forcing, are crucial in setting the buoyancy distribution of the Weddell Gyre. To test this hypothesis we develop a conceptual model of the isopycnal separating WSDW from the overlying Circumpolar Deep Water (CDW) in the Weddell Sea. Furthermore, we cast this balance between wind-induced and eddy-induced circulation in the framework of residual-mean theory (RMT) (Andrews et al., 1987; Plumb and Ferrari, 2005).

RMT has been an important tool in understanding the principal balances in the ACC's upper overturning cell (Marshall and Radko, 2003), and has recently been extended to flows around the Antarctic margins (Stewart and Thompson, 2013). This model moves away from the traditional picture that cross-shelf exchange requires large-scale along-shelf pressure gradients (Ou, 2007). Here we consider along-stream, or tangentially- averaged properties along the boundary of the Weddell Gyre. RMT is used to describe the evolution of the mean isopycnals in response to annual variations of the wind stress. This approach is motivated in part by the striking isopycnal tilt seen in observations of the gyre boundary (Naveira Garabato et al., 2002).

In §5.3 we describe our idealized domain and forcing and in §5.4 we derive a residual-mean model for the isopycnal bounding WSDW in the Weddell Gyre. In §5.5 we solve the evolution equation for the bounding isopycnal and discuss its sensitivity to wind stress and eddy diffusivity. In §5.6 we extend the model to include a representation of WSDW inflow to and outflow from the gyre. In §5.7, we compare our model predictions with observations and discuss the limitations and implications of our model. We draw conclusions in §5.8.

5.3 An idealized Weddell Gyre

Our approach adopts an idealized version of the Weddell Gyre that captures key aspects of the physics controlling isopycnal variability. Figure 5.2 shows a schematic of our conceptual model. The gyre is assumed to be circular and azimuthally uniform with an applied azimuthally-uniform surface wind stress. This geometry motivates a description in terms of cylindrical coordinate (r, θ, z), where $r = 0$ at the gyre center,

$r = R = 680\,\mathrm{km}$ at the gyre edge, and θ is anticyclonic.

To explore the properties of WSDW exported from the edge of the Weddell Gyre, the model focuses on the evolution of an isopycnal that represents the division between WSDW and CDW (Figure 5.1c). The model solves for the isopycnal's azimuthal-mean position $z = \eta(r, t)$ as a function of radius r and time t. The position at which this isopycnal outcrops from the bathymetry is denoted as $r = r_b(t)$.

5.3.1 Bathymetry

The idealized bathymetry is derived from the NOAA ETOPO1 data (Amante and Eakins, 2009) shown in Figure 5.1(b). The 1 km depth contour (magenta curve) defines the southern and western boundary of the Weddell Gyre. At the northern edge of the gyre the 1 km isobath is discontinuous and we use a straight line to approximate the boundary.

We construct the model bathymetry as an average of 75 evenly-spaced sections that extend perpendicularly from the shelf break into the gyre interior (not shown). The sections are chosen to be 680 km long so that they meet approximately in the gyre center. This produces a smooth representation of the bathymetry, but realistically captures the slope, especially around the gyre edge (Figure 5.3). A simple polynomial approximation is also provided by the solid curve in Figure 5.3,

$$\eta_b(r) = C_0 + C_5 r^5, \tag{5.1}$$

with coefficients $C_0 = -4.54 \times 10^3\,\mathrm{m}$ and $C_5 = 1.85 \times 10^{-26}\,\mathrm{m}^{-4}$.

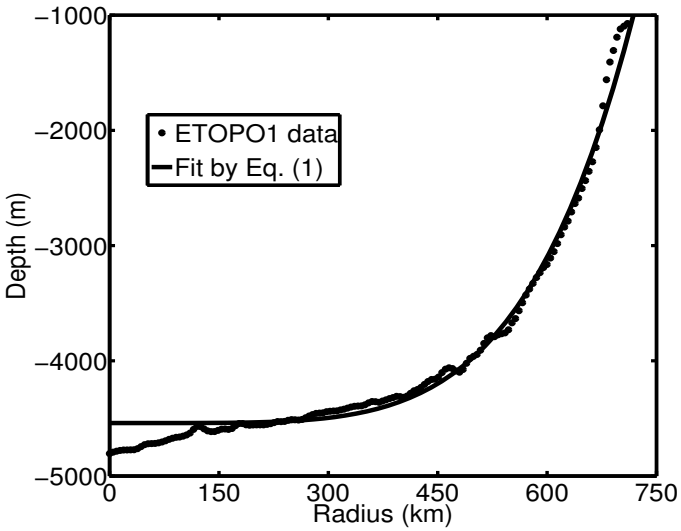

Figure 5.3: The tangentially averaged basin geometry of the Weddell Sea from ETOPO1 data (points) and an analytical fit $\eta_b(r)$ (line) given by (5.1).

5.3.2 Azimuthal winds

Wind stress amplitudes over the Weddell Gyre are poorly constrained by observations. Here we choose to adopt a simple representation of the wind stress (described below) and explore the sensitivity to this choice in §5.5.3. The wind stress profiles are derived from the CORE.2 Global Air-Sea Flux Dataset (Large and Yeager, 2009), available from 1949 to 2006 with a monthly frequency and 1° resolution. This product does not account for the modulations in the transmission of momentum from the atmosphere to the ocean related to seasonal or inter-annual changes in sea ice distribution. We focus here on the model dynamics, which are valid for any prescribed surface momentum forcing, and we discuss the implications of sea ice variability in §5.7.2. The time-mean zonal and meridional wind stress distributions as well as the the time-mean wind stress curl are shown in Figure 5.4. The wind stress curl is almost uniformly negative over the gyre, and is particularly strong ($\sim 2 \times 10^{-7}$ Nm^{-3}) along the gyre

boundary.

The components of the surface wind stress perpendicular to the 75 sections described in §5.3.1 are averaged to produce the azimuthal-mean wind stress tangential to the gyre boundary. Figure 5.4(d) shows the amplitude of each Fourier mode of the azimuthal-mean tangential wind stress at the shelf break $\tau(r = R, t)$, which is computed from the 58 year CORE.2 time series. Negative values correspond to cyclonic wind stress. With the exception of the steady mode, whose amplitude is $-0.073\,\mathrm{N\,m^{-2}}$, only the annual and semiannual modes are pronounced at the shelf break, having amplitudes of $-0.029\,\mathrm{N\,m^{-2}}$ and $-0.011\,\mathrm{N\,m^{-2}}$ respectively. The estimated standard deviation of the Fourier modes plotted in Figure 5.4(d) is $0.0044\,\mathrm{N\,m^{-2}}$ for the annual mode and less than $0.0028\,\mathrm{N\,m^{-2}}$ for other modes. The relative amplitudes of the modes are similar at all radii from the gyre center. The contribution to isopycnal displacement from each mode follows the same physical processes, since our model is approximately linear with time, as shown in §5.4. Furthermore, the observed annual cycle of AABW in the northern Weddell Sea motivates this study. Therefore, for simplicity we include only the annual mode in our conceptual model, and neglect all other modes. Numerical experiments show that the semiannual mode can modify isopycnal excursions at the gyre edge by 10%–20%; this is discussed further in §5.7.1.

Figure 5.4(e) shows the radial variation in the amplitudes of the steady and annual azimuthal wind stress modes. Both modes strengthen linearly from the gyre interior to the gyre boundary. Thus the steady and annual modes are represented

by $\overline{\tau}(r) = \overline{\tau}^0 r/R$ and $\tau_{12}(r) = \tau_{12}^0 r/R$ respectively, where $\overline{\tau}^0 = -0.072\,\mathrm{N\,m^{-2}}$ and $\tau_{12}^0 = -0.026\,\mathrm{N\,m^{-2}}$ are constants. In a circular basin, the azimuthal wind stress must vanish at $r = 0$ by symmetry. Figure 5.4(f) shows the radial variation of the phase ϕ_{12} of the annual mode, where the annual mode is expressed as $\tau_{12}(r) \cdot \sin(\omega t + \phi_{12}(r))$ and $\omega = 2\pi\,\mathrm{yr^{-1}}$. The phase ϕ_{12} varies by less than 35° for $r > 100\,\mathrm{km}$, and for $r < 100\,\mathrm{km}$ the amplitude of the annual mode is close to zero, so for simplicity we approximate $\phi_{12} \equiv 300°$ as a constant. Thus our expression for the azimuthal wind stress is

$$\tau(r,t) = \overline{\tau}(r) + \tau_{12}(r)\sin(\omega t + 5\pi/3), \tag{5.2a}$$

$$\overline{\tau}(r) = \overline{\tau}^0\,\frac{r}{R}, \qquad \tau_{12}(r) = \tau_{12}^0\,\frac{r}{R}. \tag{5.2b}$$

Here $t = 0$ corresponds to the start of January, so the model wind field has an annual cycle with maximum amplitude at $t = 5\,\mathrm{months}$, *i.e.*, at the end of May. This wind pattern is consistent with previous observations (see *e.g.* Figure 1(d) of Wang et al., 2012).

5.4 Residual-mean dynamics

We now derive an evolution equation for the bounding isopycnal $z = \eta(r,t)$ using RMT. Our formulation is similar to that of Marshall and Radko (2003), except it is cast in terms of an azimuthal average of the buoyancy around our idealized Weddell Gyre. Note that our model and its derivation in this section could be applied to any isopycnal in the Weddell Gyre.

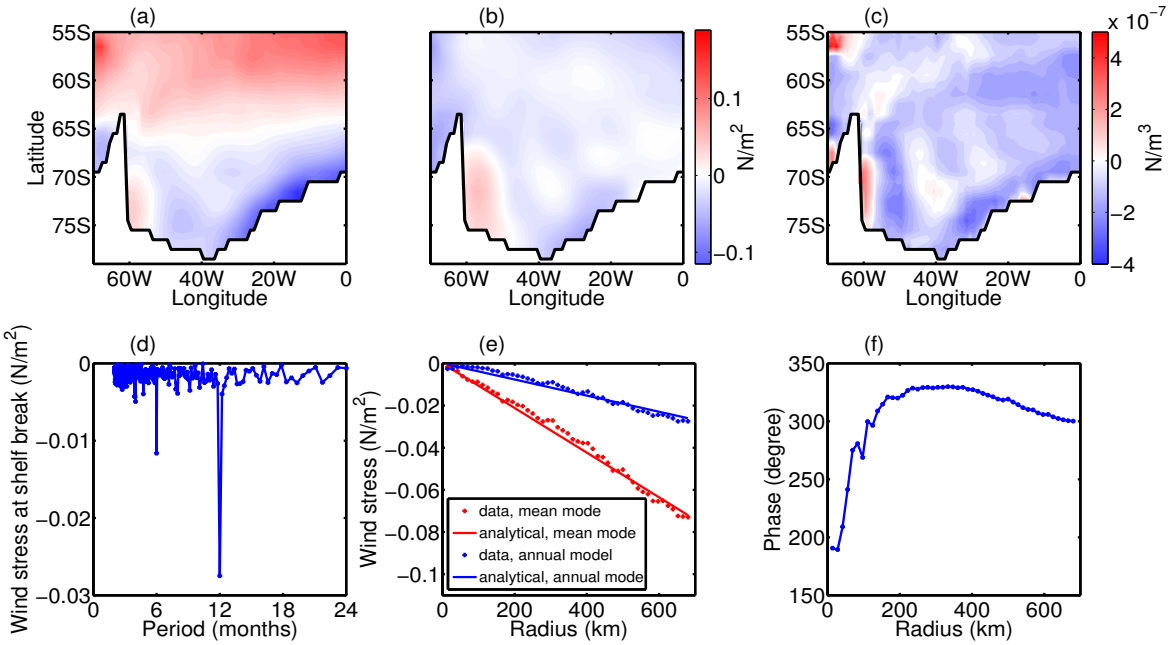

Figure 5.4: Time-averaged (1949 to 2006) (a) zonal and (b) meridional wind stress components and (c) wind stress curl over the Weddell Sea and neighboring basins. (d) Amplitude of the Fourier modes (oscillation periods) for the azimuthal-mean tangential wind stress at the gyre boundary. Details of the calculation and the standard deviation of the amplitudes are described in §5.3.2. The amplitude of the time-independent mode is $-0.073\,\mathrm{N\,m^{-2}}$ (not shown); negative amplitudes correspond to cyclonic winds. (e) Radial dependence of the steady and annual mode amplitudes, $\overline{\tau}$ and τ_{12}, of the azimuthal-mean tangential wind stress. (f) Radial dependence of the phase ϕ_{12} of the annual mode of the azimuthal-mean tangential wind stress.

Following Marshall and Radko (2003), the azimuthally-averaged buoyancy may be written as

$$\langle b \rangle_t + J(\psi^\dagger, \langle b \rangle) = 0, \tag{5.3}$$

where b is the buoyancy and $\langle \bullet \rangle = (2\pi)^{-1} \oint \bullet \, \mathrm{d}\theta$ denotes the azimuthal average. The residual steamfunction $\psi^\dagger$ describes the advecting two-dimensional velocity field in

the (r, z) plane, defined as $\mathbf{u}^\dagger = u^\dagger \mathbf{e}_r + w^\dagger \mathbf{e}_z = \nabla \times (\psi^\dagger \mathbf{e}_\theta)$ with

$$u^\dagger = -\frac{\partial \psi^\dagger}{\partial z}, \quad w^\dagger = \frac{1}{r}\frac{\partial\, r\psi^\dagger}{\partial r}. \tag{5.4}$$

A turbulent diapycnal mixing term $(\kappa_v \langle b \rangle_z)_z$ has been neglected from the right-hand side of (5.3), where κ_v is the vertical diffusivity. This term may be shown to be dynamically negligible in our model; this is discussed in detail in §5.7.2.

The residual streamfunction $\psi^\dagger$ is comprised of a mean (wind-driven) component $\langle \psi \rangle$ and an eddy component $\psi^\star$,

$$\psi^\dagger = \langle \psi \rangle + \psi^\star, \quad \langle \psi \rangle = \frac{\tau}{\rho_0 f_0}, \quad \psi^\star = \kappa s_b. \tag{5.5}$$

Following a procedure analogous to Marshall and Radko (2003), the mean streamfunction $\langle \psi \rangle$ is related to the surface wind stress using the azimuthally-averaged azimuthal momentum equation in the limit of small Rossby number. The same physical reasoning applies to both the ACC and the Weddell Gyre: in the zonal (azimuthal) mean the ACC (Weddell Gyre) cannot support a net zonal (azimuthal) pressure gradient, and thus no mean geostrophic meridional (radial) flow in the interior, so mean Ekman pumping driven by zonal (cyclonic) surface winds penetrates to depth. Here ρ_0 is the reference density and f_0 is the reference Coriolis parameter, the latitudinal variation of the Coriolis parameter is about 5% in the Weddell Gyre and has been neglected here. The eddy streamfunction arises from a downgradient eddy buoyancy flux closure (Gent and McWilliams, 1990), where κ is the eddy buoyancy diffusivity

and $s_b = -\langle b \rangle_r / \langle b \rangle_z$ is the isopycnal slope.

As the azimuthal-mean isopycnal $z = \eta(r,t)$ is a material surface in the sense of the residual advective derivative $D^\dagger/Dt \equiv \partial_t + \boldsymbol{u}^\dagger \cdot \nabla$, it may be shown (see Appendix A) that it evolves according to

$$\frac{\partial \eta(r,t)}{\partial t} = \frac{1}{r}\frac{\partial}{\partial r}\left(r\psi^\dagger\Big|_{z=\eta(r,t)} \right), \quad 0 < r < r_b(t). \tag{5.6}$$

Equation (5.6) shows that the evolution of the isopycnal must be balanced by the radial divergence of $\psi^\dagger$, *i.e.* the net radial transport between the isopycnal and the ocean bed. Inserting (5.5) into (5.6) and noting $s_b = \partial\eta/\partial r$, we obtain a forced-diffusive evolution equation for the isopycnal height η,

$$\frac{\partial \eta}{\partial t} = \frac{1}{r}\frac{\partial}{\partial r} r \left[\frac{\tau}{\rho_0 f_0} + \kappa \frac{\partial \eta}{\partial r} \right], \tag{5.7}$$

for $0 < r < r_b(t)$. Here $\kappa = \kappa(r,t)$ is the eddy buoyancy diffusivity evaluated on the isopycnal $z = \eta(r,t)$, and the $\partial\eta/\partial r$ is isopycnal slope. We impose no-flux boundary conditions ($\psi^\dagger = 0$) at the gyre center $r = 0$ and at the isopycnal outcrop $r = r_b(t)$.

The azimuthally-averaged wind stress τ must vanish at $r = 0$ by symmetry, so from (5.5) the boundary condition is

$$\psi^\dagger\Big|_{r=0} = 0 \quad \Longrightarrow \quad \frac{\partial \eta}{\partial r}\bigg|_{r=0} = 0. \tag{5.8a}$$

Similarly, at the isopycnal outcrop $r = r_b(t)$ we obtain

$$\psi^\dagger\Big|_{r=r_b} = 0 \quad \Longrightarrow \quad \left.\frac{\partial \eta}{\partial r}\right|_{r=r_b} = -\left.\frac{\tau}{\rho_0 f \kappa}\right|_{r=r_b}. \tag{5.8b}$$

The outcrop position $r = r_b(t)$ evolves with time to satisfy $\eta(r_b(t), t) = \eta_b(r_b(t))$. In numerical solutions of (5.7)–(5.8b), this evolution must be computed explicitly, as discussed in Appendix B.

As we have not prescribed any inflow nor outflow of WSDW at this point, our model conserves the total mass M beneath the isopycnal $z = \eta(r, t)$,

$$\frac{dM}{dt} = 0, \quad M = \int_0^{r_b(t)} 2\pi r \rho_0 (\eta - \eta_b)\, dr. \tag{5.9}$$

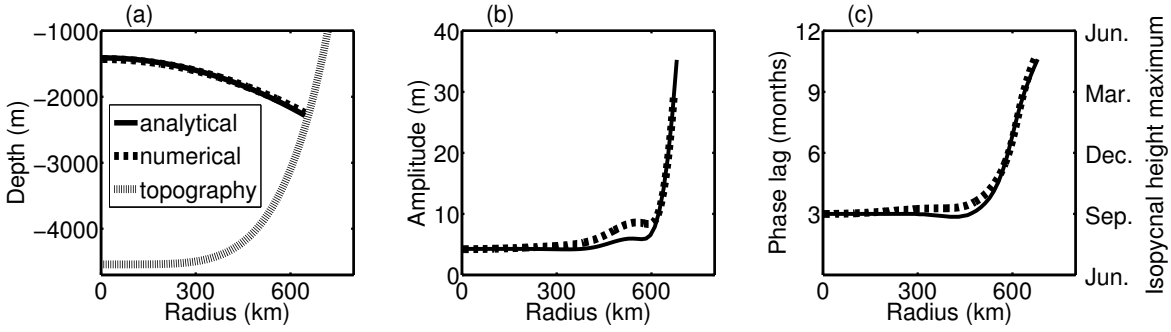

Figure 5.5: Analytical solution in a cylindrical basin (solid) and numerical solution in a curved basin (dashed) with no inflow/outflow of WSDW. (a) The time-mean isopycnal height $\overline{\eta}(r)$. (b) Amplitude of the isopycnal oscillation $|\eta'|$. (c) Phase lag of oscillation η', defined as the time interval from the wind stress maximum to the isopycnal height maximum. The wind stress maximum occurs at the beginning of June each year.

5.5 The model solution

5.5.1 Analytical solution in cylindrical basin

In this section we solve the model evolution equation (5.7) analytically in a simplified case. The solution serves as a scaling for the isopycnal's response to the annually-varying surface wind stress, and provides an intuitive interpretation of our later results. For convenience, we choose the isopycnal separating CDW from WSDW, *i.e.* $\gamma^n = 28.26\,\mathrm{kg\,m^{-3}}$, for all the following discussions. The results translate to other isopycnals with the caveat that non-linearities, such as diapycnal mixing, have been neglected in this model (see further discussion in §5.7.2).

Figure 5.1(c) shows that the WSDW isopycnal outcrops at the steepest part of the bathymetric slope. Our numerical solutions in §5.5.2 show that the change in r_b related to isopycnal excursions is typically small ($< 4\,\mathrm{km}$) because the bathymetric slope is steep here. We therefore approximate the basin as a cylinder with vertical walls at $r_b \equiv R = 680\,\mathrm{km}$. We choose $\kappa = \text{constant} = 300\,\mathrm{m^2/s}$; this yields a range of isopycnal heights that approximately matches the observed range in Figure 5.1(c). In §5.5.3 we examine the model's sensitivity to the value of κ.

To solve the isopycnal evolution equation (5.7) we separate η and τ into time-mean components $\overline{\eta}$ and $\overline{\tau}$, and time-dependent components η' and τ', *i.e.*, $\eta = \overline{\eta} + \eta'$ and $\tau = \overline{\tau} + \tau'$. Taking the time average of (5.7) yields

$$\frac{1}{r}\frac{\partial}{\partial r} r \left(\frac{\overline{\tau}}{\rho_0 f_0} + \kappa \frac{\partial \overline{\eta}}{\partial r} \right) = 0, \tag{5.10}$$

where $\overline{\tau} = \overline{\tau}^0 r/R$ from (5.2a). This equation defines the time-mean isopycnal position up to a constant, which we choose to be the the basin-averaged isopycnal depth $\eta_0 = 2\int_0^R \eta r dr/R^2$. Solving (5.10) we obtain the time-mean isopycnal profile,

$$\overline{\eta}(r) = \eta_0 + \frac{\overline{\tau}^0}{4\rho_0 f_0 \kappa R}\left(R^2 - 2r^2\right). \tag{5.11}$$

The change in isopycnal height $\Delta\overline{\eta} = \overline{\eta}(r=0) - \overline{\eta}(r=R) = \overline{\tau}^0 R/(2\rho_0 f_0 \kappa)$, depends on the amplitude of the mean wind stress component $\overline{\tau}^0$ and the eddy diffusivity κ. Physically, the time-mean isopycnal shape ensures that the time-mean wind-driven and eddy vertical velocities exactly cancel. For $\rho_0 = 1000\,\mathrm{kg\,m^{-3}}$ and $f_0 = -10^{-4}\,\mathrm{s^{-1}}$ we obtain $\Delta\overline{\eta} = 860\,\mathrm{m}$, which is consistent with the observed range of $\sim 800\,\mathrm{m}$ shown in Figure 5.1(c). The analytical profile (5.11) for $\overline{\eta}$ is shown in Figure 5.5(a) and agrees almost exactly with the numerical solution in a curved basin (see §5.5.2). The isopycnal tilt $\partial\overline{\eta}/\partial r$ is enhanced close to the gyre boundary, consistent with Figure 5.1(c).

Subtracting the evolution equation (5.7) from its time mean (5.10) yields an equation for the time-dependent component of η,

$$\frac{\partial \eta'}{\partial t} = \frac{1}{r}\frac{\partial}{\partial r} r\left(\frac{\tau'}{\rho_0 f_0} + \kappa\frac{\partial \eta'}{\partial r}\right). \tag{5.12}$$

From (5.2a) the time-dependent wind stress component is $\tau' = \mathrm{Re}\left\{-ie^{i(\omega t + 5\pi/3)}\tau_{12}(r)\right\}$, so we seek a solution of the form $\eta' = \mathrm{Re}\left\{-ie^{i(\omega t + 5\pi/3)}\hat{\eta}(r)\right\}$. Then (5.12) reduces to

an ordinary differential equation for the radial structure function $\hat{\eta}$,

$$\frac{d^2\hat{\eta}}{dr^2} + \frac{1}{r}\frac{d\hat{\eta}}{dr} - \frac{i\omega}{\kappa}\hat{\eta} = -\frac{2\tau_{12}^0}{\rho_0 f_0 \kappa R}, \tag{5.13}$$

while the boundary condition (5.8b) becomes

$$\left.\frac{\partial\hat{\eta}}{\partial r}\right|_{r=R} = -\frac{\tau_{12}^0}{\rho_0 f_0 \kappa}. \tag{5.14}$$

Note that the RHS of (5.13) is a constant. The solution to (5.13) is

$$\hat{\eta}(r) = (1+i)\frac{\tau_{12}^0}{\rho_0 f_0\sqrt{2\omega\kappa}}\frac{J_0\left(\sqrt{\frac{\omega}{2\kappa}}(1-i)r\right)}{J_1\left(\sqrt{\frac{\omega}{2\kappa}}(1-i)R\right)} - i\frac{2\tau_{12}^0}{\rho_0 f_0 \omega R}, \tag{5.15}$$

where J_0 and J_1 are the Bessel functions of the zeroth and first kinds respectively.

Equation (5.15) tells us that the isopycnal oscillates annually about its time-mean position $\overline{\eta}$ with radially-varying amplitude and phase. In Figures 5.5(b) and 5.5(c) we plot the oscillation amplitude and phase lag of $\eta'(r,t)$, where the phase lag is defined as the number of months by which the isopycnal height maximum lags the wind stress maximum at each point. The analytical result compares well with our numerical solution, which uses the curved bathymetry shown in panel (a).

Figure 5.5 shows that the character of the isopycnal oscillation undergoes a pronounced change close to the gyre boundary. This is due to the formation of a boundary layer close to $r = R$, in which mesoscale eddy diffusion dominates the evolution of η. The timescale associated with eddy diffusion may be estimated from (5.12) as

$T_{\text{eddy}} = R^2/\kappa \sim 50\,\text{yr}$, much longer than the 1 yr timescale of the wind stress variations. Using $\epsilon^{-1} = \omega R^2/\kappa \gg 1$ as an asymptotically large parameter, it follows from the large argument asymptotic form of the Bessel function (Abramowitz and Stegun, 1972) that as $\epsilon \to 0$,

$$\eta' \sim -\frac{2\tau^0_{12}}{\rho_0 f_0 \omega R} \cos\left(\omega t + \frac{5\pi}{3}\right), \quad r/R = \mathcal{O}(1), \tag{5.16a}$$

$$\eta' \sim \frac{\tau^0_{12}}{\rho_0 f_0 \sqrt{\omega\kappa}} \sin\left(\omega t - \frac{\pi}{12}\right), \quad r/R = 1 - \mathcal{O}(\epsilon^{1/2}). \tag{5.16b}$$

Thus in the gyre interior ($r/R = \mathcal{O}(1)$), the evolution of η' in (5.12) is dominated by the wind-driven vertical velocity. This results in a small oscillation with amplitude $2\tau^0_{12}/(\rho_0 f_0 \omega R) \approx 4.3\,\text{m}$. The isopycnal oscillation lags the wind stress maximum, or equivalently the wind-driven vertical velocity maximum, by 3 months, achieving its maximum in September each year (Figure 5.5c).

Close to the gyre edge a boundary layer forms in which eddies dominate the isopycnal oscillation ($r/R = 1 - \mathcal{O}(\epsilon^{1/2})$). The width of this layer may be estimated as $L_{\text{eddy}} = \epsilon^{1/2} R \sim 40\,\text{km}$. The amplitude of the oscillation in the boundary layer is an order of magnitude greater than in the interior, reaching $\tau^0_{12}/(\rho_0 f_0 \sqrt{\omega\kappa}) \approx 37.5\,\text{m}$ at the edge of the gyre. This scaling shows that the oscillation amplitude is sensitive to both the wind stress τ^0_{12} and the eddy diffusivity κ. We examine the sensitivity of the model to these parameters in §5.5.3. At the gyre boundary the isopycnal height maximum (minimum) lags the wind stress maximum by eleven (five) months. This phase corresponds closely to observations of WSDW at the Orkney Passage, and is

discussed further in §5.7.1.

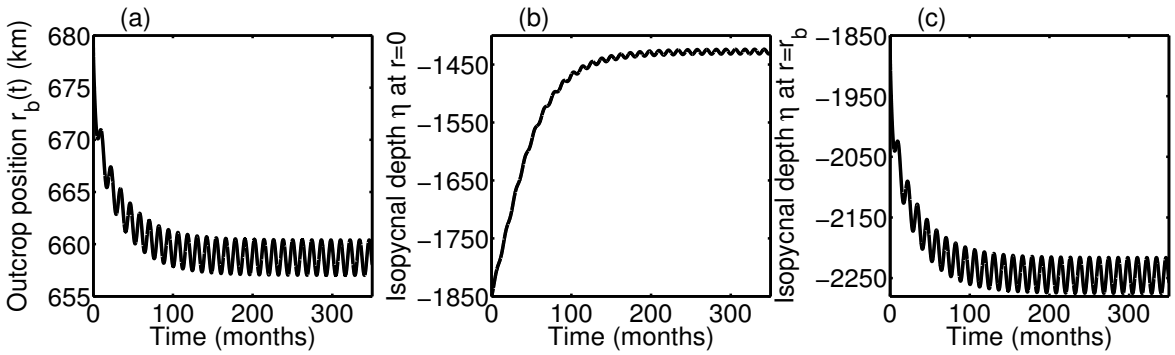

Figure 5.6: Evolution of the reference solution ($\tau^0_{12} = 0.026\,\mathrm{Nm}^{-2}$, $\kappa = 300\,\mathrm{m}^2/\mathrm{s}$), obtained numerically as discussed in §5.5.2. (a) Outcrop position $r = r_b(t)$ and isopycnal height evolution at (b) the gyre center and (c) at the boundary outcrop.

5.5.2 Numerical solutions in a curved basin

For the curved bathymetry shown in Figure 5.3, or for spatially-varying eddy diffusivity κ, the evolution equation (5.7) is no longer analytically tractable. To study these more complicated cases we solve the model equations (5.7)–(5.8b) numerically. Our numerical scheme is described in Appendix B.

Figure 5.5 compares our numerical and analytical solutions using the same parameters, except our numerical solution uses the idealized bathymetry shown in Figure 5.3. The time-mean isopycnal heights are almost identical, and there is only a slight discrepancy in the amplitude and phase of the oscillation due to the bathymetry. In particular, a boundary layer of the same width develops in both the numerical and analytical solutions, yielding similar predictions for the properties of the isopycnal oscillation at the gyre edge where WSDW escapes via the Orkney Passage.

Figure 5.6 shows plots of the time-evolution of the numerical solution. The initial condition for the isopycnal is $\eta(r, 0) \equiv \eta_0 = \text{constant}$, where η_0 the the basin-averaged

isopycnal height as in §5.5.1. Wind-driven upwelling causes the WSDW isopycnal to dome up (see Figure 5.5(a)), resulting in the outcrop position $r_b(t)$ contracting from 680 km to 658 km. The outcrop then oscillates about this position with an amplitude of around 2 km. This small oscillation amplitude is due to the sharp basin slope $d\eta_b/dr$ at the gyre edge, and justifies our treatment of r_b as a constant in §5.5.1. Figures 5.6(b) and 5.6(c) show the evolution of the isopycnal height at the gyre center $\eta(r = 0, t)$ and at the outcrop $\eta(r = r_b, t)$. They approach a sinusoidal annual oscillation with a amplitudes of around 4 m and 30 m respectively, consistent with our analytical scalings in §5.5.1.

5.5.3 Sensitivity to wind stress and eddy diffusivity

In this section we examine the sensitivity of the analytical and numerical solutions discussed in §5.5.1 and §5.5.2 to the surface wind stress and the eddy diffusivity.

In §5.3.2 the azimuthally-averaged surface wind stress $\tau(r, t)$ was derived from reanalysis data (Large and Yeager, 2009). This product is poorly constrained at high latitudes, so in Figure 5.7(a–c) we plot properties of our model solution for annual wind stress mode amplitudes τ^0_{12} in the range of 0.02–0.05 $\mathrm{N\,m^{-2}}$. Here κ is fixed at $300\,\mathrm{m^2\,s^{-1}}$. Figure 5.7(a, c) shows that τ^0_{12} has no impact on the time-mean isopycnal profile nor the phase of the isopycnal oscillation, while Figure 5.7(b, d) indicates that the amplitude of the oscillation varies linearly with τ^0_{12}. These are both consistent with our analytical scaling in §5.5.1. The isopycnal oscillation amplitude reaches 50 m at the boundary for an annual wind stress mode amplitude of $\tau^0_{12} = 0.05\,\mathrm{Nm^{-2}}$.

Direct observations of eddy diffusivities κ in the Weddell Sea or other Antarctic

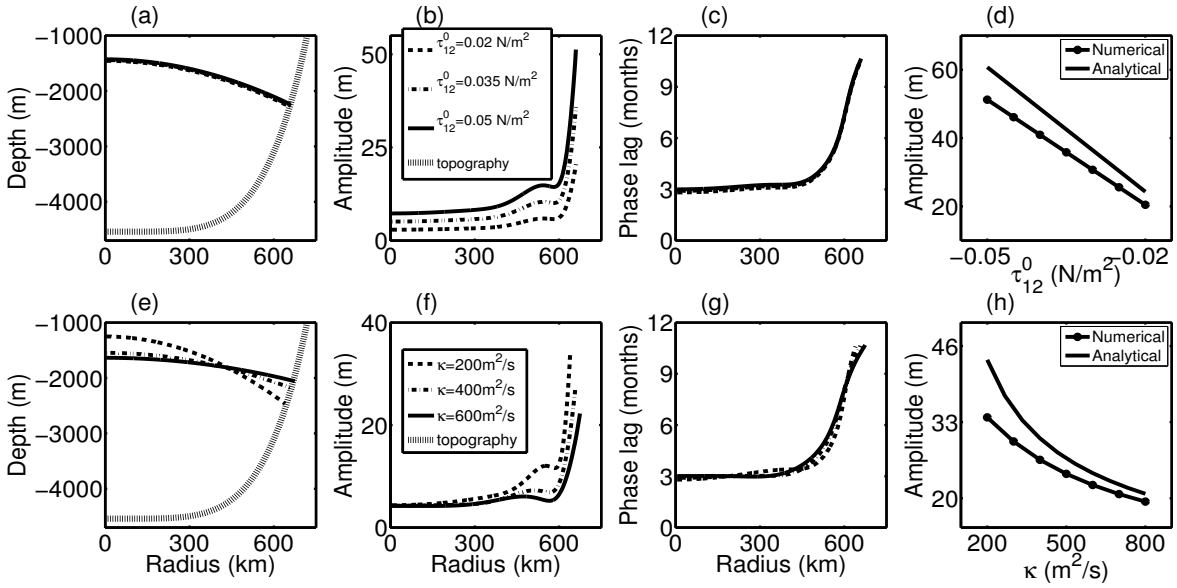

Figure 5.7: (Top row) Sensitivity of our model solution to the wind stress τ^0_{12}, with fixed $\kappa = 300\text{m}^2/\text{s}$. (Bottom row) Sensitivity to the eddy diffusivity κ, with fixed $\tau^0_{12} = 0.026\text{Nm}^{-2}$. (a, e) The time-mean isopycnal height $\overline{\eta}$. (b, f) Amplitude of the isopycnal oscillation $|\eta'|$. (c, g) Phase lag of the isopycnal oscillation η', defined as the time interval from the wind stress maximum to the isopycnal height maximum. (d) Oscillation amplitude at the isopycnal outcrop for a range of wind stress strengths τ^0_{12}. (h) Oscillation amplitude at the isopycnal outcrop for a range of eddy diffusivities κ. Panels (a–c) share the legend in (b) and panels (e–g) share the legend in (f). These solutions were computed numerically as described in §5.5.2.

coastal regions are limited, therefore the eddy diffusivity applied in §5.5.1 and §5.5.2 was selected to ensure that the time-mean isopycnal height profile matched that shown in Figure 5.1(c). As a basic sensitivity study, we assume that κ is homogeneous everywhere. In Figure 5.7(e–g) we plot properties of our model solution for κ in the range 200–600 $\text{m}^2\,\text{s}^{-1}$. This range was chosen so that the change in the time-mean isopycnal height across the basin $\Delta\overline{\eta}$ remains within a few hundred meters of the observed $\Delta\overline{\eta} \sim 800\,\text{m}$. We fix $\tau^0_{12} = 0.026\,\text{N}\,\text{m}^{-2}$ in all cases. Figure 5.7(e) shows that the time-mean isopycnal height $z = \overline{\eta}(r)$ is sensitive to κ, consistent with the analytical prediction that the isopycnal vertical range satisfies $\Delta\overline{\eta} \propto \kappa^{-1}$ from (5.11).

Figure 5.7(f, g) shows that the phase of the oscillation and its amplitude in the gyre interior are relatively insensitive to κ, while Figure 5.7(f, h) shows that the amplitude at the gyre edge can have a significant dependence on κ. This is consistent with our analytical scaling $|\eta'| \sim \kappa^{-1/2}$ for the oscillation amplitude at the gyre edge.

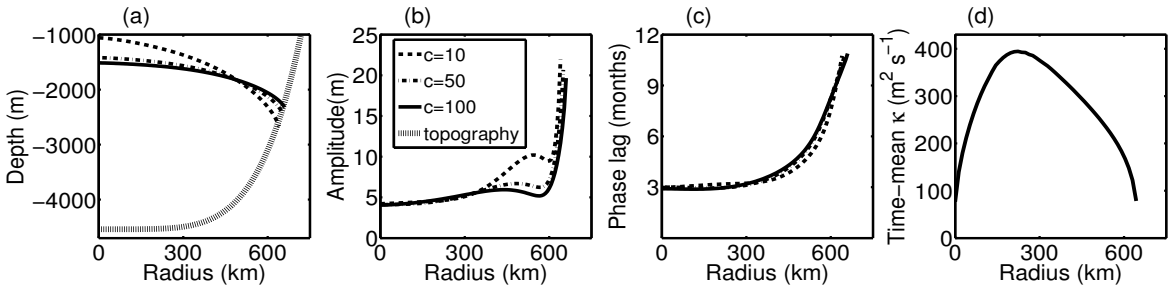

Figure 5.8: (a–c) As Figure 5.5 but for an eddy diffusivity κ constructed via (5.17) from linear 2-layer quasigeostrophic baroclinic instability theory. When the constant c in (5.17) equals to 10, 50 and 100, the corresponding domain-average κ is about 100 m^2/s, 300 m^2/s and 450 m^2/s respectively. (d) The time-mean profile of κ using $c = 50$ as the isopycnal evolves in our model.

5.5.4 Eddy suppression by the bathymetric slope

In general, the oceanic eddy buoyancy diffusivity κ exhibits strong spatial inhomogeneity, both laterally and vertically (Abernathey et al., 2010; Abernathey and Marshall, 2013). In particular, numerical simulations and laboratory experiments show that κ can be reduced by 1–2 orders of magnitude over steep continental slopes (Isachsen, 2011; Pennel et al., 2012; Stewart and Thompson, 2013). Here we attempt to determine the effect that such eddy suppression might have on the annual isopycnal oscillation using a parameterization of κ based on linear 2-layer quasigeostrophic baroclinic instability theory (*e.g.* Mechoso, 1980; Pennel et al., 2012).

From linear 2-layer quasigeostrophic baroclinic instability theory (Stone, 1972; Pedlosky, 1987), we parameterize the eddy diffusivity using the growth rates of the

Phillips problem over a sloping bottom,

$$\kappa = c\,\sigma\lambda^2. \tag{5.17}$$

Here σ is the maximum growth rate of baroclinic instability and λ is the wavelength of the most unstable mode. The parameter c is a dimensionless constant and its value is chosen so that the change in the time-mean isopycnal height across the gyre approximately matches the observed value of $\sim 800\,\mathrm{m}$. In the Phillips problem, the growth rate depends upon the isopycnal slope $s_\rho = d\eta/dr$, the bathymetric slope $s_b = d\eta_b/dr$, the thickness of the overlying CDW layer h_{CDW}, the thickness of the WSDW layer h_{WSDW}, and the reduced gravity g' for the 2-layer system (prescribed as $5 \times 10^{-4}\,\mathrm{m\,s^{-2}}$). This parameterization assumes that eddy mixing of buoyancy responds instantaneously to changes in the isopycnal slope. In reality the instability must grow to the point that baroclinic eddies form and mix along isopycnals.

Using parameterization (5.17) with $c = 50$, Figure 5.8(d) shows the time-mean profile of κ as the isopycnal evolves in our model. Note that κ evolves on seasonal time scales in response to changes in isopycnal slope and layer depths. Close to the isopycnal outcrop ($h_{\mathrm{CDW}}/h_{\mathrm{WSDW}} \ll 1$), the bathymetry is much steeper than the isopycnal slope ($|s_b/s_\rho| \gg 1$) so the eddy diffusivity is suppressed due to weaker baroclinic instability (Isachsen, 2011). Close to the gyre center the isopycnal must flatten by (5.8a), so the eddy diffusivity is also suppressed. Thus κ reaches its maximum at mid-radius. The suppression of κ close to the outcrop requires the isopycnal to steepen locally so that the mean and eddy streamfunctions in (5.5) balance in the

time-mean. This shape more closely resembles the observed isopycnal structure in Figure 5.1(c) than the case with uniform κ.

In Figure 5.8 we plot the properties of the model solution for c in the range 10–100. As in the case of uniform κ, the time-mean isopycnal height is sensitive to c. A weaker eddy diffusivity requires a larger isopycnal slope to produce the downward eddy vertical velocity necessary to balance the time-mean wind-driven upwelling. The oscillation phase is insensitive to c as in the case of uniform κ. Surprisingly, the oscillation amplitude at the isopycnal outcrop (Figure 5.8(b)) is much less sensitive to c than in the uniform-κ case, which seems inconsistent with our analytical scaling in §5.5.1. This is due to the large radial gradient of κ, which enters as a term of the form $(1/r) \cdot \partial\kappa/\partial r \cdot \partial(r\eta)/\partial r$ in (5.7) and is neglected in our analytical solution in §5.5.1. We find the ratio of the diffusive terms in (5.7) is large, *i.e.* $|(\kappa_r \eta'_r)/(\kappa \eta'_{rr})| \gg 1$, close to the gyre boundary.

5.6 The impact of inflow/outflow of WSDW

In this section we address the impact of an inflow/outflow of WSDW on the annual oscillation of the isopycnals in the Weddell Gyre. Our conceptual model is not capable of describing the full three-dimensional process of WSDW formation and export, so here we develop an azimuthally-averaged representation of the inflow to and outflow from the WSDW layer.

5.6.1 Parameterizing inflow/outflow of WSDW

For simplicity we assume that the isopycnal $z = \eta(r, t)$ divides the water masses of the gyre into two homogeneous layers: an upper layer of CDW and a lower layer

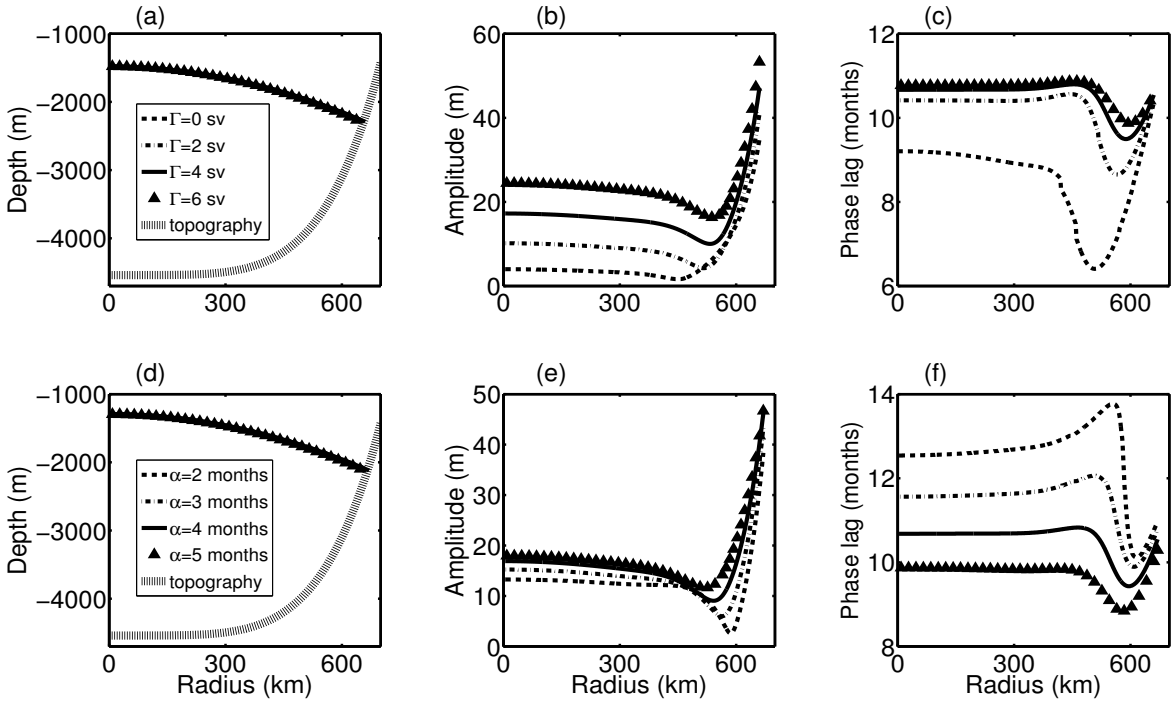

Figure 5.9: Properties of the model solution with inflow and outflow of WSDW, as discussed in §5.6. (a–c) As Figure 5.5 but for a range of inflow transport oscillation amplitudes Γ, with $\alpha = 4$ months. (d–f) As Figure 5.5 but for a range of phase lags α between the wind stress maximum and the inflow transport maximum, with $\Gamma = 4$ Sv. Panels (a–c) share the upper legend, and panels (d–f) share the lower legend.

of WSDW. The primary source of WSDW is a mixture of dense shelf water (glacial meltwater and a high-salinity shelf water caused by sea ice formation) with entrained CDW (Orsi and Wiederwohl, 2009). We parameterize production as a total transport T_i into the WSDW layer. Geostrophic estimates indicate that around 6 Sv of WSDW escapes the Weddell Gyre through Orkney Passage (Naveira Garabato et al., 2002), which is calculated by computing the geostrophic shear and estimating the barotropic component of the flow from the LADCP data. We include in our model only the component of WSDW that escapes via the Orkney Passage, so a typical strength for T_i is 6 Sv. Simulations by Kida (2011) and Wang et al. (2012) show that the WSDW inflow from the Filchner Depression often increases substantially with the

surface wind stress because the inflow is geostrophically controlled. We parameterize the seasonal cycle in the inflow of WSDW as

$$T_i(t) = T_i^0 + \Gamma \sin(\omega(t - \alpha) + 5\pi/3) \tag{5.18}$$

where $T_i^0 = 6\,\mathrm{Sv}$, α is the phase lag from the wind stress maximum, and Γ is the inflow oscillation amplitude. Wang et al. (2012) found a 4-month lag between the wind stress maximum and WSDW inflow maximum, so we use $\alpha = 4\,\mathrm{months}$ as a reference value. There is no available estimate of the amplitude Γ, so we choose $\Gamma = 4\,\mathrm{Sv}$ as a reference value.

The outflow of WSDW depends upon the thickness of the WSDW layer at the gyre edge, where the azimuthal flow encounters the Orkney Passage in the South Scotia Ridge. As illustrated in Figure 5.2 we assume that the WSDW outflows through a cross-sectional area perpendicular to the edge of our circular gyre. The depth of the Orkney Passage is around 3 km, so we assume that WSDW outflows at all radii greater than $r = r_{\mathrm{OP}} = 550\,\mathrm{km}$, where the water column depth is roughly 3 km. The total outflow transport is therefore

$$T_o = \int_{r_{OP}}^{r_b(t)} (\eta - \eta_b)(-v)dr, \tag{5.19}$$

where $v < 0$ represents a cyclonic velocity.

To parameterize the azimuthal velocity v, we assume that the weak stratification in the Weddell Gyre leads to a predominantly barotropic boundary current. This

agrees with Naveira Garabato et al. (2002) and Thompson and Heywood (2008), who observed barotropic currents on the northern and northernwestern side of the Weddell Gyre respectively. Assuming that the strength of this boundary current adjusts instantaneously to the southward Sverdrup transport in the gyre interior, and that its width remains constant, its velocity must be proportional to the wind stress at the gyre edge,

$$v = v^0 \left(1 + \frac{\tau_{12}(R,t)}{\overline{\tau}(R)}\right), \tag{5.20}$$

where the mean boundary current velocity $v^0 = -6\,\mathrm{cm\,s^{-1}}$ has been selected based on observations (Naveira Garabato et al., 2002). This parameterization is discussed in detail in Appendix C. The annual variability of T_o in (5.19) is about 3 Sv, mainly due to variations of the outflow velocity v by around 50% over an annual cycle, whereas the WSDW layer thickness $(\eta - \eta_b)$ varies by roughly 10%.

Finally, the inflow T_i and outflow T_o must be distributed across our idealized Weddell Gyre. Here we consider only the simplest case in which both the inflow and outflow are evenly spread over the area πr_b^2 spanned by the isopycnal $z = \eta(r,t)$. We therefore include them in the isopycnal evolution equation (5.7) as follows,

$$\frac{\partial \eta}{\partial t} = \frac{1}{r}\frac{\partial}{\partial r} r \left[\frac{\tau}{\rho_0 f_0} + \kappa \frac{\partial \eta}{\partial r}\right] + \frac{T_i - T_o}{\pi r_b^2}. \tag{5.21}$$

Thus (5.21), (5.8a) and (5.8b) constitute our residual-mean model for the Weddell Gyre with WSDW inflow/outflow.

5.6.2 Impact of WSDW inflow/outflow on the isopycnal oscillation

We solve the extended isopycnal evolution equation (5.21) numerically using a straightforward extension of the numerical scheme described in Appendix B. In Figure 5.9 we plot the time-mean isopycnal profile, oscillation amplitude, and phase lag for a range of Γ and α. Figure 5.9(a–c) shows the sensitivity of η to Γ with $\alpha = 4$ months, while panels (d–f) show the sensitivity of η to α with $\Gamma = 4$ Sv.

The case $\Gamma = 0$ Sv in Figure 5.9(a–c) corresponds to a constant inflow of $T_i = 6$ Sv, so the WSDW inflow does not affect the phase and amplitude of the oscillation in this case. The azimuthal velocity v is proportional to the wind stress maximum, by (5.20), so in the gyre interior the isopycnal displacements caused by the WSDW outflow and the wind-induced vertical velocities are always opposed to one another. The oscillation induced by the outflow has an amplitude of 7.3 m as compared to a 4.3 m oscillation caused by the wind stress. As a result, the phase lag of the isopycnal oscillation is approximately 9 months in the gyre interior, whereas it was 3 months in the absence of a WSDW inflow/outflow. In contrast, the addition of WSDW inflow/outflow does not modify the phase lag in the gyre's boundary layer, but does increase its amplitude by about 5 m.

Figure 5.9 shows that the time-mean isopycnal profile does not depend on Γ and α since $\overline{(T_i - T_o(t))} = 0$. Both Γ and α can significantly influence the isopycnal oscillation in the gyre interior, where their variability can modify the oscillation amplitude by 10–20 m and the oscillation phase by 2–3 months. At the gyre boundary Γ and α have little impact on the phase of isopycnal oscillation but they contribute to the am-

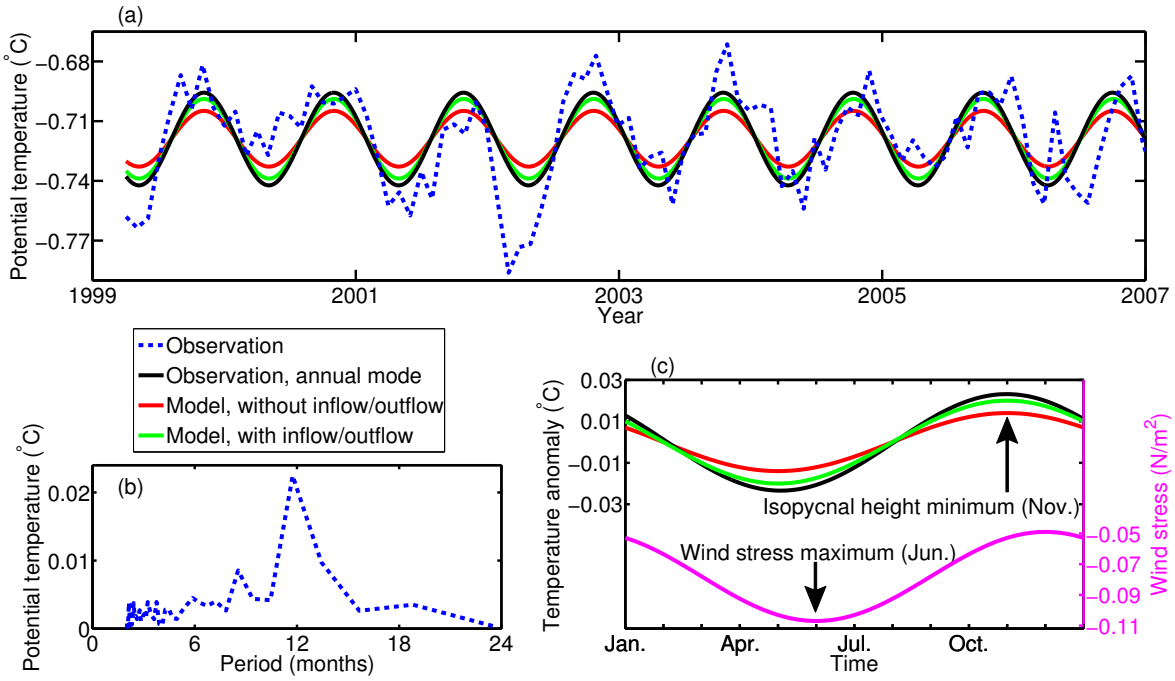

Figure 5.10: (a) Eight-year time series of potential temperature (°C) of WSDW observed by sensor M_3 moored in the northern boundary of the Weddell Sea (to the southeast of the South Orkney Islands) at $\sim$ 4100 m depth (Gordon et al., 2010). The blue dashed curve is the 30-day running mean and the black solid curve is the annual mode. The red and green solid curves are derived from our model results with isopycnal oscillation amplitudes of 35m and 50m respectively at the gyre edge. The red solid curve corresponds to the case without inflow/outflow of WSDW with $\kappa = 300\,\mathrm{m^2\,s^{-1}}$ and $\tau_{12}^0 = -0.035\,\mathrm{N\,m^{-2}}$, as discussed in §5.5.3. The green solid curve includes a time-dependent inflow of WSDW with $\alpha = 4$ months and $\Gamma = 6$ Sv, as discussed in §5.6.2. (b) The amplitude of Fourier mode of observed potential temperature from (a) as a function of oscillation period. (c) Observed and modeled temperature oscillation, as in panel (a), plotted alongside the azimuthally-averaged tangential wind stress at the shelf break, given by equation (2).

plitude by 5–15 m. In the reference case, $\Gamma = 6$ Sv and $\alpha = 4$ months, the amplitude increases from 35 m to 50 m.

5.7 Discussion

5.7.1 Comparison with data

Though the model presented here is idealized, it is instructive to compare its predictions with the observed variability of WSDW in the boundary current upstream of the outflow from the Weddell Sea. At the boundary, isopycnals may experience a vertical isopycnal displacement on the order of 100 m due to annual variability in the wind stress. We note here that vertical displacements on this scale may easily occur on much shorter time scales through tidal or internal wave fluctuations. The emphasis here is on the long-term shifts in the isopycnal depths. Mooring data provides the most reliable means to assess these annual changes in isopycnal depth.

An important contribution to our understanding of these fluctuations comes from the moored data collected in the northern boundary of the Weddell Sea (to the southeast of the South Orkney Islands) by Gordon et al. (2010). Figure 5.10(a) shows an eight-year time series of the potential temperature of WSDW at 4100 m obtained at mooring M3. A 30-day running mean (blue dashed) and the annual mode (black solid) are shown. WSDW data at shallower depths is either unavailable or modified by mixing with Warm Deep Water (Gordon et al., 2010). However, our scaling in §5.5.1 indicates that the WSDW isopycnal oscillation at 4100 m should be similar to the WSDW isopcynal oscillation at ~ 2000 m. The data from 4100 m therefore serves as an approximate test of our model's predictions.

The WSDW signal is dominated by the seasonal cycle (shown in Figure 5.10(b)), which accounts for $\sim 80\%$ of the total variability. Importantly, the annual cycle of

potential temperature reaches its warmest values around November with a temperature change of about 0.047°C across one cycle. Our idealized model predicts that the boundary separating WSDW from CDW should be at its deepest, and so the water at 4100 m should be at its warmest, around November each year (see Figure 5.5(c)). Our model closely captures the phase lag between annual wind stress variations and changes in WSDW properties at the boundary. Note that the phase of the oscillation at the gyre edge is a robust feature, being essentially independent of all model parameters.

Our model predicts that the temperature maximum close to the gyre boundary, where the moorings of Gordon et al. (2010) were situated, lags the wind stress maximum by 5 months. Yet Jullion et al. (2010) found a 5-month lag between the wind stress maximum and the WSDW temperature maximum in the Scotia Sea, which is 2–4 months transit time from the Weddell Gyre (Meredith et al., 2011). A plausible explanation takes into account that the phase varies rapidly across the gyre boundary layer. Thus a mean phase lag across the boundary is closer to 3 or 4 months rather than the 5 month lag predicted at the gyre edge. Given that enhanced diapycnal mixing in the deep Scotia Sea will tend to smear any gradients of WSDW properties (Naveira Garabato et al., 2004), we estimate that the WSDW temperature maximum in the Scotia Sea should lag the wind stress maximum by 3 months plus the transit time through the Orkney Passage. This yields an estimate of 5–7 months lag between the wind stress maximum and the WSDW temperature maximum in the Scotia Sea, which is broadly consistent with the findings of Jullion et al. (2010).

Using typical parameters our model predicts that the WSDW isopycnal should undergo a total vertical displacement of around $\sim$ 70–100 m, as discussed in §5.5 and §5.6. For a typical temperature profile for the northern Weddell Gyre (*e.g.* see Figure 1 of Gordon et al., 2010) this corresponds to a temperature change of 0.028–0.04°C in the depth range 2–4 km spanning the core of WSDW (Gordon et al., 2001). Based on this estimate, the model explains 60%–85% of the amplitude in the moored data, shown in Figures 5.10(a) and 5.10(c). Within realistic parameter ranges, *e.g.* an eddy diffusivity of $200\,\mathrm{m^2\,s^{-1}}$, a wind stress of $\tau^0_{12} = 0.04\,\mathrm{N\,m^{-2}}$ and a time-dependent inflow/outflow with $\Gamma = 4\,\mathrm{Sv}$, $\alpha = 4$ months, the outcrop isopycnal displacement can reach ~ 130 m.

Our model only accounts for the mean and annual modes of the wind variability. However, Figure 5.4(d) shows that the semiannual mode may also make a significant contribution. Extending our analysis in §5.3.2, the semiannual mode of the wind stress can be approximated as $\tau^0_6(r/R) \cdot \sin(\omega_6 t + 11\pi/6)$, where $\tau^0_6 = -0.011\,\mathrm{N\,m^{-2}}$ and $\omega_6 = 4\pi\,\mathrm{yr^{-1}}$. If this mode is included in (5.2a), the isopycnal oscillation amplitude at the boundary increases by 10%–20%, and its phase changes by roughly 10 days.

5.7.2 Model limitations

A number of important processes receive limited or no treatment in our current model. First, we assume that surface forcing comes from wind stress alone. In reality, buoyancy forcing, due to growth and melt of sea ice and air-sea fluxes, also plays a critical role in driving seasonal fluctuations of the Weddell Gyre's stratification. This aspect merits further study. Our goal of developing a conceptual model of

the Weddell Gyre led us to generate azimuthal averages of both wind stress and gyre bathymetry, whereas it is known that local bathymetric features can influence transport through modification of the boundary currents and cross-slope transport. The boundary geometry can also influence eddy diffusivities. These dynamics are only explored briefly in the current study, but in general are not well understood and are a topic of active research (Pennel et al., 2012; Stewart and Thompson, 2013). Using observed wind data rather than reanalysis wind data might also improve the model, although at this level of idealization it would be unlikely to produce qualitatively different results.

The reanalysis surface winds from Large and Yeager (2009) do not account for modifications in momentum transport between atmosphere and ocean related to sea ice. Fujisaki et al. (2010) shows that the inclusion of sea ice always leads to an increase in stress at the ocean surface, within a range of 0–50%. This is true even if the sea ice concentration is 100% (see their Figure 11b). Thus our study may underestimate the wind stress magnitude in the Weddell Sea. Peaks in surface wind stress and Antarctic sea ice extent are offset by roughly three months (Polvani and Smith, 2013) (maxima in June and September, respectively). Furthermore, sea ice coverage of the Weddell Gyre varies between roughly 50% and 100% in summer and winter, respectively (Parkinson and Cavalieri, 2012). An extreme scenario would assume that sea ice always increases the effective wind stress by 50%, leading to a gyre-averaged increase in wind stress of $\sim$25% in summer and $\sim$50% in winter. This modification enhances the wind stress annual mode amplitude by around 40%

and shifts the wind stress peak by around two weeks. This is consistent with the upper end of the range of wind stress magnitudes examined in our sensitivity study in §5.5. While the coupling with sea ice is likely necessary for predicting the timing and properties of exported water masses, these changes do not fundamentally affect the dynamics discussed in this study.

In this study we have specifically focused on seasonal variability. While our model dynamics would predict a long-term warming of exported Weddell waters in response to steadily increasing wind stress curl, we are cautious about extrapolating these results to decadal trends due to our poor understanding of mesoscale variability in these regions. It is conceivable that long-term trends in wind forcing may be compensated by enhanced eddy diffusivities as lateral gradients in the stratification adjust, as has been argued to occur in the ACC (Munday et al., 2013). A fixed eddy diffusivity is a poor representation of these dynamics. Furthermore, at longer time scales, baroclinic adjustment through Rossby waves (Anderson and Gill, 1975), which are not included in this analysis, may become important. We suggest that longer term variability should be investigated using an eddy-resolving model.

In §5.6, the inflow/outflow of WSDW are assumed homogeneous in the whole domain. In reality the effect of this inflow/outflow should be most pronounced close to the gyre boundary. We tested an alternative parameterization in which the inflow and outflow were localized to the radii spanned by the Orkney Passage, but found that it increased the oscillation amplitude at gyre boundary by at most $\sim 10\,\mathrm{m}$.

Accounting for diapycnal mixing may be expected to modify the isopycnal evo-

lution equation (5.7), breaking mass conservation (5.9) in the WSDW layer. The dynamical significance of the diapycnal mixing term $(\kappa_v \langle b \rangle_z)_z$ in (5.3) may be estimated by comparing it to advection by the mean streamfunction $J(\langle\psi\rangle, \langle b \rangle)$.

$$J(\psi^\dagger, \langle b \rangle) = (\kappa_v \langle b \rangle_z)_z \,. \tag{5.22}$$

For typical scales $z \sim 1000\,\mathrm{m}$, $r \sim 680\,\mathrm{km}$, $\tau \sim 0.03\,\mathrm{N\,m^{-2}}$, $f_0 \sim 10^{-4}\,\mathrm{s^{-1}}$, $\rho_0 \sim 1000\,\mathrm{kg\,m^{-3}}$, and $\kappa_v \sim 10^{-5}\,\mathrm{m^2\,s^{-1}}$ (Ledwell et al., 1993), we find that the ratio of diapycnal mixing to mean advection terms is around 0.02. Thus we expect the evolution of the isopycnal $z = \eta(r,t)$ to be dominated by advection by the mean and eddy streamfunctions. If diapycnal mixing is enhanced $\kappa_z \sim 10^{-4}\,\mathrm{m^2\,s^{-1}}$ then the ratio may be as large as 0.2. However, close to the gyre edge the eddy advection term dominates the evolution of η, and is an order of magnitude larger than mean advection, so we expect diapycnal mixing to have minimal impact on our results.

5.7.3 Model implications

Our model indicates that an interplay between the wind stress and the mesoscale eddy fields may influence properties of exported WSDW. From a dynamical standpoint, this model has a number of similarities to recent work carried out in an Arctic context arguing for the importance of variability in boundary currents on the larger-scale circulation (Spall, 2004). Our results remain consistent with a gyre interior that is governed by Sverdrup dynamics (Gordon et al., 1981). The novel aspect of this study points to the key adjustment to wind stress variability permitted by a

energetic mesoscale eddy field at the gyre boundary. Representation of these wind and eddy contributions through RMT results in a better agreement with observed isopycnal variability than could be achieved through classic adjustment via Rossby waves (Anderson and Gill, 1975).

The mechanism via which the WSDW isopycnal achieves relatively large vertical displacements at the gyre boundary is somewhat counter-intuitive, and warrants further explanation. The annual component of the wind stress oscillates with almost uniform phase across the gyre, inducing either uniform upwelling or uniform downwelling depending on the season. From (5.6) we estimate that the time scale for the eddy response to this forcing over the radius of the gyre is $R^2/\kappa \sim 50\,\mathrm{yr}$ for $\kappa = 300\,\mathrm{m^2\,s^{-1}}$, much longer than the one-year time scale of the wind variations. We therefore expect the isopycnal oscillation to be dominated by the uniform wind-driven upwelling/downwelling. However, uniform upwelling or downwelling is prohibited by mass conservation (5.9), so a narrow gyre-edge boundary layer forms with an isopycnal oscillation opposing that in the gyre interior. The width of this boundary layer may again be estimated from (5.6) as $W_{bl} = \sqrt{\kappa/\omega} \sim 40\,\mathrm{km}$.

As detailed in §5.5.1, the annual component of the wind-driven vertical velocity is uniform and has a maximum amplitude of $|w'_{\mathrm{wind}}| = 2\tau^0_{12}/(\rho_0 f_0 R)$. Thus the maximum wind-driven displacement of the isopycnal should scale as $\eta'_{\mathrm{wind}} \sim 2\tau^0_{12}/(\rho_0 f_0 R\omega)$, which agrees with the analytical solution in the gyre interior (5.16a). It follows that the maximum wind-driven increase in mass beneath the isopycnal scales as $\Delta M_{\mathrm{wind}} \sim \pi R^2 \cdot \tau^0_{12}/\rho_0 f_0 R\omega$. To conserve mass, there must be an opposing eddy-driven displace-

ment of the isopycnal $\Delta M_{\text{eddy}} = -\Delta M_{\text{wind}}$ in the boundary layer, which occupies a surface area of approximately $A_{bl} = 2\pi R W_{bl}$. Thus the eddy-driven boundary layer isopycnal displacement should scale as $\eta'_{\text{eddy}} \sim -\Delta M_{\text{wind}}/A_{bl} \sim -\tau^0_{12}/(\rho_0 f_0 \sqrt{\omega\kappa})$, which agrees with our analytical solution for the boundary layer (5.16b). Due to the narrow boundary layer width W_{bl}, the amplitude of the boundary layer oscillation is an order of magnitude greater than in the interior, $|\eta'_{\text{eddy}}/\eta'_{\text{wind}}| \sim 2R\sqrt{\omega/\kappa} \approx 10$. This mechanism is illustrated in Figure 5.11.

Our model shows that the representation of mesoscale eddy dynamics at the gyre boundary can significantly impact the prediction of WSDW export. Eddy variability over sloping topography remains poorly understood (Stewart and Thompson, 2013). Interactions with local bathymetric features, such as the Orkney Plateau, add further complications (Nøst et al., 2011). Resolving this variability in both models and observations is critical to arrive at a clearer description of Weddell Gyre dynamics and its contribution to the global MOC.

5.8 Conclusion

This study takes an idealized approach to the dynamics of the Weddell Gyre, motivated by recent evidence that mesoscale variability plays a key role in setting gyre properties and even global circulation properties. The key results are:

1. Using residual-mean theory we develop an azimuthally-averaged model of an idealized Weddell Gyre. Our model accounts for changes in the shape of the isopycnal separating WSDW from CDW due to surface wind stress, eddy buoyancy fluxes, WSDW inflow from the Antarctic shelves, and WSDW outflow to

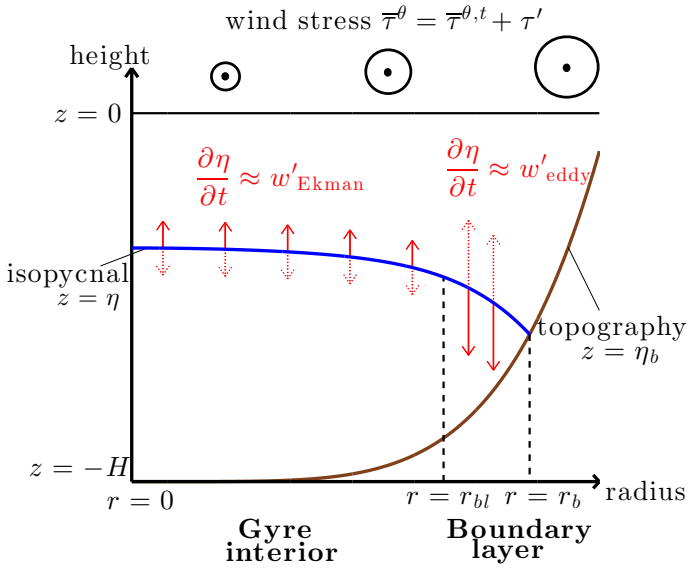

Figure 5.11: Schematic of large-amplitude isopycnal oscillations generated at the gyre boundary. In the gyre interior, the isopycnal upwelling (downwelling) is controlled by Ekman pumping/suction driven by a uniform surface wind curl. To conserve the mass of the WSDW layer mesoscale eddies act to downwell (upwell) the isopycnal in a narrow boundary layer. The boundary layer occupies a much smaller area of the isopycnal surface, so the amplitude of the oscillations is much larger than in the gyre interior. The boundary layer width is set by the strength of the mesoscale eddies and the frequency of the wind stress variability, which is predominantly annual.

the Scotia Sea.

2. The azimuthally-averaged wind stress curl is approximately uniform and oscillates almost in phase, leading to a spatially-uniform annual cycle of upwelling/downwelling driven by Ekman pumping. Mass conservation beneath the WSDW isopycnal requires that this oscillation be compensated by eddy-driven downwelling/upwelling in a narrow boundary layer, resulting in much larger isopycnal excursions close to the gyre edge.

3. Our model robustly predicts a phase lag of 5 months between the wind stress maximum and the density minimum at the gyre edge, which agrees closely with

observations in the northern Weddell Sea (Gordon et al., 2010). For typical parameters the model's isopycnal oscillation explains at least 50% of the amplitude of the observed temperature variations. This phase lag may be sensitive to modifications in surface momentum fluxes due to seasonal sea ice coverage.

5.9 Appendix A: The isopycnal evolution equation

Here we derive an evolution equation for the azimuthally-averaged isopycnal height $z = \eta(r,t)$ from the adiabatic residual-mean equations in a cylindrical basin. We start by noting that the residual velocity field is non-divergent by (5.4),

$$\nabla \cdot \mathbf{u}^\dagger = \frac{1}{r}\frac{\partial\, r u^\dagger}{\partial r} + \frac{\partial w^\dagger}{\partial z} = 0. \tag{5.23}$$

Integrating (5.23) from the ocean bed $z = \eta_b(r)$ to the WSDW isopycnal $z = \eta(r,t)$ and applying Leibniz's rule, we obtain

$$\frac{1}{r}\frac{\partial}{\partial r}\left[r\int_{\eta_b(r)}^{\eta(r,t)} u^\dagger dz\right] - \frac{1}{r}\frac{\partial \eta}{\partial r}\left[r u^\dagger\right]_{z=\eta(r)} + \frac{1}{r}\frac{\mathrm{d}\eta_b}{\mathrm{d}r}\left[r u^\dagger\right]_{z=\eta_b(r)} + \left[w^\dagger\right]_{\eta_b(r)}^{\eta(r,t)} = 0. \tag{5.24}$$

Equation (5.3) states that the azimuthally-averaged buoyancy is materially conserved following the residual velocity, so fluid parcels located on the WSDW isopycnal $z = \eta(r,t)$ will always remain on that isopycnal, *i.e.*

$$\frac{D^\dagger}{Dt}(z - \eta) = 0 \quad \text{at } z = \eta(r,t), \tag{5.25}$$

where $D^\dagger/Dt = \partial/\partial t + \mathbf{u}^\dagger \cdot \nabla$ is the residual-mean material derivative. As $w^\dagger = D^\dagger z/Dt$, (5.25) can be rewritten as

$$w^\dagger\big|_{z=\eta} = \frac{\partial \eta}{\partial t} + u^\dagger\big|_{z=\eta} \frac{\partial \eta}{\partial r}. \tag{5.26}$$

We also require that there be no flow normal to the ocean bed,

$$\psi^\dagger = 0, \quad \text{or} \quad \mathbf{u}^\dagger \cdot \nabla(z - \eta_b) = 0 \quad \text{at } z = \eta_b(r). \tag{5.27}$$

Using (5.26) and (5.27) to evaluate the rightmost term on the left-hand side of (5.24), we obtain

$$\frac{\partial \eta}{\partial t} = -\frac{1}{r}\frac{\partial}{\partial r}\left[r \int_{\eta_b(r)}^{\eta(r,t)} u^\dagger \, dz \right]. \tag{5.28}$$

Finally, we use the definition $u^\dagger = -\partial\psi^\dagger/\partial z$ from (5.4) to evaluate the integral on the right-hand side of (5.28) as

$$\frac{\partial \eta}{\partial t} = \frac{1}{r}\frac{\partial}{\partial r}\left(r\psi^\dagger\big|_{z=\eta(r,t)} \right). \tag{5.29}$$

5.10 Appendix B: Numerical scheme for a curved basin

This Appendix describes the numerical scheme for our residual-mean evolution equation (5.7). This derivation may be extended trivially to include the inflow and outflow of WSDW, as in (5.19). The outcrop position $r = r_b(t)$ changes with time, and must be tracked as part of the solution. To achieve this we perform a coordinate transfor-

mation from r to

$$\chi(r,t) = \frac{R}{r_b(t)} r. \tag{5.30}$$

For convenience we define the thickness of the WSDW layer as $h(\chi(r,t),t) = \eta(\chi(r,t),t) - \eta_b(\chi(r,t))$. In (χ,t) coordinates derivatives with respect to r and t may be evaluated using the chain rule as

$$\left.\frac{\partial h}{\partial r}\right|_t = \frac{R}{r_b}\left.\frac{\partial h}{\partial \chi}\right|_t, \quad \left.\frac{\partial h}{\partial t}\right|_\chi = \frac{\chi}{r_b}\frac{dr_b}{dt}\left.\frac{\partial h}{\partial \chi}\right|_t + \left.\frac{\partial h}{\partial t}\right|_r. \tag{5.31}$$

By substituting (5.31) into (5.7) we obtain an evolution equation for the layer thickness h in (χ,t) coordinates,

$$\left.\frac{\partial h}{\partial t}\right|_\chi = \frac{R}{r_b}\frac{1}{\chi}\frac{\partial}{\partial \chi}\chi\left(\frac{\tau}{\rho_0 f_0} + \frac{R}{r_b}\kappa\frac{\partial \eta}{\partial \chi}\right) + \frac{\chi}{r_b}\frac{dr_b}{dt}\frac{\partial h}{\partial \chi}. \tag{5.32}$$

The first term on the right-hand side of (5.32) is simply the radial divergence of the residual vertical velocity, corresponding to the right-hand side of (5.7). The second term accounts for the fact that changing r_b changes the mapping between r and χ by (5.30), leading to a mass redistribution in (χ,t) space. Note that $h(\chi = R,t) = 0$ by definition, so $\partial h/\partial t|_{\chi=R} = 0$. Inserting this into (B2) we obtain an evolution equation for r_b in (χ,t) space,

$$\frac{dr_b}{dt} = -\left.\frac{\dfrac{\partial}{\partial \chi}\chi\left(\dfrac{\tau}{\rho_0 f} + \dfrac{R}{r_b}\kappa\dfrac{\partial \eta}{\partial \chi}\right)}{R\dfrac{\partial h}{\partial \chi}}\right|_{\chi=R}. \tag{5.33}$$

Here we have replaced χ with R outside of derivatives with respect to χ.

We solve numerically using regular array of points $\{\chi_i \,|\, i = 0, \ldots, N\}$ with $\chi_0 = 0$ and $\chi_N = R$. Equation (5.32) provides an evolution equation for the layer thicknesses $\{h_i \,|\, i = 0, \ldots, N-1\}$ and (5.33) allows us to evolve the outcrop position r_b. We discretize all derivatives using second-order centered finite differences. The boundary conditions (5.8a) and (5.8b) are used to set ghost points χ_{-1} and χ_{N+1} at each time step, allowing us to evaluate centered finite differences at χ_0 and χ_N. The grid resolution is 1 km and the time step is 960 s, chosen to ensure that the CFL criterion is satisfied. We have verified that the numerical solution convergences under refinement of the numerical grid, and also converges in parallel with a finite-volume scheme for the same equations. We present the results of the finite-difference scheme because it can track the outcrop position $r_b(t)$ with much greater accuracy, while closely conserving mass in the WSDW layer.

5.11 Appendix C: Boundary current parameterization

Beckmann et al. (1999) present model evidence from the BRIOS GCM that the Weddell Gyre transport exhibits a pronounced annual cycle correlated with the local wind stress curl. Here we parameterize the western boundary current using the classic Stommel/Munk model for barotropic wind-driven gyre (Vallis, 2006). We neglect the baroclinic component of the boundary current because the baroclinic adjustment timescale is on the order of years (Anderson and Gill, 1975). We also note that the barotropic component dominates the transport close to the Orkney Passage due to the weak stratification (Naveira Garabato et al., 2002) .

In the gyre interior, the wind stress curl drives a southward Sverdrup flow $\int u^{(y)}\,dz = (\nabla \times \tau \hat{\boldsymbol{e}}_\theta)/(\rho_0 \beta)$, where $u^{(y)}$ is the meridional velocity. In our model this flow is spatially uniform because we impose an azimuthally-symmetric wind stress with uniform curl $\nabla \times \tau \hat{\boldsymbol{e}}_\theta = 2\tau|_{r=R}/R$ from (5.2a)–(5.2b). We represent the outflow of WSDW through the Orkney Passage by calculating the boundary current transport through a radial section $\theta = \theta_{OP}$, $r > r_{OP}$ across our idealized Weddell Gyre (see Figure 5.2). We assume that the azimuthal western boundary current transport balances the total southward Sverdrup transport at the latitude of the Orkney Passage, $T_{Sv} = 4\cos(\theta_{OP})\tau|_{r=R}/\rho_0\beta$.

For simplicity we approximate the boundary current as a spatially-uniform azimuthal velocity at radii greater than $r = r_{bc}$, which is assumed to encompass the Orkney Passage, $r_{bc} < r_{OP}$. The azimuthal mass flux in the boundary current is $T_{bc} = \int_{r_c}^{R} v_{bc}(-\eta_b)dr$, where $v_{bc}, T_{bc} < 0$ describe a cyclonic (northward) transport. Requiring that the Sverdrup and boundary current transports balance, $T_{Sv} = T_{bc}$, we obtain

$$v_{bc} = \frac{4\cos(\theta_{OP})\tau|_{r=R}}{\rho_0 \beta \int_{r_{bc}}^{R}(-\eta_b)dr}. \tag{5.34}$$

The only unknown on the right-hand side of (5.34) is the boundary current extent r_{bc}. However, classic Stommel/Munk theory indicates that the boundary current width should be independent of the wind stress curl (Vallis, 2006). Thus, given r_{bc} equation (5.34) simply relates v_{bc} and $\tau|_{r=R}$ via a constant of proportionality. Rather than try to parameterize θ_{OP} and r_{bc} to match the geometry of the real Weddell

gyre, we instead take a typical boundary current speed for $v_{bc}^0 = -0.06\,\mathrm{m\,s^{-1}}$ from observations (Naveira Garabato et al., 2002), and assume that r_{bc} is sufficiently broad to accommodate the necessary transport T_{bc}. We can therefore simplify (5.34) as

$$v_{bc} = v_{bc}^0 \left(1 + \frac{\tau_{12}|_{r=R}}{\overline{\tau}|_{r=R}}\right). \tag{5.35}$$

Conclusion

1, About Ocean Deep Convection

In the first part of this thesis, we study the ocean deep convection. We reveal that for polar oceans that typically have a quasi-two-layer stratification during the wintertime, thermobaricity and cabbeling are crucial energy sources for powering the deep convection. Our studies provide a big caveat to the physical oceanography community that most people still treat ocean convection as mainly caused by traditional Rayleigh-Taylor instability. Our studies illustrate the following contrasts between the thermobaricity-cabbeling-powered convection and the traditionally-considered convection. (i) The former occurs in a quasi-two-layer ocean as required for the production of OCAPE and the cabbeling acceleration, while the later occurs in a quasi-homogeneous ocean. The effects of OCAPE and cabbeling become stronger for a larger contrast of temperature between the two layers. Most ocean deep convection occurs in wintertime polar oceans, where the stratification is widely observed to be quasi-two-layer (Gordon and Huber, 1995; Schott et al., 1993). The Weddell and Ross seas typically have a larger temperature contrast between the two layers than in the Greenland and Labrador Seas. (ii) Surface buoyancy forcing is important for both cases. However, the latter requires the buoyancy forcing to reduce the stratification

to below zero (i.e., N^2 <0) and become Rayleigh-Taylor unstable. In contrast, the former requires the buoyancy forcing to reduce the stratification to be small enough but still stably stratified (N^2 >0, see chapter 2), and the nonlocal OCAPE release and the cabbeling effects can take control and induce deep convection. (iii) The former occurs by much faster timescales and stronger strength ($\sim$ days, $\sim$ 5-10 cm/s) than the latter oceans ($\sim$ weeks-months, $\sim$ 1-3 cm/s). This is because the former has a much larger threshold of PE than the latter, due to the quasi-two-layer stratification, and hence the former can hold large amounts of OCAPE and releases it abruptly in a strong magnitude.

Our thesis reveals a severe challenge for current climate models to represent the climatic roles of deep convection, as detailed below. Ocean deep convection typically occurs very locally, i.e., with convective plumes of a horizontal scale $\sim$0.1-10 km. Current large-scale ocean models are unable to resolve these convection events. They use some convective mixing scheme (e.g., KPP) to parameterize convection effects. Our thesis shows that these convective schemes can kill real physical signals of the OCAPE-cabbeling-powered convection (Chapter 3). This is because the release of OCAPE requires the nonlocal (0.5-1 km) vertical rearrangement of fluid parcels, while the current convective schemes typically apply strong local diapycnal mixing in the vertical wherever the water column is statically unstable. The convective schemes can also significantly miss the timing of the start of convection event, since they can not represent the cabbeling instability that often triggers the deep convection at 0.01-0.1km lengthscale. Therefore, current ocean GCMs may significantly underestimate

the strength of ocean convection and the consequent deep water formation and vertical heat/salt transports (see Chapter 3). The possible solution of this problem should be improving the convective parameterization in ocean GCMs to account for OCAPE and cabbeling instability, since it is still far away for the GCMs to reach a resolution ($\sim$1-10 m) that resolves deep convection.

But how important is thermobaricity-cabbeling-powered convection in contrast to the traditionally-considered convection? A potential method to estimate this importance is to plot the global map of OCAPE (especially during winter season in each hemisphere) using assimilated data like ECCO2. Our initial steps actually show the presence of a significant 600km-scale OCAPE pattern in the winter Weddell Sea. Our next step is to use a nonhydrostatic plume-resolved 3D model to simulate the possibility that this OCAPE pattern can be triggered to power strong basin-wide deep convection and cause significant impacts (similar to Chapter 3 but using a 3D model). Currently the direct observation for deep convection is rare and difficult (e.g., in winter Weddell Sea), which significantly limits our understanding for these associated processes. It is possible that using seagliders or Argo floats may improve the related observations.

The Weddell Sea is a key region for the production of AABW. Currently there is little observation that provides the estimate of the contribution of open-ocean deep convection in contrast to the processes around the continental margins for the Weddell Sea. Certain climate modeling shows that the contribution of the former is about 20% (K. Snow 2016, personal communication). Our Chapters 2 and 3 demonstrate that

open-ocean deep convection occurring in the Weddell Sea is most likely to be powered by OCAPE and cabbeling instability. Further, as shown above, current climate modeling would most likely largely underestimate the strength of open-ocean deep convection and hence the resulting AABW formation. Therefore, OCAPE-cabbeling-powered deep convection is likely to contribute more than 20% of the AABW formation, which is significantly and should certainly be better represented in climate models.

2, About APE

APE is an important concept because the geostrophic turbulence accounts for more than 80% of the KE in the World Ocean (Ferrari and Wunsch, 2008) and APE is the key local energy source for turbulence through baroclinic instability. However, the traditionally defined Lorenz APE or QG APE shows the large-scale baroclinicity rather than the local baroclinicity. Therefore, they are difficult to directly characterize the EKE. The usual approach for discussing baroclinic instability, and the interaction between eddies, bathymetry and standing meanders includes using PV dynamics, Eady growth rate and the energy fluxes in the Lorenz diagram (Thompson, 2010; Chen et al., 2014). In contrast to energy fluxes, our defined eddy-size-constrained APE density (Chapter 4) is derived from a snapshot of stratification data (rather than a time series of data as required to derive energy flux). It can directly reflect the local baroclinicity at around the eddy scale and it truly represents the maximum magnitude of PE available to be locally converted to EKE through baroclinic instability, although in reality only part of local APE can be converted to EKE in the steady state. Our new

APE concept clearly shows the rich signature of eddies in the stratification through the thermal wind relations, although it can also be induced by the local bathymetry features and the breaking of mean APE into eddy APE via baroclinic instability, etc.

The current satellite observations can only (partly) deliver the information of geostrophic turbulence on the ocean surface, e.g., through the remote sensing of SSH and SST. To deliver the eddy information at ocean depths, it is potentially useful to use the stratification observations from Argo floats to map the global eddy-size-constrained APE density (our Chapter 4 only shows the related map from the simulation data). This will give us the eddies' signature in the stratification.

The energy partitioning of local eddies, i.e., EKE vs our defined eddy-size-constrained APE, can be a useful quantity to investigate the interaction of eddies with local bathymetry and standing meanders. For example, above the ridges or the slope, the local APE (baroclinicity) can be high but the EKE is low due to the suppression of baroclinicity by bathymetry. Essentially, baroclinic instability requires the horizontal shear of PV to change sign vertically, while the EKE and local APE are represented by the relative vorticity and the stretching term in the PV budget, respectively. Quantifying this energy partitioning (EKE vs local APE) as a function of bathymetry and understanding the mechanism behind are important and should be investigated in a future study.

3, About High-latitude Gyre Dynamics

The gyre dynamics, as discussed in Chapter 5, is nonlinearly controlled by local wind and geostrophic turbulence, especially when the effects of local bathymetry

and eddy saturation are involved. The dynamics in reality can be more complicated in the presence of tides-induced diapycnal mixing around the continental shelves (Flexas et al., 2015), which is neglected in our study. These factors together drive the Antarctic Slope Front, the gyre boundary currents, the heat exchange between ocean and the ice shelf (Stewart and Thompson, 2013), and the export of AABW (Su et al., 2014).

High-latitude gyre dynamics may be treated as an isolated system to a certain extent (as in our Chapter 5). However, the gyre can significantly interact with the global MOC (and hence climate) especially through the export/import of water masses (AABW, CDW) and sea ice. Since currently the strongest wind trend occurs on the ACC area, an important question related to climate change is to understand how this local wind trend may nonlocally influence the processes around the Antarctic ice shelves (i.e., heat exchange, AABW production). This should be investigated using a model that resolves the turbulent flows around the ice shelves, which is lacked in most climate models. Understanding the coupling between the ACC and the Weddell gyre dynamics is crucial for the prediction of future Antarctic ice trend.

It is interesting to consider the coupling between ocean convection, gyre dynamics, and the sea-ice. Ocean deep convection can induce heat upwelling and melt sea-ice (i.e., Polynya), while the gyre flow and the wind can circulate the sea-ice. On the other hand, sea-ice can influence the momentum input from wind to the gyre. The sea-ice related brine-rejection could influence the gyre budget of buoyancy. Note that

the resolving of sea-ice in a model is important to accurately represent the surface cooling fluxes (Newsom et al., 2016). Finally, the vertical undulation of isopycnals ($\sim$ hundreds of meters) due to turbulence and wind variability (Chapter 5) may trigger the release of OCAPE and hence deep convection.

The dynamics around the Antarctic continental slope are very important since they dominate the production of AABW and controls the ice budget. However, the dynamics there are special and have been poorly understood. This area typically has a very small deformation radius ($\sim$ 1-5 km) due to the shallowness of ocean above the slope and the weak stratification there. This means that an extremely high resolution model is required to resolve the turbulence there. It often has a strong surface buoyancy forcing (brine rejection, cooling), wind forcing, local mixing (e.g., the production process of AABW), rich bathymetry features, and a small aspect ratio ($\leq 1/100$, due to a large continental slope). It is not clear whether thermobaricity and cabbeling can significantly modulate the production of AABW in the mixing process and modulate the acceleration of AABW flows along the continental slope. It is uncertain whether frontogenesis and the mixed layer instability play a role there in shaping the vertical heat transport. These interesting questions should be investigated in the future.

Bibliography

Abernathey, R. P. and J. Marshall, 2013: Global surface eddy diffusivities derived from satellite altimetry. *J. Geophys. Res.: Oceans*, **118**, 901–916.

Abernathey, R. P., J. Marshall, M. Mazloff, and E. Shuckburgh, 2010: Enhancement of mesoscale eddy stirring at steering levels in the Southern Ocean. *J. Phys. Oceanogr.*, **40 (1)**, 170–184.

Abramowitz, M. and I. A. Stegun, 1972: *Handbook of mathematical functions with formulas, graphs, and mathematical tables*. Dover Publications.

Adkins, J. F., A. P. Ingersoll, and C. Pasquero, 2005: Rapid climate change and conditional instability of the glacial deep ocean from the thermobaric effect and geothermal heating. *Quat. Sci. Rev.*, **24 (5)**, 581–594.

Ahuja, R. K., A. V. Goldberg, J. B. Orlin, and R. E. Tarjan, 1992: Finding minimum-cost flows by double scaling. *Mathematical programming*, **53 (1-3)**, 243–266.

Akitomo, K., 1999a: Open-ocean deep convection due to thermobaricity: 1. Scaling argument. *J. Geophys. Res.: Oceans*, **104 (C3)**, 5225–5234.

Akitomo, K., 1999b: Open-ocean deep convection due to thermobaricity: 2. Numerical experiments. *J. Geophys. Res.: Oceans*, **104 (C3)**, 5235–5249.

Akitomo, K., 2005: Numerical study of baroclinic instability associated with thermobaric deep convection at high latitudes: Idealized cases. *Deep-Sea Res. Oceanogr., A*, **52 (6)**, 937–957.

Akitomo, K., 2006: Thermobaric deep convection, baroclinic instability, and their roles in vertical heat transport around Maud Rise in the Weddell Sea. *J. Geophys. Res.: Oceans*, **111 (C9)**, C09 027.

Akitomo, K., 2007: Restriction of convective depth in the Weddell Sea. *Geophys. Res. Lett.*, **34 (10)**, L10 610.

Akitomo, K., 2011: Two types of thermobaric deep convection possible in the Greenland Sea. *J. Geophys. Res.: Oceans*, **116**, C08 012.

Akitomo, K., T. Awaji, and N. Imasato, 1995a: Open-ocean deep convection in the weddell sea: Two-dimensional numerical experiments with a nonhydrostatic model. *Deep Sea Research Part I: Oceanographic Research Papers*, **42 (1)**, 53–73.

Akitomo, K., K. Tanaka, T. Awaji, and N. Imasato, 1995b: Deep convection in a lake triggered by wind: Two-dimensional numerical experiments with a nonhydrostatic model. *J. Oceanogr.*, **51 (2)**, 171–185.

Alley, R. B., 2007: Wally was right: Predictive ability of the north atlantic conveyor belt hypothesis for abrupt climate change. *Annu. Rev. Earth Planet. Sci.*, **35**, 241–272.

Alvarez-Solas, J., S. Charbit, C. Ritz, D. Paillard, G. Ramstein, and C. Dumas, 2010: Links between ocean temperature and iceberg discharge during heinrich events. *Nature Geoscience*, **3 (2)**, 122–126.

Amante, C. and B. W. Eakins, 2009: *ETOPO1 1 arc-minute global relief model:*

procedures, data sources and analysis. National Geophysical Data Center, Marine Geology and Geophysics Division.

Anderson, D. L. T. and A. E. Gill, 1975: Spin-up of a stratified ocean, with applications to upwelling. *Deep-Sea Res.: Oceanogr. Abstr.*, **22 (9)**, 583–596.

Andrews, D. G., J. R. Holton, and C. B. Leovy, 1987: *Middle atmosphere dynamics*, Vol. 40. Academic Press.

Antonov, J., et al., 2010: World ocean atlas 2009, vol. 2, salinity, edited by s. levitus, 184 pp. *US Gov. Print. Off., Washington, DC*.

Arakawa, A., 1997: Computational design for long-term numerical integration of the equations of fluid motion: two-dimensional incompressible flow. Part I. *J. Comput. Phys.*, **135 (2)**, 103–114.

Arakawa, A. and W. H. Schubert, 1974: Interaction of a cumulus cloud ensemble with the large-scale environment, Part I. *J. Atmos. Sci.*, **31 (3)**, 674–701.

Arbic, B. K., 2000: Generation of mid-ocean eddies: The local baroclinic instability hypothesis. Tech. rep., DTIC Document.

Årthun, M., K. W. Nicholls, and L. Boehme, 2013: Wintertime Water Mass Modification near an Antarctic Ice Front. *J. Phys. Oceanogr.*, **43 (2)**.

Arzel, O., A. Colin de Verdière, and M. H. England, 2010: The role of oceanic heat transport and wind stress forcing in abrupt millennial-scale climate transitions. *Journal of Climate*, **23 (9)**, 2233–2256.

Ashkenazy, Y., M. Losch, H. Gildor, D. Mirzayof, and E. Tziperman, 2013: Multiple sea-ice states and abrupt moc transitions in a general circulation ocean model. *Climate dynamics*, **40 (7-8)**, 1803–1817.

Banderas, R., J. Álvarez-Solas, and M. Montoya, 2012: Role of co2 and southern ocean winds in glacial abrupt climate change.

Beckmann, A., H. H. Hellmer, and R. Timmermann, 1999: A numerical model of the Weddell Sea: Large-scale circulation and water mass distribution. *J. Geophys. Res.: Oceans*, **104**, 23 375–23 391.

Bertsekas, D. P., 1988: The auction algorithm: A distributed relaxation method for the assignment problem. *Ann. Oper. Res.*, **14 (1)**, 105–123.

Bland, R. G. and D. L. Jensen, 1992: On the computational behavior of a polynomial-time network flow algorithm. *Mathematical Programming*, **54 (1-3)**, 1–39.

Brady, E. C. and B. L. Otto-Bliesner, 2011: The role of meltwater-induced subsurface ocean warming in regulating the atlantic meridional overturning in glacial climate simulations. *Climate dynamics*, **37 (7-8)**, 1517–1532.

Broecker, W. S., 1994: Massive iceberg discharges as triggers for global climate change. *Nature*, **372**, 421–424.

Broecker, W. S., G. Bond, M. Klas, G. Bonani, and W. Wolfli, 1990: A salt oscillator in the glacial atlantic? 1. the concept. *Paleoceanography*, **5 (4)**, 469–477.

Broecker, W. S., D. M. Peteet, and D. Rind, 1985: Does the ocean-atmosphere system have more than one stable mode of operation? *Nature*, **315 (6014)**, 21–26.

Bryan, K. and M. D. Cox, 1968: A nonlinear model of an ocean driven by wind and differential heating: Part i. description of the three-dimensional velocity and density fields. *Journal of the Atmospheric Sciences*, **25 (6)**, 945–967.

Buizert, C., et al., 2014: Greenland temperature response to climate forcing during the last deglaciation. *Science*, **345 (6201)**, 1177–1180.

Burkard, R. E., M. Dell'Amico, and S. Martello, 2009: *Assignment Problems, Revised Reprint*. SIAM.

Cai, W., 1996: The stability of nadmf under mixed boundary conditions with an improved diagnosed freshwater flux. *Journal of physical oceanography*, **26 (6)**, 1081–1087.

Carlson, A. E. and P. U. Clark, 2012: Ice sheet sources of sea level rise and freshwater discharge during the last deglaciation. *Reviews of Geophysics*, **50 (4)**.

Carmack, E. C., 1979: Combined influence of inflow and lake temperatures on spring circulation in a riverine lake. *J. Phys. Oceanogr.*, **9 (2)**, 422–434.

Carmack, E. C., W. J. Williams, S. L. Zimmermann, and F. A. McLaughlin, 2012: The Arctic Ocean warms from below. *Geophys. Res. Lett.*, **39 (7)**.

Chapman, C. C., A. M. Hogg, A. E. Kiss, and S. R. Rintoul, 2015: The dynamics of southern ocean storm tracks. *Journal of Physical Oceanography*, **45 (3)**, 884–903.

Chelton, D. B., M. G. Schlax, and R. M. Samelson, 2011: Global observations of nonlinear mesoscale eddies. *Progress in Oceanography*, **91 (2)**, 167–216.

Chen, R., G. R. Flierl, and C. Wunsch, 2014: A description of local and nonlocal eddy–mean flow interaction in a global eddy-permitting state estimate. *Journal of Physical Oceanography*, **44 (9)**, 2336–2352.

Clark, P. U., S. W. Hostetler, N. G. Pisias, A. Schmittner, and K. J. Meissner, 2007: Mechanisms for an 7-kyr climate and sea-level oscillation during marine isotope stage 3. *Ocean Circulation: Mechanisms and Impacts-Past and Future Changes of Meridional Overturning*, 209–246.

Clark, P. U., N. G. Pisias, T. F. Stocker, and A. J. Weaver, 2002: The role of the thermohaline circulation in abrupt climate change. *Nature*, **415 (6874)**, 863–869.

Clarke, R. A. and J. C. Gascard, 1983: The formation of Labrador Sea water. Part I: Large-scale processes. *J. Phys. Oceanogr.*, **13 (10)**, 1764–1778.

Clement, A. C. and M. Cane, 1999: A role for the tropical pacific coupled ocean-atmosphere system on milankovitch and millennial timescales. part i: A modeling study of tropical pacific variability. *Mechanisms of global climate change at millennial time scales*, 363–371.

Collins, W. D., et al., 2006: The community climate system model version 3 (ccsm3). *Journal of Climate*, **19 (11)**, 2122–2143.

De Steur, L., D. M. Holland, R. D. Muench, and M. G. McPhee, 2007: The warm-

water Halo around Maud Rise: Properties, dynamics and impact. *Deep-Sea Res. Oceanogr., A*, **54 (6)**, 871–896.

Deacon, G., 1979: The Weddell Gyre. *Deep-Sea Res. Oceanogr., A*, **26 (9)**, 981–995.

Denbo, D. W. and E. D. Skyllingstad, 1996: An ocean large-eddy simulation model with application to deep convection in the Greenland Sea. *J. Geophys. Res.: Oceans*, **101 (C1)**, 1095–1110.

Derigs, U., 1985: The shortest augmenting path method for solving assignment problems – motivation and computational experience. *Ann. Oper. Res.*, **4 (1)**, 57–102.

Dinniman, M. S., J. M. Klinck, and W. O. Smith Jr, 2011: A model study of Circumpolar Deep Water on the West Antarctic Peninsula and Ross Sea continental shelves. *Deep-Sea Res. II*, **58 (13)**, 1508–1523.

Dokken, T. M. and E. Jansen, 1999: Rapid changes in the mechanism of ocean convection during the last glacial period. *Nature*, **401 (6752)**, 458–461.

Emanuel, K. A., D. N. J., and C. S. Bretherton, 1994: On large-scale circulations in convecting atmospheres. *Quart. J. Roy. Meteor. Soc.*, **120 (519)**, 1111–1143.

Feistel, R., 2003: A new extended Gibbs thermodynamic potential of seawater. *Prog. Oceanogr.*, **58 (1)**, 43–114.

Ferrari, R. and C. Wunsch, 2008: Ocean circulation kinetic energy: Reservoirs, sources, and sinks. *Annual Review of Fluid Mechanics*, **41 (1)**, 253.

Flexas, M. d. M., M. P. Schodlok, L. Padman, D. Menemenlis, and A. H. Orsi, 2015: Role of tides on the formation of the antarctic slope front at the weddell-scotia confluence. *Journal of Geophysical Research: Oceans*, **120 (5)**, 3658–3680.

Fujisaki, A., H. Yamaguchi, and H. Mitsudera, 2010: Numerical experiments of air–ice drag coefficient and its impact on ice–ocean coupled system in the Sea of Okhotsk. *Ocean Dynam.*, **60 (2)**, 377–394.

Ganopolski, A. and S. Rahmstorf, 2001: Rapid changes of glacial climate simulated in a coupled climate model. *Nature*, **409 (6817)**, 153–158.

Ganopolski, A. and S. Rahmstorf, 2002: Abrupt glacial climate changes due to stochastic resonance. *Physical Review Letters*, **88 (3)**, 038 501.

Garwood Jr, R. W., S. M. Isakari, and P. C. Gallacher, 1994: Thermobaric convection. *Geoph. Monog. Series*, **85**, 199–209.

Gent, P. R. and J. C. McWilliams, 1990: Isopycnal mixing in ocean circulation models. *J. Phys. Oceanogr.*, **20 (1)**, 150–155.

Gildor, H., Y. Ashkenazy, E. Tziperman, and I. Lev, 2014: The role of sea ice in the temperature-precipitation feedback of glacial cycles. *Climate dynamics*, **43 (3-4)**, 1001–1010.

Gildor, H. and E. Tziperman, 2003: Sea-ice switches and abrupt climate change. *Philosophical Transactions of the Royal Society of London A: Mathematical, Physical and Engineering Sciences*, **361 (1810)**, 1935–1944.

Gill, A. E., 1982: *Atmosphere-Ocean dynamics*, Vol. 30. Academic press.

Goldberg, A. V., 1997: An efficient implementation of a scaling minimum-cost flow algorithm. *Journal of algorithms*, **22 (1)**, 1–29.

Goldberg, A. V. and R. E. Tarjan, 1989: Finding minimum-cost circulations by canceling negative cycles. *Journal of the ACM (JACM)*, **36 (4)**, 873–886.

Gordon, A. L., 1978: Deep Antarctic Convection West of Maud Rise. *J. Phys. Oceanogr.*, **8 (4)**, 600–612.

Gordon, A. L., 1991: Two stable modes of Southern Ocean winter stratification. *Elsevier Oceanogr. Ser.*, **57**, 17–35.

Gordon, A. L., B. Huber, D. McKee, and M. Visbeck, 2010: A seasonal cycle in the export of bottom water from the Weddell Sea. *Nature Geosci.*, **3 (8)**, 551–556.

Gordon, A. L. and B. A. Huber, 1990: Southern Ocean winter mixed layer. *J. Geophys. Res.: Oceans*, **95 (C7)**, 11 655–11 672.

Gordon, A. L. and B. A. Huber, 1995: Warm Weddell deep water west of Maud Rise. *J. Geophys. Res.: Oceans*, **100 (C7)**, 13 747–13.

Gordon, A. L., D. G. Martinson, and H. W. Taylor, 1981: The wind-driven circulation in the Weddell-Enderby Basin. *Deep-Sea Res. Oceanogr., A*, **28 (2)**, 151–163.

Gordon, A. L., A. H. Orsi, R. Muench, B. A. Huber, E. Zambianchi, and M. Visbeck, 2009: Western Ross Sea continental slope gravity currents. *Deep-Sea Res. Pt. II*, **56 (13)**, 796–817.

Gordon, A. L., M. Visbeck, and B. Huber, 2001: Export of Weddell Sea deep and bottom water. *J. Geophys. Res.: Oceans*, **106 (C5)**, 9005–9017.

Gregory, D., J. J. Morcrette, C. Jakob, A. C. M. Beljaars, and T. Stockdale, 2000: Revision of convection, radiation and cloud schemes in the ecmwf integrated forecasting system. *Quart. J. Roy. Meteor. Soc.*, **126 (566)**, 1685–1710.

Gula, J., M. J. Molemaker, and J. C. McWilliams, 2015: Gulf stream dynamics along the southeastern us seaboard. *Journal of Physical Oceanography*, **45 (3)**, 690–715.

Harcourt, R. R., 2005: Thermobaric cabbeling over Maud Rise: Theory and large eddy simulation. *Prog. Oceanogr.*, **67 (1)**, 186–244.

Harcourt, R. R., E. L. Steffen, R. W. Garwood, and E. A. D'Asaro, 2002: Fully Lagrangian floats in Labrador Sea deep convection: Comparison of numerical and experimental results. *J. Phys. Oceanogr.*, **32 (2)**, 493–510.

He, F., J. D. Shakun, P. U. Clark, A. E. Carlson, Z. Liu, B. L. Otto-Bliesner, and J. E. Kutzbach, 2013: Northern hemisphere forcing of southern hemisphere climate during the last deglaciation. *Nature*, **494 (7435)**, 81–85.

Hemming, S. R., 2004: Heinrich events: Massive late pleistocene detritus layers of the north atlantic and their global climate imprint. *Reviews of Geophysics*, **42 (1)**.

Hieronymus, M., 2014: A note on the influence of spatially varying diffusivities on the evolution of buoyancy with a nonlinear equation of state. *Journal of Physical Oceanography*, **44 (12)**, 3255–3261.

Hieronymus, M. and J. Nycander, 2013a: The budgets of heat and salinity in nemo. *Ocean Modelling*, **67**, 28–38.

Hieronymus, M. and J. Nycander, 2013b: The buoyancy budget with a nonlinear equation of state. *Journal of Physical Oceanography*, **43 (1)**, 176–186.

Hieronymus, M. and J. Nycander, 2015: Finding the minimum potential energy state by adiabatic parcel rearrangements with a nonlinear equation of state: An exact solution in polynomial time. *Journal of Physical Oceanography*, **45 (7)**, 1843–1857.

Hogg, A. M., H. A. Dijkstra, and J. A. Saenz, 2013: The energetics of a collapsing meridional overturning circulation. *Journal of physical oceanography*, **43 (7)**, 1512–1524.

Hoppema, M., E. Fahrbach, G. Rohardt, and A. Wisotzki, 2006: Warm events and ice cover near Maud Rise, Weddell Sea. *Geophys. Res. Abstr.*, **8**, 04 398.

Huang, R. X., 2005: Available potential energy in the world's oceans. *Journal of Marine Research*, **63 (1)**, 141–158.

Huang, R. X., 2014: Energetics of lateral eddy diffusion/advection: Part I. Thermodynamics and energetics of vertical eddy diffusion. *Acta Oceanol. Sin.*, **33 (3)**, 1–18.

Ingersoll, A. P., 2005: Boussinesq and anelastic approximations revisited: Potential energy release during thermobaric instability. *J. Phys. Oceanogr.*, **35 (8)**, 1359–1369.

IOC, SCOR, and IAPSO, 2010: *The International Thermodynamic Equations of Seawater-2010: Calculation and Use of Thermodynamic Properties*. Intergovernmental Oceanographic Commission, Manuals and Guides, UNESCO.

Isachsen, P. E., 2011: Baroclinic instability and eddy tracer transport across sloping bottom topography: How well does a modified Eady model do in primitive equation simulations? *Ocean Modell.*, **39 (1)**, 183–199.

Jackett, D. R., T. J. McDougall, R. Feistel, D. G. Wright, and S. M. Griffies, 2006: Algorithms for Density, Potential Temperature, Conservative Temperature, and the Freezing Temperature of Seawater. *J. Atmos. Oceanic Technol.*, **23 (12)**, 1709–1728.

Jochum, M., P. Malanotte-Rizzoli, and A. Busalacchi, 2004: Tropical instability waves in the atlantic ocean. *Ocean Modelling*, **7 (1)**, 145–163.

Jones, H. and J. Marshall, 1997: Restratification after deep convection. *J. Phys. Oceanogr.*, **27 (10)**, 2276–2287.

Jonker, R. and A. Volgenant, 1987: A shortest augmenting path algorithm for dense and sparse linear assignment problems. *Computing*, **38 (4)**, 325–340.

Jullion, L., S. C. Jones, A. C. Naveira Garabato, and M. P. Meredith, 2010: Wind-controlled export of Antarctic Bottom Water from the Weddell Sea. *Geophys. Res. Lett.*, **37 (9)**, L09 609.

Kida, S., 2011: The impact of open oceanic processes on the Antarctic Bottom Water outflows. *J. Phys. Oceanogr.*, **41 (10)**, 1941–1957.

Killworth, P. D., 1979: On chimney formations in the ocean. *Journal of Physical Oceanography*, **9 (3)**, 531–554.

Knorr, G. and G. Lohmann, 2007: Rapid transitions in the atlantic thermohaline circulation triggered by global warming and meltwater during the last deglaciation. *Geochemistry, Geophysics, Geosystems*, **8 (12)**.

Knutti, R., J. Flückiger, T. Stocker, and A. Timmermann, 2004: Strong hemispheric coupling of glacial climate through freshwater discharge and ocean circulation. *Nature*, **430 (7002)**, 851–856.

Krokhmal, P. A. and P. M. Pardalos, 2009: Random assignment problems. *Eur. J. Oper. Res.*, **194 (1)**, 1–17.

Kuhn, H. W., 1955: The hungarian method for the assignment problem. *Naval research logistics quarterly*, **2 (1-2)**, 83–97.

Landau, L. D. and E. M. Lifshitz, 1959: *Fluid mechanics*. Pergamon Press.

Lange, M. A., S. F. Ackley, P. Wadhams, G. S. Dieckmann, and H. Eicken, 1989: Development of sea ice in the Weddell Sea. *Ann. Glaciol.*, **12**, 92–96.

Large, W. G., J. C. McWilliams, and S. C. Doney, 1994: Oceanic vertical mixing: A review and a model with a nonlocal boundary layer parameterization. *Reviews of Geophysics*, **32 (4)**, 363–403.

Large, W. G. and S. G. Yeager, 2009: The global climatology of an interannually varying air–sea flux data set. *Climate Dynam.*, **33 (2-3)**, 341–364.

Lawler, E. L., 1976: *Combinatorial Optimization: Networks and Matroids*. Courier Corporation.

Ledwell, J. R., A. Watson, and C. S. Law, 1993: Evidence for slow mixing across the pycnocline from an open-ocean tracer-release experiment. *Nature*, **364 (6439)**, 701–703.

Liu, Z., et al., 2009: Transient simulation of last deglaciation with a new mechanism for bølling-allerød warming. *Science*, **325 (5938)**, 310–314.

Locarnini, R. A., T. Whitworth, and W. D. Nowlin, 1993: The importance of the Scotia Sea on the outflow of Weddell Sea Deep Water. *J. Mar. Res.*, **51 (1)**, 135–153.

Lorenz, E. N., 1955: Available potential energy and the maintenance of the general circulation. *Tellus*, **7 (2)**, 157–167.

Macdonald, A. M. and C. Wunsch, 1996: An estimate of global ocean circulation and heat fluxes. *Nature*, **382 (6590)**, 436–439.

Marcott, S. A., et al., 2011: Ice-shelf collapse from subsurface warming as a trigger for heinrich events. *Proceedings of the National Academy of Sciences*, **108 (33)**, 13 415–13 419.

Marshall, J. and T. Radko, 2003: Residual-mean solutions for the Antarctic Circumpolar Current and its associated overturning circulation. *J. Phys. Oceanogr.*, **33 (11)**, 2341–2354.

Marshall, J. and F. Schott, 1999: Open-ocean convection: Observations, theory, and models. *Rev. Geophys.*, **37 (1)**, 1–64.

Marshall, J. and K. Speer, 2012: Closure of the meridional overturning circulation through southern ocean upwelling. *Nature Geoscience*, **5 (3)**, 171–180.

Martello, S., D. Pisinger, and D. Vigo, 2000: The three-dimensional bin packing problem. *Oper. Res.*, **48 (2)**, 256–267.

Martello, S. and P. Toth, 1987: Linear assignment problems. *North-Holland Math. Stud.*, **132**, 259–282.

Martinson, D. G., 1990: Evolution of the southern ocean winter mixed layer and sea ice: Open ocean deepwater formation and ventilation. *Journal of Geophysical Research: Oceans*, **95 (C7)**, 11 641–11 654.

McDougall, T. J., 1987: Thermobaricity, cabbeling, and water-mass conversion. *J. Geophys. Res.: Oceans*, **92 (C5)**, 5448–5464.

McDougall, T. J., 2003: Potential enthalpy: A conservative oceanic variable for evaluating heat content and heat fluxes. *J. Phys. Oceanogr.*, **33 (5)**, 945–963.

McKee, D. C., X. Yuan, A. L. Gordon, B. A. Huber, and Z. Dong, 2011: Climate

impact on interannual variability of Weddell Sea Bottom Water. *J. Geophys. Res.: Oceans*, **116**, C5020.

McManus, J., R. Francois, J.-M. Gherardi, L. Keigwin, and S. Brown-Leger, 2004: Collapse and rapid resumption of atlantic meridional circulation linked to deglacial climate changes. *Nature*, **428 (6985)**, 834–837.

McPhee, M. G., 2000: Marginal thermobaric stability in the ice-covered upper ocean over Maud Rise. *J. Phys. Oceanogr.*, **30 (11)**, 2710–2722.

McPhee, M. G., 2003: Is thermobaricity a major factor in Southern Ocean ventilation? *Antarct. Sci.*, **15 (01)**, 153–160.

McPhee, M. G., et al., 1996: The antarctic zone flux experiment. *Bull. Amer. Meteor. Soc.*, **77 (6)**, 1221–1232.

Mechoso, C. R., 1980: Baroclinic instability of flows along sloping boundaries. *J. Atmos. Sci.*, **37 (6)**, 1393–1399.

Menemenlis, D., J.-M. Campin, P. Heimbach, C. Hill, T. Lee, A. Nguyen, M. Schodlok, and H. Zhang, 2008: Ecco2: High resolution global ocean and sea ice data synthesis. *Mercator Ocean Quarterly Newsletter*, **31**, 13–21.

Meredith, M. P., A. L. Gordon, A. C. Naveira Garabato, E. P. Abrahamsen, B. A. Huber, L. Jullion, and H. J. Venables, 2011: Synchronous intensification and warming of Antarctic Bottom Water outflow from the Weddell Gyre. *Geophys. Res. Lett.*, **38**, L03 603.

Meredith, M. P., A. C. Naveira Garabato, A. L. Gordon, and G. C. Johnson, 2008: Evolution of the Deep and Bottom Waters of the Scotia Sea, Southern Ocean, during 1995-2005. *J. Climate*, **21 (13)**, 3327–3343.

Mignot, J., A. Ganopolski, and A. Levermann, 2007: Atlantic subsurface temperatures: Response to a shutdown of the overturning circulation and consequences for its recovery. *Journal of Climate*, **20 (19)**, 4884–4898.

Mikolajewicz, U. and E. Maier-Reimer, 1994: Mixed boundary conditions in ocean general circulation models and their influence on the stability of the model's conveyor belt. *Journal of Geophysical Research: Oceans*, **99 (C11)**, 22 633–22 644.

Muench, R. D. and A. L. Gordon, 1995: Circulation and transport of water along the western Weddell Sea margin. *J. Geophys. Res.: Oceans*, **100**, 18–18.

Munday, D. R., H. L. Johnson, and D. P. Marshall, 2013: Eddy Saturation of Equilibrated Circumpolar Currents. *J. Phys. Oceanogr.*, **43 (3)**, 507–532.

Naveira Garabato, A. C., E. L. McDonagh, D. P. Stevens, K. J. Heywood, and R. J. Sanders, 2002: On the export of Antarctic bottom water from the Weddell Sea. *Deep-Sea Res. Pt. II*, **49 (21)**, 4715–4742.

Naveira Garabato, A. C., K. L. Polzin, B. A. King, K. J. Heywood, and M. Visbeck, 2004: Widespread intense turbulent mixing in the Southern Ocean. *Science*, **303 (5655)**, 210–213.

Newsom, E. R., C. M. Bitz, F. O. Bryan, R. Abernathey, and P. R. Gent, 2016:

Southern ocean deep circulation and heat uptake in a high-resolution climate model. *Journal of Climate*, **29 (7)**, 2597–2619.

Nøst, O., M. Biuw, V. Tverberg, C. Lydersen, T. Hattermann, Q. Zhou, L. H. Smedsrud, and K. M. Kovacs, 2011: Eddy overturning of the Antarctic Slope Front controls glacial melting in the Eastern Weddell Sea. *J. Geophys. Res.: Oceans*, **116 (C11)**, C11 014.

Orsi, A., G. Johnson, and J. Bullister, 1999: Circulation, mixing, and production of antarctic bottom water. *Progress in Oceanography*, **43 (1)**, 55–109.

Orsi, A. H. and C. L. Wiederwohl, 2009: A recount of Ross Sea waters. *Deep-Sea Res. II*, **56 (13)**, 778–795.

Ou, H. W., 2007: Watermass Properties of the Antarctic Slope Front: A Simple Model. *J. Phys. Oceanogr.*, **37 (1)**, 50–59.

Parkinson, C. L. and D. J. Cavalieri, 2012: Antarctic sea ice variability and trends, 1979–2010. *The Cryosphere Discuss.*, **6 (2)**, 931–956.

Pedlosky, J., 1987: *Geophysical fluid dynamics*. Springer-Verlag New York Inc.

Pennel, R., A. Stegner, and K. Béranger, 2012: Shelf Impact on Buoyant Coastal Current Instabilities. *J. Phys. Oceanogr.*, **42**, 39–61.

Plumb, R. A. and R. Ferrari, 2005: Transformed Eulerian-mean theory. Part I: Nonquasigeostrophic theory for eddies on a zonal-mean flow. *J. Phys. Oceanogr.*, **35 (2)**, 165–174.

Polvani, L. M. and K. L. Smith, 2013: Can natural variability explain observed Antarctic sea ice trends? New modeling evidence from CMIP5. *Geophys. Res. Lett.*

Press, W. H., 2007: *Numerical recipes 3rd edition: The art of scientific computing*. Cambridge university press.

Radko, T., A. Bulters, J. D. Flanagan, and J.-M. Campin, 2014: Double-diffusive recipes. Part I: Large-scale dynamics of thermohaline staircases. *J. Phys. Oceanogr.*, **44 (5)**, 1269–1284.

Rahmstorf, S., 1995: Multiple convection patterns and thermohaline flow in an idealized ogcm. *Journal of Climate*, **8 (12)**, 3028–3039.

Rahmstorf, S., 1996: Bifurcations of the atlantic thermohaline circulation in response to changes in the hydrological cycle. *Oceanographic Literature Review*, **5 (43)**, 435.

Rahmstorf, S., 2002: Ocean circulation and climate during the past 120,000 years. *Nature*, **419 (6903)**, 207–214.

Rahmstorf, S. and R. Alley, 2002: Stochastic resonance in glacial climate. *Eos, Transactions American Geophysical Union*, **83 (12)**, 129–135.

Rahmstorf, S. et al., 1994: Rapid climate transitions in a coupled ocean-atmosphere model. *Nature*, **372 (6501)**, 82–85.

Rasmussen, T. L., D. W. Oppo, E. Thomsen, and S. J. Lehman, 2003: Deep sea

records from the southeast labrador sea: Ocean circulation changes and ice-rafting events during the last 160,000 years. *Paleoceanography*, **18 (1)**.

Rasmussen, T. L. and E. Thomsen, 2004: The role of the north atlantic drift in the millennial timescale glacial climate fluctuations. *Palaeogeography, Palaeoclimatology, Palaeoecology*, **210 (1)**, 101–116.

Reddy, J. N., 2002: *Energy principles and variational methods in applied mechanics*. John Wiley & Sons.

Reid, R. O., B. A. Elliott, and D. B. Olson, 1981: Available Potential Energy: A Clarification. *J. Phys. Oceanogr.*, **11 (1)**, 15–29.

Renfrew, I., J. C. King, and T. Markus, 2002: Coastal polynyas in the southern Weddell Sea: Variability of the surface energy budget. *J. Geophys. Res.: Oceans*, **107 (C6)**, 16–1.

Rintoul, S., C. Hughes, and D. Olbers, 2001: The antarctic circumpolar current system. *In: Ocean Circulation and Climate/G. Siedler, J. Church and J. Gould, eds. New York: Academic Press. p.*, 271–302.

Roullet, G., X. Capet, and G. Maze, 2014: Global interior eddy available potential energy diagnosed from argo floats. *Geophysical Research Letters*, **41 (5)**, 1651–1656.

Roullet, G. and P. Klein, 2009: Available potential energy diagnosis in a direct numer-

ical simulation of rotating stratified turbulence. *Journal of fluid mechanics*, **624**, 45–55.

Roullet, G. and P. Klein, 2010: Cyclone-anticyclone asymmetry in geophysical turbulence. *Physical review letters*, **104 (21)**, 218 501.

Roullet, G., J. C. McWilliams, X. Capet, and M. J. Molemaker, 2012: Properties of steady geostrophic turbulence with isopycnal outcropping. *Journal of Physical Oceanography*, **42 (1)**, 18–38.

Saenz, J. A., R. Tailleux, E. D. Butler, G. O. Hughes, and K. I. Oliver, 2015: Estimating lorenz's reference state in an ocean with a nonlinear equation of state for seawater. *Journal of Physical Oceanography*, **45 (5)**, 1242–1257.

Salby, M. L., 1996: *Fundamentals of atmospheric physics*, Vol. 61. Academic press.

Sallée, J., K. Speer, R. Morrow, and R. Lumpkin, 2008: An estimate of lagrangian eddy statistics and diffusion in the mixed layer of the southern ocean. *Journal of Marine Research*, **66 (4)**, 441–463.

Schmid, M., N. M. Budnev, N. G. Granin, M. Sturm, M. Schurter, and A. Wüest, 2008: Lake baikal deepwater renewal mystery solved. *Geophys. Res. Lett.*, **35 (9)**.

Schott, F. and K. D. Leaman, 1991: Observations with moored acoustic Doppler current profilers in the convection regime in the Golfe du Lion. *J. Phys. Oceanogr.*, **21 (4)**, 558–574.

Schott, F., M. Visbeck, and J. Fischer, 1993: Observations of vertical currents and convection in the central Greenland Sea during the winter of 1988–1989. *J. Geophys. Res.: Oceans*, **98 (C8)**, 14 401–14 421.

Shaffer, G., S. M. Olsen, and C. J. Bjerrum, 2004: Ocean subsurface warming as a mechanism for coupling dansgaard-oeschger climate cycles and ice-rafting events. *Geophysical Research Letters*, **31 (24)**.

Shakun, J. D., et al., 2012: Global warming preceded by increasing carbon dioxide concentrations during the last deglaciation. *Nature*, **484 (7392)**, 49–54.

Spall, M. A., 2004: Boundary currents and watermass transformation in marginal seas. *J. Phys. Oceanogr.*, **34 (5)**, 1197–1213.

Steffensen, J. P., et al., 2008: High-resolution greenland ice core data show abrupt climate change happens in few years. *Science*, **321 (5889)**, 680–684.

Stewart, A. L. and A. F. Thompson, 2013: Connecting antarctic cross-slope exchange with southern ocean overturning. *Journal of Physical Oceanography*, **43 (7)**, 1453–1471.

Stone, P. H., 1972: A simplified radiative-dynamical model for the static stability of rotating atmospheres. *J. Atmos. Sci*, **29 (3)**, 405–418.

Stouffer, R. J., et al., 2006: Investigating the causes of the response of the thermohaline circulation to past and future climate changes. *Journal of Climate*, **19 (8)**, 1365–1387.

Su, Z. and A. P. Ingersoll, 2016: On the minimum potential energy state and the eddy-size-constrained ape density. *Journal of Physical Oceanography*, accepted.

Su, Z., A. P. Ingersoll, and F. He, 2016a: On the abruptness of bolling-allerod warming. *Journal of Climate*, doi:10.1175/JCLI–D–15–0675.1.

Su, Z., A. P. Ingersoll, A. L. Stewart, and A. F. Thompson, 2016b: Ocean convective available potential energy. part i: Concept and calculation. *Journal of Physical Oceanography*, **46 (4)**, 1081–1096.

Su, Z., A. P. Ingersoll, A. L. Stewart, and A. F. Thompson, 2016c: Ocean convective available potential energy. part ii: Energetics of thermobaric convection and thermobaric cabbeling. *Journal of Physical Oceanography*, **46 (4)**, 1097–1115.

Su, Z., A. L. Stewart, and A. F. Thompson, 2014: An idealized model of weddell gyre export variability. *Journal of Physical Oceanography*, **44 (6)**, 1671–1688.

Tailleux, R., 2013a: Available potential energy and exergy in stratified fluids. *Annual Review of Fluid Mechanics*, **45 (1)**, 35.

Tailleux, R., 2013b: Available potential energy density for a multicomponent boussinesq fluid with arbitrary nonlinear equation of state. *Journal of Fluid Mechanics*, **735**, 499–518.

Talley, L. D., V. Lobanov, V. Ponomarev, A. Salyuk, P. Tishchenko, I. Zhabin, and S. Riser, 2003: Deep convection and brine rejection in the Japan Sea. *Geophys. Res. Lett.*, **30 (4)**, 1159.

Talley, L. D., P. Tishchenko, V. Luchin, A. Nedashkovskiy, S. Sagalaev, D. J. Kang, M. Warner, and D. H. Min, 2004: Atlas of Japan (East) Sea hydrographic properties in summer, 1999. *Prog. Oceanogr.*, **61 (2)**, 277–348.

Thiagarajan, N., A. V. Subhas, J. R. Southon, J. M. Eiler, and J. F. Adkins, 2014: Abrupt pre-bolling-allerod warming and circulation changes in the deep ocean. *Nature*, **511 (7507)**, 75–78.

Thompson, A. F., 2010: Jet formation and evolution in baroclinic turbulence with simple topography. *Journal of Physical Oceanography*, **40 (2)**, 257–278.

Thompson, A. F. and K. J. Heywood, 2008: Frontal structure and transport in the northwestern Weddell Sea. *Deep-Sea Res. Pt. I*, **55 (10)**, 1229–1251.

Thompson, A. F. and A. C. Naveira Garabato, 2014: Equilibration of the antarctic circumpolar current by standing meanders. *Journal of Physical Oceanography*, **44 (7)**, 1811–1828.

Thompson, A. F. and J.-B. Sallée, 2012: Jets and topography: Jet transitions and the impact on transport in the antarctic circumpolar current. *Journal of physical Oceanography*, **42 (6)**, 956–972.

Trenberth, K., 2005: Uncertainty in Hurricanes and Global Warming. *Science*, **308 (5729)**, 1753–1754.

Tseng, Y.-h. and J. H. Ferziger, 2001: Mixing and available potential energy in stratified flows. *Physics of Fluids (1994-present)*, **13 (5)**, 1281–1293.

Tulloch, R., J. Marshall, C. Hill, and K. S. Smith, 2011: Scales, growth rates, and spectral fluxes of baroclinic instability in the ocean. *Journal of Physical Oceanography*, **41 (6)**, 1057–1076.

Turner, J. S., 1979: *Buoyancy effects in fluids*. Cambridge University Press.

Vallis, G. K., 2006: *Atmospheric and oceanic fluid dynamics: fundamentals and large-scale circulation*. Cambridge University Press.

Visbeck, M., J. Marshall, T. Haine, and M. Spall, 1997: Specification of eddy transfer coefficients in coarse-resolution ocean circulation models*. *Journal of Physical Oceanography*, **27 (3)**, 381–402.

Wadhams, P., J. Holfort, E. Hansen, and J. P. Wilkinson, 2002: A deep convective chimney in the winter Greenland Sea. *Geophys. Res. Lett.*, **29 (10)**, 76–1.

Wang, Q., S. Danilov, E. Fahrbach, J. Schröter, and T. Jung, 2012: On the impact of wind forcing on the seasonal variability of Weddell Sea Bottom Water transport. *Geophys. Res. Lett.*, **39 (6)**, 6603.

Weaver, A. J., O. A. Saenko, P. U. Clark, and J. X. Mitrovica, 2003: Meltwater pulse 1a from antarctica as a trigger of the bølling-allerød warm interval. *Science*, **299 (5613)**, 1709–1713.

Weiss, R. F., E. C. Carmack, and V. M. Koropalov, 1991: Deep-water renewal and biological production in Lake Baikal. *Nature*, **349 (6311)**, 665–669.

Williams, R. G., C. Wilson, and C. W. Hughes, 2007: Ocean and atmosphere storm tracks: The role of eddy vorticity forcing. *Journal of Physical Oceanography*, **37 (9)**, 2267–2289.

Winters, K. B. and R. Barkan, 2013: Available potential energy density for boussinesq fluid flow. *Journal of Fluid Mechanics*, **714**, 476–488.

Winters, K. B., P. N. Lombard, J. J. Riley, and E. A. D'Asaro, 1995: Available potential energy and mixing in density-stratified fluids. *J. Fluid Mech.*, **289**, 115–128.

Winton, M., 1995: Energetics of deep-decoupling oscillations. *Journal of physical oceanography*, **25 (3)**, 420–427.

Winton, M. and E. Sarachik, 1993: Thermohaline oscillations induced by strong steady salinity forcing of ocean general circulation models. *Journal of Physical Oceanography*, **23 (7)**, 1389–1410.

Wolfe, C. L. and P. Cessi, 2011: The adiabatic pole-to-pole overturning circulation. *Journal of Physical Oceanography*, **41 (9)**, 1795–1810.

Yin, F., 1995: A mechanistic model of ocean interdecadal thermohaline oscillations. *Journal of physical oceanography*, **25 (12)**, 3239–3246.

Young, W. R., 2010: Dynamic Enthalpy, Conservative Temperature, and the Seawater Boussinesq Approximation. *J. Phys. Oceanogr.*, **40 (2)**, 394–400.

Zhai, X. and D. P. Marshall, 2013: Vertical eddy energy fluxes in the north atlantic subtropical and subpolar gyres. *Journal of Physical Oceanography*, **43 (1)**, 95–103.

Zhang, G. J., 2009: Effects of entrainment on convective available potential energy and closure assumptions in convection parameterization. *J. Geophys. Res.: Atmos.*, **114 (D7)**.

Zhang, G. J. and N. A. McFarlane, 1995: Sensitivity of Climate Simulations to the Parameterization of Cumulus Convection in the Canadian Climate Centre General Circulation Model. *Atmos.-Ocean*, **33 (3)**, 407–446.

Zhang, X., G. Lohmann, G. Knorr, and C. Purcell, 2014: Abrupt glacial climate shifts controlled by ice sheet changes. *Nature*, **512 (7514)**, 290–294.

Zhu, J., Z. Liu, X. Zhang, I. Eisenman, and W. Liu, 2014: Linear weakening of the amoc in response to receding glacial ice sheets in ccsm3. *Geophysical Research Letters*, **41 (17)**, 6252–6258.